



TECHNICAL REPORT 0-7001-1
TxDOT PROJECT NUMBER 0-7001

Utilizing Steel Fiber Reinforced Concrete as a Substitute Reinforcement for CIP- PCP Bridge Deck

Soon Kwang Jeong
Hansol Jang
Yongjae Yu
Elias Saqan
Hwa-Ching Wang
Thanos Drimalas
Zach Webb
Kevin Folliard
Oguzhan Bayrak

November 2023

Published March 2025

<https://library.ctr.utexas.edu/ctr-publications/0-7001-1.pdf>



Technical Report Documentation Page

| | | | | | |
|--|--|--------------------------------|--|---|--|
| 1. Report No. FHWA/TX-25/0-7001-1 | | 2. Government Accession No. | | 3. Recipient's Catalog No. | |
| 4. Title and Subtitle Utilizing Steel Fiber Reinforced Concrete as a Substitute Reinforcement for CIP-PCP Bridge Deck | | | | 5. Report Date Submitted: November 2023 | |
| | | | | 6. Performing Organization Code | |
| 7. Author(s) Soon Kwang Jeong, Hansol Jang, Yongjae Yu, Elias Saqan, Hwa-Ching Wang, Thanos Drimalas, Zach Webb, Kevin Folliard, Oguzhan Bayrak | | | | 8. Performing Organization Report No. 0-7001-1 | |
| 9. Performing Organization Name and Address Center for Transportation Research The University of Texas at Austin 3925 W. Braker Lane, 4 th Floor Austin, TX 78759 | | | | 10. Work Unit No. (TRAIS) | |
| | | | | 11. Contract or Grant No. 0-7001 | |
| 12. Sponsoring Agency Name and Address Texas Department of Transportation Research and Technology Implementation Division P.O. Box 5080 Austin, TX 78763-5080 | | | | 13. Type of Report and Period Covered Technical Report May 2019 – December 2023 | |
| | | | | 14. Sponsoring Agency Code | |
| 15. Supplementary Notes Project performed in cooperation with the Texas Department of Transportation. | | | | | |
| 16. Abstract This research focuses on optimizing the design of cast-in-place, precast-panel (CIP-PCP) bridge decks by developing recommendations for standard ready-mix steel fiber reinforced concrete (SFRC) using domestically produced steel fibers. The project, stemming from the efficient and durable nature of CIP-PCP decks, builds upon prior work at the University of Texas and aims to minimize the reliance on conventional reinforcement in the CIP sections by adding steel fibers as an alternative reinforcement. The research team conducted extensive material and structural testing to identify the optimal SFRC and reinforcement layout for CIP-PCP bridge decks. Experimental results indicate that SFRC with fibers longer than 1.5 inches and a service residual flexural strength exceeding 480 psi can effectively replace the current reinforcement used in the interior span of CIP-PCP bridge decks. Further analysis of the overhang region suggests that SFRC has the potential to substitute for 31% of the existing TxDOT reinforcement. | | | | | |
| 17. Key Words Steel Fiber, Fiber-Reinforced Concrete, CIP-PCP, Bridge Deck | | | | 18. Distribution Statement No restrictions. This document is available to the public through the National Technical Information Service, Springfield, Virginia 22161; www.ntis.gov . | |
| 19. Security Classif. (of report) Unclassified | 20. Security Classif. (of this page) Unclassified | 21. No. of pages 209 | | 22. Price | |



THE UNIVERSITY OF TEXAS AT AUSTIN
CENTER FOR TRANSPORTATION RESEARCH

Utilizing Steel Fiber Reinforced Concrete as a Substitute Reinforcement for CIP-PCP Bridge Deck

Soon Kwang Jeong
Hansol Jang
Yongjae Yu
Elias Saqan
Hwa-Ching Wang
Thanos Drimalas
Zachary D. Webb
Kevin Folliard
Oguzhan Bayrak

| | |
|-----------------------|---|
| CTR Technical Report: | 0-7001-1 |
| Report Date: | Submitted: December 2023 |
| Project: | 0-7001 |
| Project Title: | Utilizing Steel Fiber Reinforced Concrete as a Substitute Reinforcement for CIP-PCP Bridge Deck |
| Sponsoring Agency: | Texas Department of Transportation |
| Performing Agency: | Center for Transportation Research at The University of Texas at Austin |

Project performed in cooperation with the Texas Department of Transportation and the Federal Highway Administration.

Center for Transportation Research
The University of Texas at Austin
3925 W. Braker Lane, 4th floor
Austin, TX 78759

<http://ctr.utexas.edu/>

Disclaimers

Author's Disclaimer: The contents of this report reflect the views of the authors, who are responsible for the facts and the accuracy of the data presented herein. The contents do not necessarily reflect the official view or policies of the Federal Highway Administration or the Texas Department of Transportation (TxDOT). This report does not constitute a standard, specification, or regulation.

Patent Disclaimer: There was no invention or discovery conceived or first actually reduced to practice in the course of or under this contract, including any art, method, process, machine manufacture, design or composition of matter, or any new useful improvement thereof, or any variety of plant, which is or may be patentable under the patent laws of the United States of America or any foreign country.

Engineering Disclaimer

NOT INTENDED FOR CONSTRUCTION, BIDDING, OR PERMIT PURPOSES.

Project Engineer: Oguzhan Bayrak

Professional Engineer License State and Number: Texas No. 106598

P.E. Designation: Research Supervisor

Acknowledgments

The authors extend sincere gratitude to the Texas Department of Transportation (TxDOT) for generously funding and supporting this research study. The invaluable contributions of the project manager, Joanne Steele, and the dedicated members of the Project Monitoring Committee – Steven Austin, Rachel Cano, Lianxiang Du, Christina Gutierrez, Andy Naranjo, Joe Roche, Ahmed Al-Basha, Nader Mavaddat, Niyi Arowojolu – significantly enhanced the overall success and impact of this project.

Table of Contents

| | |
|---|----|
| Chapter 1. Introduction | 1 |
| 1.1. Overview | 1 |
| 1.2. Scopes and Objectives | 1 |
| 1.3. Organization of Report | 2 |
| Chapter 2. Literature Review | 4 |
| 2.1. Notation..... | 4 |
| 2.2. State-of-the-Art in SFRC | 5 |
| 2.2.1. Fiber Properties | 5 |
| 2.2.2. Typical Mix Design | 8 |
| 2.2.3. Material Properties..... | 11 |
| 2.2.4. Durability of SFRC | 14 |
| 2.2.5. Design Specifications and Guidelines for SFRC | 16 |
| 2.3. Mechanical Properties for Structural Modeling..... | 22 |
| 2.3.1. Behavior in Compression..... | 22 |
| 2.3.2. Behavior in Tension..... | 31 |
| 2.4. Experimental Investigations of SFRC | 37 |
| 2.4.1. PCP-CIP Bridge Deck Construction | 37 |
| 2.4.2. SFRC in Bridge Decks and flat slabs..... | 41 |
| 2.4.3. SFRC in Beams and other structures | 46 |
| 2.4.4. Conclusions..... | 50 |
| 2.5. Analytical Investigations of SFRC Structure..... | 50 |
| 2.5.1. Membrane and Shell Elements | 50 |
| 2.5.2. Slabs and Decks | 54 |
| 2.5.3. Beams..... | 56 |
| 2.5.4. Conclusions..... | 57 |
| 2.6. Summary and Conclusions | 57 |
| Chapter 3. Laboratory Evaluation of Steel Fibers for TxDOT Class S Concrete. 59 | |
| 3.1. Overview of Materials | 59 |
| 3.1.1. Characterization of Materials..... | 60 |
| 3.2. Fresh Properties of FRC Mixtures | 61 |
| 3.2.1. Slump, Air Content, Fresh Temperature | 61 |
| 3.2.2. Set Time, Bleed Water, and Unit Weight | 63 |
| 3.3. Hardened Properties of FRC Concrete | 65 |

| | |
|---|-----|
| 3.3.1. Compressive Strength | 65 |
| 3.3.2. Splitting Tensile Strength | 68 |
| 3.3.3. Elastic Modulus | 70 |
| 3.3.4. Drying Shrinkage | 73 |
| 3.3.5. Coefficient of Thermal Expansion..... | 75 |
| 3.3.6. Impact Testing | 76 |
| 3.3.7. Flexural Toughness (ASTM C1609) | 77 |
| 3.3.8. Simplified Double-Punch Test..... | 78 |
| 3.4. Durability of SFRC Concrete..... | 80 |
| 3.4.1. Alkali-Silica Reaction..... | 80 |
| 3.4.2. Chloride Diffusion and Corrosion Potential | 80 |
| 3.4.3. Freezing and Thawing..... | 82 |
| 3.4.4. Salt Scaling | 82 |
| 3.5. Summary | 84 |
| Chapter 4. Deck Strip Test..... | 85 |
| 4.1. Overview | 85 |
| 4.2. Design of Test Matrix | 85 |
| 4.2.1. Types of Concrete | 85 |
| 4.2.2. Types of SFRC..... | 86 |
| 4.2.3. Specimen Dimension | 86 |
| 4.3. Specimen Preparation | 87 |
| 4.3.1. Precast panel fabrication | 87 |
| 4.3.2. Specimen Casting..... | 89 |
| 4.4. Material Testing and Properties | 91 |
| 4.4.1. Fresh Concrete Properties: Slump Test..... | 91 |
| 4.4.2. Examination of Panel Girder Gap..... | 91 |
| 4.4.3. Uniaxial Compression and MOE Tests..... | 92 |
| 4.4.4. Flexural Bending Test (ASTM C1609) | 93 |
| 4.4.5. Uniaxial Tension Test..... | 95 |
| 4.5. Test Setup and Instrumentation | 97 |
| 4.6. Test Results | 98 |
| 4.6.1. Longitudinal Direction..... | 98 |
| 4.6.2. Transverse Direction | 106 |
| 4.7. Test Result Analysis | 119 |

| | |
|---|-----|
| 4.7.1. Effect of Fiber Types | 119 |
| 4.7.2. Effect of Fiber Dosage | 121 |
| 4.7.3. Specimens without Reinforcement | 122 |
| 4.8. Summary and Conclusions | 123 |
| Chapter 5. Numerical Analysis of Structure | 125 |
| 5.1. Overview | 125 |
| 5.2. Initial Model Assessment..... | 125 |
| 5.3. Analysis of SFRC Slab Strips | 130 |
| 5.3.1. Series 1 | 130 |
| 5.3.2. Series 2..... | 141 |
| 5.4. Numerical Assessment of Modified Reinforcement Requirements..... | 150 |
| 5.5. Summary and Conclusions | 152 |
| Chapter 6. Full-Scale Test..... | 153 |
| 6.1. Overview | 153 |
| 6.2. Full-Scale Specimen Testing Program..... | 153 |
| 6.2.1. Specimen Configuration and Test Matrix | 153 |
| 6.2.2. Limit States | 155 |
| 6.3. Specimen Preparation | 156 |
| 6.3.1. Precast Panel Fabrication | 156 |
| 6.3.2. Preparation Before Casting | 156 |
| 6.3.3. Concrete Casting | 156 |
| 6.4. Material Testing and Results | 158 |
| 6.4.1. Fresh Concrete Properties: Slump Test..... | 158 |
| 6.4.2. Uniaxial Compression and MOE Tests..... | 159 |
| 6.4.3. Flexural Bending Test (ASTM C1609) | 160 |
| 6.4.4. Uniaxial Tension Test | 161 |
| 6.5. Test Setup and Instrumentation | 162 |
| 6.6. Test Results..... | 164 |
| 6.6.1. Differential shrinkage measurement | 165 |
| 6.6.2. Single Axle Load | 165 |
| 6.6.3. Tandem Axle Load | 170 |
| 6.6.4. Overhang Load..... | 175 |
| 6.7. Analysis of Test Results..... | 181 |
| 6.7.1. Load-Displacement Curves..... | 182 |

| | |
|--|-----|
| 6.7.2. Reinforcement Strain Limit | 182 |
| 6.7.3. Crack Resisting Performance..... | 183 |
| 6.8. Overhang: Yield-Line Analysis | 184 |
| 6.9. Summary and Conclusions | 187 |
| Chapter 7. Conclusion and Design Recommendations | 189 |
| 7.1. Overview | 189 |
| 7.2. Findings from Material Testing Program | 189 |
| 7.3. Findings from Casting Structural Specimen | 189 |
| 7.4. Findings from Deck Strip Test Result | 190 |
| 7.4.1. Material Testing | 190 |
| 7.4.2. Structural Testing..... | 192 |
| 7.5. Findings from Full-Scale Test Result | 194 |
| 7.5.1. Structural Testing..... | 194 |
| 7.5.2. Yield-line Analysis | 196 |
| 7.6. Recommendations..... | 197 |
| Chapter 8. Value of Research | 198 |
| 8.1. Introduction..... | 198 |
| 8.2. Contribution to Knowledge..... | 198 |
| 8.3. Improvement on Engineering Design | 199 |
| 8.4. Cost-effectiveness | 199 |
| 8.5. Safety | 199 |
| References..... | 200 |
| Appendix A. Sectional Analysis of Deck Strip | 209 |

List of Tables

| | |
|--|-----|
| Table 2.1 Bedding strip dimensions (TxDOT bridge design specifications, 2018) | 40 |
| Table 2.2 Transverse and longitudinal reinforcement for PCP(TxDOT bridge design specifications, 2018)..... | 40 |
| Table 3.1 Materials being evaluated in the laboratory testing program | 59 |
| Table 3.2 Description of steel fibers evaluated in this project..... | 60 |
| Table 3.3 Chemical Composition of Cementitious Materials (% by mass)..... | 60 |
| Table 3.4 Mixture proportions used in laboratory testing program | 61 |
| Table 3.5 Fresh Concrete Properties containing Steel Fiber (SFS) | 62 |
| Table 3.6 Fresh Concrete Properties containing Steel Fiber (SFD)..... | 62 |
| Table 3.7 Fresh Concrete Properties containing Steel Fiber (SFH)..... | 63 |
| Table 3.8 Results of ASTM C1609 flexural toughness testing. | 78 |
| Table 3.9 Visual Rating of Concrete Surface per ASTM C672 | 83 |
| Table 4.1 Class S concrete specification..... | 85 |
| Table 4.2 Three types of steel fibers | 86 |
| Table 4.3 Test matrix | 87 |
| Table 4.4 Slab-strip specimen uniaxial compression test results..... | 92 |
| Table 4.5 Slab-strip specimen flexural test results | 93 |
| Table 4.6 Direct tension test results | 95 |
| Table 5.1 Summary of Series 1 reinforcement details | 131 |
| Table 5.2 Overview of Series 1 specimen capacity predictions | 132 |
| Table 5.3 Summary of Series 2 reinforcement details | 142 |
| Table 5.4 Overview of Series 1 specimen capacity predictions | 142 |
| Table 6.1 Reinforcement layout for each region | 155 |
| Table 6.2 AASHTO LRFD (2020) load factors and maximum factored load.... | 155 |
| Table 6.3 Slab-strip specimen material test results..... | 159 |
| Table 6.4 ASTM C1609/C1609M Flexural beam test results | 160 |
| Table 6.5 Direct tension test results | 161 |
| Table 6.6 Moment capacities calculated for yield-line analysis | 186 |
| Table 6.7 Summary of yield-line analysis for overhang regions | 187 |
| Table 8.1 Selected Benefit Area of Project 0-7001 | 198 |

List of Figures

| | |
|---|----|
| Figure 1.1 Standard design detail for CIP-PCP bridge deck on prestressed concrete I-beam (Reprinted from TxDOT Bridge Division Standards (2015))..... | 1 |
| Figure 2.1 Types of fibers (ACI 544, 2018) | 5 |
| Figure 2.2 Strain hardening and softening (Birely et al., 2018) | 7 |
| Figure 2.3 Fiber workability with respect to factors (Chu, Li, Kwan, 2018) | 10 |
| Figure 2.4 Tension testing methods for concrete (Bayrak et al., 2013)..... | 12 |
| Figure 2.5 Fiber orientation from X-ray scan (Suuronen et al., 2014) | 13 |
| Figure 2.6 Actual and simplified stress distribution of SFRC (ACI 544, 2018) .. | 18 |
| Figure 2.7 Flexural and normal stress distribution of SFRC (ACI 544, 2018)..... | 20 |
| Figure 2.8 Example of compressive stress-strain responses of plain concrete and SFRC..... | 23 |
| Figure 2.9 Post-cracking behavior of concrete (NC) and fiber-reinforced concrete (FRC) (Lee et al., 2011a) | 32 |
| Figure 2.10 Final crack patterns for specimens (Minelli et al., 2014)..... | 48 |
| Figure 2.11 Comparison of analyses on Panel C2F3V3 (1 MPa \approx 0.145 ksi)..... | 52 |
| Figure 2.12 Comparison of analyses from Susetyo et al. (2013), Lee et al. (2016), and Kauffman et al. (2019) (Reprinted from Kaufmann et al., 2019) | 54 |
| Figure 3.1 Initial and final set times for mixtures with 1% fiber dosage..... | 64 |
| Figure 3.2 Cumulative bleed water for FRC mixtures..... | 64 |
| Figure 3.3 Unit weight of mixtures..... | 65 |
| Figure 3.4 Compression strength results of portland cement concrete mixtures with varied fiber types and dosages | 66 |
| Figure 3.5 Compression strength results of 20% Class F Ash mixtures with varied fiber types and dosages | 66 |
| Figure 3.6 Compression strength results of 35% Class F Ash mixtures with varied fiber types and dosages | 67 |
| Figure 3.7 Compression strength results of Ternary Blend (30% Class C and 5% Silica Fume mixtures with varied fiber types and dosages..... | 67 |
| Figure 3.8 Splitting tensile data for Portland cement concrete mixtures with varied fiber types and dosages | 68 |
| Figure 3.9 Splitting tensile data for 20% Class F Fly Ash concrete mixtures with varied fiber types and dosages | 69 |
| Figure 3.10 Splitting tensile data for 35% Class C Fly Ash concrete mixtures with varied fiber types and dosages | 69 |

| | |
|---|----|
| Figure 3.11 Splitting tensile data for 30% Class C Fly Ash and 5% silica fume Class C Fly Ash concrete mixtures with varied fiber types and dosages | 70 |
| Figure 3.12 Modulus of Elasticity for Portland cement concrete mixtures with varied fiber types and dosages | 71 |
| Figure 3.13 Modulus of Elasticity for 20% Class F concrete mixtures with varied fiber types and dosages | 71 |
| Figure 3.14 Modulus of Elasticity for 35% Class C concrete mixtures with varied fiber types and dosages | 72 |
| Figure 3.15 Modulus of Elasticity for 35% Class C concrete mixtures with varied fiber types and dosages | 72 |
| Figure 3.16 Drying shrinkage data for portland cement concrete mixtures with different fiber types and dosages | 73 |
| Figure 3.17 Drying shrinkage data for concrete mixtures containing 20% Class F fly ash with different fiber types and dosages | 74 |
| Figure 3.18 Drying shrinkage data for concrete mixtures containing 35% Class C fly ash with different fiber types and dosages | 74 |
| Figure 3.19 Drying shrinkage data for concrete mixtures containing ternary blend with different fiber types and dosages | 75 |
| Figure 3.20 Coefficient of Expansion data for concrete mixtures containing varied amounts of steel fibers. | 75 |
| Figure 3.21 Impact testing to first crack | 76 |
| Figure 3.22 Impact testing to determine the number of blows to failure..... | 76 |
| Figure 3.23 Test set-up for measuring flexural toughness of FRC (ASTM C1609) | 77 |
| Figure 3.24 Typical ASTM C1609 test results and relevant toughness parameters | 77 |
| Figure 3.25 Simplified Double-Punch Test (after Riding et al., 2022)..... | 78 |
| Figure 3.26 Typical simplified double-punch results and equation used to calculate tensile stress. | 79 |
| Figure 3.27 Simplified Double-Punch Test results for one fiber source (SFD) ... | 79 |
| Figure 3.28 Exposure block expansion | 80 |
| Figure 3.29 Chloride ingress of FRC samples using mXRF | 81 |
| Figure 3.30 Marine exposure block in Port Aransas, TX | 81 |
| Figure 3.31 Durability factor ASTM C666..... | 82 |
| Figure 3.32 Results of visual rating of concrete mixtures containing steel fiber subjected to freeze/thaw cycles per ASTM C672..... | 83 |
| Figure 4.1 Longitudinal direction specimen | 86 |

| | |
|--|-----|
| Figure 4.2 Transverse direction specimen | 86 |
| Figure 4.3 Precast panels before concrete casting | 88 |
| Figure 4.4 Roughened panel surface using brooms | 88 |
| Figure 4.5 Concrete panel curing..... | 88 |
| Figure 4.6 Specimen before casting..... | 89 |
| Figure 4.7 Concrete casting using concrete bucket | 90 |
| Figure 4.8 Leveling and smoothing of specimen..... | 90 |
| Figure 4.9 Curing of specimen..... | 90 |
| Figure 4.10 Uneven surface of S1-3 specimen due to low slump | 91 |
| Figure 4.11 Cut cross-section of (a) 1.5 inch hooked end fiber SFRC and (b) 1 inch twisted fiber SFRC specimens | 92 |
| Figure 4.12 ASTM C1609 test results | 94 |
| Figure 4.13 Dog-bone test setup | 95 |
| Figure 4.14 Uniaxial tension test results..... | 96 |
| Figure 4.15 Deck strip test setup: (a) isometric view and (b) side view and instrumentations..... | 97 |
| Figure 4.16 S1-1 test results, (a) stabilized crack pattern, (b) measured critical crack width, and (c) load-displacement curve | 99 |
| Figure 4.17 S1-2 specimen test results, (a) stabilized crack pattern, (b) measured critical crack width, and (c) load-displacement curve | 101 |
| Figure 4.18 S1-3 specimen test results, (a) stabilized crack pattern, (b) measured critical crack width, and (c) load-displacement curve | 102 |
| Figure 4.19 S1-4 specimen test results, (a) stabilized crack pattern, measured critical crack width to rebar stress (b) total load (c) , and (d) load-displacement curve..... | 104 |
| Figure 4.20 S1-5 specimen test results, (a) stabilized crack pattern, (b) measured critical crack width, and (c) load-displacement curve | 106 |
| Figure 4.21 S2-1 specimen test results, (a) stabilized crack pattern, (b) measured critical crack width, and (c) load-displacement curve | 108 |
| Figure 4.22 S2-2 specimen test results, (a) stabilized crack pattern, (b) measured critical crack width to rebar stress (c) measured critical crack width to total load, and (d) load-displacement curve | 110 |
| Figure 4.23 S2-3 specimen test results, (a) stabilized crack pattern, (b) measured critical crack width to rebar stress (c) measured critical crack width to total load, and (d) load-displacement curve | 112 |

| | |
|--|-----|
| Figure 4.24 S2-4 specimen test results, (a) stabilized crack pattern, (b) measured critical crack width to rebar stress (c) measured critical crack width to total load, and (d) load-displacement curve | 114 |
| Figure 4.25 S2-5 specimen test results, (a) stabilized crack pattern, (b) measured critical crack width, and (c) load-displacement curve | 115 |
| Figure 4.26 S2-6 specimen test results, (a) stabilized crack pattern, (b) measured critical crack width to rebar stress (c) measured critical crack width to total load, and (d) load-displacement curve | 117 |
| Figure 4.27 S2-7 specimen test results, (a) stabilized crack pattern, (b) measured critical crack width to rebar stress (c) measured critical crack width to total load, and (d) load-displacement curve | 119 |
| Figure 4.28 Fiber type effect: (a) load-displacement curve and (b) critical crack width to rebar stress | 120 |
| Figure 4.29 Comparison of different fiber types using (a) flexural beam test and (b) direct tension test..... | 121 |
| Figure 4.30 Fiber dosage effect: (a) load- displacement curve, (b) measured critical crack width to rebar stress, and (c) measured critical crack width to total load..... | 122 |
| Figure 5.1 Test setup for specimens tested by Birely et al. (2018)..... | 127 |
| Figure 5.2 Constitutive models for specimens tested by Birely et al. (2018)..... | 127 |
| Figure 5.3 Preliminary quarter-symmetry model for specimens tested by Birely et al. (2018)..... | 128 |
| Figure 5.4 Nonlinear finite element analysis comparison for specimens tested by Birely et al. (2018) | 129 |
| Figure 5.5 Representative Abaqus model for Series 1 specimens | 131 |
| Figure 5.6 Typical tension stress-strain response | 131 |
| Figure 5.7 Load-deflection comparison for S1-1 | 132 |
| Figure 5.8 Crack pattern for S1-1 at P = 8 kip..... | 133 |
| Figure 5.9 Stabilized crack pattern for S1-1 | 134 |
| Figure 5.10 Load-deflection comparison for S1-2..... | 135 |
| Figure 5.11 Crack pattern for S1-2 at P = 12 kip..... | 135 |
| Figure 5.12 Stabilized crack pattern for S1-2 | 136 |
| Figure 5.13 Load-deflection comparison for S1-3..... | 137 |
| Figure 5.14 Crack pattern for S1-3 at P = 8 kip..... | 137 |
| Figure 5.15 Stabilized crack pattern for S1-3 | 138 |
| Figure 5.16 Load-deflection comparison for S1-4..... | 139 |

| | |
|---|-----|
| Figure 5.17 Stabilized crack pattern for S1-4 | 139 |
| Figure 5.18 Load-deflection comparison for S1-5..... | 140 |
| Figure 5.19 Stabilized crack pattern for S1-5 | 141 |
| Figure 5.20 Representative Abaqus model for Series 2 specimens | 141 |
| Figure 5.21 Load-deflection comparison for S2-1 | 143 |
| Figure 5.22 Crack pattern for S2-1 at P = 8 kip..... | 143 |
| Figure 5.23 Stabilized crack pattern for S2-1 | 144 |
| Figure 5.24 Load-deflection comparison for S2-2..... | 145 |
| Figure 5.25 Stabilized crack pattern for S2-2 | 145 |
| Figure 5.26 Load-deflection comparison for S2-3..... | 146 |
| Figure 5.27 Stabilized crack pattern for S2-3 | 147 |
| Figure 5.28 Load-deflection comparison for S2-4..... | 148 |
| Figure 5.29 Stabilized crack pattern for S2-4 | 148 |
| Figure 5.30 Load-deflection prediction for S2-5 | 149 |
| Figure 5.31 Simulated crack pattern for S2-5 | 150 |
| Figure 5.32 Assumed tension behavior for parametric study | 151 |
| Figure 5.33 Load-deflection comparison for reinforcement spacing study | 151 |
| Figure 5.34 Crack pattern comparison for reinforcement spacing study | 152 |
| Figure 6.1 Full-scale (a) dimensions and (b) test regions | 154 |
| Figure 6.2 Specimen before casting..... | 156 |
| Figure 6.3 Concrete casting procedure | 157 |
| Figure 6.4 Concrete surface after casting | 157 |
| Figure 6.5 Specimen curing using burlap | 158 |
| Figure 6.6 Concrete slump..... | 159 |
| Figure 6.7 Compressive strength of SFRC | 160 |
| Figure 6.8 Flexural beam test results | 161 |
| Figure 6.9 Uniaxial tensile test results | 162 |
| Figure 6.10 Loading method and instrumentation | 162 |
| Figure 6.11 Instrumentations (a) Strain gauge location, (b) VWGs location, (c) Single axle potentiometer locations, and (d) Tandem axle potentiometer locations | 164 |
| Figure 6.12 Measured differential shrinkage result | 165 |
| Figure 6.13 Single axle over girder configuration | 166 |

| | |
|--|-----|
| Figure 6.14 S1 region test results, (a) stabilized crack pattern, (b) load-displacement curve, and (c) maximum reinforcement strain..... | 167 |
| Figure 6.15 S2 region test results, (a) stabilized crack pattern, (b) load-displacement curve, (c) maximum reinforcement strain, and (d) maximum crack width | 169 |
| Figure 6.16 Tandem axle near panel joints configuration | 170 |
| Figure 6.17 T1 region test results, (a) stabilized crack pattern, (b) load-displacement curve, and (c) maximum reinforcement strain..... | 172 |
| Figure 6.18 T2 region test results, (a) stabilized crack pattern, (b) load-displacement curve, (c) maximum reinforcement strain, (d) maximum crack width of longitudinal direction, and (e) maximum crack width of transverse direction..... | 174 |
| Figure 6.19 Overhang edge loading configuration | 175 |
| Figure 6.20 Service level (a) single axle loading and (b) Tandem loading | 176 |
| Figure 6.21 O1 region test result: (a) stabilized crack, (b) load-displacement curve, and (c) crack width measurement | 177 |
| Figure 6.22 O2 region test result: (a) stabilized crack, (b) load-displacement curve, and (c) crack width measurement | 179 |
| Figure 6.23 O3 region test result: (a) stabilized crack, (b) load-displacement curve, and (c) crack width measurement | 180 |
| Figure 6.24 O4 region test result: (a) stabilized crack, (b) load-displacement curve, and (c) crack width measurement | 181 |
| Figure 6.25 Load-displacement curves of Tandem loading cases | 182 |
| Figure 6.26 Load-strain curves of Tandem loading cases | 183 |
| Figure 6.27 Crack measurements at transverse and longitudinal panel joints | 184 |
| Figure 6.28 Yield-line of O3 region | 185 |
| Figure 6.29 Recommended overhang reinforcement layout..... | 188 |
| Figure 7.1 1 inch panel to girder gap check: (a) 1.5 inch hooked end fiber SFRC and (b) 1 inch twisted fiber SFRC | 190 |
| Figure 7.2 Comparison of different fiber types using (a) flexural beam test and (b) direct tension test | 191 |
| Figure 7.3 Comparison by fiber dosages using (a) flexural beam test and (b) direct tension test | 192 |
| Figure 7.4 Effect of different fiber types in (a) load-displacement and (b) crack resistance..... | 193 |
| Figure 7.5 Effect of different fiber dosages in (a) load-displacement and (b) crack resistance..... | 194 |
| Figure 7.6 Interior test results, (a) load-displacement and (b) crack resistance . | 195 |

| | |
|---|-----|
| Figure 7.7 Service level (a) single axle loading and (b) Tandem loading | 196 |
| Figure 7.8 Recommended reinforcement layout..... | 197 |

Chapter 1. Introduction

1.1. Overview

Bridge decks in Texas are commonly constructed using prestressed, precast panels (PCP) topped with a layer of traditional, cast-in-place (CIP) reinforced concrete (RC), as shown in Figure 1.1. Beyond Texas, there are six other states in the United States (US) that use PCP construction: California, Colorado, Missouri, New York, North Carolina, and Washington. In North America, outside of the US, the Ministry of Transportation in Ontario, Canada uses them. CIP-PCP bridge decks have several advantages over traditional CIP decks; for example, they are more efficient to construct (e.g., less formwork and construction time), and they have better durability over their service life (Bayrak et al., 2013). Researchers at the University of Texas have previously investigated several strategies for optimizing the design and construction of such systems (Bayrak et al., 2013; Coselli et al., 2006). The intent of the current research project is to develop recommendations for standard, ready-mix designs for structural classes of concrete with domestically produced steel fibers in order to further optimize the design of CIP-PCP bridge decks. More specifically, the goal is to eliminate as much of the conventional reinforcement as possible in the CIP portions of the deck.

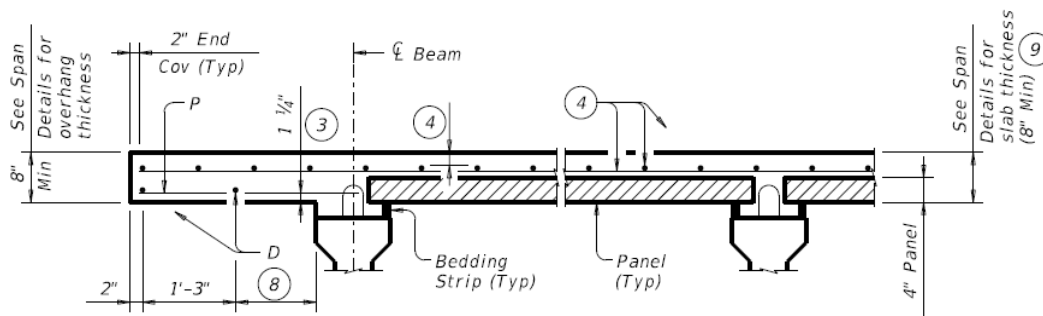


Figure 1.1 Standard design detail for CIP-PCP bridge deck on prestressed concrete I-beam (Reprinted from TxDOT Bridge Division Standards (2015))

1.2. Scopes and Objectives

This research is dedicated to advancing the comprehension and utilization of steel fiber-reinforced concrete in cast-in-place slabs constructed atop stay-in-place precast concrete panels. The research scope encompasses extensive activities focused on developing mix designs and optimizing top mat reinforcement detailing to enhance structural performance. The critical elements of this study involve targeted mixture design and material testing, numerical modeling to evaluate the

structural behavior of slabs on precast concrete panels, and idealized and full-scale structural testing programs designed to validate proposed design recommendations.

The specific objectives of this research are multifaceted. Firstly, the investigation aims to evaluate the feasibility of integrating steel fiber-reinforced concrete into bridge decks with precast concrete panels, with a specific emphasis on minimizing standard reinforcement. Additionally, the research endeavors to determine the minimum structural properties necessary for fiber-reinforced concrete in bridge deck applications, contemplating the potential for full replacement of conventional deck reinforcement. Laboratory testing protocols are devised to ascertain the optimal fiber dosage for meeting structural requirements. The study also aims to offer comprehensive recommendations on properties tailored to diverse applications. Furthermore, the research seeks to propose prescriptive/performance-based mixture design guidance to mitigate issues related to bridge deck cracking and corrosion. Ultimately, full-scale specimens have been tested to validate analyses, modeling efforts, and ensure the holistic structural performance of steel fiber-reinforced concrete in bridge decks.

1.3. Organization of Report

The research project was structured into distinct chapters, encompassing, literature review, experimental investigation, and analysis. Each chapter of this report systematically presents the outcomes and key findings derived from these respective tasks.

- Chapter 2 – Literature Review: General overview of previous research related to steel fiber reinforced concrete, CIP-PCP bridge deck, and provisions for design and evaluate SFRC CIP-PCP bridge deck.
- Chapter 3 – Material Selection and Testing: A comprehensive laboratory evaluation on SFRC designed for bridge deck.
- Chapter 4 – Deck Strip Test: Evaluation of idealized deck strip equipped with various fiber types and fiber dosage.
- Chapter 5 – Numerical Analysis: Analysis using nonlinear finite element analysis to verify test results from Chapter 4 and further optimization of required reinforcement for SFRC CIP-PCP bridge deck.
- Chapter 6 – Full-Scale Test: The assessment of load resisting capacity and crack control performance of CIP design with reinforcement layout and SFRC mixture design determined through previous chapters.

- Chapter 7 – Conclusion and Design Recommendations: The previous chapters' findings and conclusions are summarized, accompanied by recommendations for applying these insights effectively to an actual bridge deck.
- Chapter 8 – Value of Research: The chapter discusses the value of the current research project in improving CIP-PCP bridge deck construction through incorporating SFRC in selected benefit areas.

Chapter 2. Literature Review

In accordance with the scope of TxDOT Project 0-7001: Utilizing Steel Fibers as Concrete Reinforcement in Bridge Decks, the Research Team at the University of Texas at Austin has carried out a literature review to examine the state-of-the-art in steel fiber-reinforced concrete (SFRC) mixture design, as well as previous experimental and numerical work related to the structural performance of infrastructure constructed with SFRC. For completeness, a review of previous research on PCP-CIP decks is also provided.

The literature review summarized in this chapter has been grouped into the following four main sections: State-of-the-Art in SFRC, Mechanical properties of SFRC, Experimental investigation of PCP-CIP Decks and SFRC Members, Analytical investigation of SFRC member, and Summary and Conclusions.

2.1. Notation

To simplify notation, one common set of symbols and definitions has been used throughout this project report. Apart from model-specific variables, all symbols within this memorandum are defined below.

| | | |
|----------------------------|---|--|
| d_f | = | fiber diameter |
| E_c | = | initial tangent stiffness of concrete |
| f_c | = | compressive stress in concrete |
| f'_c | = | compressive strength of concrete |
| f'_{cf} | = | compressive strength of fiber concrete |
| f'_t | = | tensile strength of concrete $\approx 4\sqrt{f'_c}$ (units of psi) |
| f_{res}^t | = | tensile residual strength of fiber concrete |
| f'_r | = | flexural strength of concrete |
| $f_{res(\frac{L}{150})}^r$ | = | flexural residual strength of concrete |
| l_f | = | fiber length |
| n | = | the number of fibers added per m^3 of concrete |
| V_f | = | fiber content in volume fraction |
| w_{cr} | = | crack width |
| W_f | = | fiber content in weight fraction |
| $\approx 3V_f$ | | |
| β | = | material parameter that describes shape of the stress-strain diagram |
| ε_c | = | compressive strain in concrete |
| ε'_c | = | strain at peak compressive stress of fiber-reinforced concrete |
| ε'_{cf} | = | strain at peak compressive stress of fiber-reinforced concrete |
| ε_t | = | tensile strain in concrete |
| τ | = | bond shear stress between fiber and matrix |

2.2. State-of-the-Art in SFRC

2.2.1. Fiber Properties

Fiber geometry, aspect ratio, and length are the most influential fiber characteristics on the behavior of the SFRC mixtures they are added to. These properties affect the fiber to concrete bond, pullout strength, fresh-state workability and hardened properties of SFRC mixtures. This section provides a digestion of studies which compare a variety of different steel fibers and considers their effects on the hardened and fresh-state properties of concrete.

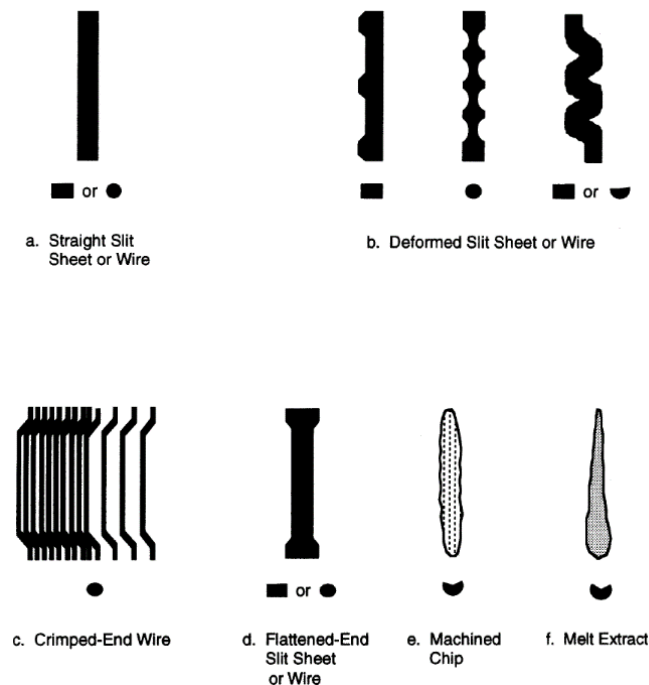


Figure 2.1 Types of fibers (ACI 544, 2018)

2.2.1.1. Bayasi and Soroushian (1992)

Bayasi and Soroushian (1992) compared differential fiber geometry, volume fraction, and aspect ratio of the fresh state properties of SFRC. Straight, crimped, and hooked fiber types were evaluated with fiber lengths ranging from 1 to 2.5 in. and fiber volume fractions ranging from 0.5 to 3 %. They found that, while standard slump tests could be used to evaluate the fresh state properties, inverted slump cone, and Vebe time testing were more effective and consistent in determining SFRC fresh state flowability. For rotary drum mixing of SFRC, they found that fibers should be added slowly over several minutes to avoid clumping or aggregation. It was found that workability was damaged by fiber volume at a rate that was similar

for all the tested fiber geometries. Crimped fibers were the best-performing fibers at preserving workability at any given volume fraction.

2.2.1.2. Soulioti et al. (2011)

This study evaluated the effects of waved fibers and hooked fibers at volume fractions of 0.5, 1, and 1.5 % in concrete with a 0.5 water-to-cement ratio (Soulioti et al., 2011). Compression testing was performed on 6-in. cubes that had been cured for 28 days for each fiber type at each volume fraction. ASTM C1609/ C1609M testing was also performed on 4 x 4 x 16 in. specimens to establish toughness curves. Slump and air content for the mixtures were tested, and found that hooked fibers had lower slump values at 1.5 % volume fraction. Air content was found to increase along with volume fraction. Toughness testing revealed that hooked fibers had improved toughness properties over the waved fibers at each volume fraction. The compressive strengths of mixtures containing wavy fibers were higher for all but 0.5 % volume fraction, where strengths were similar to hooked fiber mixtures.

2.2.1.3. Isla et al. (2015)

Fiber pull-out tests were performed from different inclinations to measure how fiber orientation affected fiber failure (Isla et al., 2015). Hooked and straight fibers of different lengths were pulled from different strengths of mortar and concrete mixtures. Fibers were pulled out at inclinations of 0, 30, and 60 degrees from normal. Straight fibers exhibited uniform pullout behavior, while hooked fibers achieved higher average pullout strengths but suffered larger strength deviations. It was explained that because fiber pullout strength is dependent on adhesion to the surrounding concrete matrix, concrete mixtures with denser cement matrices result in increasing the effectiveness of steel fibers. Fibers removed from higher strength concrete mixtures often failed in partial or total fiber failure rather than fiber pullout. Higher angles of inclination resulted in matrix failure that removed small conical sections of the surrounding cement matrix. The pullout strength of straight fibers was dependent on friction and bond with the surrounding cement matrix, while hooked fibers primarily relied on mechanical strengths developed by hooked ends.

2.2.1.4. Marcalikova et al. (2019)

Compressive, splitting tensile, and three-point bending tests were used to compare the effect of fiber geometry and fiber volume (Marcalikova et al., 2019). Straight and hooked fibers were added to 0.625 water-to-cement ratio concrete at fiber volumes of 0.5 and 1 %. Compressive strengths among all tested mixtures were similar, while straight fibers exhibited lower strength than hooked fibers in splitting

tensile tests. In lower-dose mixtures, hooked fibers had significantly lower flexural strengths than straight fibers, while mixtures with higher volumes of fibers exhibited similar strengths. Flexural tests identified that hooked fibers added in higher fiber volumes were most likely to exhibit strain hardening after the first cracking occurred.

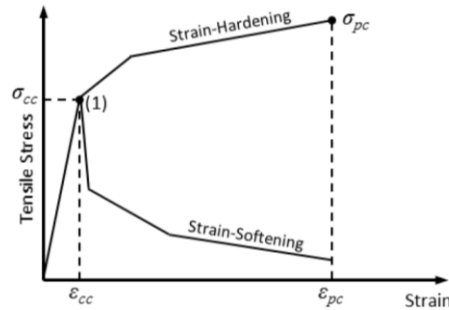


Figure 2.2 Strain hardening and softening (Birely et al., 2018)

2.2.1.5. Shannag et al. (1997)

Shannag et al. (1997) studied the effects of interfacial bonds in fiber-reinforced cementitious systems using straight fibers. Fiber embedment length, volume fraction, concrete matrix strengths, and interfacial crack lengths were varied to monitor their effects on pullout strength. Fiber embedment lengths varied from 0.25 to 0.70 in., and volume fraction varied from 3 to 6 %. Densified small particle (DSP) systems using high quantities of superplasticizer, silica fume, and low water-to-cement ratio were compared to standard mortar mixtures. Up to three times the frictional bond strength and debonding energy were observed in DSP mixtures compared to their standard mortar counterparts. This was largely attributed to the denser microstructure provided by the DSP mixtures. Increasing fiber embedment length and volume fraction increased the peak pullout load and capacity of tested mixtures.

2.2.1.6. Zile and Zile (2013)

Zile and Zile (2013) performed pullout tests of two types of hooked fibers, a crimped fiber and a straight fiber, at different embedment lengths, from 0.6 to 1.2 in., to measure pullout strength and observe failure conditions. After the peak pullout load was reached, a rapid decrease in the fiber/concrete adhesive strength and an increase in damage at the fiber/concrete interface was observed in straight fibers. Hooked fibers exhibited pull-out after the straightening of the embedded hooked end. Crimped fibers were more likely to fail by fiber rupture at higher embedment lengths. A proposed model for pullout strength is suggested that factors in the friction of the sliding fiber as well as the plastic bending of the curved portions of the fiber. The mechanical contribution depends on the amount of work

to straighten the fiber, explaining the higher loads required to pull out crimped fibers.

2.2.1.7. Conclusions

The primary conclusions related to fiber properties are as follows:

1. Fiber geometries have a larger impact on hardened SFRC properties than fresh state properties.
2. Fiber geometry and concrete strength change how the fiber fails during flexural loading.
3. Deformed fibers such as hooked, helical, or wavy generate additional mechanical action during fiber pullout that increases the force needed to successfully remove the fiber from the concrete matrix.
4. Increasing the strength of the interfacial transition zone increases the strength of the fiber/concrete interface, leading to higher pullout strength.

2.2.2. Typical Mix Design

Class S concrete mixtures meeting the requirements within standard specification Item 421 are typically used for bridge decks constructed in Texas. Notable requirements for Class S concrete include a minimum design compressive strength of 4000 psi, a maximum water-to-cement ratio of 0.45, and a maximum acceptable slump of 5.5 in. This section addresses current practices in SFRC mixtures aimed to achieve similar requirements with emphasis given to the effects of steel fiber additions on the fresh state properties of SFRC.

2.2.2.1. ACI Committee 544

Maintaining workability while providing a thorough and consistent distribution of steel fibers throughout the mixture is necessary to attain a usable and dependable SFRC mixture. Both concerns can often be addressed in the mixing process where the order of additions and time between steps are essential to avoid fiber clumping or segregation. ACI Committee 544 outlines the following strategies for mixing procedures when using conventional ready-mix concrete:

1. Add the fibers to the truck mixer after all other ingredients, including the water, have been added and mixed. Steel fibers should be added to the mixer hopper at a rate of about 100 lbs. (45 kg) per minute, with the mixer rotating at full speed. The fibers should be added in a clump-free state so that the mixer blades can carry the fibers into the mixer. The mixer should then be

slowed to the recommended mixing speed and mixed for 40 to 50 revolutions. Steel fibers have been added manually by emptying the containers into the truck hopper or via a conveyor belt or blower. Using this method, steel fibers can be added at the batch plant or on the job site.

2. Add the fibers to the aggregate stream in the batch plant before the aggregate is added to the mixer. Steel fibers can be added manually on top of the aggregate on the charging conveyor belt or via another conveyor emptying onto the charging belt. The fibers should be spread out along the conveyor belt to prevent clumping.
3. Add the fibers on top of the aggregate after they are weighed in the batcher. The normal flow aggregate out of the weigh batcher will distribute the fibers. Steel fibers can be added manually or via a conveyor.

2.2.2.2. Mohammadi et al. (2008)

Concrete mixtures incorporating two different lengths of corrugated steel fibers, 2 in. and 1 in., were subjected to inverted slump cone, Vebe time, and compaction tests to investigate how the fresh state properties were affected by fiber length and volume fraction. Mixtures with a fiber volume fraction of 2 % exhibited higher Vebe and inverted slump cone times and lower compaction factors than mixtures with a volume fraction of 1 % for both fiber lengths (Mohammadi et al., 2008). Mixtures with shorter fibers exhibited higher compaction factors and faster Vebe and inverted slump cone times than mixtures containing longer fibers at similar fiber volume fractions.

2.2.2.3. Chu et al. (2018)

Four different types of hooked steel fibers with varying lengths and diameters were added in volumes ranging from 0.5 to 2 % in order to correlate fiber factors to the effect on fresh and hardened state properties (Chu et al., 2018). The target slump for each mixture was set to at most 6 in., and coarse aggregate, fine aggregate, and superplasticizer proportions were adjusted to reach this target. A two-step process of mixing the mortar first and adding aggregates and fibers over an extended mixing time was used to avoid fiber clumping. They found that mixtures containing very high fiber volume fractions could maintain the target slump with proper mixing procedures and mixture adjustments. Poisson's ratio was measured and was found to be reduced by up to 10 % based on fiber geometries. Fiber factors $V_f * (\frac{l_f}{d_f})^2$ and nl^3 were found to give the best correlations to slump without a superplasticizer, as shown in Figure 2.3. They found that the number of steel fibers, n , was the greatest estimator of workability as the interaction between steel fibers was what commonly causes fiber clumping.

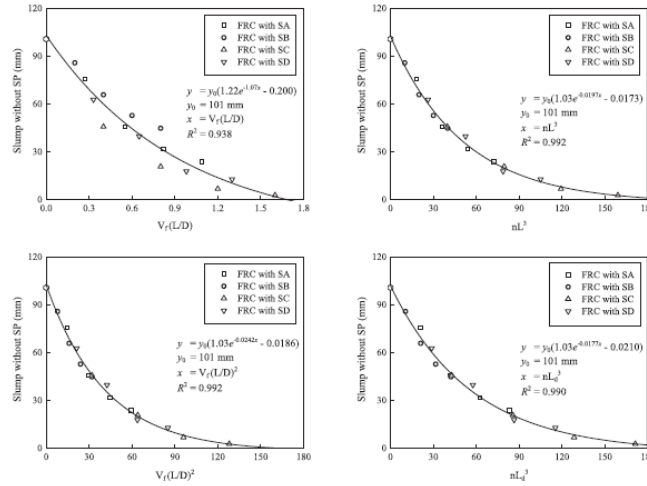


Fig. 7. Slump without SP versus fiber factors $V_f(L/D)$ and $V_f(L/D)^2$.

Fig. 8. Slump without SP versus fiber factors nL^2 and nL_d^2 .

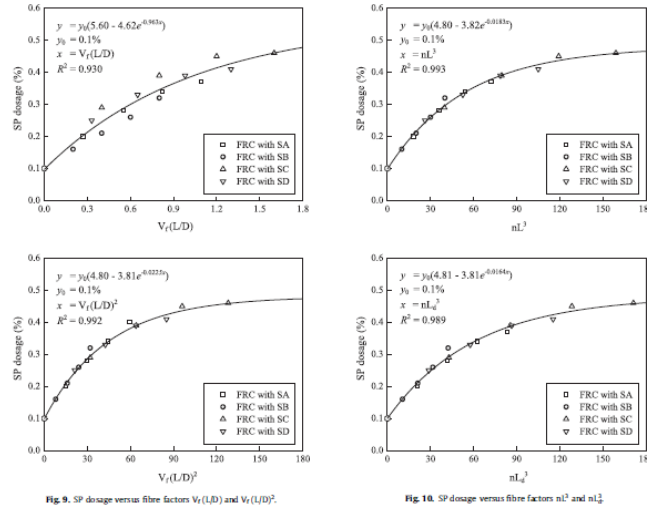


Fig. 9. SP dosage versus fiber factors $V_f(L/D)$ and $V_f(L/D)^2$.

Fig. 10. SP dosage versus fiber factors nL^2 and nL_d^2 .

Figure 2.3 Fiber workability with respect to factors (Chu, Li, Kwan, 2018)

2.2.2.4. Ferrara and Meda (2007)

Ferrara and Meda (2007) sampled cores from precast prestressed roof elements to measure fiber distribution among the self-compacting SFRC. Companion mixtures were also made to observe how fiber distribution was affected by vibration on mixtures with and without viscosity-enhancing admixtures (VEA). Compressive and four-point bending tests were performed to record the hardened state properties of these mixtures. Fly ash was used in the mixture lacking VEA to increase workability. Cylinders lacking VEA required approximately 20 minutes of vibration, while mixtures with VEA required only 5 minutes of vibration, reducing segregation and creating a more even distribution of fibers. X-ray examination of core elements revealed good fiber distribution and overall homogeneity.

2.2.2.5. Conclusions

The primary conclusions related to fiber properties are as follows:

1. SFRC fresh state properties are dominated by fiber content volume, which decreases slump and stiffens fresh concrete.
2. Superplasticizers and VEAs are often used in SFRC mixtures to counteract this effect.
3. Vibration should be used sparingly in SFRC due to its propensity to segregate steel fibers to the bottom of the mixture.

2.2.3. Material Properties

The addition of steel fibers has many positive effects on the hardened behavior of concrete mixtures. However, their behavior is liable to change based on the properties of the surrounding concrete matrix. This section summarizes previous studies investigating how the concrete/fiber composite can be affected by changes in either material.

2.2.3.1. Bayrak et al. (2013)

Bayrak et al. (2013) analyzed approaches to optimize reinforcement in the cast-in-place concrete placed on bridge decks and to explore methods of controlling cracking in precast, prestressed bridge deck panels. To this end, steel fibers were considered to enhance the durability and extend the service life of bridge decks by controlling cracking. An analysis of current methods used to obtain SFRC toughness was performed and identified the need for a simple, reliable test which provided reproducible data (see Figure 2.4). Double punch testing (DPT) was investigated due to its simplicity, small specimen size, and ability to generate failure via multiple cracks. Two hundred and forty double punch tests were performed to assess the usefulness of the test method for measuring SFRC toughness. The test uses 6 x 6 in. cylindrical concrete specimens and compresses them vertically between two steel punchers with a smaller diameter. These punches produced radial transverse tension, causing the specimens to fail due to multiple radial cracks. The failure via multiple cracks allows the steel fibers to bridge several crack faces rather than being isolated to action along a single large crack face. This highlights the post-cracking stress redistribution benefits of SFRC. This study concluded that DPT was useful for evaluating SFRC and provided a simple way to obtain reliable data.

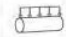
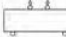
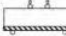

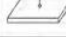


| TEST INFORMATION ¹ | | SIMPLICITY ² | | | | RELIABILITY ³ | | REPRODUCIBILITY ³ |
|-------------------------------|---|---------------------------------|-------------------------------|----------------|--------------|--------------------------|--|----------------------------------|
| Designation | Layout | Specimen Fabrication & Handling | Test Setup & Support Fixtures | Test Procedure | Test Machine | Failure Mechanism | Within-Batch Precision (COV) | Inter-Laboratory Precision (COV) |
| ASTM C496 |  | Easy | Easy | Easy | Standard | Single Major Crack | ± 5% PL | Not Available |
| ASTM C1609 |  | Moderate | Difficult | Moderate | Closed-Loop | Single Major Crack | ± 8% PL ± 20% RS | Not Available |
| ASTM C1399 |  | Moderate | Difficult | Difficult | Standard | Single Major Crack | ± 20% RS | ± 40% RS |
| ASTM C1550 |  | Difficult | Difficult | Difficult | Closed-Loop | Multiple Cracks | ± 6% PL ± 10% RS | ± 9% PL ± 9% RS |
| EFNARC Panel Test |  | Difficult | Difficult | Moderate | Closed-Loop | Multiple Cracks | Not Available | Not Available |
| Uniaxial Direct Tensile Test |  | Difficult | Moderate | Moderate | Closed-Loop | Single Major Crack | Not Available | Not Available |
| Double-Punch Test |  | Easy | Easy | Easy | Standard | Multiple Cracks | ± 10% Initial Slope ± 5% Peak Load ± 20% Residual Strength | Not Available |

Figure 2.4 Tension testing methods for concrete (Bayrak et al., 2013)

2.2.3.2. Simoes et al. (2017)

The primary objective of this research was to evaluate how concrete compressive strength and the geometry of steel fibers influence the behavior of the fiber/matrix interface (Simoes et al., 2017). Two types of hooked fibers were cast inside three different concrete matrices designed for 28-day compressive strengths of 2900, 8700, and 14,500 psi. Pullout strengths and fiber failure conditions were recorded. The increase in concrete strength was found to greatly increase the fiber/matrix bond strength. The mechanical action generated by hooked fibers was found to be more important in weaker strength concrete mixtures where the fiber/matrix bond was weaker. Higher compressive strength concrete increased the number of fibers that failed by tension fracture rather than pullout. Higher compressive strengths in concrete also increased the friction generated after peak load for fibers that did fail by pullout. Fibers that possessed more complex hooks were found to have higher pullout strengths than fibers with simpler hooks.

2.2.3.3. Suuronen et al. (2013)

X-ray scans were performed on twelve cores taken from a self-consolidating SFRC mixture used as a floor slab (Suuronen et al., 2013). They found that depending on where in the slab the core was taken, be it the center or near the end of a slab, the alignment of the steel fibers varied significantly. They discovered that the fibers tended to align parallel to nearby formwork. X-ray scan techniques were developed, which allow detailed X-ray scans to accurately capture fiber orientation and shape even in highly congested sections (see Figure 2.5).

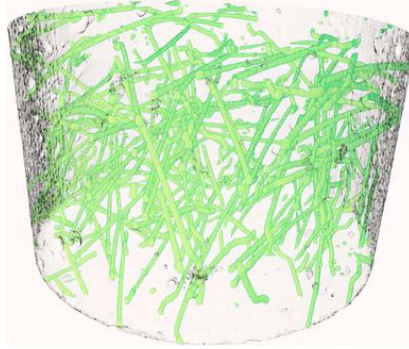


Figure 2.5 Fiber orientation from X-ray scan (Suuronen et al., 2014)

2.2.3.4. Ferrara et al. (2008)

Three different SFRC mixture types – vibrated, self-consolidating, and segregating-consolidating – were subjected to four-point bending and non-destructive monitoring of fiber distribution through alternate current impedance spectroscopy (Ferrara et al., 2008). Beams were cut from slabs and rotated before testing to find the effects on bending behavior. Beams were rotated to see whether fiber settlement or dispersion had caused different behavior based on orientation. Beams tested upside down or sideways to the casting direction reported lower flexural strengths than beams orientated finish face up. The effectiveness of self-compacting concrete to orient the fibers along the casting direction and preventing their downward settlement through careful gradation and minimizing the average spacing between the solid particles was noted. In vibrated mixtures, four-point bending strengths were very scattered, while the settlement of fibers due to vibration resulted in the lowest four-point bending strength of beams tested finish face down.

2.2.3.5. Ye et al. (2018)

Dynamic impact tests were performed using a split Hopkins bar on SFRC with volume fractions of 0, 0.75, and 1.5 % (Ye et al., 2018). A dynamic damage constitutive model for SFRC composites under compression was proposed. The study found that strain, elastic modulus, and ultimate stress of SFRC increased with fiber content and strain rate.

2.2.3.6. Chern and Young (1989)

Chern and Young (1989) investigated the performance of SFRC as compressive creep and shrinkage reinforcement. Straight fiber with 0 to 2 % volume fraction was used. Testing was conducted for 170 days. Higher volume fraction gave smaller creep, shrinkage, and deformation. Overall, fibers lessen the long-term deformation of concrete.

2.2.4. Durability of SFRC

The creation of durable and long-lasting building material capable of surviving anticipated field conditions is the goal of any concrete mixture, and SFRC is no exception. Available research investigating the effects of common durability concerns such as acid attack and corrosion of SFRC are summarized below.

2.2.4.1. Granju and Ullah Balouch (2005)

SFRC prisms of 4 x 4 x 20 in. containing hooked fibers were prepared with a water-to-cement ratio of 0.6 to reach a 28-day compressive strength of 5800 psi (Granju and Ullah Balouch, 2005). Samples were cured for 24 hours before being dried and then cracked in three-point bending. Half of the specimens' cracks were sealed with tape and marine silicone mastic, while the other half were kept exposed. The beams were then subjected to a marine-like environment for 1 year during which cycles of one-week exposure to salted fog and one-week of drying were alternated. After being removed from the marine environment, the specimens were tested again in three-point bending until they reached 0.2 in. of deflection. The unprotected specimens were heavily corroded but had a uniformly higher peak flexural strength as well as higher post-peak flexural behavior. The higher flexural strength of more corroded specimens was likely due to the corrosion increasing the frictional bond between cement and fiber. No concrete bursting or spalling due to fiber corrosion was observed during testing. On unprotected, cracked specimens', fibers within 0.12 in. of beam faces and along the crack width were observed to be corroded. Researchers found that once the crack width had decreased to less than 0.004 in., corrosion could no longer be observed in fibers along the crack face.

2.2.4.2. Chen et al. (2015)

Seventy low-carbon hooked fibers were subjected to accelerated corrosion using two different methods and then tested in tension until failure (Chen et al., 2015). Fibers designated by the researchers as Group D were subjected to cycles of submersion in NaCl solution for an hour and 11 hours of drying in a 284°F oven for 5 to 60 days. Group G fibers were corroded using a galvanostatic method. The degree of corrosion was measured by total weight loss after tensile testing. Group D fibers experienced pitting and cross-sectional change, while group G fibers experienced uniform corrosion that maintained the cross-sectional uniformity while decreasing total area. Both fibers lost tensile strength as their degree of corrosion increased. However, group D fibers lost significantly more strength per degree of corrosion, likely due to the pitting caused by the cyclic exposure type.

2.2.4.3. Marcos-Menson et al. (2019)

Marcos-Menson et al. (2019) conducted a literature review of different types of acid attack and how the inclusion of structural steel fibers affect the durability of concrete. Biotic and abiotic sources of acid attack were evaluated, and their actions on SFRC were discussed. The researchers postulated that steel fibers' ability to limit the propagation of cracks and preclude spalling may help to slow the erosion front caused by sulphuric acid attack and the secondary reaction, sulfate attack. Steel fibers are more resistant to corrosion than typical reinforcing steel. Fibers only begin to corrode after the full chemical dissolution front has reached the fiber, causing the pH to drop between 4 and 6 and initiating the dissolution of the cement matrix surrounding the fiber. An evaluation of eleven studies which subjected SFRC to various forms of acid attack through a handful of different test methods found disagreement on whether steel fibers have a negligible impact on the propagation of the chemical erosion front in SFRC's exposed to BSA sulfate attack. The same studies debated whether steel fibers' effects on sulfate-induced cracking are inconsequential or beneficial. However, when exposed to inorganic acid attack from hydrochloric or nitric acid, there is limited research to suggest that SFRC does reduce the chemical erosion rates. Binder type and quality recommendations for promoting acid resistance in SFRC are suggested but limited to common recommendations. The primary recommendation for improving acid durability is to improve microstructure density through the use of SCMs or lowering water-binder ratios. Their review found that the influence of acids on cracked sections of SFRC lacks the research and consensus necessary to develop a clear understanding of behavior.

“Fibres embedded in the chemically-eroded concrete layer may corrode but will not lead to expansion-induced cracking or spalling, and the loss of tensile capacity of the fibre may be accompanied by a significant loss of strength of the surrounding matrix due to the acid attack on the cement paste, which in any case leads to total loss of bearing capacity. Whereas, non-critical corrosion has been observed on steel fibres embedded in the neutralized concrete layer, entailing no corrosion-induced cracking or spalling.” (Marcos-Meson et al., 2019)

2.2.4.4. Conclusions

The primary conclusions related to the material performance of SFRC are as follows:

1. Fiber orientation can have significant effects on the hardened properties of SFRC. The effects of fiber orientation on the mechanical response of SFRC

are well documented, but reliable methods for promoting fiber alignment in non-SCC SFRC mixtures are currently unavailable.

2. When added to concrete, steel fibers are more resistant to corrosion than typical steel reinforcing bars since corroded steel fibers do not expand enough to cause spalling like typical steel reinforcing.

2.2.5. Design Specifications and Guidelines for SFRC

This section describes design specifications and guidelines for fibers, including steel fibers, in current design codes and reference documents. Standards include AASHTO LRFD *Bridge Design Specifications*, ACI 318 *Building Code Requirements for Structural Concrete* (ACI 318-19), and ACI Committee 544 *Report on Fiber Reinforced Concrete* (ACI 544.1R-8R).

2.2.5.1. AASHTO-LRFD

The current AASHTO-LRFD (2020) specification does not explicitly consider SFRC a structural material for bridge deck construction. The specification includes fiber-reinforced polymer concrete to improve durability and glass-fiber reinforcement concrete to perform special functions. Structural applications involving SFRC are absent within the AASHTO LRFD standard.

2.2.5.2. ACI Committee 318

The Building Code Requirements for Structural Concrete and Commentary on Building Code Requirements for Structural Concrete (ACI Committee 318, 2019) allows for non-prestressed beams constructed with fiber-reinforced concrete to be designed without the traditional minimum area of shear reinforcement when all the following requirements are met:

1. Member height is less than or equal to 24 in.
2. Required shear strength does not exceed the factored shear strength provided by concrete.
3. Normal-weight concrete is used.
4. Concrete compressive strength less than or equal to 6 ksi.
5. Crimped or hooked-end fibers are used.
6. Fiber-reinforced concrete conforms to ASTM C1116.
7. Contains at least 100 lb. of steel fibers per yd^3 of concrete (approximately 0.75 % by volume)

2.2.5.3. ACI Committee 544

The series of reports developed by ACI Committee 544, ACI 544.1R through ACI 544.8R (ACI Committee 544, 1996, 2017, 2008, 2018; ACI Committee 214, 2010; ACI Committee 544, 2015, 2016a, 2016b) summarize the types, properties, testing methods, and applications of fiber reinforced concrete (FRC) materials, including SFRC. ACI 544.1R recapitulates the basic properties of FRC and literature that examines fiber properties. ACI 544. 2R, 3R, 4R, 5R, and 8R introduce guidelines for the application of FRC, the performance of FRC in structures, and methods to incorporate the material properties into the analysis. Reports 6R and 7R introduce design procedures for some structural members, elevated slabs, and precast concrete tunnel segments.

2.2.5.4. ASTM C1609/C1609M with RILEM TC 162-TDF

ASTM C1609/C1609M (ASTM, 2019) is a standard four-point flexure testing method for measuring the flexural strength of a rectangular beam. Peak load (P_p), residual load at a deflection of $L/600$ (P^D_{600}), residual load at $L/150$ (P^D_{150}), and flexural toughness up to $L/150$ (T^D_{150}) can be measured from the test. The flexural resistance for each deflection point and the FRC equivalent flexural strength ratio at $L/150$ ($R^D_{T,150}$) can then be calculated from measured values.

$$R^D_{T,150} = \frac{150 \cdot T^D_{150}}{f_p \cdot b \cdot h^2} \quad (2.1)$$

The nominal bending moment carried by an SFRC beam without conventional reinforcement (M_{n-FRC}) is calculated based on the assumption that concrete compressive stress varies linearly along the compression region, and a constant residual tensile stress is acting in the tensile region (Figure 2.6). The ultimate tensile strength of cracked SFRC (f_{ut-FRC}) and ultimate moment capacity (M_{n-FRC}) are estimated based on residual strength at $L/150$ (f^D_{150}), which is calibrated from ASTM C1609/C1609M. The following equations are used to determine the ultimate tensile strength and moment capacity of FRC.

$$f_{ut-FRC} = 0.37 \cdot f^D_{150} \quad (2.2)$$

$$M_{n-FRC} = f_{150}^D \cdot \frac{b \cdot h^2}{6} \quad (2.3)$$

For the serviceability limit state, the residual strength at $L/600$ (f_{600}^D) is used instead of $L/150$.

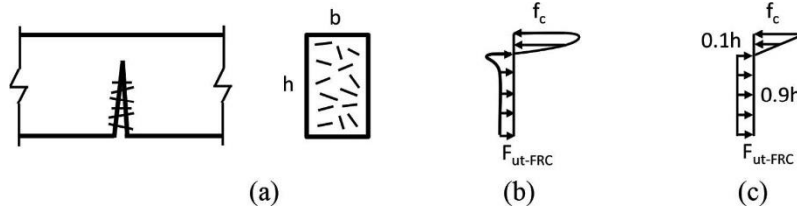


Figure 2.6 Actual and simplified stress distribution of SFRC (ACI 544, 2018)

2.2.5.5. BS EN 14651: 2005 with fib 2013 Model Code 2010

BS EN 14651: 2005 (BSI, 2005) uses a 6-in. square cross-section with a 20-in. span beam. The specimen is saw-cut for an inch and subjected to three-point bending. The deflection and crack-mouth opening displacement-load diagram are obtained from the test. The flexural residual load ($F_{R,i}$) and flexural residual strength are estimated for each opening displacement i .

$$f_{R,i} = \frac{3 \cdot F_{R,i} \cdot L}{2 \cdot b \cdot h_{sp}^2} \quad (2.4)$$

From the force equilibrium in the schematic stress block (Figure 2.7), the nominal moment and ultimate tensile strength can be estimated. In the rigid-plastic model, ultimate tensile strength, f_{FTu} , is assumed to be constant, which relates to the measured value from BS EN 14651 ($f_{R,3}$). This approach only deals with the ultimate limit state of a flexural member.

$$f_{FTu-FRC} = \frac{f_{R,3}}{3} \quad (2.5)$$

$$M_{nu-FRC} = f_{R,3} \frac{b \cdot h_{sp}^2}{6} \quad (2.6)$$

Another method assumes a linear relationship between the crack width and residual strength. This method can explain both the ultimate and service limit state of flexural members. Tensile strength and nominal moment for service and ultimate limit state are computed as a function of the maximum allowable crack width, w_u , using Equations (2.9) and (2.10).

$$f_{Fts-FRC} = 0.45 \cdot f_{R,1} \quad (2.7)$$

$$f_{Ftu-FRC} = 0.45 \cdot f_{R,1} - \frac{w_u}{CMOD_3} (0.45f_{R,1} - 0.5f_{R,3} + 0.2f_{R,1}) \quad (2.8)$$

$$M_{ns-FRC} = f_{R,1} \frac{bh_{sp}^2}{6} \quad (2.9)$$

$$M_{nu-FRC} = f_{R,3} \frac{bh_{sp}^2}{6} \quad (2.10)$$

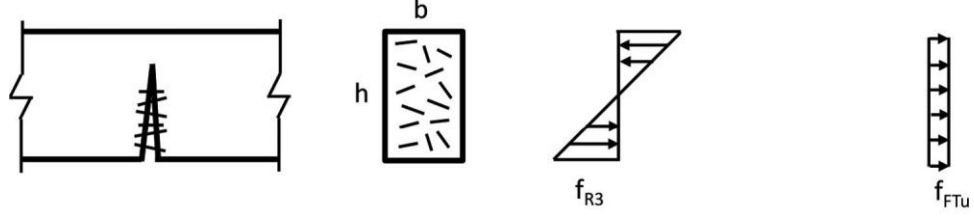


Figure 2.7 Flexural and normal stress distribution of SFRC (ACI 544, 2018)

The above methods describe the flexural moment capacity of SFRC only. Superposition is used if the design incorporates both steel fibers and conventional reinforcement.

$$M_{n-HFRC} = M_{n-RC} + M_{n-FRC} \quad (2.11)$$

Model Code 2010 (*fib* 2013) also provides design equations for the shear capacity of SFRC with longitudinal reinforcement but no shear reinforcement. The shear capacity recommended by Model Code 2010 is described as follows.

$$V_{FRC} = 26.8 \left\{ \frac{0.18}{\gamma_c} k_s \left[100\rho \left(1 + 7.5 \frac{f_{ut-FRC}}{f_t} \right) f'_c \right]^{\frac{1}{3}} + 0.15\sigma_{cp} \right\} bd \quad (2.12)$$

$$> (v_{min} + 0.15\sigma_{cp})bd$$

$$k_s = 1 + \sqrt{\frac{8}{d}} \leq 2.0 \quad (2.13)$$

Where, γ_c is the partial safety factor for concrete without fibers, k_s is size effect factor, ρ is longitudinal reinforcement ratio, and σ_{cp} is average normal stress acting on the concrete cross-section. According to the code, fiber reinforcement can substitute minimum shear reinforcement if $f_{ut-FRC} > 0.6\sqrt{f'_c}$.

2.2.5.6. Parametric-Based Design Method (ACI 544. 8R)

The parametric-based design method evaluates the stress and strain diagram of FRC for elastic compression and tension, elastic compression but nonlinear tension, and plastic compression and nonlinear tension. This method requires at least three parameters which can be obtained from either ASTM C1609/C1609M or BS EN 14651: 2005: the ratio of compressive to tensile strength (w), post-crack tensile residual strength ($\mu\sigma_{cr}$), and allowable compressive and tensile strain ($\beta_{tu}\epsilon_{cr}$). Solving the force equilibrium equation gives the depth of the neutral axis (kh) in the stress diagram.

$$k = \frac{2\mu\beta_{tu}}{-w^2 + 2\beta_{tu}(w + \mu) + 2\mu - 1} \quad (2.14)$$

With the neutral axis computed, the first moment of the cross-section can be estimated as follows.

$$M_n = ((3w\beta_{tu}^2 - w^3 + 3\mu\beta_{tu}^2 - 3\mu + 2)\frac{k^2}{\beta_{tu}^2} - 3\mu(2k - 1))M_{cr} \quad (2.15)$$

$$M_{cr} = \frac{\sigma_{cr}bh^2}{6} \quad (2.16)$$

With respect to post-peak behavior, SFRC responses are divided into strain softening and strain hardening. The type of response (softening or hardening) depends on fiber volume fraction, aspect ratio, and fiber types. Note that the tensile response of SFRC is dependent on the test method; that is, a bending test and direct tension test may not show the same tensile behavior due to differences in boundary conditions.

2.2.5.7. Conclusions

The primary conclusions related to design specifications and guidelines for SFRC are as follows:

1. ACI 318 allows steel fibers as a substitute for minimum shear reinforcement in certain conditions.
2. ACI 544 gives considerations in using steel fibers and their design provisions.
3. The flexural capacity of SFRC is calculated based on equations suggested in RILEM TC 162-TDF, fib 2013 Model Code 2010, and parametric study model. The equations are empirical and require test results from either ASTM C1609/ C1609M or BS EN 14651.
4. Model Code 2010 suggests design equations for the shear capacity of SFRC with longitudinal reinforcement.

2.3. Mechanical Properties for Structural Modeling

Behavioral models for SFRC are characterized by formulations which account for the influence of fiber volumetric ratio, in addition to fiber shape and aspect ratio, on key parameters. In some cases, the fiber contribution is superimposed with an existing plain or reinforced concrete model and, in others, the fiber contribution is coupled. The following two sections describe compression and tension behavioral models, respectively.

2.3.1. Behavior in Compression

This section discusses various compressive stress-strain relationships that have been proposed in the literature for SFRC. Typically, these models modify the initial stiffness and strain at peak stress of conventional stress-strain relations for plain concrete. They also modify the post-peak slope to represent the increase in toughness provided by the fiber reinforcement. Ultimately, the stress-strain relations depend on the concrete strength, fiber content, and fiber type, among a few other important factors. An example of a compressive stress-strain curve for SFRC is presented in Figure 2.8.

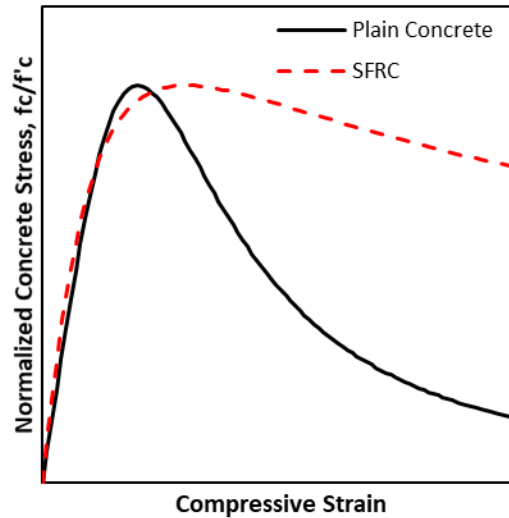


Figure 2.8 Example of compressive stress-strain responses of plain concrete and SFRC

2.3.1.1. Ezeldin and Balaguru (1992)

Ezeldin and Balaguru (1992) evaluated 18 concrete mixtures containing hooked-end steel fibers using standard 4 x 8 in. concrete cylinder uniaxial compression tests to classify the compressive stress-strain behavior of SFRC. The concrete strength was varied from 5 to 12 ksi. Three fiber volumes were investigated: 0.4, 0.6, and 0.8 %. Additionally, fiber length and diameter were varied to study three aspect ratios (aspect ratio = l_f/d_f): 60, 75, and 100.

The results of the experiments led to several key observations about the compressive stress-strain response of SFRC. First, the addition of fiber reinforcement led to an increase in both peak stress (approximately 20 % on average) and its associated strain (approximately 30 %, on average) for the normal-strength specimens. Additionally, the elastic modulus was observed to have increased. These increases were less apparent in the high-strength specimens. The toughness, the area under the stress-strain curve, was also markedly increased in all specimens due to the more ductile post-peak response of SFRC. Ezeldin and Balaguru (1992) noted that these relationships were primarily dependent on the reinforcing index of the mixture. They defined the reinforcing index as the product of the fiber weight fraction and aspect ratio.

To account for these differences in the behavior with respect to plain concrete, Ezeldin and Balaguru (1992) proposed modifications to the uniaxial compression stress-strain model for unconfined concrete proposed by Carreira and Chu (1985). The general form of the original stress-strain curve is described by Equations (2.17) and (2.18).

$$\frac{f_c}{f'_c} = \frac{\beta \left(\frac{\varepsilon_c}{\varepsilon'_c} \right)}{\beta - 1 + \left(\frac{\varepsilon_c}{\varepsilon'_c} \right)^\beta} \quad (2.17)$$

$$\beta = \frac{1}{1 - \frac{f'_c}{\varepsilon'_c E_c}} \geq 1.0 \quad (2.18)$$

Using their own results and results from fiber-reinforced mortar tested by Fanella and Naaman (1985), Ezeldin and Balaguru (1992) developed two expressions for β , one for hooked-end fibers and one for straight fibers, given by Equations (2.19) and (2.20), respectively. Furthermore, Equation (2.19) applies to reinforcing index values ranging from 0.75 to 2.5, and Equation (2.20) applies to reinforcing index values ranging from 2 to 5.

$$\beta = 1.093 + 0.7132 \left[W_f \left(\frac{l_f}{d_f} \right) \right]^{-0.926} \quad (2.19)$$

$$\beta = 1.093 + 7.4818 \left[W_f \left(\frac{l_f}{d_f} \right) \right]^{-1.387} \quad (2.20)$$

When Equations (2.19) and (2.20) are used in Equation (2.17), f'_c becomes f'_{cf} and ε'_c becomes ε'_{cf} , given in Equations (2.21) and (2.22), respectively. Note that the inputs for these equations are restricted to U.S. customary units (psi).

$$f'_{cf} = f'_c + 509 W_f \left(\frac{l_f}{d_f} \right) \quad (2.21)$$

$$\varepsilon'_{cf} = \varepsilon'_c + 0.000446W_f \left(\frac{l_f}{d_f} \right) \quad (2.22)$$

2.3.1.2. Hsu and Hsu (1994)

To develop empirical equations to describe the compression behavior of high-strength SFRC, Hsu and Hsu (1994) tested high-strength (f'_c greater than 10 ksi), fiber-reinforced specimen (3 x 6 in. cylinders) with three fiber volume fractions (0.5, 0.75, and 1 %) and varying levels of tie confinement, provided by 12-gage steel wire. The steel fibers had hooked ends and an aspect ratio of 60.

Hsu and Hsu (1994) noted that the strength development rate of high-strength SFRC was similar to that of high-strength concrete without fiber reinforcement. Furthermore, they noted similar observations to Ezeldin and Balaguru (1992), namely that toughness increased due to improved post-peak behavior and that the strain associated with peak stress increased. However, unlike Ezeldin and Balaguru (1992), Hsu and Hsu (1994) did not note significant increases in compressive strength (i.e., $f'_c = f'_{cf}$). Similarly to Ezeldin and Balaguru (1992), Hsu and Hsu (1994) proposed a stress-strain relationship for high-strength SFRC based on the formulation for plain concrete proposed by Carreira and Chu (1985). Equation (2.23) is a variation of Equation (2.17) that includes a modification factor (n) for the material parameter from Equation (2.18) to account for the differences in post-peak behavior between unconfined, normal- and high-strength concrete. Furthermore, there is an additional curve for post-peak behavior, which applies to a concrete stress-strain state past a certain threshold for unconfined, high-strength concrete.

$$\frac{f_c}{f'_c} = \begin{cases} \frac{n\beta \left(\frac{\varepsilon}{\varepsilon'_c} \right)}{n\beta - 1 + \left(\frac{\varepsilon}{\varepsilon'_c} \right)^{n\beta}} & \dots \quad 0 \leq \frac{\varepsilon_c}{\varepsilon'_c} < \frac{\varepsilon_d}{\varepsilon'_c} \\ 0.6e^{-0.7 \left(\frac{\varepsilon_c - \varepsilon_d}{\varepsilon'_c} \right)^{0.8}} & \dots \quad \frac{\varepsilon_c}{\varepsilon'_c} \geq \frac{\varepsilon_d}{\varepsilon'_c} \end{cases} \quad (2.23)$$

where,

ε_d = strain at $0.6f'_c$ on the descending branch of the stress-strain curve for high-strength, fiber-reinforced concrete

Similar to Ezeldin and Balaguru (1992), Hsu and Hsu (1994) proposed several additional curve-fits to complete the model for unconfined concrete.

$$\beta = \left(\frac{f'_c}{1.717V_f^3 + 8.501} \right)^3 - 0.26V_f + 2.742 \quad (2.24)$$

$$\varepsilon'_c = a_1 f'_c + C_1 \quad (2.25)$$

$$E_c = a_2 f'_c + C_2 \quad (2.26)$$

where,

- a_1 = constant calibrated for V_f equal to 0.5, 0.75, or 1.0 %
- a_2 = constant calibrated for V_f equal to 0.5, 0.75, or 1.0 %
- C_1 = constant calibrated for V_f equal to 0.5, 0.75, or 1.0 %
- C_2 = constant calibrated for V_f equal to 0.5, 0.75, or 1.0 %

In addition to Equations (2.24) to (2.26), Hsu and Hsu (1994) developed specific curve-fits for confined concrete strength, peak strain, and the material parameter, β , for fiber volume fractions of 0.5, 0.75, or 1.0 %, which were dependent on the confinement reinforcement ratio.

2.3.1.3. Keyvani Someh and Saeki (1996)

Keyvani Someh and Saeki (1996) tested 6 x 12 in. cylinders with an average compressive strength of about 4 ksi and straight fibers to develop a compressive stress-strain curve for SFRC. They investigated an aspect ratio of 50 with approximately 1.5 in. long fibers. Furthermore, three fiber contents were tested: 0.7, 1.4, and 2 %. The observations of Keyvani Someh and Saeki (1996) were similar to those of previous researchers. Namely, their test specimens achieved their peak compressive stress at a higher strain, and their post-peak behavior was improved with respect to plain concrete. The assertion that peak compressive stress is largely unaffected by the addition of steel fibers, also made by Hsu and Hsu (1994), was corroborated.

Keyvani Someh and Saeki (1996) proposed the following equations to modify the basic relationship for plain concrete proposed by Carreira and Chu (1985) in Equation (2.17) (units of kgf/cm², 1 kgf/cm² \approx 14.223 psi):

$$\varepsilon'_{cf} = 0.00131 f'_c{}^{0.147} \quad (2.27)$$

$$\beta = 0.794 \left[f'_c \left(1 + V_f \frac{l_f}{d_f} \right) \right]^{0.113} \quad (2.28)$$

2.3.1.4. Mansur, Chin, and Wee (1999)

To expand upon previous work completed on high-strength SFRC, Mansur, Chin, and Wee (1999) tested a combination of concrete cylinders, cubes, and prisms with strengths ranging from about 10 to 17.5 ksi. Furthermore, they compared a vertical casting direction (traditional cylinder and prisms with long dimension vertical) versus a horizontal casting direction (prisms with long dimension horizontal) to study the influence of casting direction on fiber orientation. Hooked-end fibers with a diameter of 0.02 in. and a length of 1.2 in were used. All mixtures were prepared with a 1 % fiber volume fraction.

Mansur et al. (1999) found that casting direction, relative to the loading direction, was influential for certain parameters. The initial tangent modulus was found to be lower for the vertically cast specimens compared to the horizontal ones. The peak compressive stress was found to be practically independent (differences within 5 %) of fiber content and casting direction. In some cases, the vertical casting direction provided a slower post-peak decay than the specimens that were cast horizontally. Lastly, they observed a slight directionality effect on strain at peak stress, where vertically cast specimens tended to have higher strains associated with peak stress.

Similar to past researchers, Mansur et al. (1999) proposed modifications to the plain concrete formulation proposed by Carreira and Chu (1985), as shown in Equations (2.29) through (2.37). Note that input and output for Equations (2.30) through (2.37) are restricted to megapascals (1 MPa \approx 0.145 ksi) and that Equation (2.18) still applies for β .

$$\frac{f_c}{f'_c} = \frac{k_1 \beta \left(\frac{\varepsilon_c}{\varepsilon'_c} \right)}{k_1 \beta - 1 + \left(\frac{\varepsilon_c}{\varepsilon'_c} \right)^{k_2 \beta}} \quad (2.29)$$

For cylindrical specimens,

$$E_c = (10,300 - 400V_f) f'_c{}^{1/3} \quad (2.30)$$

$$\varepsilon'_c = \left[0.0005 + 0.00000072 \left(V_f \frac{l_f}{d_f} \right) \right] f'_c{}^{0.35} \quad (2.31)$$

$$k_1 = \begin{cases} 1 & \dots & 0 \leq \frac{\varepsilon_c}{\varepsilon'_c} \leq 1 \\ \left(\frac{50}{f'_c} \right)^{3.0} \left[1 + 2.5 \left(V_f \frac{l_f}{d_f} \right)^{2.5} \right] & \dots & \frac{\varepsilon_c}{\varepsilon'_c} \geq 1 \end{cases} \quad (2.32)$$

$$k_2 = \begin{cases} 1 & \dots & 0 \leq \frac{\varepsilon_c}{\varepsilon'_c} \leq 1 \\ \left(\frac{50}{f'_c} \right)^{1.3} \left[1 - 0.11 \left(V_f \frac{l_f}{d_f} \right)^{2.5} \right] & \dots & \frac{\varepsilon_c}{\varepsilon'_c} \geq 1 \end{cases} \quad (2.33)$$

For horizontally cast prisms,

$$E_c = 10,300 f'_c{}^{1/3} \quad (2.34)$$

$$\varepsilon'_c = 0.00048 f'_c{}^{0.35} \quad (2.35)$$

$$k_1 = \begin{cases} 1 & \dots & 0 \leq \frac{\varepsilon_c}{\varepsilon'_c} \leq 1 \\ A \left(\frac{40}{f'_c} \right)^{2.0} & \dots & \frac{\varepsilon_c}{\varepsilon'_c} \geq 1 \end{cases} \quad (2.36)$$

$$k_2 = \begin{cases} 1 & \dots & 0 \leq \frac{\varepsilon_c}{\varepsilon'_c} \leq 1 \\ B \left(\frac{40}{f'_c} \right)^{1.3} & \dots & \frac{\varepsilon_c}{\varepsilon'_c} \geq 1 \end{cases} \quad (2.37)$$

where,

- A = 0.96 for fiber reinforced concrete and 1.00 for plain concrete
- B = 0.80 for fiber reinforced concrete and 1.00 for plain concrete

2.3.1.5. Natajara, Dhang, and Gupta (1999)

While many of the models discussed thus far were developed for hooked-end fibers, Natajara, Dhang, and Gupta (1999) focused on the behavior of relatively normal-strength concrete (strengths ranging from 4300 to 7300 psi) reinforced with round crimped fibers. They investigated volume fractions ranging from 0.5 to 1.0 % and elected to modify the compressive stress-strain curve proposed by Carreira and Chu (1985). Natajara et al. (1999) noted benefits for crimped fibers that were similar to those of hooked-end fibers: a significant increase in toughness and marginal increases in compressive strength and strain at peak stress. They recommended the following equations for concrete reinforced with crimped steel fiber, with the input of megapascals (1 MPa \approx 0.145 ksi):

$$f'_{cf} = f'_c + 2.1604 W_f \frac{l_f}{d_f} \quad (2.38)$$

$$\varepsilon'_{cf} = \varepsilon'_c + 0.0006 W_f \frac{l_f}{d_f} \quad (2.39)$$

$$\beta = 0.5811 + 1.93 \left(W_f \frac{l_f}{d_f} \right)^{-0.7406} \quad (2.40)$$

Equation (2.40) may be used in conjunction with Equation (2.17), provided that the normal compressive strength is replaced by Equation (2.38) and the normal strain at peak stress is replaced by Equation (2.39).

2.3.1.6. Bencardino, Rizzuti, Spadea, and Swamy (2008)

Bencardino, Rizzuti, Spadea, and Swamy (2008) performed a review of existing compressive stress-strain models using existing data in the literature as well as performing additional testing of cylinder specimens reinforced with hooked-end fibers in volume fractions of 1.0, 1.6, and 3.0 % - much higher than most of the data presented by previous researchers. Based on several comparisons made using their own data and data published in the literature, Bencardino et al. (2008) concluded that, while all published models agreed well with the data used to calibrate them, the models typically did not perform as well for other experimental data. They recommended further refinement to enable a generalized approach for the full stress-strain modeling of SFRC in compression.

2.3.1.7. Lee, Oh, and Cho (2015)

Another review of existing stress-strain laws was completed by Lee, Oh, and Cho (2015); furthermore, they tested additional 6 x 12 in. cylinders with fiber volumetric ratios from 0.5 to 2.0 %. Based on these experimental results, Lee et al. (2015) drew conclusions similar to those of past researchers about the influence of fiber content and aspect ratio on various aspects of behavior, such as peak stress, strain at peak stress, and toughness. Using a modified form stress-strain curve of Carreira and Chu (1985), and restricting input to megapascals (1 MPa \approx 0.145 ksi):

$$\frac{f_c}{f'_c} = \frac{A \left(\frac{\epsilon_c}{\epsilon'_c} \right)}{A - 1 + \left(\frac{\epsilon_c}{\epsilon'_c} \right)^B} \quad (2.41)$$

$$A = \begin{cases} \frac{1}{1 - \frac{f'_c}{\varepsilon'_c E_c}} & \dots & 0 \leq \frac{\varepsilon_c}{\varepsilon'_c} \leq 1 \\ 1 + 0.723 \left(V_f \frac{l_f}{d_f} \right)^{-0.957} & \dots & \frac{\varepsilon_c}{\varepsilon'_c} \geq 1 \end{cases} \quad (2.42)$$

$$B = \begin{cases} \frac{1}{1 - \frac{f'_c}{\varepsilon'_c E_c}} & \dots & 0 \leq \frac{\varepsilon_c}{\varepsilon'_c} \leq 1 \\ \left(\frac{f'_c}{50} \right)^{0.064} \left[1 + 0.882 \left(V_f \frac{l_f}{d_f} \right)^{-0.882} \right] \geq A & \dots & \frac{\varepsilon_c}{\varepsilon'_c} \geq 1 \end{cases} \quad (2.43)$$

$$\varepsilon'_c = \left(0.0003 V_f \frac{l_f}{d_f} + 0.0018 \right) f_c'^{0.12} \quad (2.44)$$

$$E_c = \left(-367 V_f \frac{l_f}{d_f} + 5520 \right) f_c'^{0.41} \quad (2.45)$$

2.3.2. Behavior in Tension

The pre-cracking tensile behavior of SFRC remains practically unchanged with respect to plain concrete; however, the post-cracking behavior becomes significantly more complex. Several researchers have proposed methodologies to estimate the relation between tensile stress and crack width in the post-cracking range. Crack development is also impacted greatly by the inclusion of fibers, and conventional crack width and crack spacing models do not adequately account for the influence of fibers. As such, some researchers have proposed alternative methods for estimating crack spacings and widths for SFRC. An example is shown in Figure 2.9.

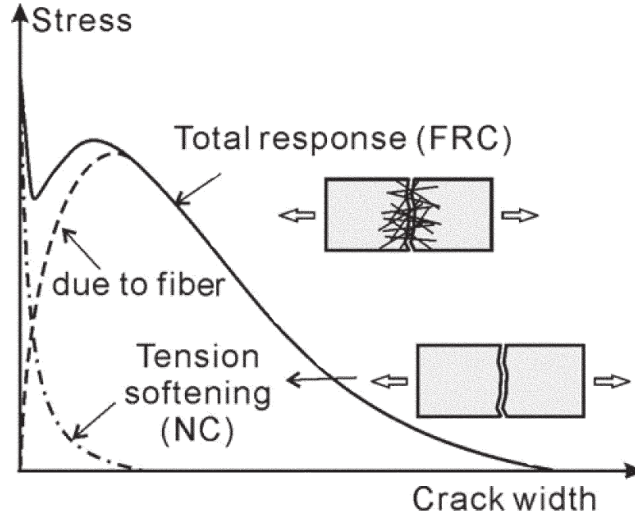


Figure 2.9 Post-cracking behavior of concrete (NC) and fiber-reinforced concrete (FRC) (Lee et al., 2011a)

2.3.2.1. Marti, Pfy, Sigrist, and Ulaga (1999)

Marti, Pfy, Sigrist, and Ulaga (1999) proposed a circular slab method for evaluating the tension behavior of SFRC in lieu of more common methods such as the modulus of rupture test. The result of their experimental investigation resulted in recommendations for modeling the uniaxial tension behavior of SFRC. Marti et al. (1999) recommended modeling the fibers with a random orientation (based on research by Aveston & Kelly, 1973) and assuming fiber pullout was the governing failure mode. Therefore, fiber bond strength was one of the primary parameters. Furthermore, they asserted that at a crack width of one-half the fiber length, all fibers bridging the crack will have pulled out and recommended the following parabolic tension softening relationship:

$$f_t = \frac{V_f l_f \tau}{2d_f} \left(1 - \frac{2w_{cr}}{l_f} \right)^2 \quad (2.46)$$

They also recommended a constant average bond shear stress as follows:

$$\tau = 2f'_t \quad (2.47)$$

2.3.2.2. Voo and Foster (2003)

Voo and Foster (2003), using similar baseline assumptions (i.e., randomly, evenly distributed fibers in three dimensions), proposed a model which considered variable engagement lengths for fibers. The primary difference between their model and the one proposed by Marti et al. (1999) was the inclusion of a global orientation factor (K_f) to adjust the model for material-specific parameters. Furthermore, they imposed cutoffs based on fiber fracture. The basic Variable Engagement Model, considering fiber pullout, is described by Equations (2.48) and (2.49).

$$f_t = \frac{V_f l_f \tau}{d_f} K_f \quad (2.48)$$

$$K_f = \frac{\text{atan}\left(\frac{w_{cr}}{\alpha}\right)}{\pi} \left(1 - \frac{2w_{cr}}{l_f}\right)^2 \quad (2.49)$$

where,

$$\begin{aligned} \alpha &= \text{material parameter} \\ &= d_f/3.5 \end{aligned}$$

2.3.2.3. Lee, Cho, and Vecchio (2011a, 2011b, 2013a)

Lee, Cho, and Vecchio (2011a, 2011b) developed and verified an analytical model called the Diverse Embedment Model (DEM) for calculating the tensile response of SFRC. It is largely an extension of the VEM; however, they also made considerations for relatively small elements where fiber orientation may be influenced by the element boundaries. The original DEM required a double numerical integration and was considered to be fairly complicated; therefore, a simplified version was proposed (Lee, Cho, & Vecchio, 2013a).

The simplified DEM (SDEM) considers the fiber slip on the shorter embedded side to be equal to the crack width and neglects the variation of slip along the fiber. Lee et al. (2013a) introduced two correction factors to allow for this simplification. The SDEM does not require double numerical integration; as such, it is much easier to implement. Furthermore, it was shown that the simplifications marginally influence the final computed results (Lee et al., 2013a). The contributions of the frictional bond behavior (f_{st}), mechanical anchorage (f_{eh}), and concrete contribution (f_{ct}) are summarized in Equations (2.50) through (2.53).

$$f_{st} = \alpha_f V_f K_{st} \tau_f \frac{l_f}{d_f} \left(1 - \frac{2w_{cr}}{l_f}\right)^2 \quad (2.50)$$

$$f_{eh} = \alpha_f V_f K_{eh} \tau_{eh} \frac{2}{d_f} (l_i - 2w_{cr}) \quad (2.51)$$

$$f_{ct} = f_t' e^{-15w_{cr}} \quad (2.52)$$

$$f_t = \begin{cases} f_{st} + f_{ct} & \dots \text{ straight fibers} \\ f_{st} + f_{eh} + f_{ct} & \dots \text{ hooked-end fibers} \end{cases} \quad (2.53)$$

where,

- α_f = fiber orientation factor (Lee et al., 2011a)
- K_{st} = average frictional bond behavior factor
- τ_f = frictional bond strength
- K_{eh} = average mechanical anchorage behavior factor
- τ_{eh} = mechanical anchorage pullout strength
- l_i = distance between mechanical anchorages of fiber

2.3.2.4. Lee, Cho, and Vecchio, (2013b)

The previously discussed tension models relate to the response of SFRC without conventional reinforcement. An additional model was proposed for SFRC reinforced with conventional steel bars to account for the tension stiffening effect of conventional reinforcement (Lee, Cho, & Vecchio, 2013b). If an SFRC contains conventional reinforcement, one of the aforementioned models should be used with the one presented in this section, and the maximum of the two should be used to represent the tension response. Lee et al. (2013b) proposed modifications to the tension stiffening model for reinforced concrete proposed by Bentz (2005), which accounts for the fact that cracked concrete can, on average, carry tensile stresses between cracks due to bond stresses between the concrete and reinforcement. The original model given by Bentz (2005) is shown in Equation (2.54), and the modified form for SFRC (Lee et al., 2013b) is shown in Equations (2.55) and (2.56).

$$f_t = \frac{f'_t}{1 + \sqrt{3.6m\varepsilon_t}} \quad (2.54)$$

$$f_t = \frac{f'_t}{1 + \sqrt{3.6c_fm\varepsilon_t}} \quad (2.55)$$

$$c_f = \begin{cases} 0.6 + \frac{1}{0.058} \left(\frac{l_f}{d_f} \right)^{0.9} \frac{100V_f}{m^{0.8}} & \dots \text{ straight fibers} \\ 0.6 + \frac{1}{0.034} \left(\frac{l_f}{d_f} \right) \frac{(100V_f)^{1.5}}{m^{0.8}} & \dots \text{ hooked-end fibers} \end{cases} \quad (2.56)$$

where,

m = conventional reinforcement bond parameter

2.3.2.5. Deluce, Lee, and Vecchio (2014)

The last important consideration for the tensile behavior of SFRC is the crack spacing (s_{cr}). The crack spacing is often used in conjunction with tensile strains to estimate crack widths in reinforced concrete analysis procedures, as shown in Equation (2.57). Traditional crack spacing models do not account for the influence of steel fibers on crack spacing. Deluce, Lee, and Vecchio (2014) proposed modifications to the crack spacing model proposed in the 1978 Model Code (CEB-FIP, 1978). These changes, summarized in Equations (2.58) through (2.62) for a uniaxial strain condition, were shown to provide reasonable estimates of crack spacing and width in SFRC elements.

$$w_{cr} = \varepsilon_t s_{cr} \quad (2.57)$$

$$s_m = 2 \left(c_a + \frac{s_b}{10} \right) k_3 + \frac{k_1 k_2}{s_{mi}} \quad (2.58)$$

$$s_b = 0.5 \sqrt{\frac{\pi d_b^2}{\rho_{eff}}} \quad (2.59)$$

$$s_{mi} = \frac{\rho_{eff}}{d_b} + k_f \frac{\alpha_f V_f}{d_f} \quad (2.60)$$

$$k_3 = 1 - \frac{\min(V_f, 0.015)}{0.015} \left(1 - \frac{1}{k_f}\right) \quad (2.61)$$

$$k_f = \frac{l_f}{50d_f} \geq 1.0 \quad (2.62)$$

where,

- c_a = effective concrete clear cover
- k_1 = bond characteristic parameter
- k_2 = strain condition parameter
- d_b = conventional reinforcement bar diameter
- ρ_{eff} = effective conventional reinforcement ratio

2.3.2.6. Conclusions

The primary conclusions related to mechanical properties of SFRC for structural modeling are as follows:

1. Many models have been proposed for modeling the tension and compression response of SFRC. While there are several relatively general, applicable tension models, there are few generally applicable compression models.
2. The tension behavior is critical for an accurate modeling and analysis of SFRC members. Differences in the post-peak, cracking, and toughness properties must be appropriately accounted for. Compression behavior appears to be less important based on the review to-date; however, it may become more significant in compression-controlled failures.

2.4. Experimental Investigations of SFRC

The use of prestressed precast panels (PCP) as stay-in-place formwork dates back to the 1960's in Texas. Several advantages of PCPs for bridge deck construction include such as increased speed, cost-effectiveness, and safety. While much work has been completed to optimize conventional reinforcement layouts, this project suggests SFRC as a substitute for conventional cast-in-place concrete in order to further optimize the design of PCP-CIP bridge decks. This alternative is expected to increase construction efficiency and potentially improve the cracking behavior of bridge decks. The following sections review the available literature related to PCP-CIP construction (Section 3.1.1) and the use of SFRC in structural members (Section 3.1.2).

2.4.1. PCP-CIP Bridge Deck Construction

2.4.1.1. Kluge and Sawyer (1975)

Early research on PCP-CIP deck construction focused on the feasibility of the method. The concern about the interfacial bond between the cast-in-place and precast portions of the deck led to research that examines the monolithic behavior of PCP-CIP decks. Kluge and Sawyer (1975) assessed the bond between precast panels and CIP concrete with four specimens. PCPs of each specimen have a smooth surface or U-bar shear reinforcement. Specimens were 7 in. thick (3-in. PCP and 4-in. CIP), 18 in. wide, and 8 ft. long and were tested for both static and cyclic loading. All the specimens failed in one-way shear. In addition, there was no separation between the PCP and the CIP topping without intended shear transfer. This indicates that the bond between smooth PCP and CIP is sufficient, and no other reinforcement is required across the interface of the two materials. Current codes require a rough surface of panels to prevent the potential splitting problem.

2.4.1.2. Bieschke and Klinger (1982)

Another issue in fabricating PCPs, is that the extended pre-tensioning strands hinder a continuous casting bed. Bieschke and Klinger (1982) investigated PCP-CIP decks without strand extension. A full scale, 50 ft. by 18 ft., with 9 in. in thickness, bridge deck was tested. Two types of PCPs were tested: one with strand extensions and one without strand extensions. Loading included both static and fatigue loadings. The result indicates that panels without strand extension performed the same as those with strand extension. Current TxDOT standards require a minimum 3 in. transverse reinforcing projection.

2.4.1.3. Merrill (2002)

Merrill (2002) summarized the history, specifications, benefits, and drawbacks of the CIP-PCP bridge deck construction method. Merrill (2002) concluded that since the PCP-CIP deck requires little formwork and reduces on-site concrete casting, it allows the bridge to be completed and opened to traffic sooner. Safety can be improved because it requires significantly less form removal work. This method also provides improved durability by high-quality coarse and fine aggregate for deck panels. TxDOT established design specifications, such as rebar spacing, precast and CIP concrete thickness, and pre-tensioning method, to accelerate design and construction procedures. Typical problems associated with PCP-CIP deck construction are cracks near panel boundaries. Longitudinal cracking, which is generated along the girders, is generally due to drying shrinkage, restraint by panel ends, and lack of mortar between panels and girders. Transverse cracking is commonly due to concrete shrinkage, restraint by panels, and gaps between panels. Most crack problems are solved with appropriate solutions such as high-density foams, thorough compaction near girders, shrinkage, and temperature reinforcing steels.

2.4.1.4. Coselli et al. (2006)

Recently, detailed specifications for PCP placement and the optimization of PCP-CIP deck design were reported. Coselli et al. (2006) investigated the behavior of bridge slabs at expansion joints by building a full-scale CIP-PCP specimen. The size of the specimen was 32 ft. by 18 ft., with different girder spacings of 8 ft. and 10 ft. Both full-depth CIP 8 in. deck and PCP-CIP 8 in. deck (4 in. PCP and 4 in. CIP) were incorporated in the design. The researchers found that the interior loading condition had a higher capacity compared to the overhang due to the benefit of arching action. Increasing the load from HS-20 to HS-25 loading showed a linear increase in deflection. The researchers concluded that although the PCP-CIP deck showed inevitable cracking due to restrained shrinkage, this did not generate any detrimental effect on the capacity of the structure.

2.4.1.5. Foster (2010)

The goal of this research was to optimize the PCP-CIP bridge deck by reducing the required reinforcement for the system. Several tests with different top mat reinforcement ratios were evaluated to investigate control crack width across PCP joints (Foster, 2010). Constant bending moment testing, point load testing, and direct tension testing were performed. Constant bending moment testing used two 8ft. by 8 ft. PCPs connected with CIP topping. However, this test showed some problems, such as the deviation of the first crack location from the center. To further

investigate, point load tests with notched specimens were completed. The tests showed that sufficient tensile strength of the topping is essential to control transverse crack widths. The researchers concluded that the longitudinal top mat reinforcement should follow existing standards of No. 4 bars at 9 in. spacing.

2.4.1.6. Kwon (2012)

Kwon (2012) performed testing on two bridges (Wharton-Weems Overpass and Lampasas River Bridge) and conducted large-scale restrained shrinkage tests to optimize the transverse reinforcement design of PCP-CIP bridge decks. The bridge was constructed with No.4 bars at 6 in. spacing or welded-wire reinforcement with an equivalent reinforcement area. This resulted in a 30 % reduction in the transverse steel area compared to the TxDOT standard. The researcher found that strains in the transverse direction did not change significantly and concluded that reduction of transverse reinforcement is acceptable. This research also proposed a new method for the prediction of prestress loss in PCP.

2.4.1.7. Munsterman (2017)

Munsterman (2017) tried to estimate the adequacy of current TxDOT standards for reinforcing steel in the negative moment region of bridge decks. He monitored three newly constructed bridges: San Marcos SH123 Bridge, Bastrop SH71 Entrance Ramp, and Round Rock UPPR Ramp. Each bridge used three types of reinforcement layouts with different reinforcement ratios. Strain gauges for each position measured the top mat reinforcement strain for different live load cases. The field data showed that the amount of steel reinforcement did not affect measured strain at diverse positions. Further, field observations of cracking in the deck displayed that current reinforcement gives appropriate crack-controlling performance.

2.4.1.8. TxDOT Bridge Design Guide (2018)

Current standards for PCP-CIP decks are contained within the TxDOT Bridge Design Guide. The following list summarizes the key provisions for PCP-CIP construction.

1. Allowed for the bridges that have girder spacing that exceed 6 ft.
2. Maximum panel length is 9 ½ ft.
3. Panels are placed on bedding strips. The material for bedding strips is high-density foam, and the height of the strip is adjusted according to the deflection of girders and the width of the strips. (Table 2.1)

4. Precast panels intrude over the bedding strips for a minimum of 1 ½ in.
5. The typical thickness of panels is 4 in., and the total depth for the deck should be at least 8 in.
6. The concrete used for panels is class H concrete with $f'_{ci} = 3.5ksi$ and $f'_c = 5ksi$ minimum. For the CIP region, class S concrete with $f'_c = 4ksi$ is required.
7. Transverse reinforcement in panels should be extended about 3 (+1/2 -1 ½) in.
8. If the panel ends and the CIP deck extends, longitudinal reinforcement should be continued for 1 ft.
9. The transverse and longitudinal reinforcement of PCP follows Table 2.2.
10. The longitudinal and transverse top mat reinforcements are No. 4 at 9 in. spacing.
11. The concrete cover for the bottom is 1-1/4 in., and 2 in. for the top and end of overhangs.

Table 2.1 Bedding strip dimensions (TxDOT bridge design specifications, 2018)

| Width [in.] | Height | |
|-------------|--------------|---------------|
| | Minimum[in.] | Maximum [in.] |
| 1 | ½ | 2 |
| 1 ¼ | ½ | 2 ½ |
| 1 ½ | ½ | 3 |
| 1 ¾ | ½ | 3 ½ |
| 2 | ½ | 4 |

Table 2.2 Transverse and longitudinal reinforcement for PCP(TxDOT bridge design specifications, 2018)

| Types | Span | Reinforcement |
|--------------|----------------------|--|
| Transverse | Up to 3 ft. 6 in. | No. 4 Gr. 60 bars at 6 in. spacing |
| | 3 ft. 6 in. to 5 ft. | same as over 5' or use No. 4 Gr.60 bars at 6 in. spacing |
| | Over 5 ft. | 3/8" or ½" strand with 14.4 kips pre-tensioning at 6 in. spacing |
| longitudinal | N/A | No. 3 Gr. 50 at max 6 in. spacing |
| | N/A | 3/8 in. dia strands at max 4 ½ in. spacing |
| | N/A | ½ in. dia strands at max 6 in. spacing |

2.4.2. SFRC in Bridge Decks and flat slabs

Bridge decks are commonly designed empirically, based on standard detailing practices, with built-in considerations for flexural strength, as well as temperature and shrinkage effects. Both one-way deck strip and full-scale deck testing are typically utilized in the laboratory to represent real bridge deck behavior. The following summarizes available literature dealing with one-way strips and full-scale bridge decks with SFRC.

2.4.2.1. Barros and Figueiras (1999)

Barros and Figueiras (1999) tested the performance of SFRC slab strips with different fiber volume fractions. Two types of hooked end fibers, having aspect ratios of 60 and 75, with different volume fractions ranging from 0 to 0.75 %, were used. Compressive and notched beam tests were performed to assess the compression stress-strain relationship and post-peak tensile behavior. The longer fibers were used for slab strip testing. The slab strips were reinforced with steel wire mesh reinforcement. Failure load, displacement at the center, and crack width were measured for the different fiber volume fractions.

The failure load of test specimens increased as the volume fraction of the steel fibers increased. About twice the load was carried when 0.75 % of fibers were added. Like other studies, higher volume fractions also showed greater ductility. Crack widths in the central region were 3.94, 3.15, and 1.57 in. for the volume fractions 0.385, 0.56, and 0.75 %, respectively.

2.4.2.2. Naaman and Chandransu (2004)

Naaman and Chandransu (2004) focused on the performance of a typical deck with high-performance fiber reinforced concrete. They emphasized the possibility of fiber reinforcement as a substitute for negative moment reinforcement as well as temperature and shrinkage reinforcement. Two-span continuous slab specimens were tested to evaluate the effect of fibers in the concrete. Test specimens had 6 in. depth, 4 in. width, and two 5 ft. spans. The depth of the specimens and positive moment reinforcement were determined based on the AASHTO-LRFD specification. Decks were supported on steel girders, and some of the slabs were prestressed with steel strands. The load-displacement behavior of the decks with fiber reinforcement and reduced conventional reinforcement was comparable to or more favorable than the control case (conventional reinforced concrete). The average width of the crack was 30 % smaller, and the spacing between cracks was 1/7 of the AASHTO standard. In addition, prestressed decks showed no sign of cracking at maximum service load, even near supports. The fibers used for the test were high-density molecular polyethylene.

2.4.2.3. Dunn et al. (2005)

Dunn et al. (2005) implemented field testing of the first steel-free deck bridge in the United States, which was placed in Tama County, Iowa. A full-depth CIP deck without steel reinforcement, except for the overhang region, was constructed. The need for steel reinforcement was questioned because the internal arching action of the bridge alone can resist exerted loads from traffic and the environment. Longitudinal restraint was achieved by shear studs on the steel bridge girders, and transverse confinement was made possible by steel straps that were welded between steel girder top flanges. The additional restraint provided by the steel straps assisted in controlling concrete deck cracking. This allowed fiber-reinforced polymers in the concrete to assist in controlling shrinkage and temperature cracks and their propagation. Seven cases of live load testing using two trucks showed that the steel free bridge deck in Tama County can resist service loads by having 1/6 of deflection limit, 50 % of concrete tensile strength, and 6 % of steel strap yield stress.

2.4.2.4. Naaman et al. (2007)

Naaman et al. (2007) experimented on full-depth slab panels with high-performance FRC subjected to concentrated loading. The research aimed to simulate the punching shear failure of a conventional bridge deck system. High-performance fibers stood for three different fibers: polyvinyl-alcohol, ultra-high molecular weight polyethylene, and twisted steel (TOREX), each having volumetric fractions of 2, 1.75, and 2 %, respectively. Each of the fibers was incorporated into specimens with different reinforcement patterns. Ten specimens were fabricated. Nine of the specimens had different fibers or reinforcement, and one of the specimens had reinforcement only conforming to AASHTO standards.

Each specimen was a square slab with a 31 by 31 in. width and 7 in. depth. Each specimen was loaded concentrically at the center, with a steel base supporting each edge. Tests were aimed to measure the punching shear resistance, the energy absorption capacity, and the spalling resistance. Energy absorption was calculated up to 1.75 in. displacement at the center of specimens. The experimental result indicated that fibers benefit slabs' punching shear capacity, energy absorption capacity, and spalling action. Twisted steel fiber and Torex fiber had a superior advantage compared to conventional reinforced concrete or other fibers. The peak load of twisted steel fiber concrete was two to five times larger than the conventional concrete slab. Also, it had 2.6 times higher post-cracking strength. Torex fibers alone without any reinforcing bars exhibited punching shear capacity comparable to conventional concrete reinforced with No. 3 at 4 in.

2.4.2.5. McMahon and Birely (2018)

McMahon and Birely (2018) experimented on full-scale SFRC bridge decks. Hooked-end steel fibers of 0.5 % volume fraction were poured into freshly mixed class S concrete, and the 0.5 % volume ratio was determined based on the test done by Birely et al. (2018). A fiber volume of 0.5 % satisfactorily improved the tensile performance of the concrete and reduced required steel bars. Initially, four slab-strip beams were tested to investigate the one-way strength of the SFRC concrete beam. One-way strength was the cornerstone for a yield-line analysis, which estimates the capacity of a full-scale bridge deck. The slab strips were 7 ft. long, 18 in. wide, and 7.5 to 9 in. deep. Four specimens were distinguished by whether the specimen had either steel reinforcement or fiber reinforcement. The full-scale deck specimen had two spans with two overhangs on each end. Testing regions were subjected to single and tandem loads that correspond to AASHTO-LRFD and the HS-20 design truck. Loads were increased monotonically until failure. For each load application, decks failed in punching shear.

The deck strip testing showed that SFRC decks had a higher capacity than conventional reinforced concrete decks. In addition, SFRC limited the width of the crack and developed more cracks. In other words, the average crack width was smaller in SFRC. However, at large deflections, up to failure, the SFRC specimen demonstrated larger concentrated cracks. Full-scale testing indicated that the expected ultimate capacity by yield-line analysis corresponded to the overhang part of the bridge deck. However, yield-line analysis underestimated the capacity of the interior span. The failure capacity of the deck was up to 5 times the result of the yield-line analysis. This is due to the arching action.

2.4.2.6. Roesler et al. (2004)

Industrial floor slab benefits from SFRC for its toughness and durability. Roesler et al. (2004) performed monotonic loading tests of concrete slab-on-ground that had types of fibers in them. A total of five small-scale concrete slabs were tested. Two of them had two types of steel fiber, which were hooked and crimped with volume fractions of 0.35 and 0.5 %, respectively. The other two specimens had synthetic macro-fibers with different volume fractions, which are 0.32 and 0.48 %. The other was made with plain concrete. The slabs had a dimension of 7.2 by 7.2 ft. with a thickness of 5 in.. Deflections at various points of slabs were measured using LVDTs, and compressive tensile stress was measured through embedded strain gauges.

The test results showed that the load-deflection curves of the specimens were similar up to the first flexural cracking point. After first cracking, there was a sudden drop in load-carrying capacity. However, steel fibers resulted in

significantly higher post-cracking load and toughness, which is defined here as the area underneath the load-deflection curve. The flexural strength of SFRC slabs was 40 % greater than that of a plain concrete slab. Steel fibers showed better improvement in the ultimate load capacity of slabs than synthetic macro-fibers.

2.4.2.7. Khaloo and Afshari (2004)

Khaloo and Afshari (2005) estimated the influence of steel fiber volume, steel fiber length, and base concrete strength on the flexural strength of SFRC slabs. Twenty-eight slabs with dimensions of 32.3 by 32.3 in. with a thickness of 3.2 in. were tested. The slabs were classified by their volume fraction, 0.5, 1.0, and 1.5 %, aspect ratios, 41.9 and 52.4, and concrete strength, 4 and 6 ksi. The fibers were crimped with a rectangular cross-section. The specimens were placed on four corners, and a point load was applied at the center of the slabs.

Ultimate strength can be compared to the initiation of the first critical crack on the slab. The experimental result showed that fibers have no influence on the slab's ultimate strength but did change the post-cracking behavior. After cracking, slabs with volume fraction higher than 1.0 %, had increased energy absorption. The fiber length also influenced absorption. The reason for the failure of slabs was pulled out of fibers. Analytical estimation was performed based on yield-line theory considering SFRC tensile strength. The equation suggested that it overestimated the ability of steel fibers in concrete.

2.4.2.8. Mobasher and Destree (2010)

Mobasher and Destree (2010) used a high dosage of steel fibers as the only method of reinforcement for pile-supported elevated slabs. The span-to-depth ratio of the slabs ranged from 8 to 20. Using steel fibers for the slabs may be advantageous since slabs provide horizontal fiber orientation that is beneficial for the plane structure and less stress concentration due to moment interaction with arching action. Three types of fibers, which were undulated fiber, cone-end fiber, and hooked-end fiber, were used. The volume fractions of fibers were 0.5 to 1.3 %.

Flat round indeterminate slab tests were used to obtain material parameters for the composite. The specimens were 5.9 in. thick with a 31-in. diameter and simply-supported throughout the edge. The results were compared to the ASTM C1550, three-point bending flexural beam test. The experimental result excelled moment capacity by the direct calculation since it could replicate complex indeterminate slab behavior. Since there were few theoretical models for the flexural behavior of SFRC, back-calculation from the finite element model was used to obtain material properties. An elastic-plastic model was used to represent the compressive and

tensile strength of SFRC. Nominal moment capacity was calculated based on these strength data and was used for the design of full-scale testing.

Two full-scale elevated slab specimens with different span/depth ratios, 28 and 30, with the same fiber dosage, 1.3 %. The models had 16 columns and 3 spans, 16.4 and 19.7 ft., respectively, on each side. The specimens were subjected to highly concentrated point loading, uniformly distributed loadings, and wheel loads. The specimens were loaded to the ultimate load, and deflections and crack widths were measured. For the smallest span/depth ratio, the maximum load was 133.7 kips. However, specimens having a larger span/depth ratio failed at 105.6 kips. Initial stiffness and cracking point do not differ significantly, but the loading capacity dropped notably.

2.4.2.9. Michels et al. (2012)

Michels et al. (2012) investigated flat slab systems utilizing steel fiber as the only reinforcement. The main objective was to measure the bearing capacity of the flat slab under symmetrical loading around the columns. In addition, the dispersion and orientation of steel fibers were collected with growing specimen height. 1.3 % volume fraction of undulated steel fiber was the fiber dosage for all the specimens. Material testing with cylinders showed the uniaxial tensile strength $f_{ct} = 0.36ksi$, the bending tensile strength $f_{ct,b} = 0.8ksi$, and the residual tensile strength $f_{ct,res} = 0.54ksi$. No vibration or compaction techniques were used in casting the concrete to avoid homogeneous fiber dispersion.

The test result showed that the linear elastic limit of the slab increased as the thickness of the slab increased. Also, the total bearing capacity of the specimen was directly correlated to the slab height. However, for the same rotation angle, the thicker element showed a larger crack opening, which resulted in a lower residual tensile strength and faster capacity decreasing speed. The variation of horizontal fiber orientation was significant as the height of the specimen increased. This was because of the fiber sink due to the gravity force. This effect is negligible if the specimen thickness is less than 15 in. The stiff cement matrix could reduce this problem. The failure mode of specimens showed no punching shear. Instead, all the members exhibit ductile flexural failure. This is because the upper region cannot bear enough tensile strength to form diagonal shear cracking.

2.4.2.10. Fall et al. (2014)

Fall et al. (2014) examined the effect of steel fibers on load redistribution and the load-carrying capacity of slabs. The octagonal slabs had a 7.2 ft. span and were supported in two directions. Three slab specimens were fabricated with conventional reinforcement, fiber reinforcement, steel reinforcement, and only

fiber reinforcement. Steel-reinforced specimens had uneven reinforcement in different directions. The fibers used in the experiments were double hook-end steel fibers with 0.45 % volume fraction. The thickness of specimens was determined based on the yield-line method to generate flexural failure rather than shear failure. Since the compaction of SFRC could bring unwanted fiber distribution to the base material, self-compacting concrete was used, and no external vibration was performed.

Compared to the conventionally reinforced concrete specimen, SFRC with steel reinforcement increased the proportion of load redistribution. Measured loads at the supports showed a smaller difference. In addition, the influence of effective support length was reduced by incorporating SFRC into conventional reinforcement. SFRC contributed to the increase in the ultimate load-carrying capacity of the slabs. This was the amount similar to the sum of only steel reinforcement and only SFRC. On the other hand, steel fiber alone did not provide enough strength that it did not experience bending hardening.

2.4.2.11. Tan and Venkateshwaran (2017)

The punching shear capacity of twelve 28 x 28 in. SFRC slabs with thicknesses ranging from 3.6 to 6 in. were tested under central point loading (Tan and Venkateshwaran, 2017). Two types of hooked end fibers were used in four fiber volume fractions of 0.25, 0.5, 0.75, and 1 %. Slabs were cured for 28 days and deflections were measured using displacement transducers on the bottom of the slab. The yield-line theory was used to accurately estimate the load carrying capacities, while models traditionally used for punching shear estimation were inaccurate. All 12 slabs failed in flexure rather than punching shear failure. Toughness values were dramatically increased in mixtures which contained higher fiber volume fractions.

2.4.3. SFRC in Beams and other structures

2.4.3.1. Dinh et al. (2011)

Dinh et al. (2011) studied the performance of hooked-end steel fibers as a substitute for shear reinforcement for beams. The shear strength of the SFRC was evaluated with bending stress at an objective crack width that was obtained from standard ASTM C1609/ C1609M, four-point bending tests. They tested 27 large-scale beams under concentrated loading. Test variables were fiber aspect ratios (55 and 80), fiber volume fraction (0.75 to 1.5 %), beam size (18 in. to 27 in. depth), and longitudinal reinforcement ratio (1.6 to 2.7 %). Regular concrete beams of each beam size were also tested for reference.

Test results indicated that 26 specimens failed in shear, and one failed in flexure by crushing the compression zone. Compared to one large crack formation in regular concrete beams, an average of seven diagonal cracks appeared in SFRC beams. This indicates that the presence of fibers helped transfer tensile force through cracks. Measurement of diagonal shear crack width at failure showed that crack width is dependent on the length of the fiber. The crack width at failure was considered as 5 % of the fiber length. From peak shear strength data and estimated average tensile strength from ASTM C1609/ C1609M bending test, the semi-empirical strength model for shear in SFRC beams was introduced. The model only considers shear resistance due to concrete compression region and diagonal tension resistance of steel fibers, neglecting dowel force and aggregate interlock friction.

2.4.3.2. Minelli et al. (2014)

Nine full-scale beams with a depth ranging from 20 to 60 in. were cast with SFRC mixtures containing fiber volume fractions of 0, 0.6, and 1 % (Minelli et al., 2014). The beams were designed to be shear-critical and tested with a concentrated load at the midspan. The goal of the study was to observe the impact of steel fibers on the size effect in concrete. The size effect in concrete, most notably observed in shear-governed failure modes for beams without stirrups, is a phenomenon where the average shear stress resistance of a concrete element is inversely proportional to its size (i.e., beam height). The large number of cracks generated in the SFRC beams worked to mitigate the size effect by dispersing the load between multiple smaller cracks rather than a single large crack. The increased toughness as a result of the fibers' load dispersion allowed SFRC beams to reach the full flexural capacity. Therefore, it was concluded that the inclusion of steel fibers in concrete can counteract the size effect in concrete, much like conventional stirrups do. Deeper elements may be able to take advantage of the benefits of fibers to effectively increase ultimate strength and avoid brittle shear failures. Figure 2.10 shows crack propagation through the same-sized beams with increasing fiber volume fractions.

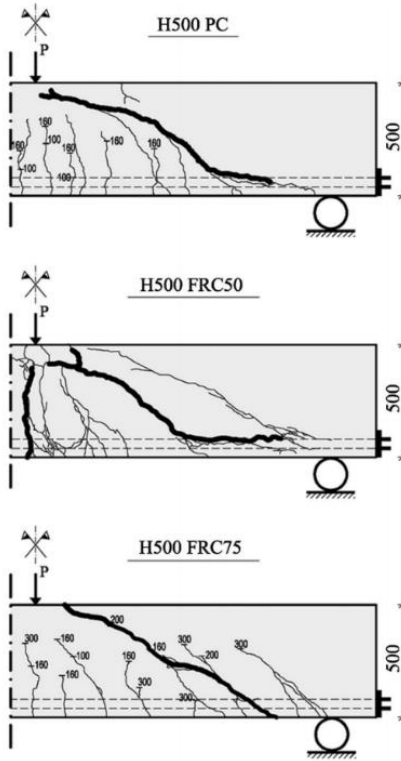


Figure 2.10 Final crack patterns for specimens (Minelli et al., 2014)

2.4.3.3. Zarrinpour et al. (2015)

The current ACI 318 code allows SFRC as a replacement for minimum shear reinforcement under certain conditions, including a maximum section depth of 24 in. (see Section 2.4.2). Zarrinpour et al. (2015) tested slender beams that have longer depth than code specifications. The only variable was the depth of specimens, which were 18 in., 24 in., 36 in., and 48 in. Hooked-end fiber with a 0.75 % volume fraction was used, which corresponds to the ACI 318 requirement. Also, specimens were exposed to the weather for a long period, and based on these specimens, the durability of SFRC concrete was evaluated.

The results of these tests showed the potential of SFRC as a shear reinforcement substitute even for the longest depth. The ultimate shear strength of SFRC beams was up to 2.25 times that of the conventional reinforced beams, regardless of their size. This indicates that there was no size effect influencing the shear strength of beams. Additionally, there was no degradation of specimens due to the weather. However, the author acknowledged that some other studies concluded that there is a size effect acting on SFRC slender beams (Minelli et al., 2014; Shoaib, Lubell, & Bindiganavile, 2014).

2.4.3.4. Abas et al. (2013)

Abas et al. (2013) tested a composite slab comprising a deep trapezoidal steel deck and SFRC. The strength of the composite deck rested on the longitudinal shear capacity between dissimilar surfaces, which is the surface between steel and concrete. To control flexural cracking near the interior support, welded wire mesh was often used. Tests were aimed to verify the effectiveness of steel fibers in crack resisting at the negative moment regions, slip between the steel deck and SFRC, and load-carrying capacity.

Specimens had 27.6 in. width, 5.6 to 6 in. depth, and two 11 ft. spans. A total of eight slab specimens were fabricated and tested: one with rebar and plain concrete, two with rebar and SFRC, and four with only SFRC. The steel fiber fractions ranged from 0.2 to 0.34 %, and two types of hooked fibers with aspect ratios of 64 and 80 were used. Specimens were loaded at four points selected to induce a maximum negative moment at the interior support. Three load cells were used to measure distributed loads at each support. Laser displacement transducers gauged the deflection at mid-span.

The test results showed that fibers improve the slip load and peak load of the specimens. For the same amount of volume fraction, shorter but many fibers exhibited better slip load capacity. Fiber reinforcement alone could bear as much peak load as plain concrete with mesh reinforcement. When exposed to service load levels, steel fibers provided a crack-resisting capacity similar to that of the mesh reinforcement. At about 50 % of the slip load, cracking became excessive. The increase in volume fraction did not significantly affect crack control. However, even for a very small amount of reinforcing mesh combined with fiber significantly improved crack resistance. Cracking remained within acceptable limits up to 60 % of slip load.

2.4.3.5. Mashimo et al. (2005)

In Japan, SFRC is used for tunnel lining. This lining showed problems such as spalling or falling of concrete. Mashimo et al. (2006) performed a laboratory test to disclose the reason for a certain issue. Variables were steel fiber length and volume, humidity, and wind inside the tunnel. The time duration for the crack occurrence and concrete strain from shrinkage were also measured. The test result indicated that the main reason for spalling was humidity. The crack opening age was not affected by the type of concrete. However, long-term durability was improved in the SFRC lining.

2.4.4. Conclusions

The primary conclusions related to experimental investigations of the structural performance of PCP-CIP decks and SFRC are as follows:

1. The PCP-CIP bridge deck is an efficient and reliable construction method that is widely used in Texas. TxDOT suggests provisions to accelerate and clarify design procedures.
2. SFRC with volume fractions of 0.25 to 1.5 % with aspect ratios up to 80 have been investigated for structural applications.
3. Steel fibers can improve the tensile capacity, shear capacity, and crack resistance of concrete due to the post-peak tensile resistance of SFRC. Slab flexural strengths may increase by up to 100 % or even 400 % when arching action occurs. The benefits of fiber reinforcement typically improve as the fiber dosage increases.

2.5. Analytical Investigations of SFRC Structure

The analytical and numerical evaluation of SFRC can be conducted using the same methods as for plain or reinforced concrete, so long as the influence of the fiber reinforcement is accounted for. As discussed in the preceding sections, the actual behavior of SFRC may vary substantially from that of plain or reinforced concrete, most notably in the post-cracking response. As previously discussed, many researchers have proposed constitutive models to account for these differences in behavior between SFRC and plain or reinforced concrete. Furthermore, researchers have applied these models with several widely accepted analysis methods to predict the behavior of various types of steel-fiber reinforced elements. This section summarizes the results and conclusions of such efforts, which are organized by their structure type.

2.5.1. Membrane and Shell Elements

Numerical models for membrane and shell elements made of SFRC have been developed based on the experimental data obtained from membrane (or panel) element testers, such as that constructed at the University of Toronto in 1979. This membrane element tester was first used to conduct the experimental investigation that would lead to the development of the Modified Compression-Field Theory (MCFT) (Vecchio & Collins, 1986), which was eventually adapted for use in shear design provisions around the world (AASHTO, 2020; CSA, 2014; *fib*, 2013). Since then, many universities have constructed similar test setups (for example, University of Houston and University of Washington), and some have expanded to

shell element testers, where out-of-plane loading conditions may be applied (for example, University of Toronto and ETH Zürich). These tests are often used to investigate more complicated material behavior (e.g., concrete in shear) in an idealized manner without the added difficulties of non-uniform boundary conditions, which are typically present in “real” structures. They are also being used to validate and calibrate nonlinear finite element analysis programs. This section will focus on the development of numerical models for fiber reinforced concrete membrane and shell elements based on experimental results obtained from membrane element testers and other test setups.

2.5.1.1. Susetyo, Gauvreau, and Vecchio (2013)

Susetyo, Gauvreau, and Vecchio (2013) analyzed ten concrete panel specimens, which were tested to investigate fiber reinforcement as a replacement for minimum shear reinforcement (Susetyo, Vecchio, & Gauvreau, 2011), using the nonlinear finite element analysis program VecTor2 (Wong, Vecchio, & Trommels, 2013), which uses the MCFT (Vecchio & Collins, 1986) and the Disturbed Stress Field Model (DSFM) (Vecchio, 2000) as its theoretical base. The panels were 35 x 35 x 2.75 in. and were reinforced with 40 D8 deformed wires in their longitudinal direction. Two control panels contained 10 D4 deformed wires in the transverse direction, and the remaining eight panels contained hooked-end steel fibers in dosages ranging from 0.5 to 1.5 %. One series of panels had a concrete compressive strength of 7.3 ksi, and the other was 11.6 ksi.

Prior to performing any analyses, Susetyo et al. (2013) compared the measured compression stress-strain, compression softening, tension stiffening and softening, and cracking responses to available analytical expressions. They noted several deficiencies in the modeling approach for the tension response of SFRC. Namely, no existing crack spacing model could accurately predict how closely the cracks were spaced due to the fiber reinforcement. Additionally, the tension-softening response tended to be underpredicted by existing models.

Susetyo et al. (2013) performed two analysis series: one with a custom, strain-based tension-softening model based on uniaxial tension tests and one with the Variable Engagement Model (Voo & Foster, 2003). While the traditionally reinforced panels were well-modeled, the fiber-reinforced panels' capacities were typically overestimated – by as much as 76 %. Furthermore, the failure modes were inaccurately predicted, which was thought to be due to the method of calculating crack slip within the formulation of the DSFM and the influence of fiber reinforcement on these calculations (Susetyo et al., 2013). Ultimately, they concluded that additional work must be done to develop more suitable tension-softening and crack spacing models.

2.5.1.2. Lee, Cho, and Vecchio (2016)

Shortly after the work completed by Susetyo et al. (2013), several new behavioral models were proposed, many in direct response to the analytical challenges noted by Susteyo et al. (2013) (Deluce et al., 2014; Lee et al., 2011b, 2011a, 2013a, 2013b). Lee, Cho, and Vecchio (2016) subsequently reanalyzed the panels tested by Susetyo et al. (2011) using an updated analysis procedure, again based on the DSFM (Vecchio, 2000), with the new constitutive relationships, namely the SDEM (Lee et al., 2013a) for modeling the tension response of fiber reinforced concrete. All predictions for the fiber reinforced panels were substantially improved with average predicted-to-experimental ratios of 0.99 for both ultimate stress and strain. As an example, results from analyses on Panel C2F3V3 ($f'_c = 8.99$ ksi and $V_f = 1.5$ %) are compared in Figure 2.11. Based on these results, it appears that the updated analysis procedure remedied the primary concerns noted by Susetyo et al. (2013) for panel-type elements.

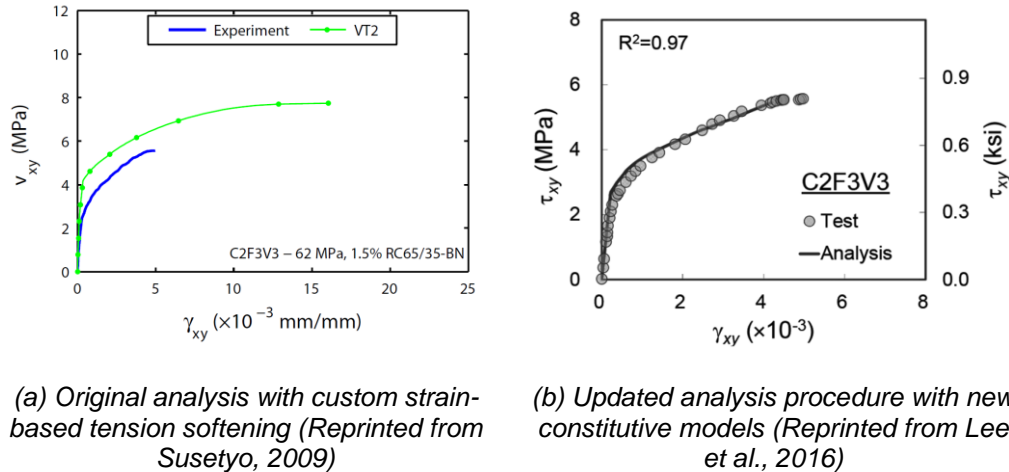


Figure 2.11 Comparison of analyses on Panel C2F3V3 (1 MPa \approx 0.145 ksi)

2.5.1.3. Hrynyk and Vecchio (2017)

Hrynyk and Vecchio (2017) proposed a modeling procedure for conventionally reinforced and SFRC shell structures subject to out-of-plane impact loads using thick-shell elements. Shell elements are typically subdivided into layers, which allows for the resolution of through-depth stress and strain variation (for example, variation in longitudinal stress due to bending). The proposed methodology was implemented in a nonlinear finite element analysis program that used the constitutive models of the MCFT (Vecchio & Collins, 1986) and had been recently adapted to perform the following functions:

1. Model cyclic and dynamic effects (Hrynyk, 2013)
2. Model modern material types, such as FRC (Hrynyk, 2013)
3. Model out-of-plane shear with alternative sectional models (Hrynyk & Vecchio, 2015)
4. Employ the constitutive formulations of the DSFM (Vecchio, 2000)

To evaluate their proposed modeling procedure, they analyzed seven 71 x 71 x 5.1 in. slab-like specimens tested by Hrynyk and Vecchio (2014). Three of the specimens were constructed with conventional reinforcement and the remaining four contained dosages of hooked-end steel fibers ranging from 0.5 to 1.5 %. Note that, as in Lee et al. (2016), the SDEM (Lee et al., 2013a) was used to model the fiber reinforced concrete tension response. Hrynyk and Vecchio (2017) found that, overall, many aspects of behavior were well-predicted by their proposed procedure, particularly during the impact event; however, they noted that error increased in the post-impact and post-peak responses, as well as instabilities after several impact load stages.

2.5.1.4. Kaufman, Mata-Falcón, and Amin (2019)

The preceding three numerical investigations were all based on either the MCFT or its extension, the DSFM. A different compression field solution for fiber reinforced concrete elements was proposed by Kaufman, Mata-Falcón, and Amin (2019) based on the Cracked Membrane Model (CMM) (Kaufmann & Marti, 1998). Kauffman et al. (2019) noted a few potential limitations of rotating crack models (for example, the MCFT), most notably that they were incapable of predicting failures related to aggregate interlock for FRC with high fiber volume content. Ultimately, they proposed an adaptation of the CMM that included modifications for the addition of fibers in the concrete constitutive and equilibrium equations, which were typically based on average fiber bond stress. To evaluate their proposed procedure, Kauffman et al. (2019) analyzed the panels tested by Susetyo et al. (2011). For fiber dosages greater than 0.5 %, Kauffman et al. (2019) demonstrated that the CMM provided reasonable agreement with the experimental results, even when using a linear elastic constitutive model for concrete in compression. The results presented by Kauffman et al. (2019) were typically in line with the predictions reported by Susetyo et al. (2013) and Lee et al. (2016), as shown in Figure 2.12.

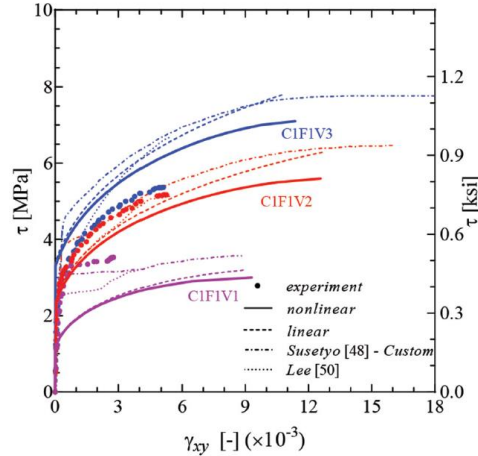


Figure 2.12 Comparison of analyses from Susetyo et al. (2013), Lee et al. (2016), and Kauffman et al. (2019) (Reprinted from Kaufmann et al., 2019)

2.5.2. Slabs and Decks

While the previous section discussed numerical investigations that are necessary and important for validating and calibrating various nonlinear behavioral models and analysis techniques, this section describes numerical investigations performed on slab- and deck-type structures. The review-to-date suggests that few researchers have investigated the performance of FRC specifically for bridge decks numerically, and none have done so using CIP-PCP construction.

2.5.2.1. Maya et al. (2012)

Maya et al. (2012) developed a model to evaluate the punching shear capacity of an SFRC flat slab system. Their model was based on the critical shear crack theory and it incorporated the contribution of fibers into the equation. Before yielding steel reinforcement, the compressive response was modeled with a linear stress-strain relation. The tension response was modeled with a uniform stress that represented the average tensile strength of SFRC. For the ultimate flexural capacity, the compressive stresses in concrete were idealized with a rectangular stress block. This physical-mechanical modeling approach allows easy incorporation of SFRC into the punching shear behavior of SFRC. The average bridging stress of steel fiber is estimated based on the crack opening strength at a distance from the soffit of the slabs equal to one-third of the depth.

The proposed model was examined using previous 140 SFRC slab-column experiment data. The model reflects the effect of fiber volume and slab rotation on the slab punching shear capacity. As the fiber volume increases, the punching shear

capacity and deformational capacity increase. In addition, as the slab rotation increases, fibers tend to contribute more to the resistance.

2.5.2.2. Destrée and Mandl (2008)

Destrée and Mandl (2008) reviewed full-scale experimental work completed on flat slab specimens in the preceding two decades and outlined a design methodology based on yield-line theory (Gvozdev, 1960; Ingerslev, 1923; Johansen, 1962). Using full-scale test results, they compared the proposed yield-line methodology to a more basic method based on prismatic SFRC beam tests. Destrée and Mandl (2008) showed that, for this particular case study, the global safety factor increased by a factor of 2.8 when comparing the yield-line theory with simple flexural theories, which indicates that the yield-line theory is more closely aligned with the reality of large, suspended flat slabs. However, it should be noted that, even when accounting for the average safety factor applied in the case study (1.45), the results were still overly conservative (predicted capacities were on the order of 2 to 3.5 times smaller than reality).

2.5.2.3. Cheng and Parra-Montesinos (2010)

As part of an experimental study to evaluate steel fiber for punching shear resistance in slab-column connections under monotonic loading, Cheng and Parra-Montesinos (2010) also evaluated the flexural capacity of the slabs using yield-line analysis. They tested and analyzed ten specimens, with compressive strengths ranging from 3700 to 8600 psi. The experimental program also included two fiber types (hooked end and twisted) and two different reinforcement mat layouts (0.56 or 0.83 % each way). Their analysis methodology followed the one proposed by Elstner and Hognestad (1956) and provided good agreement, on average, with the experimental capacities (average experimental-to-calculated-strength ratio of 1.08).

2.5.2.4. Elsaigh, Robberts, and Kearsley (2011)

Researchers from Pretoria University proposed a modeling approach for SFRC ground slabs, including a material model (Elsaigh, Robberts, & Kearsley, 2011) and a slab model (Elsaigh, Kearsley, & Robberts, 2011). To represent tension softening, they proposed a trilinear tension response, as well as a simplified, elastic-perfectly-plastic compression response. These assumed relationships were used in conjunction with experimental load-displacement results to back-calculate the material model. In application to nonlinear finite element analysis, Elsaigh, Robberts, and Kearsley (2011) noted the importance of calibrating the element size with respect to the fracture energy. Using the back-calculated material response from the beams, Elsaigh, Kearsley, and Robberts (2011) developed a nonlinear

finite element analysis model with shell elements to calculate the response of a full-scale SFRC ground slab subjected to center-point loading. While there was excellent agreement in the pre-peak response, there were substantial discrepancies in the post-peak response. They also performed a parametric study to investigate potential methods to improve the response of SFRC ground slabs. Ultimately, their methodology may be suitable for modeling pre-peak behavior, but there is little data to support their methodology for the post-peak behavior of ground slabs.

2.5.2.5. Fall, Shu, Rempling, Lundgren, and Zandi (2014)

As part of the previously mentioned experimental study on two-way slab systems, Fall et al. (2014) analyzed the slabs using yield-line theory. Similar to Destrée and Mandl (2008), they noted that yield-line theory tended to underestimate slab capacities significantly. They noted tensile membrane action and strain hardening of the conventional reinforcement as being potential sources for the large discrepancies between the measured and estimated responses.

2.5.2.6. Birely, Park, McMahon, Shi, and Rew (2018)

In addition to the previously discussed experimental study (McMahon & Birely, 2018), Birely, Park, McMahon, Shi, and Rew (2018) also investigated moment-curvature analysis, yield-line theory, and two-way shear analysis. Using an inverse analysis, Birely et al. (2018) back-calculated the tension softening response and used the results to conduct a moment-curvature analysis. They reported errors between 0.4 and 33 % for the slab strips they tested. In the analysis of the full-scale bridge decks, they noted similar restrictions as mentioned previously for yield-line theory (Destrée & Mandl, 2008; Fall et al., 2014) and, conversely, noted that modified two-way shear design procedures may overestimate experimental loads.

2.5.3. Beams

While small-scale beam tests have been used in the calibration of many of the previously discussed numerical studies, this section will highlight the analysis of full-scale SFRC beams.

2.5.3.1. Minelli and Vecchio (2006)

Minelli and Vecchio (2006) performed nonlinear finite element analysis on three series of prestressed beams reinforced with steel fibers and made with high-strength concrete. Specifically, they focused on the application of the MCFT (Vecchio & Collins, 1986) and the DSFM (Vecchio, 2000) to the numerical analysis of such beams. The three series were comprised of I-shaped, U-shaped, and rectangular cross-sections. Ultimately, they found that, in all cases, the response of beams could

be accurately predicted using plane-stress elements in the framework of an MCFT-/DSFM-based nonlinear finite element procedure.

2.5.4. Conclusions

The primary conclusions related to analytical investigations of the structural performance of SFRC are as follows:

1. Different structural elements have been successfully analyzed with various techniques, from simple analytical methods (e.g., yield-line theory) to more complex nonlinear finite element analysis procedures.
2. There is a gap in modeling CIP-PCP structures, particularly when SFRC is used. It is envisioned that the experimental program of Project 0-7001 will help address this research need.

2.6. Summary and Conclusions

The research team has presented a comprehensive review of the published literature related to the design of SFRC, as well as relevant experimental and numerical investigations. The primary conclusions of this literature review are as follows:

1. The post-peak toughness behavior of SFRC relies on fiber/concrete bond strength. Fiber/concrete bond strength is highly dependent on the development of the concrete matrix and interfacial transition zone. Under flexural loading, high fiber/concrete bond strength will change fiber failure conditions from fiber pullout to fiber fracture failure.
2. The effects of fiber orientation on the mechanical response of SFRC are well documented, but reliable methods for promoting fiber alignment in non-SCC SFRC mixtures are currently unavailable.
3. Fiber count n may be a better predictor of the effect of fibers on fresh state performance than commonly used fiber factors, which rely on fiber size and surface area.
4. The addition of fibers to concrete has been shown through experimental investigation to enhance the tensile (and thereby the cracking) behavior of concrete. The recommended dosages to improve behavior vary depending on the member type and application.
5. Common test methods to observe the tensile behavior of SFRC include ASTM 1609 (flexural toughness), ASTM D5379/D5379M-19 (v-notched beam), ASTM C1399 (modified flexural toughness) and uniaxial direct tension testing. Double punch testing should be investigated due to its

potential to quantify post-crack toughness with relative ease of performance.

6. Fiber content by volume rarely exceeds 2 % in most practical applications. Increasing fiber content above this volume results in diminishing returns for post-crack flexural strength while further decreasing fresh-state workability.
7. Fibers with mechanical deformations, including hooked, helical, and wavy, offer the most benefit to the post-crack ductility of ordinary concrete mixes.
8. Many models have been proposed for modeling the tension and compression response of SFRC. While there are several relatively general, applicable tension models, there are few generally applicable compression models.
9. The tension behavior is critical for an accurate modeling and analysis of SFRC members. Differences in the post-peak, cracking, and toughness properties must be appropriately accounted for. Compression behavior appears to be less important based on the review to-date.
10. SFRC with volume fractions of 0.25 to 1.5 % with an aspect ratio up to 80 is used for structures. Deck strip testing for bridge deck measures positive and negative moment capacities. Fiber dosages required for sufficient tensile strength and crack opening resistance should be determined through material testing suggested in ACI 544.
11. Common test methods to observe the tensile behavior of SFRC include ASTM 1609 (flexural toughness), ASTM D5379/D5379M-19 (v-notched beam), ASTM C1399 (modified flexural toughness) and uniaxial direct tension testing. Double punch testing should be investigated due to its potential to quantify post-crack toughness with relative ease of performance.
12. Different structural elements utilizing SFRC can be analyzed based on the properties of the SFRC, from simple analytical methods (e.g., yield-line theory) to more complex nonlinear finite element analysis.
13. There is a gap in modeling CIP-PCP structures, particularly when SFRC is used. It is envisioned that structural tests of Project 0-7001 will help address this research need.

Chapter 3. Laboratory Evaluation of Steel Fibers for TxDOT Class S Concrete

This chapter presents the findings of a comprehensive laboratory investigation on the use of steel fibers for fiber reinforced concrete. Three types of steel fibers were evaluated separately at three dosages with different cementitious mixtures to produce fiber reinforced concrete that would meet TxDOT Class S Concrete for bridge decks. Fresh and hardened properties are presented and discussed along with the concrete durability made with these fibers.

3.1. Overview of Materials




Table 3.1 summarizes the materials selected and procured for this project. These materials were used for the laboratory testing. A single ASTM C150 Type I/II Cement was selected for all laboratory tests along with three supplementary cementitious materials (SCMs). Local coarse and fine aggregates were selected for the fresh and hardened concrete properties. Durability testing incorporated additional materials such as reactive sand from Corpus Christi, TX. and a manufactured limestone sand and limestone coarse aggregate from San Antonio, TX.

Three steel fibers were procured to be sufficient in quantity for both laboratory and large-scale testing. Two sourced fibers have a length of 1.5” and one fiber has a length of 1”. Table 3.2 provides the properties and image of each fiber type.

Table 3.1 Materials being evaluated in the laboratory testing program

| Material | Sources/types | Information on sources/types of materials/Designations |
|-----------------------------------|---|--|
| Portland cement | <ul style="list-style-type: none"> Type I/II | <ul style="list-style-type: none"> PC – San Antonio, TX. |
| Supplementary cementing materials | <ul style="list-style-type: none"> Class F fly ash Class C fly ash Condensed silica fume | <ul style="list-style-type: none"> FAF FAC SF |
| Fine Aggregates | <ul style="list-style-type: none"> River sand Reactive Sand Manufactured Sand | <ul style="list-style-type: none"> Austin, TX. Robstown, TX. San Antonio, TX. |
| Coarse Aggregates | <ul style="list-style-type: none"> River gravel Crushed limestone | <ul style="list-style-type: none"> Austin, TX. San Antonio, TX. |
| Chemical Admixtures | <ul style="list-style-type: none"> High-range water reducer Air-entraining agent | For freeze-thaw and salt scaling testing |
| Fibers | <ul style="list-style-type: none"> Steel fibers | <ul style="list-style-type: none"> SFS (1.5’') SFD (1.5’') SFH (1’') |

Table 3.2 Description of steel fibers evaluated in this project

| | SFD | SFS | SFH |
|--------------|---|---|--|
| Shape |  Hooked end |  Crimped |  Twisted |
| Length | 35 mm (1.4 in.) | 38 mm (1.5 in.) | 25 mm (1 in.) |
| Diameter | 0.55 mm (0.021 in.) | 1.14 mm (0.045 in.) | 0.55 mm (0.020 inch) |
| Aspect ratio | 65 | 30 | 50 |

3.1.1. Characterization of Materials

All cements and fly ashes used in this research are commercially available products. Each material was analyzed with x-ray fluorescence (XRF) to determine the bulk oxide contents. Table 3.3 provides the chemical composition of the cement and fly ash.

Table 3.3 Chemical Composition of Cementitious Materials (% by mass)

| Material | SiO₂ | Al₂O₃ | Fe₂O₃ | CaO | SO₃ | MgO | K₂O | Na₂O | LOI |
|-----------------|------------------------|------------------------------------|------------------------------------|------------|-----------------------|------------|-----------------------|------------------------|------------|
| CM1 | 20.6 | 5.0 | 3.4 | 64.8 | 2.8 | 1.1 | | | 3.0 |
| Class F Fly Ash | 53.0 | 21.69 | 5.00 | 12.26 | 0.53 | 2.58 | 0.98 | 0.15 | 0.25 |
| Class C Fly Ash | 36.98 | 19.42 | 5.52 | 24.90 | 1.42 | 5.06 | 0.59 | 1.92 | 0.20 |

Table 3.4 summarizes the mixture proportions being used in the laboratory testing program. All mixtures were cast in accordance with TxDOT Class S bridge deck concrete specifications, with recommended modifications to the aggregate content for fiber-reinforced concrete. Specifically, the sand content was increased by using a maximum coarse aggregate factor of 0.55 (as recommended by ACI 544.3). For all mixtures, a target slump of 3-5 inches was achieved through the judicious use of polycarboxylate-based high-range water reducers. A subset of the mixtures shown in Table 3.4 have been selected for full-scale structural testing. Through close collaboration with a local ready-mix supplier, the Performing Agency has demonstrated the feasibility of commercial SFRC production for bridge deck applications.

Table 3.4 Mixture proportions used in laboratory testing program

| Mixture | Fiber dosage (% by vol.)* | Steel Fiber Source | | | | Class F Fly Ash (%) | Class C Fly Ash (%) | Silica Fume (%) |
|-------------------|---------------------------|--------------------|-----|-----|------|---------------------|---------------------|-----------------|
| | | SFS | SFD | SFH | None | | | |
| PC-0 | 0 | | | | X | | | |
| PC-0.5 | 0.5 | X | X | X | | | | |
| PC-1.0 | 1.0 | X | X | X | | | | |
| PC-1.5 | 1.5 | X | X | X | | | | |
| FA(F)-20-0 | 0 | | | | X | 20 | | |
| FA(F)-20-0.5 | 0.5 | X | | | | 20 | | |
| FA(F)-20-1.0 | 1.0 | X | X | X | | 20 | | |
| FA(F)-20-1.5 | 1.5 | X | | | | 20 | | |
| FA(C)-35-0 | 0 | | | | X | | 35 | |
| FA(C)-35-0.5 | 0.5 | X | X | | | | 35 | |
| FA(C)-35-1.0 | 1.0 | X | X | X | | | 35 | |
| FA(C)-35-1.5 | 1.5 | X | | | | | 35 | |
| FA(C)-30-SF-5-0 | 0 | | | | X | | 30 | 5 |
| FA(C)-30-SF-5-0.5 | 0.5 | X | | | | | 30 | 5 |
| FA(C)-30-SF-5-1.0 | 1.0 | X | | X | | | 30 | 5 |
| FA(C)-30-SF-5-1.5 | 1.5 | X | | | | | 30 | 5 |

* 1 percent by volume = 130 lbs/yd³

3.2. Fresh Properties of FRC Mixtures

3.2.1. Slump, Air Content, Fresh Temperature

For each concrete mixture, the slump, air content and fresh temperature were measured and are provided in Table 3.5, Table 3.6, and Table 3.7 for each of the different fiber types. A superplasticizer was used to achieve a slump between 4 and 6 inches. Without the superplasticizer, an increase in fiber dosage decreased the slump. The air content was measured however an air-entraining agent was not used to increase the air content.

Table 3.5 Fresh Concrete Properties containing Steel Fiber (SFS)

| Mixture Name | Fiber dosage (% by volume) | Slump (in.) | Air Content (%) | Fresh Temperature (F) |
|-----------------------|---------------------------------------|------------------------|----------------------------|----------------------------------|
| PC-0 | 0 | 5.0 | 2.2 | 72.6 |
| PC-0.5 (S) | 0.5 | 4.5 | 2.1 | 73.1 |
| PC-1.0 (S) | 1.0 | 5.0 | 2.2 | 72.2 |
| PC-1.5 (S) | 1.5 | 4.5 | 1.9 | 72.2 |
| FA(F)-20-0 | 0 | 6.5 | 2.4 | 71.8 |
| FA(F)-20-0.5 (S) | 0.5 | 6.5 | 1.8 | 71.4 |
| FA(F)-20-1.0 (S) | 1.0 | 5.5 | 1.8 | 72.8 |
| FA(F)-20-1.5 (S) | 1.5 | 6.0 | 2.2 | 73.1 |
| FA(C)-35-0 | 0 | 5.5 | 2.3 | 72.2 |
| FA(C)-35-0.5 (S) | 0.5 | 6.0 | 1.8 | 72.3 |
| FA(C)-35-1.0 (S) | 1.0 | 4.5 | 2.1 | 72.2 |
| FA(C)-35-1.5 (S) | 1.5 | 6.5 | 1.9 | 71.9 |
| FA(C)-30-SF-5-0 | 0 | 6.0 | 2.1 | 71.8 |
| FA(C)-30-SF-5-0.5 (S) | 0.5 | 4.5 | 2.4 | 72.2 |
| FA(C)-30-SF-5-1.0 (S) | 1.0 | 4.0 | 2.2 | 73.2 |
| FA(C)-30-SF-5-1.5 (S) | 1.5 | 5.0 | 2.3 | 72.5 |

Table 3.6 Fresh Concrete Properties containing Steel Fiber (SFD)

| Mixture Name | Fiber dosage (% by volume) | Slump (in.) | Air Content (%) | Fresh Temperature (F) |
|---------------------|---------------------------------------|------------------------|----------------------------|----------------------------------|
| PC-0 | 0 | 5.0 | 2.2 | 72.6 |
| PC-0.5 (D) | 0.5 | 4.5 | 1.8 | 73.4 |
| PC-1.0 (D) | 1.0 | 5.5 | 2.3 | 73.6 |
| PC-1.5 (D) | 1.5 | 5.0 | 2.1 | 74.0 |
| FA(F)-20-0 | 0 | 6.5 | 2.4 | 71.8 |
| FA(F)-20-1.0 (D) | 1.0 | 4.0 | 1.6 | 72.3 |
| FA(C)-35-0 | 0 | 5.5 | 2.3 | 72.2 |
| FA(C)-35-0.5 (D) | 0.5 | 4.5 | 2.1 | 71.8 |
| FA(C)-35-1.0 (D) | 1.0 | 5.0 | 2.3 | 72.0 |

Table 3.7 Fresh Concrete Properties containing Steel Fiber (SFH)

| Mixture Name | Fiber dosage (% by volume) | Slump (in.) | Air Content (%) | Fresh Temperature (F) |
|-----------------------|---------------------------------------|------------------------|----------------------------|----------------------------------|
| PC-0 | 0 | 5.0 | 2.2 | 72.6 |
| PC-0.5 (H) | 0.5 | 6.5 | 2.1 | 72.8 |
| PC-1.0 (H) | 1.0 | 7.0 | 1.7 | 73.2 |
| PC-1.5 (H) | 1.5 | 5.5 | 2 | 71 |
| FA(F)-20-0 | 0 | 6.5 | 2.4 | 71.8 |
| FA(F)-20-1.0 (H) | 1.0 | | | |
| FA(C)-35-0 | 0 | 5.5 | 2.3 | 72.2 |
| FA(C)-35-1.0 (H) | 1.0 | | | |
| FA(C)-30-SF-5-0 | 0 | 6.0 | 2.1 | 71.8 |
| FA(C)-30-SF-5-1.0 (H) | 1.0 | | | |

3.2.2. Set Time, Bleed Water, and Unit Weight

The set time and bleed water were evaluated with one fiber type and dosage. Three cementitious systems (straight portland cement, 35% Class C fly ash and a ternary blend) were used in conjunction with this fiber type and dosage. Figure 3.1 provides the set time results. The set time slightly increased with the 1% fiber dosage. It increased the most with the ternary blend mixture. The cumulative bleeding of the mixtures is shown in Figure 3.2. ASTM C232 was used to evaluate the amount of bleed water produced for each mixture. The 1% fiber mix increased the cumulative bleeding for each mixture. Figure 3.3 provides the unit weight of mixtures containing 1% steel fiber. The unit weight increased between 3-4 pounds depending on the cementitious mixture.

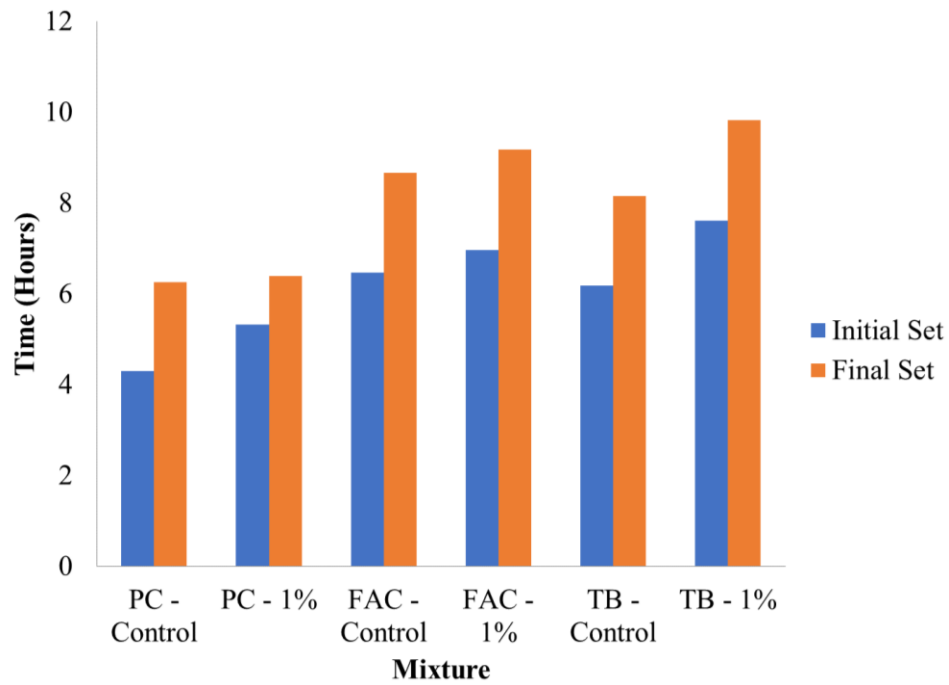


Figure 3.1 Initial and final set times for mixtures with 1% fiber dosage

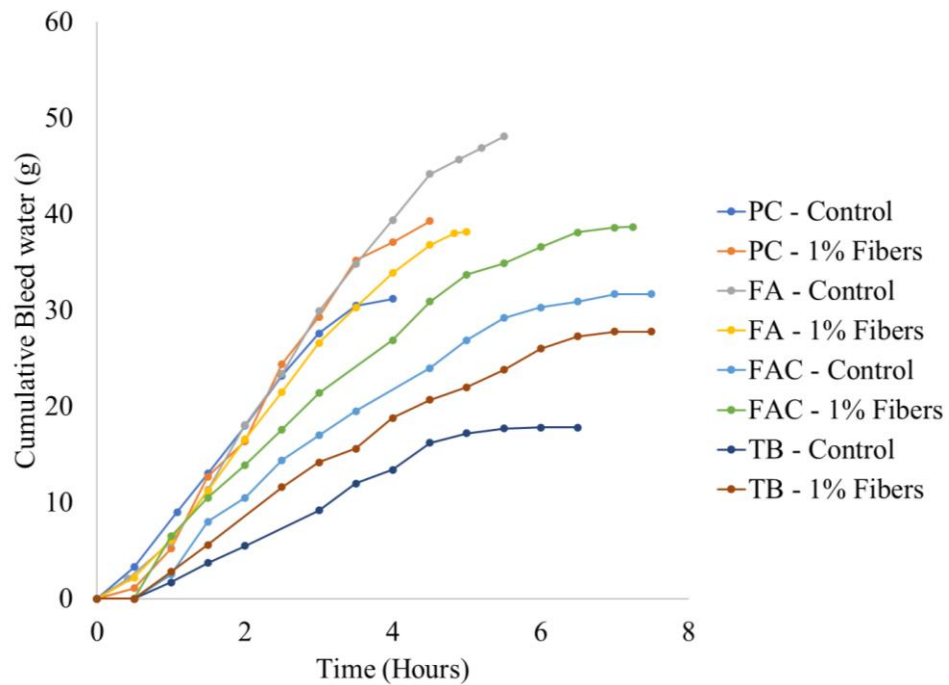


Figure 3.2 Cumulative bleed water for FRC mixtures

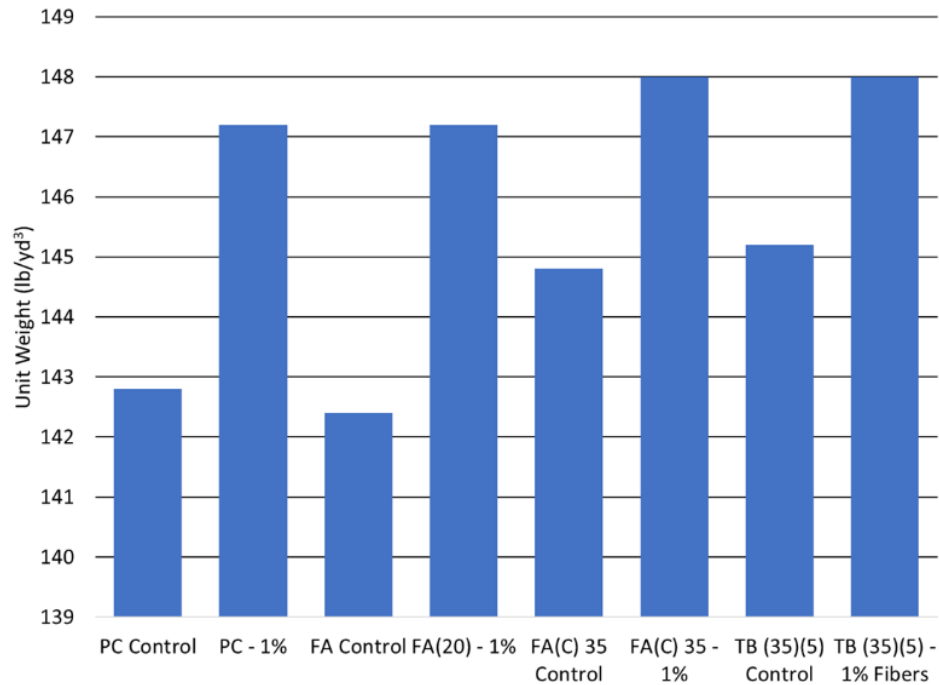


Figure 3.3 Unit weight of mixtures

3.3. Hardened Properties of FRC Concrete

3.3.1. Compressive Strength

The compressive strength of FRC mixtures was evaluated. Figure 3.4 to Figure 3.7 show the 28-day compressive strength results for mixtures with different fiber types and dosages with 4 types of cementitious systems (100% portland cement, 20% Class F Fly Ash, 35% Class C Fly ash, and ternary blends). For the 100% portland cement mixtures, containing fibers slightly increased the compression strength at 28 days at 1.5% fiber dosage. At 0.5 and 1.0% fiber dosage, SFH had a decreased compression strength compared to the other two fiber types

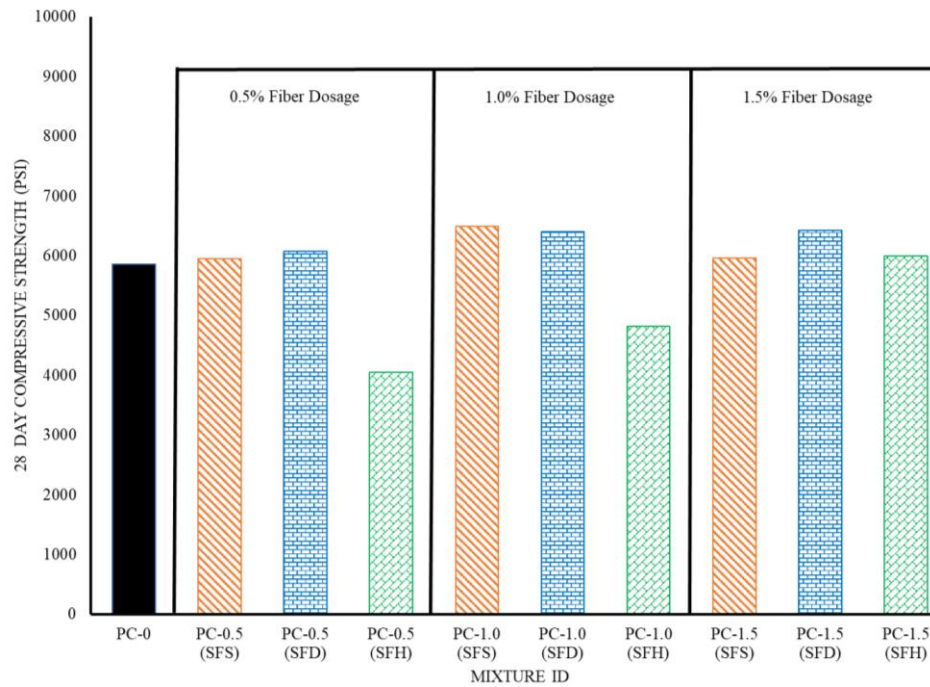


Figure 3.4 Compression strength results of portland cement concrete mixtures with varied fiber types and dosages

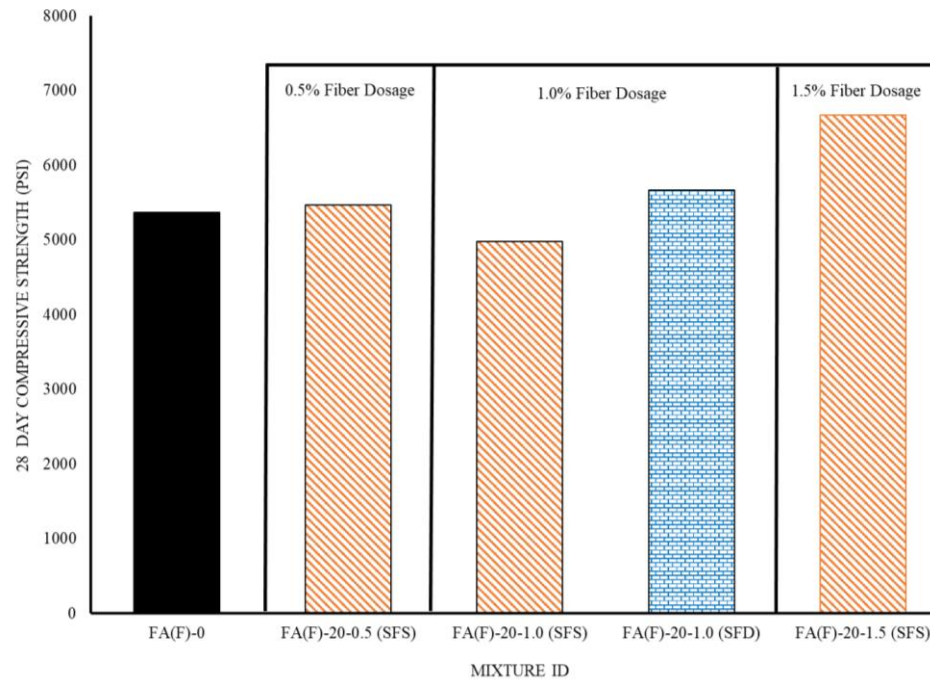


Figure 3.5 Compression strength results of 20% Class F Ash mixtures with varied fiber types and dosages

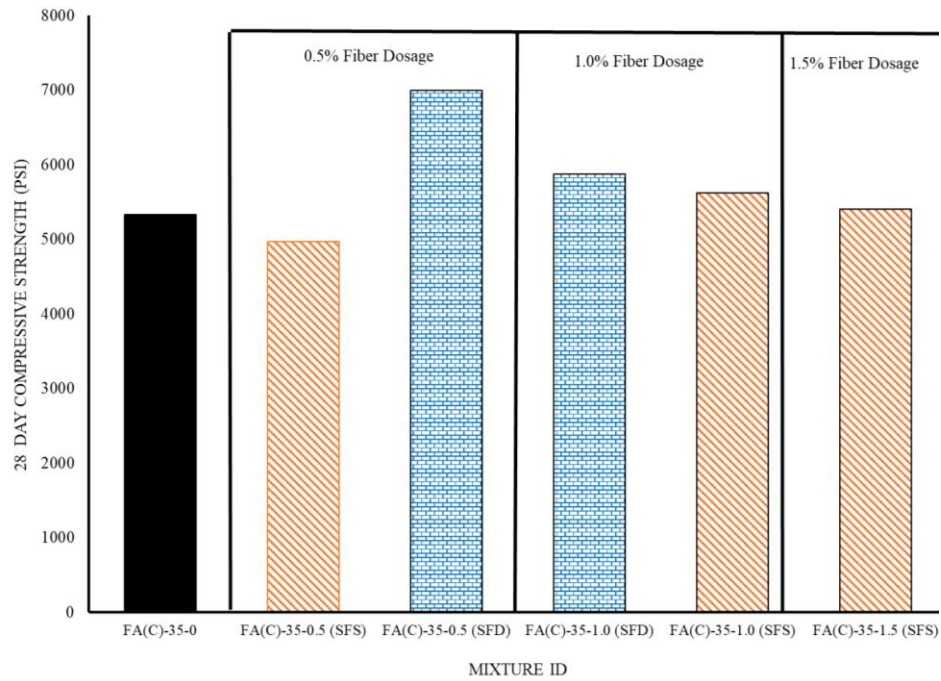


Figure 3.6 Compression strength results of 35% Class F Ash mixtures with varied fiber types and dosages

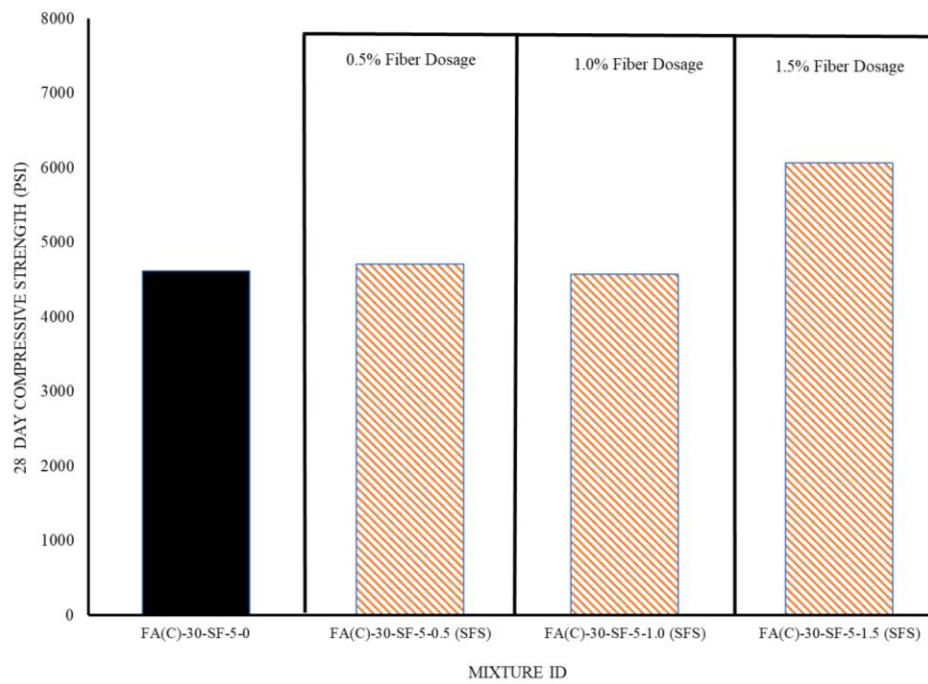


Figure 3.7 Compression strength results of Ternary Blend (30% Class C and 5% Silica Fume) mixtures with varied fiber types and dosages

3.3.2. Splitting Tensile Strength

The splitting tensile strength of SFRC mixtures was evaluated. Figure 3.8 to Figure 3.11 show the 28-day splitting tensile testing results for SFRC mixtures with different fiber type and dosages with 4 types of cementitious systems (100% portland cement, 20% Class F Fly Ash, 35% Class C Fly ash, and ternary blends). An increase in fiber dosage to 0.5% increased the splitting tensile strength. The splitting tensile strengths were similar between 0.5 and 1%. Increasing the dosage to 1.5% increased the tensile strength.

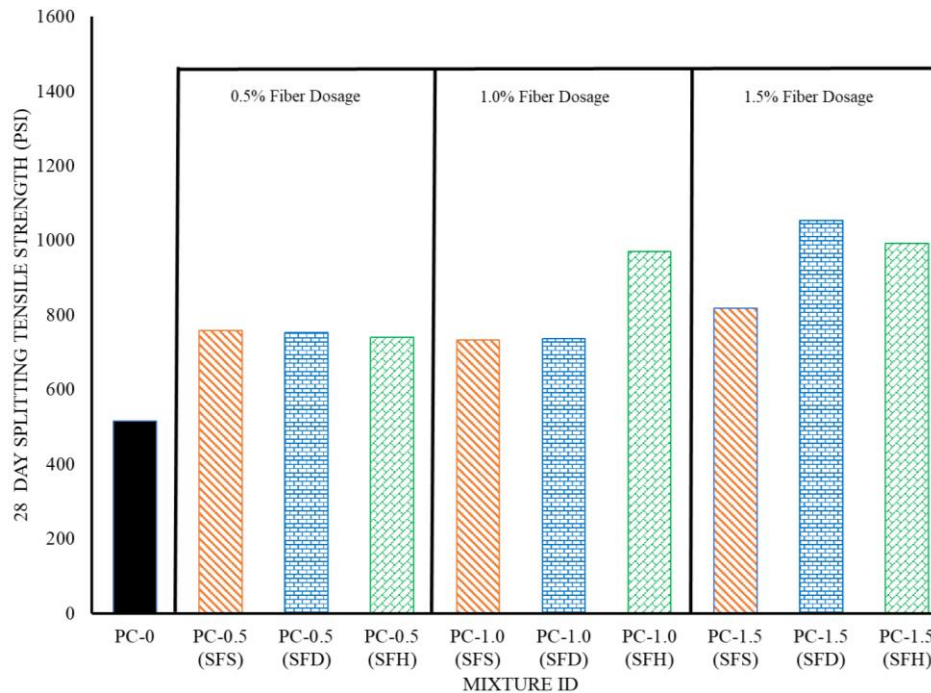


Figure 3.8 Splitting tensile data for Portland cement concrete mixtures with varied fiber types and dosages

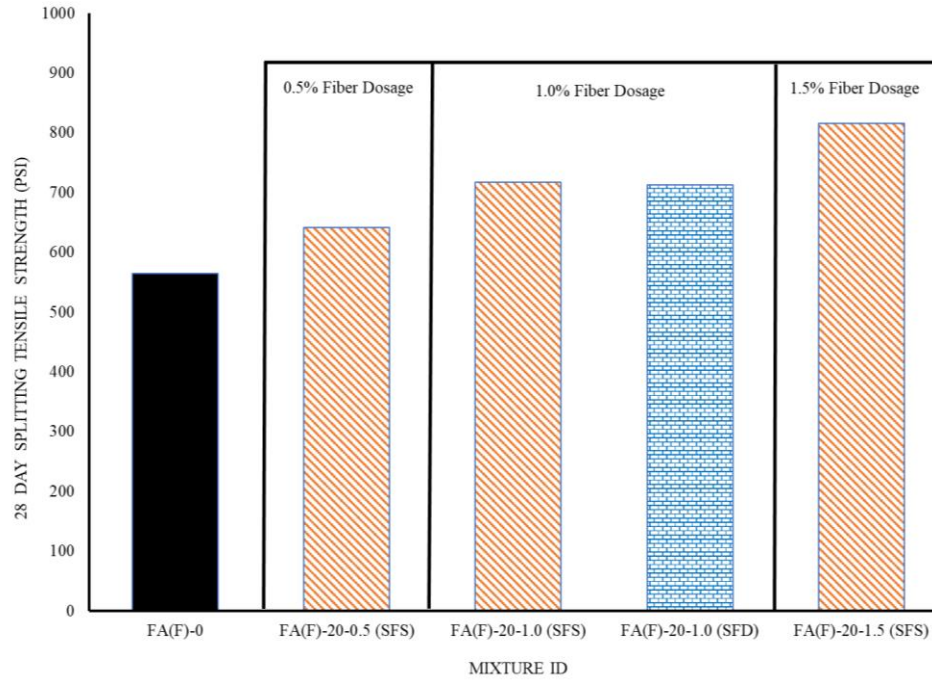


Figure 3.9 Splitting tensile data for 20% Class F Fly Ash concrete mixtures with varied fiber types and dosages

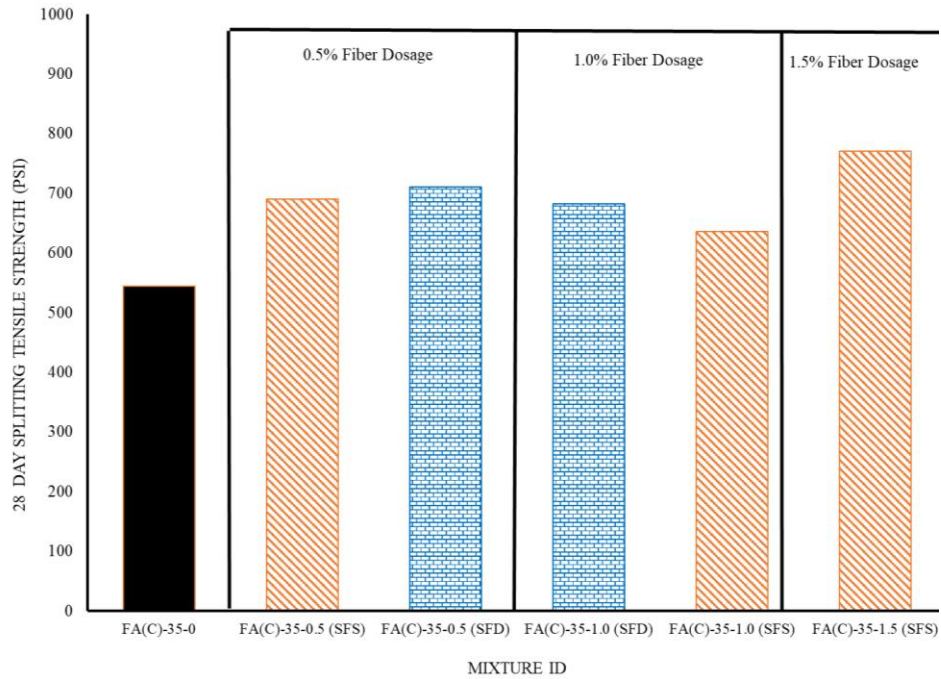


Figure 3.10 Splitting tensile data for 35% Class C Fly Ash concrete mixtures with varied fiber types and dosages

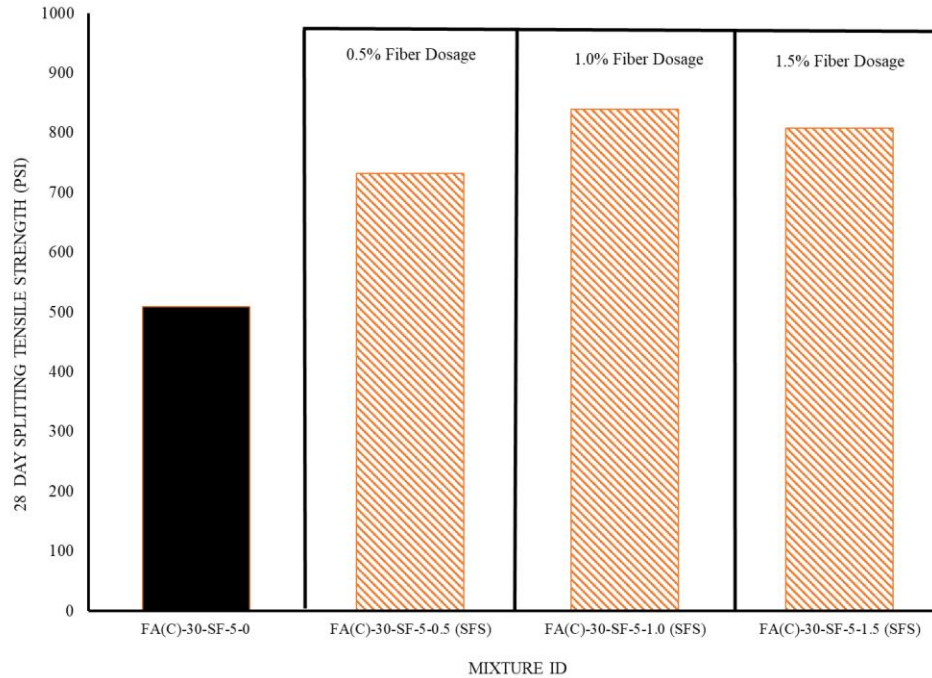


Figure 3.11 Splitting tensile data for 30% Class C Fly Ash and 5% silica fume Class C Fly Ash concrete mixtures with varied fiber types and dosages

3.3.3. Elastic Modulus

The elastic modulus for the fiber reinforced mixtures was evaluated and are shown in Figure 3.12 to Figure 3.15. Overall, the fiber type and dosage did not significantly change the elastic modulus of the concrete.

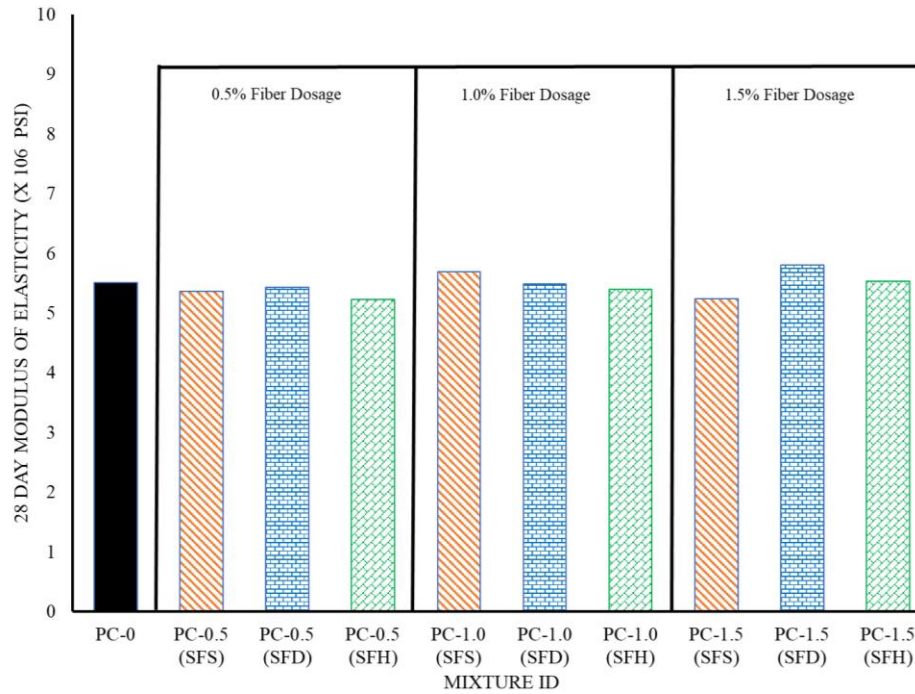


Figure 3.12 Modulus of Elasticity for Portland cement concrete mixtures with varied fiber types and dosages

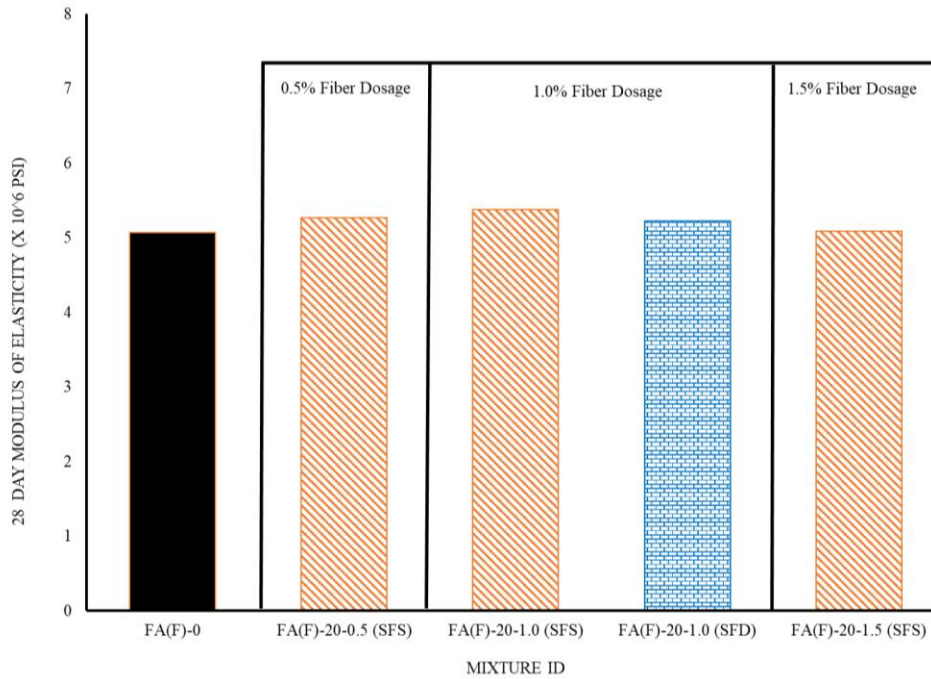


Figure 3.13 Modulus of Elasticity for 20% Class F concrete mixtures with varied fiber types and dosages

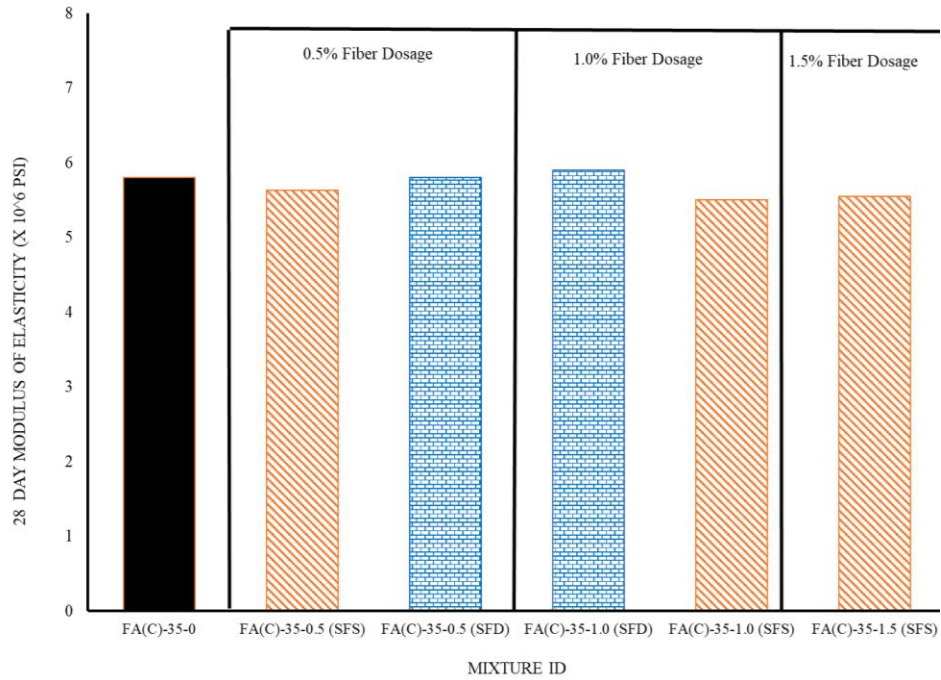


Figure 3.14 Modulus of Elasticity for 35% Class C concrete mixtures with varied fiber types and dosages

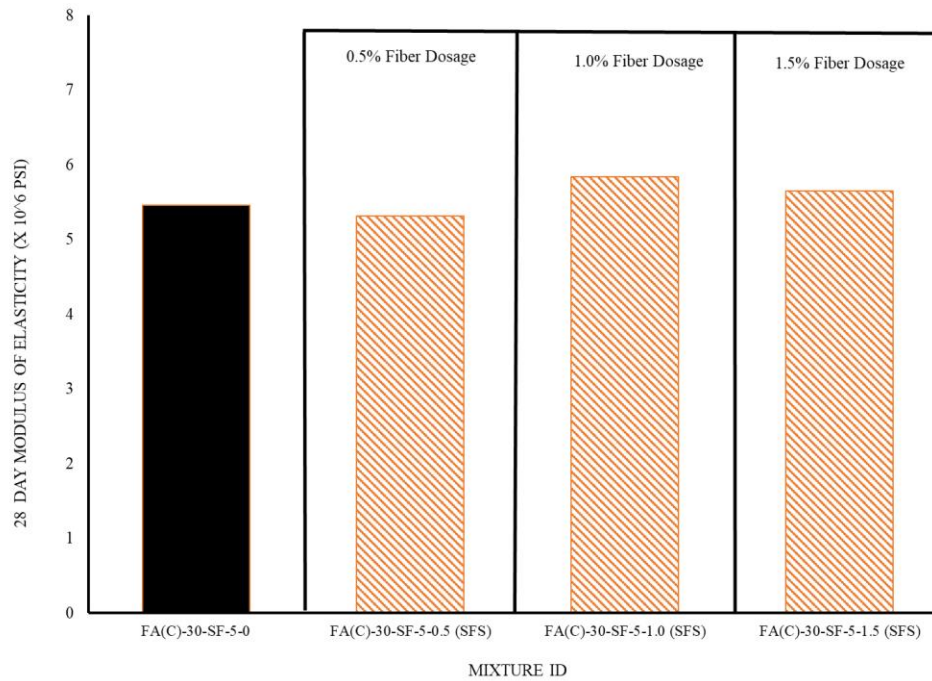


Figure 3.15 Modulus of Elasticity for 35% Class C concrete mixtures with varied fiber types and dosages

3.3.4. Drying Shrinkage

There are several factors that affect drying shrinkage of concrete including: volume fraction of the hydrated cement paste, the elastic modulus of the aggregate, and the relative humidity of the environment. For typical concrete, the typical drying shrinkage values are in the range of 400 to 1000 microstrain. Since the volume instability occurs in the hydrated cement paste, minimizing the cement paste volume will result in lower drying shrinkage values (closer to 400 microstrain). Figure 3.16 to Figure 3.19 show the drying shrinkage for mixtures containing different fiber types and dosages with different cementitious systems. In general, a small decrease in drying shrinkage occurred with samples containing steel fibers.

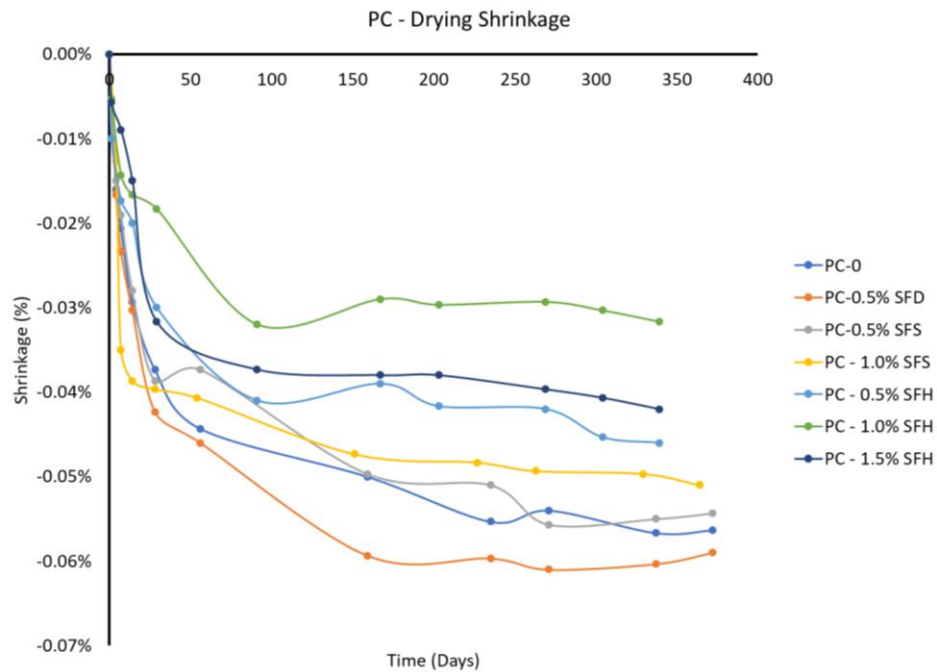


Figure 3.16 Drying shrinkage data for portland cement concrete mixtures with different fiber types and dosages

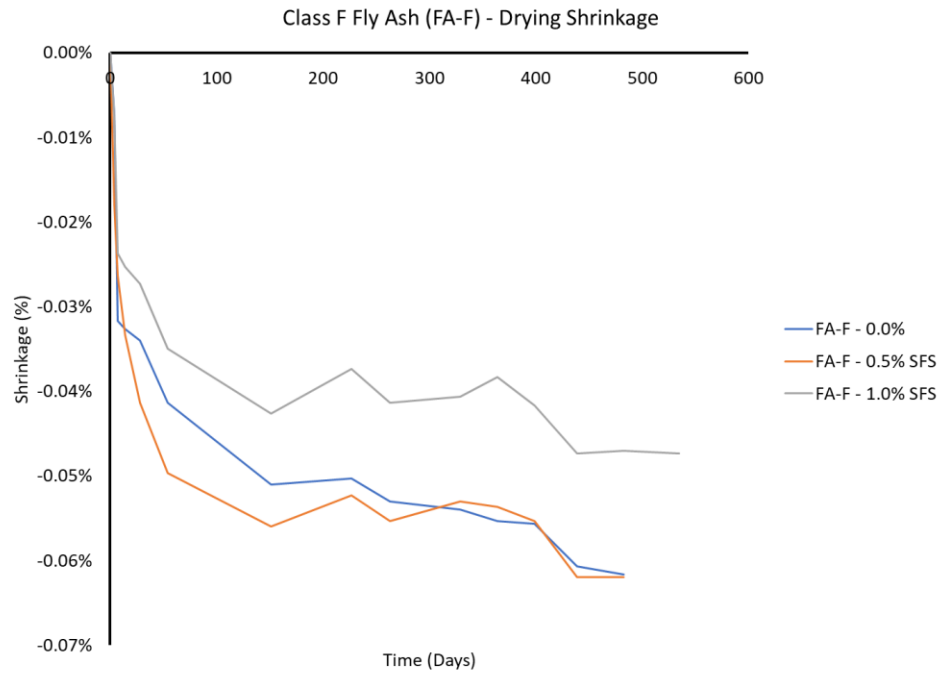


Figure 3.17 Drying shrinkage data for concrete mixtures containing 20% Class F fly ash with different fiber types and dosages

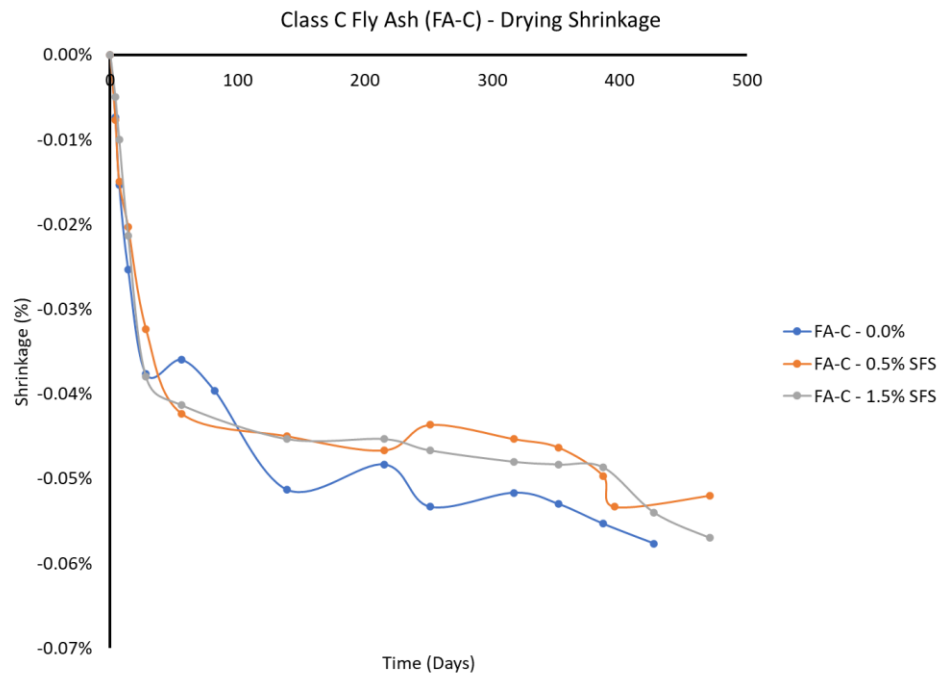


Figure 3.18 Drying shrinkage data for concrete mixtures containing 35% Class C fly ash with different fiber types and dosages

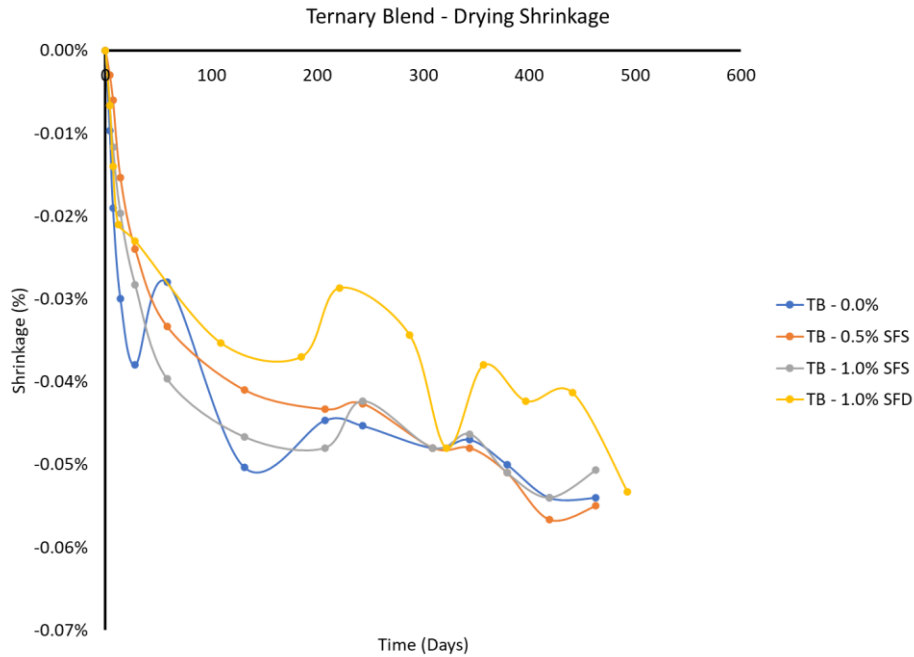


Figure 3.19 Drying shrinkage data for concrete mixtures containing ternary blend with different fiber types and dosages

3.3.5. Coefficient of Thermal Expansion

TxDOT test method Tex-428-A was used to evaluate the coefficient of thermal expansion (CoTE) for concrete mixtures containing steel fibers. CoTE results were similar between 0 and 0.5% fiber dosage. The CoTE did increase with 1 and 1.5% steel fibers. The CoTE of 1 and 1.5% were similar. This data is shown in Figure 3.20.

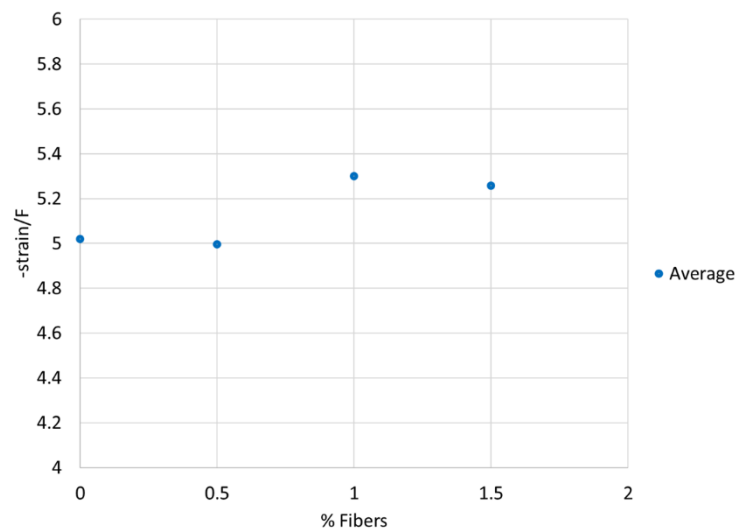


Figure 3.20 Coefficient of Expansion data for concrete mixtures containing varied amounts of steel fibers.

3.3.6. Impact Testing

Impact testing results following ACI 544 are shown below in Figure 3.21 and Figure 3.22. Figure 3.21 shows the number of blows to first crack. The 1.5% fiber dosage took 3 times the number of blows to first crack. Figure 3.22 shows that the amount of blows to failure increases with the fiber dosage.

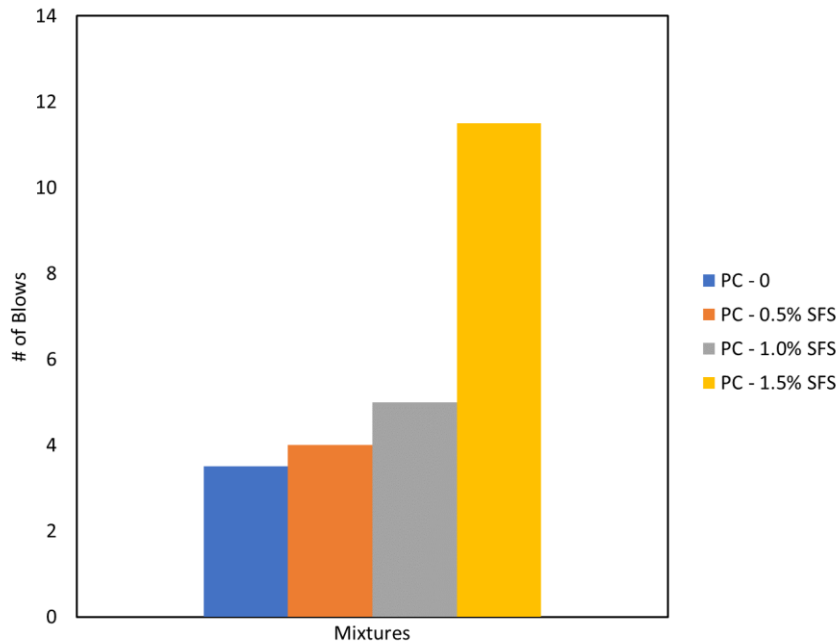


Figure 3.21 Impact testing to first crack

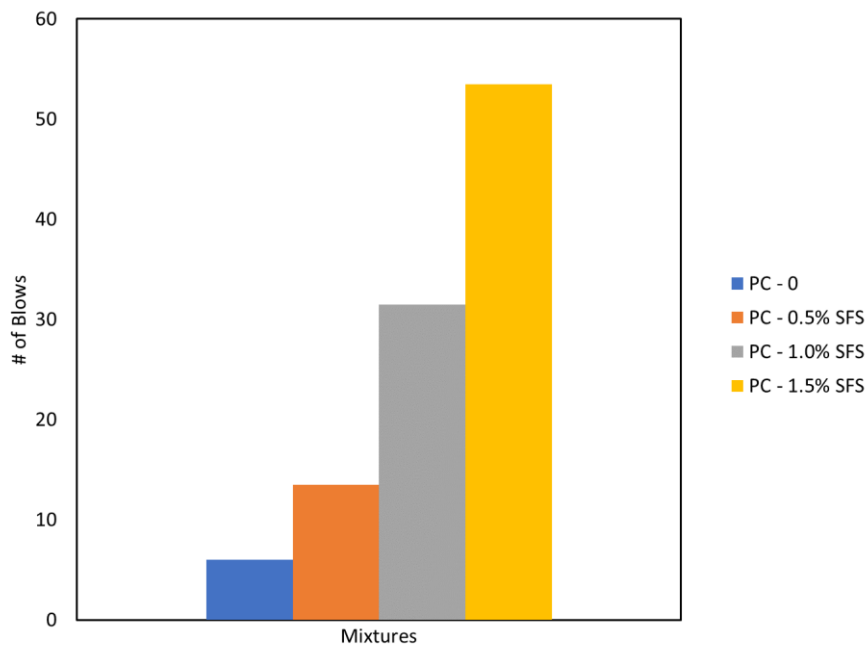


Figure 3.22 Impact testing to determine the number of blows to failure

3.3.7. Flexural Toughness (ASTM C1609)

The post-crack flexural behavior of concrete mixtures containing the various fibers and dosages was assessed using ASTM C1609, as depicted in Figure 3.23. The data obtained from this testing was processed and relevant toughness parameters were calculated, as described in Figure 3.24.

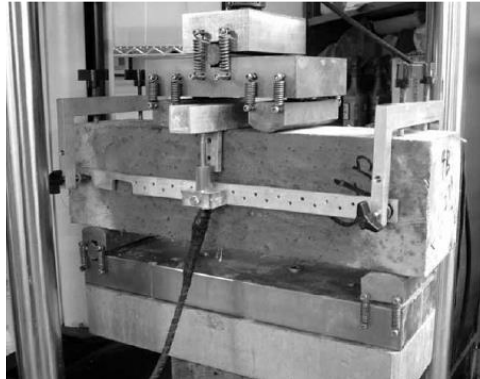


Figure 3.23 Test set-up for measuring flexural toughness of FRC (ASTM C1609)

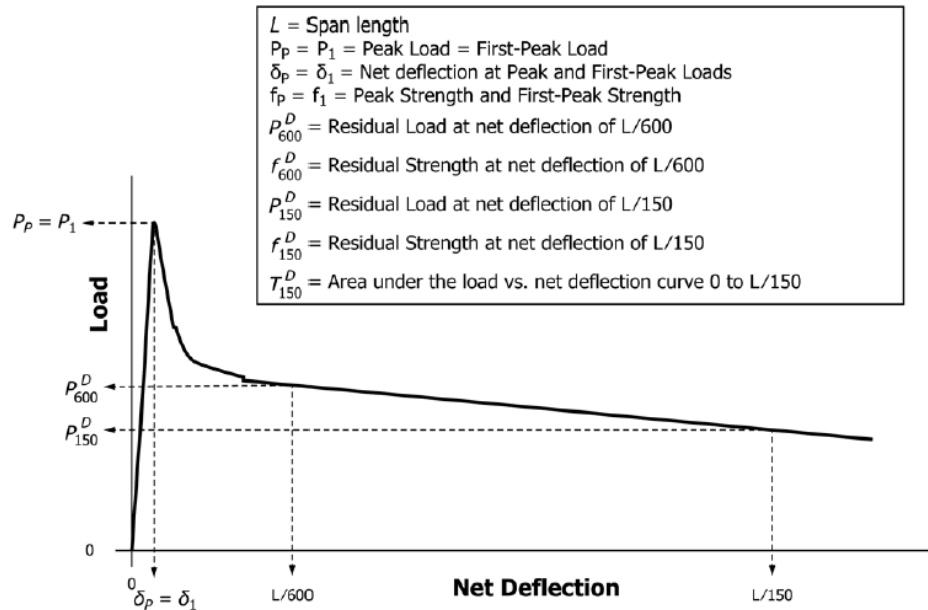


FIG. 3 Example of Parameter Calculations for First-Peak Load Equal to Peak Load (Not to Scale)

Figure 3.24 Typical ASTM C1609 test results and relevant toughness parameters

Table 3.8 shows the results of ASTM C1609, including the presentation of the relevant toughness parameters. As is often the case with ASTM C1609, some tests do not generate accurate data, especially when testing lower fiber dosages. For each mixture testing, two samples were tested (A and B).

Table 3.8 Results of ASTM C1609 flexural toughness testing.

| Mixture ID (Fiber) - Sample | f_l | f_p | f_{600} | f_{150} | Toughness | $f_{e, 150}^d$ | $R_{T,150}^D$ |
|-----------------------------|-------|-------|-----------|-----------|-----------|----------------|---------------|
| PC-1.0 (SFD) - A | 3555 | | 2600 | 2180 | 256 | 2400 | 0.68 |
| PC-1.0 (SFS) - A | 3150 | | 1490 | 1175 | 91 | 860 | 0.27 |
| PC-1.5 (SFD) - A | 3600 | 3940 | 3500 | 2300 | 317 | 2970 | 0.83 |
| PC-1.5 (SFD) - B | 3470 | | 2620 | 1830 | 168 | 1580 | 0.45 |
| FA(F)-20-1.0 (SFD) - A | 3410 | 3515 | 2890 | 1790 | 165 | 1550 | 0.45 |
| FA(C)-35-0.5 (SFD) - A | 3975 | | 2050 | 1580 | 208 | 1960 | 0.49 |
| FA(C)-35-1.0 (SFS) - A | 2490 | 2490 | 2330 | 1410 | 207 | 1950 | 0.78 |
| FA(C)-35-1.0 (SFS) - B | 3040 | | 1790 | 1120 | 102 | 960 | 0.32 |
| FA(C)-35-1.0 (SFD) - A | 3700 | | 2680 | 1900 | 153 | 1440 | 0.39 |
| FA(C)-30-SF-5-1.5 (SFS) | 3460 | | 3035 | 1790 | 256 | 2405 | 0.69 |

3.3.8. Simplified Double-Punch Test

A simplified version of the double-punch test was performed, based on the method developed by Riding et al. (2022). Figure 3.25 depicts the test set-up for this method, which employs a standard concrete compression machine (load-controlled) and dial gauge. Figure 3.26 shows typical test results for this test, along with the equation used to calculate the tensile stress. Figure 3.27 shows the results of simplified double-punch testing using one of the fibers (SFD) featured in this study.

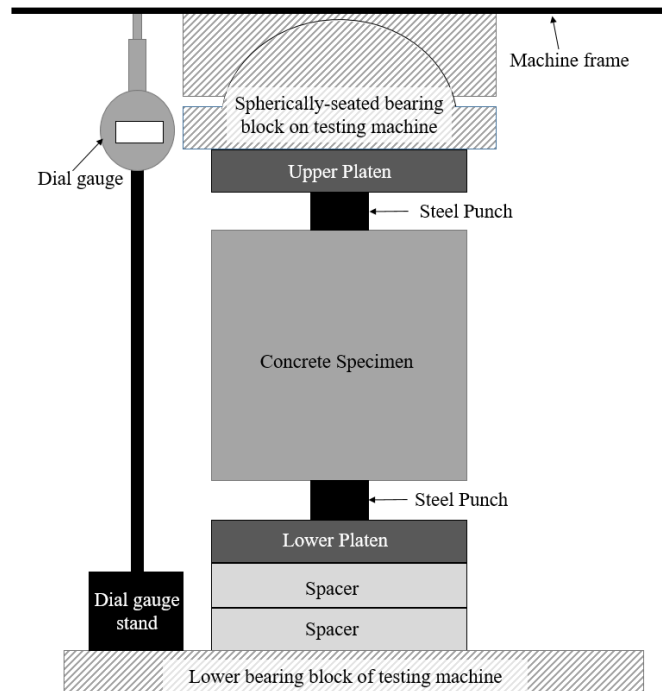


Figure 3.25 Simplified Double-Punch Test (after Riding et al., 2022)

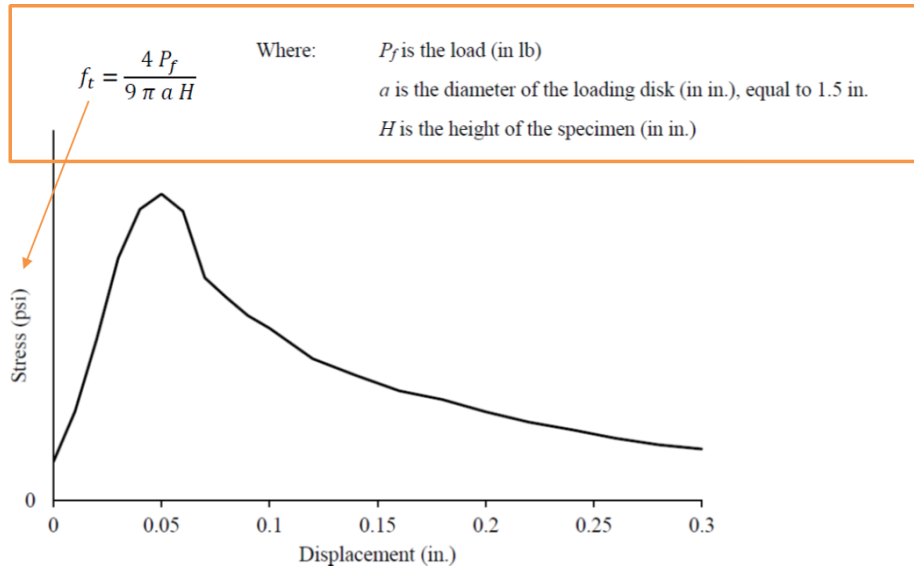


Figure 3.26 Typical simplified double-punch results and equation used to calculate tensile stress.

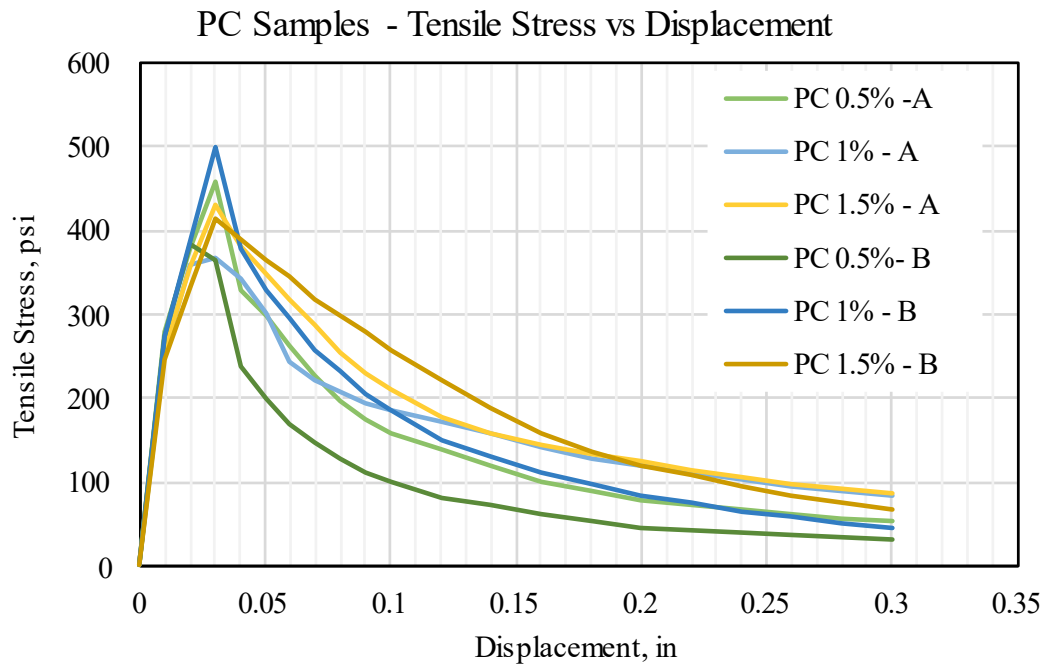


Figure 3.27 Simplified Double-Punch Test results for one fiber source (SFD)

3.4. Durability of SFRC Concrete

3.4.1. Alkali-Silica Reaction

Large outdoor exposure blocks were cast to see the effects of steel fibers in reducing ASR expansion. Figure 3.28 provides the exposure block data after 900 days. An expansion of 0.04% indicates that the block has cracked due to ASR. A reactive sand was used to initiate ASR. The mixture with 1% fiber has suppressed the expansion by 50% compared to the control block.

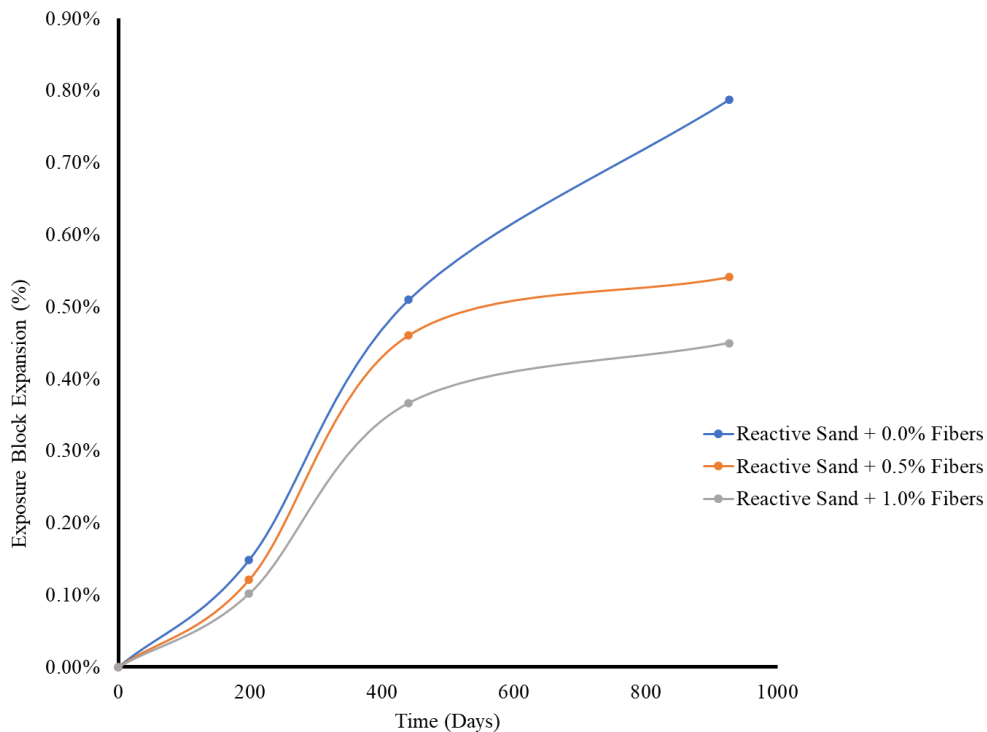


Figure 3.28 Exposure block expansion

3.4.2. Chloride Diffusion and Corrosion Potential

Concrete samples cast with 100% portland cement and increasing steel fiber dosages were cast and placed in sodium chloride solution for 56 days. The samples were removed from the solution and sent for analysis using micro X-ray Fluorescence (mXRF). Figure 3.29 shows the chloride ingress for the different samples. Overall, all of the mixtures allowed chloride ingress to the 2-inch depth. The control mixture (0% fiber) allowed more chlorides in the first 0.25 inches.

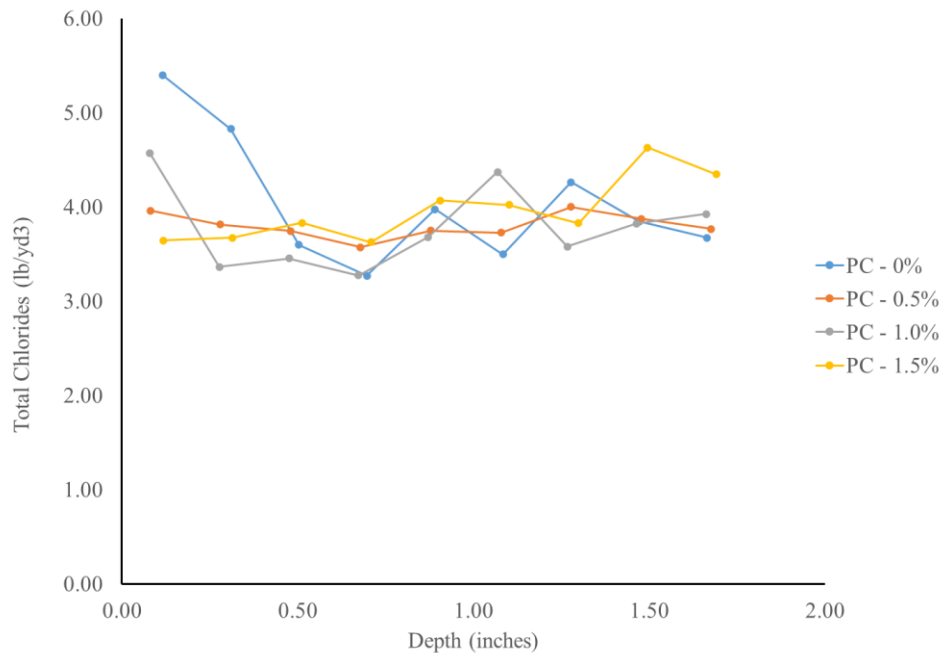


Figure 3.29 Chloride ingress of FRC samples using mXRF

In 2021, a marine outdoor exposure block consisting of 100% portland cement and 1% steel fibers was placed on the Texas coast to evaluate its long-term corrosion performance. The sample is placed vertically in the ocean at a depth of 2 feet while the remaining 2 feet are above the water line. At 2 years, the traditional reinforcement has not shown corrosion at 1- and 2-inch depths. However, the sample does show signs of corrosion from the steel fibers on the surface. Figure 3.30 shows the marine exposure block at 2 years.



Figure 3.30 Marine exposure block in Port Aransas, TX

3.4.3. Freezing and Thawing

ASTM C666 was conducted on a set of mixtures containing 0 and 1% steel fiber. Two types of cementitious mixtures were evaluated. Figure 3.31 shows the dynamic modulus change for the four mixtures. All of the mixtures lasted the entire 300 cycles and did not show any reduction of dynamic modulus with the use of steel fibers. In addition, the weight change of the samples did not change significantly throughout the test.

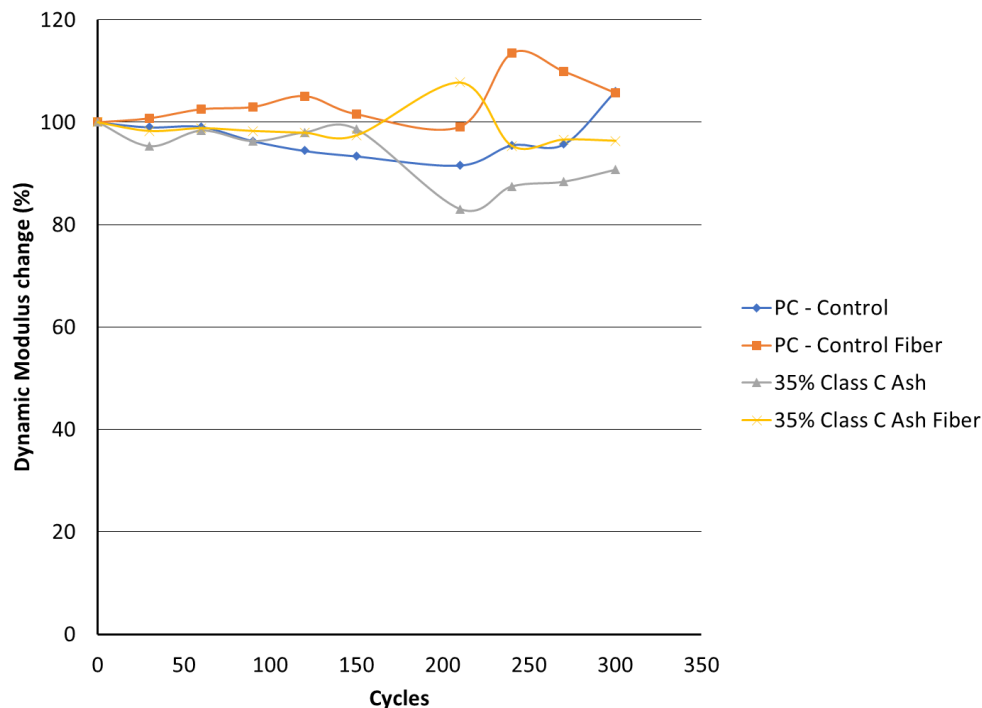


Figure 3.31 Durability factor ASTM C666

3.4.4. Salt Scaling

ASTM C672 was used to evaluate resistance to scaling of a horizontal concrete surface exposed to freezing-and-thawing cycles in the presence of deicing chemicals. Samples from concrete mixtures containing steel fibers were subjected to up to 50 freeze thaw cycles while submerged in calcium chloride solution. After 5, 10, 15, 25, and every 25 cycles thereafter the surface of the concrete samples was rated visually in accordance with the following scale in Table 3.9.

Table 3.9 Visual Rating of Concrete Surface per ASTM C672

| Rating | Condition of Surface |
|--------|---|
| 0 | No scaling |
| 1 | Very slight scaling (3mm [1/8in.] depth, max, no coarse |
| 2 | Slight to moderate scaling |
| 3 | Moderate scaling (some coarse aggregate visible) |
| 4 | Moderate to severe scaling |
| 5 | Severe scaling (coarse aggregate visible over entire surface) |

Visual interpretation of the surface conditions of concrete samples provides qualitative results that can aid in predicting durability trends. Results from this test method are subjective depending on each operator's visual interpretation. Potential for salt scaling did not increase with the inclusion of steel fibers. Figure 3.32 provides the visual ratings for the four mixtures.

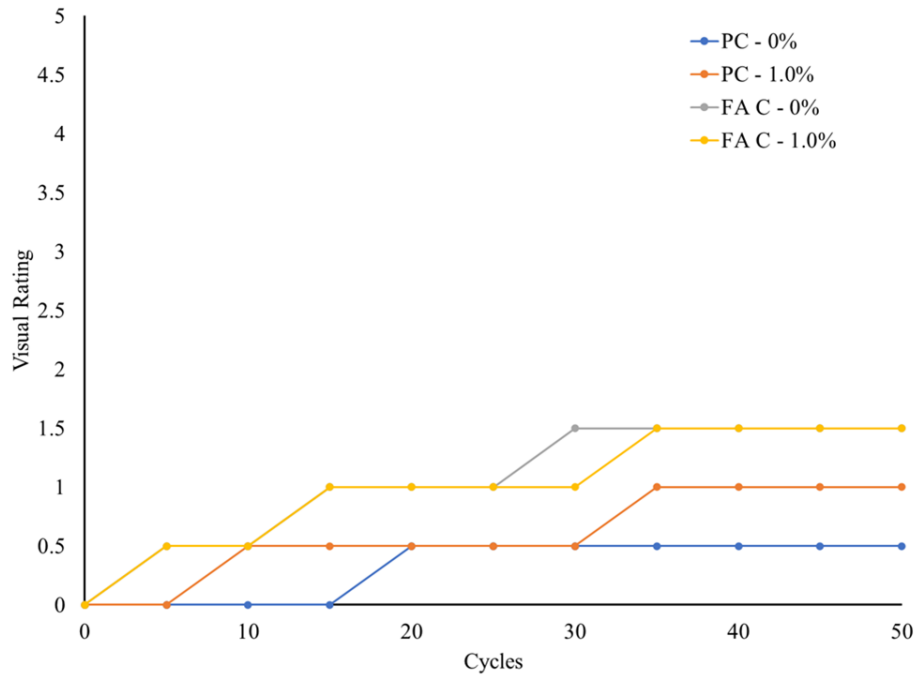


Figure 3.32 Results of visual rating of concrete mixtures containing steel fiber subjected to freeze/thaw cycles per ASTM C672

3.5. Summary

The results of a comprehensive laboratory evaluation have shown that steel fibers can be placed into TxDOT Class S concrete up to a 1.5% fiber dosage and do not show concerns for concrete production. The tensile properties increased with increasing fiber dosages. The inclusion of steel fibers has reduced the expansion of outdoor exposure blocks, indicating that SFRC exhibits greater durability than plain concrete. Long-term monitoring of ASR and marine blocks will continue.

Chapter 4. Deck Strip Test

4.1. Overview

Precast concrete panels with in-situ cast-in-place concrete topping (CIP-PCP) are designed using the AASHTO standard empirical design method. The TxDOT design standard adheres to the same conditions as the empirical design procedures to ensure that the bridge deck can satisfy state standards regarding service, fracture, and strength limits. To better comprehend and anticipate the behavior of an SFRC CIP-PCP bridge deck, the research team performed two series of idealized four-point bending deck strip tests.

Deck strip tests are intended to assess load-resisting and crack control capabilities close to vulnerable crack regions along panel layouts. This task aims to compare the performance of different types of SFRC design, which vary in fiber type and fiber volume fraction. With the results from deck strip tests, finite element analysis is performed to further optimize the reinforcement layout for the SFRC CIP-PCP bridge deck. The optimized reinforcement layout is incorporated into the full-scale bridge deck test.

In the opening section of this chapter, the experimental program's test matrix is presented. Subsequently, the fabrication procedure for specimens, material properties, and the description and verification of test findings are detailed. The chapter concludes with a summary of conclusions and key findings.

4.2. Design of Test Matrix

4.2.1. Types of Concrete

The concrete used in the experimental program was supplied by a local ready-mixed concrete plant. Steel fibers were incorporated into the concrete mixture along with aggregate. To assure laboratory casting workability, a superplasticizer was added to the mixture in the proportions specified for Class S. Table 4.1 displays the specifications for Class S concrete.




Table 4.1 Class S concrete specification

| TxDOT class S concrete | |
|---|----------|
| Design strength, Min f'_c [psi] | 4000 |
| Max water/cement ratio | 0.45 |
| Coarse aggregate size [in.] | 0.75-1.5 |
| Max cementitious material [lb/yd ³] | 700 |
| Slump | 3-5.5 |

4.2.2. Types of SFRC

Three types of fibers with different dosages are used for the experiment. The three types of fibers, A, B, and C, represent hooked end, crimped, and twisted shapes, respectively (see Table 4.2). The nomenclatures for SFRC were set different from material section. The volume fractions used for slab strip experimental programs are 1% and 1.5%.

Table 4.2 Three types of steel fibers

| | Fiber A | Fiber B | Fiber C |
|--------------|---|---|--|
| Shape |  Hooked end |  Crimped |  Twisted |
| Length | 35 mm (1.4 in.) | 38 mm (1.5 in.) | 25 mm (1 in.) |
| Diameter | 0.55 mm (0.021 in.) | 1.14 mm (0.045 in.) | 0.55 mm (0.020 inch) |
| Aspect ratio | 65 | 30 | 50 |

4.2.3. Specimen Dimension

The research team ran two series of slab strip tests simulating longitudinal direction and transverse direction panel joints. Longitudinal direction specimens, indicated by an S1 at the beginning of the specimen ID, had dimensions of 8.5 in. x 8 ft. x 16 ft. 7 in. and had the transverse panel direction incorporating prestressing through strands (Figure 4.1). In addition, the panel joint replicates the girder line, which increases the panel thickness to 10 in. On the other hand, transverse specimens, denoted as S2 in the specimen ID, are 8.5 in. x 8 ft. x 16 ft. 1 in., and their longitudinal panel direction had welded wire reinforcement (Figure 4.2). The panel joint for the transverse specimen accommodated 1 in. gaps between panels.



Figure 4.1 Longitudinal direction specimen

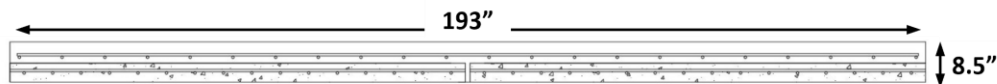


Figure 4.2 Transverse direction specimen

Existing TxDOT top mat reinforcement details were tested to compare the structural cracking performance of SFRC bridge decks built with various top mat details and SFRC mix designs. Standard detail requires #4 standard reinforcing bars spaced 9 in. (0.27 sq. in./ft.) for longitudinal and transverse directions. Specimens with SFRC differ in fiber types and reinforcement ratios. Specimens with SFRC either have 18 in. spacing #4 reinforcements (0.13 sq. in./ft.) or none at all. Flexural reinforcement for the first series of the specimen, S1, had a 3.25 in. distance from the top surface. On the other hand, the transverse specimen, S2, featured flexural reinforcement that was 2.75 inches away from the top surface. The specimen matrix for the deck strip test is presented in Table 4.3.

Table 4.3 Test matrix

| Specimen ID | Bridge Direction | Fiber type | Volume fraction | Reinforcement layout |
|--------------------|-------------------------|-------------------|------------------------|-----------------------------|
| S1-1 | Longitudinal | Plain Concrete | - | #4@9" |
| S1-2 | Longitudinal | Fiber A | 1% | #4@18" |
| S1-3 | Longitudinal | Fiber B | 1% | #4@18" |
| S1-4 | Longitudinal | Fiber C | 1% | #4@18" |
| S1-5 | Longitudinal | Fiber B | 1% | None |
| S2-1 | Transverse | Plain Concrete | - | #4@9" |
| S2-2 | Transverse | Fiber A | 1% | #4@18" |
| S2-3 | Transverse | Fiber A | 1.5% | #4@18" |
| S2-4 | Transverse | Fiber B | 1% | #4@18" |
| S2-5 | Transverse | Fiber A | 1% | None |
| S2-6 | Transverse | Plain Concrete | - | #4@18" |
| S2-7 | Transverse | Fiber A | 0.5% | #4@18" |

4.3. Specimen Preparation

4.3.1. Precast panel fabrication

Twenty four precast panels sized 8 ft. x 8 ft. x 4 in. each were manufactured by Valley Precast, Inc. Originally, twenty precast panels were fabricated for ten deck strip tests. Subsequently, an additional four panels were produced to conduct additional tests (S2-6 and S2-7). For transverse panel reinforcement, 0.5 in. diameter prestressing strands with 14.4 kips per strand were positioned every 6 in. and extended outward by 3 in. Deformed welded wire reinforcement of 0.22 sq. in. was installed for the longitudinal panel. The configuration of the reinforcement at a construction site is shown in Figure 4.3. Precast panels were broom-finished to

ensure composite action with the cast-in-place concrete (Figure 4.4). Panels were removed from the formwork after being cured using burlap for a day (Figure 4.5).



Figure 4.3 Precast panels before concrete casting



Figure 4.4 Roughened panel surface using brooms



Figure 4.5 Concrete panel curing

4.3.2. Specimen Casting

In preparation for concrete casting, precast panels were positioned atop the wooden platform, and the strands were carefully cut in close proximity to the panel surface. This ensured a seamless alignment between the formwork and panel surfaces. The use of laboratory-fabricated steel formwork involved securing it both from the top and bottom using formwork ties and struts. Following the fastening of the formworks, reinforcements were strategically placed and securely tied to the bolsters to anchor them in the intended position. Figure 4.6 illustrates the specimen's appearance before the concrete casting procedure.



Figure 4.6 Specimen before casting

Prior to casting, the precast panel surface was kept wet using a pressure sprayer. The ready mix SFRC was delivered via a concrete truck. A total of 3 cubic yards of concrete was ordered to cast the structural and material specimens. Before the casting process, slumps were tested to ensure that the concrete achieved a minimum 4.5-inch slump. Subsequently, the concrete was cast using a concrete bucket (Figure 4.7), and after casting, the concrete surface was leveled and smoothed using screed and floats (Figure 4.8). The specimen underwent curing by covering it with a plastic sheet (Figure 4.9).



Figure 4.7 Concrete casting using concrete bucket



Figure 4.8 Leveling and smoothing of specimen

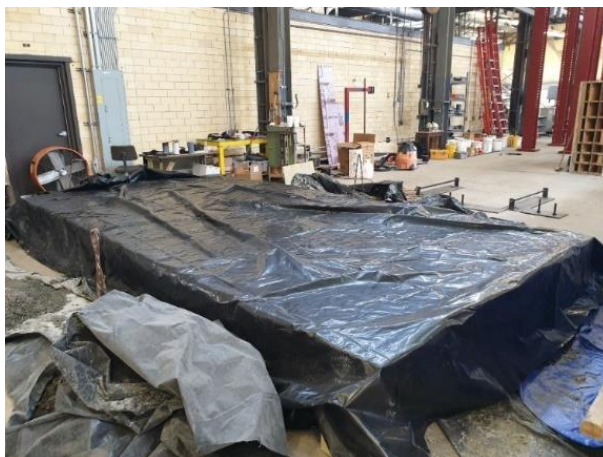


Figure 4.9 Curing of specimen

4.4. Material Testing and Properties

To determine the SFRC structure's performance, the mechanical properties of the material must be evaluated. In order to get the necessary mechanical aspects of SFRC, three different types of tests—uniaxial compression, uniaxial tension, and flexural—were carried out. In addition, the workability of the fresh-state concrete was measured during the casting process.

4.4.1. Fresh Concrete Properties: Slump Test

In this research, the steel fibers were incorporated into the concrete mixture along with the aggregate. The target concrete slump was 4.5 inches, but there was a 1 to 2-inch slump loss during delivery due to the presence of fibers. Consequently, one specimen, S1-3, was cast with a 2-inch slump, resulting in uneven surfaces and diminished crack resistance in this particular specimen (Figure 4.10). To address these challenges, our team opted to order concrete with a 3-inch higher slump than initially desired. Additionally, chemical admixtures were introduced to maintain workability during the casting process.



Figure 4.10 Uneven surface of S1-3 specimen due to low slump

Another observation made during casting was the formation of fiber clumps, known as fiber balls, which specifically occurred in the Fiber C 1% SFRC mix. These fiber balls posed a risk of clogging the concrete pump when casting with a hydraulic pump.

4.4.2. Examination of Panel Girder Gap

After testing, specimens were cut and examined for concrete flowability at the panel joint over the girder region. Figure 4.11 illustrates the cross-section of the girder

line. The findings reveal that the SFRC, both with 1-inch and 1.5-inch lengths, effectively flowed into a 1-inch gap between the panel and the simulated girder.



Figure 4.11 Cut cross-section of (a) 1.5 inch hooked end fiber SFRC and (b) 1 inch twisted fiber SFRC specimens

4.4.3. Uniaxial Compression and MOE Tests

The compression and modulus of elasticity (MOE) tests were conducted in accordance with the ASTM C39 and ASTM C469 standards to analyze the material behavior of SFRC under compression. Using a FORNEY machine, 4 in. by 8 in. cylinders were subjected to a consistent loading rate, enabling the measurement of both compressive strength and MOE. The deformation during compression was measured using a compressometer. Each specimen underwent testing with a minimum of two cylinders. A summary of the test results can be found in Table 4.4.

Table 4.4 Slab-strip specimen uniaxial compression test results

| Specimen ID/ Description | Cast-in-place | | Precast concrete | |
|-----------------------------|---------------|--------------|------------------|--------------|
| | E_c [ksi] | f'_c [ksi] | E_c [ksi] | f'_c [ksi] |
| S1-1 | 4305.5 | 6.3 | 5101.6 | 9.6 |
| S1-2 | 4309.6 | 6.2 | 5548 | 11.3 |
| S1-3 | 3814.3 | 5.3 | 5731.5 | 11.4 |
| S1-4 | 4071.4 | 5.7 | 5437.3 | 11.2 |
| S1-5 | 5157.1 | 7.0 | 5870.8 | 10.7 |
| S2-1 | 3241.7 | 5.9 | 5090.3 | 11.4 |
| S2-2 | 4443.5 | 6.3 | 5730.9 | 10.8 |
| S2-3 | 4197.4 | 5.6 | 5178.3 | 11.2 |
| S2-4 | 3886.5 | 5.7 | 5437.3 | 11.2 |
| S2-5 | 3894.6 | 5.2 | 5770.9 | 11.7 |
| S2-6 | 5284.6 | 7.2 | 4809.1 | 9.2 |
| S2-7 | 4953.7 | 6.1 | 5271.6 | 8.9 |

4.4.4. Flexural Bending Test (ASTM C1609)

For this task, the ASTM C1609/C1609M method was employed to determine both peak flexural strength and residual strength. During the casting of slab-strip specimens, beams measuring 4 in. x 4 in. x 14 in. were formed. Flexural loading of the beams was executed using a 20-kip-capacity material testing system (MTS) alongside the Flextest 60 equipment. The span length, denoted as "L," was set at 12 in. Initially, a loading rate of 0.02 in./min was maintained until the displacement reached 0.013 in. (L/900). Subsequently, the speed was increased to 0.05 in./min until the completion of the test. The fundamental parameters derived from the flexural test encompass the initial peak strength and the residual strength at a displacement of 0.08 in. (L/150) for the SFRC beam, offering insights crucial for assessing structural members. The flexural test results are shown in Figure 4.12 and summarized in Table 4.5.

Table 4.5 Slab-strip specimen flexural test results

| Specimen ID/ Description | SFRC Type | C1609 test | | |
|-----------------------------|--------------|--------------|---------------------------------|---------------------------------|
| | | f'_r [ksi] | $f'_{res(\frac{L}{600})}$ [ksi] | $f'_{res(\frac{L}{150})}$ [ksi] |
| S1-2 | Fiber A 1% | 0.712 | 0.412 | 0.266 |
| S1-3 | Fiber B 1% | 0.574 | 0.331 | 0.184 |
| S1-4 | Fiber C 1% | 0.759 | 0.632 | 0.407 |
| S1-5 | Fiber B 1% | 0.750 | 0.382 | 0.276 |
| S2-2 | Fiber A 1% | 0.726 | 0.510 | 0.358 |
| S2-3 | Fiber A 1.5% | 0.788 | 0.576 | 0.396 |
| S2-4 | Fiber B 1% | 0.761 | 0.416 | 0.228 |
| S2-5 | Fiber A 1% | 0.643 | 0.520 | 0.359 |
| S2-7 | Fiber A 0.5% | 0.741 | 0.261 | 0.195 |

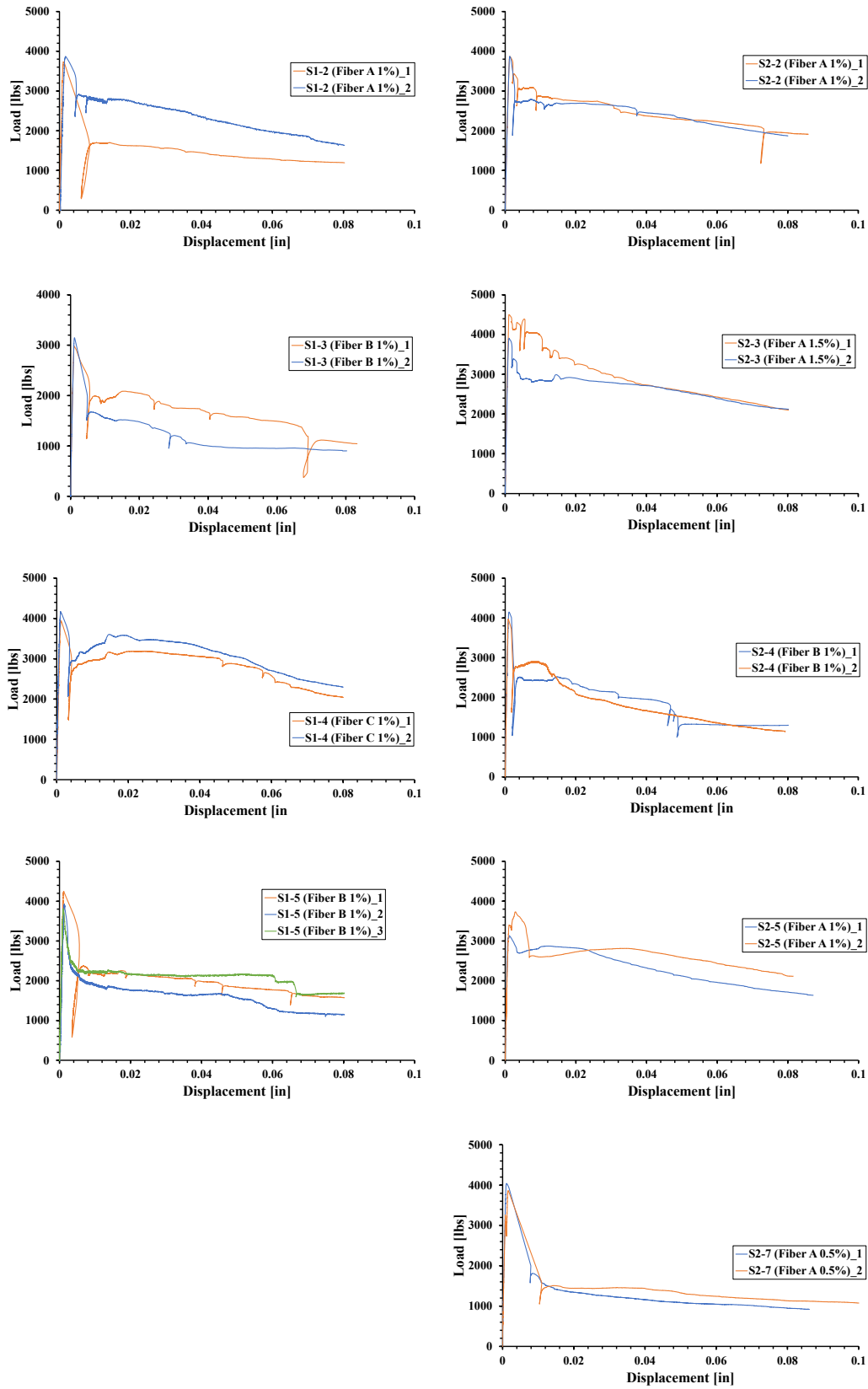


Figure 4.12 ASTM C1609 test results

4.4.5. Uniaxial Tension Test

The uniaxial tension test determines a material's tensile stress-strain curve, which is a crucial value to estimate the residual stress of SFRC. However, ASTM International does not specify a standard uniaxial tension test method. Therefore, in this research program, dog bone specimens with four linear strain conversion transducers (LSCTs) were used to obtain stress-strain curves for pre-cracking and post-cracking regions (Figure 4.13). Samples were loaded at a monotonically loaded speed of 0.003 in./min. with a 300-kips-capacity MTS machine. Tension test results are summarized in Figure 4.14 and Table 4.6. Due to the occurrence of cracks in the cross-section deformation zone across numerous specimens, the figure exclusively presents results from tests featuring central cracks.



Figure 4.13 Dog-bone test setup

Table 4.6 Direct tension test results

| Specimen ID/ Description | SFRC Type | Direct tension test | |
|-----------------------------|--------------|---------------------|-------------------|
| | | f'_t [ksi] | f_{res}^t [ksi] |
| S1-2 | Fiber A 1% | 0.545 | 0.148 |
| S1-3 | Fiber B 1% | 0.439 | 0.091 |
| S1-4 | Fiber C 1% | 0.467 | 0.134 |
| S1-5 | Fiber B 1% | 0.516 | 0.094 |
| S2-2 | Fiber A 1% | 0.524 | 0.108 |
| S2-3 | Fiber A 1.5% | 0.471 | 0.152 |
| S2-4 | Fiber B 1% | 0.487 | 0.102 |
| S2-5 | Fiber A 1% | 0.341 | 0.076 |
| S2-7 | Fiber A 0.5% | 0.487 | 0.073 |

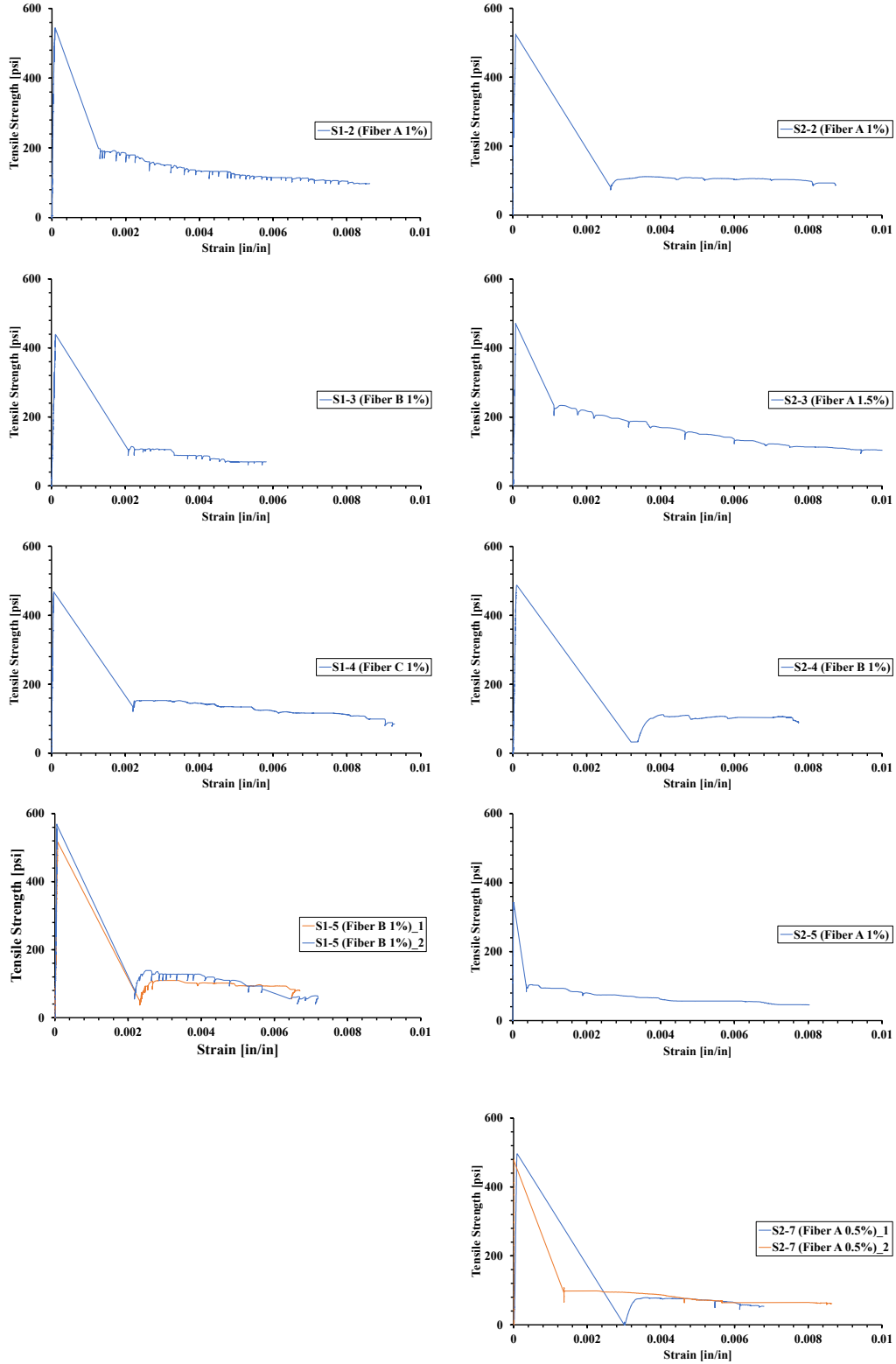


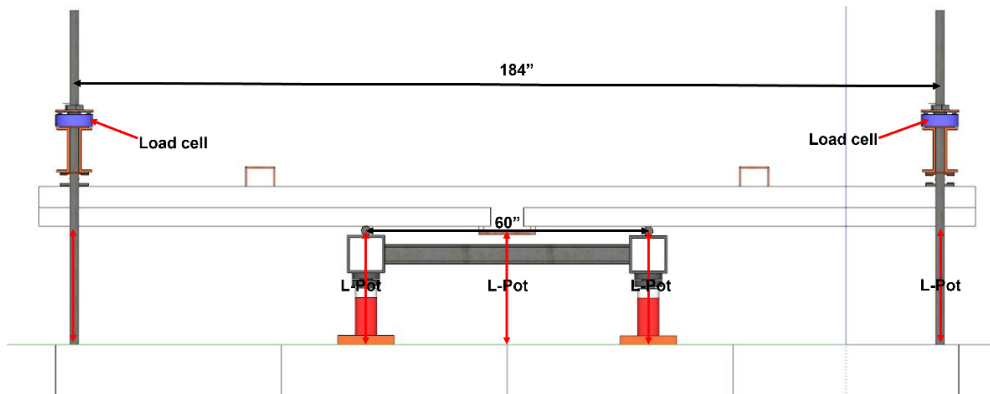
Figure 4.14 Uniaxial tension test results

4.5. Test Setup and Instrumentation

In order to evaluate how successfully SFRC included specimens control fractures and withstand loads under idealized flexural loading conditions, CIP-PCP deck strip specimens were designed, constructed, and tested for failure. Figure 4.15 (a) shows the actual setup of the idealized constant bending moment test. The deck supports and loading beams were rollers welded on top of two support beams spaced 4 ft. apart. The beams were loaded with the four hydraulic rams. Distributed loads throughout the specimen were measured by two supporting beams with pinned and roller connections at the ends of the deck. Instrumentation was provided to measure the strain, stresses, and deflections of the specimen. Strain gauges were installed on #4 bars along the constant moment region at the end supports. To measure loads, load cells were put in the end-support beams. Ten linear potentiometers were installed to record displacements at the specimen's center, loading points, and supports. Additionally, high-precision non-contact OptoTrak optical measurement equipment was used to detect surface strain and crack width during testing. Figure 4.15(b) shows the instrumentation for the test.



(a)



(b)

Figure 4.15 Deck strip test setup: (a) isometric view and (b) side view and instrumentations

4.6. Test Results

This section presents test results for the specimens outlined in Table 4.3. The service limit state baselines, as specified in AASHTO-LRFD section 5.6.7, include a crack width limit of 0.013 inches and a reinforcement stress limit of 36 ksi. Furthermore, the deflection of the specimens up to the service-level load, 40% of the ultimate load (Jang et al., 2023), was analyzed. Consequently, the following three points were investigated.

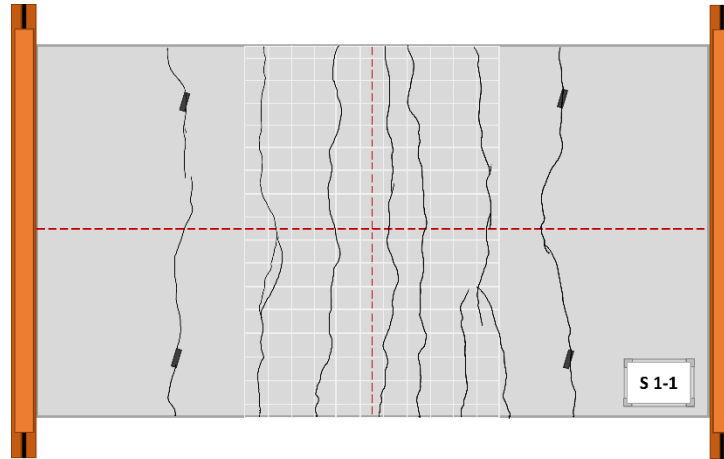
- The specimens were assessed to see if they exceeded the crack limit before the reinforcement stress limit. In addition, the researchers compared the crack-resisting performance of every specimen with that of the control specimen.
- The deflection limit of the existing TxDOT detail up to service level load was derived from the load-displacement relationship. To check if the specimen maintained serviceability, SFRC specimens were compared to the control specimen.

4.6.1. Longitudinal Direction

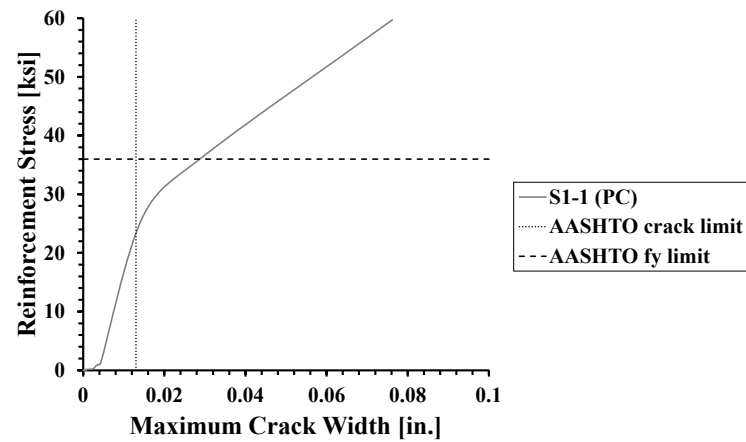
The longitudinal direction of the bridge was assessed in the first series of test matrices. The orientation of the strands in the longitudinal direction matched that of the flexural reinforcements. A panel joint simulated a thicker slab with bedding strips and a top flange that imitated a steel beam. The slab was 10 in. thick in the middle. Over the area of the constant moment, numerous cracks would appear. The critical crack becomes noticeably wider once all the stable cracks have developed. The surface near the simulated girder line was significantly cracked in all five specimens.

4.6.1.1. S1-1

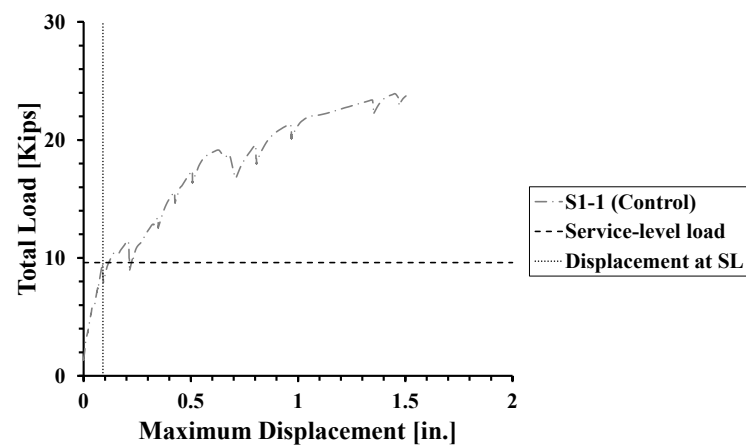
The control specimen in the longitudinal direction was S1-1, featuring #4 bars spaced at 9 inches for flexural reinforcement. Figure 4.16 (a), (b), and (c) depict the stabilized crack pattern, crack control ability, and load-displacement curve, respectively. The rebar stress reached 23 ksi, surpassing the AASHTO crack limit. The ultimate load capacity was 23.9 kips, indicating a service-level load of 9.6 kips. Consequently, comparisons were conducted for the crack size corresponding to a reinforcement stress of 23 ksi and the displacement at a 9.6 kips load.



(a)



(b)



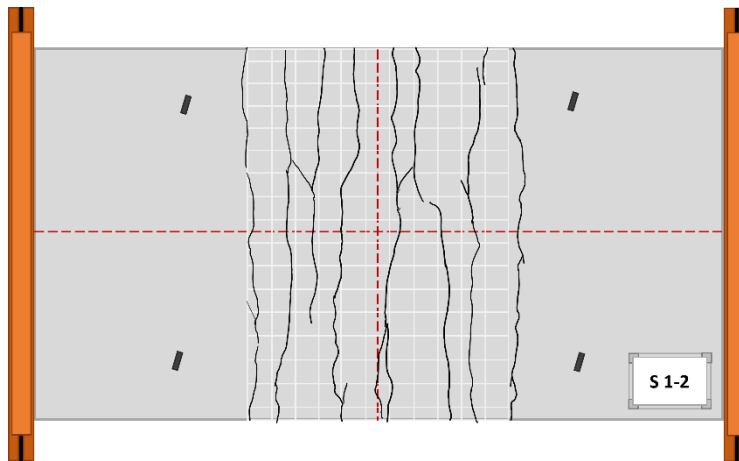
(c)

Figure 4.16 S1-1 test results, (a) stabilized crack pattern, (b) measured critical crack width, and (c) load-displacement curve

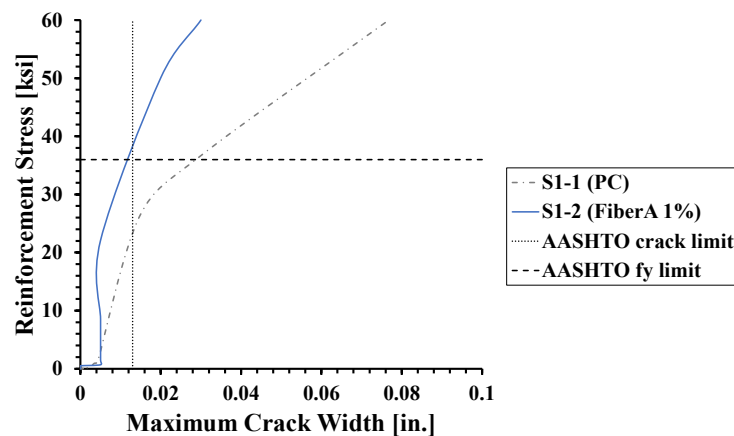
4.6.1.2. S1-2

The Fiber A 1% mix was used as a CIP in Specimen S1-2. It had #4 bars every 18 inches for flexural reinforcement. Figure 4.17 (a), (b), and (c) demonstrate the stabilized crack pattern, crack control ability, and load-displacement curve, respectively. The results obtained from this experiment are as follows.

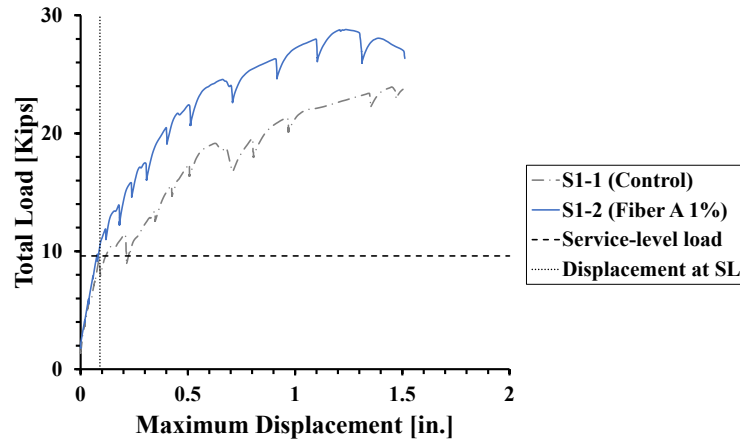
- The critical cracks in the S1-2 sample exceeded the AASHTO crack limits at 36 ksi. This means that Fiber A 1% with half reinforcement outperformed the current TxDOT detail regarding crack resistance.
- According to the load-displacement curve, the specimen had higher stiffness and load capacity than the control specimen throughout the test.



(a)



(b)



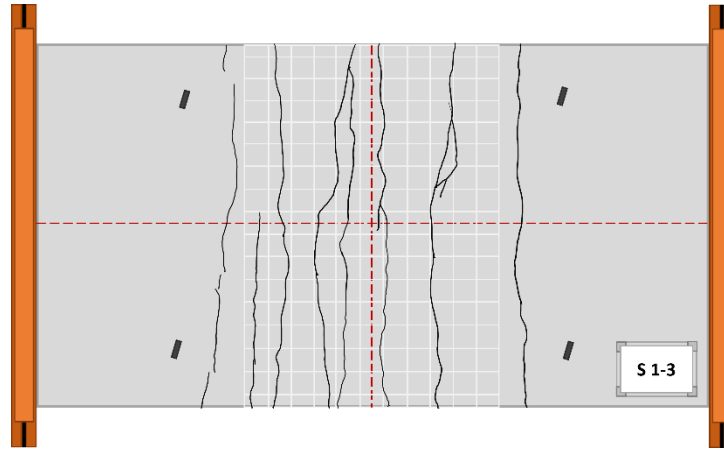
(c)

Figure 4.17 S1-2 specimen test results, (a) stabilized crack pattern, (b) measured critical crack width, and (c) load-displacement curve

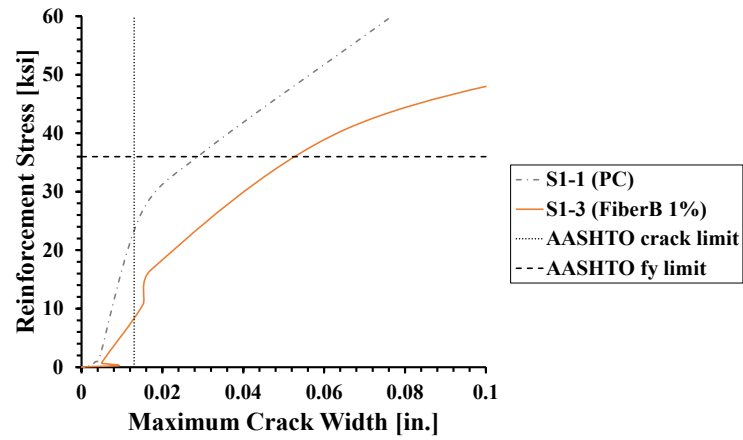
4.6.1.3. S1-3

Specimen S1-3 utilized a topping material with a 1% mix of Fiber B, and it included #4 bars spaced at 18 inches for flexural reinforcement. Figure 4.18 (a), (b), and (c) illustrate its stabilized crack pattern, crack control effectiveness, and load-displacement curve. Following are the findings of this experiment.

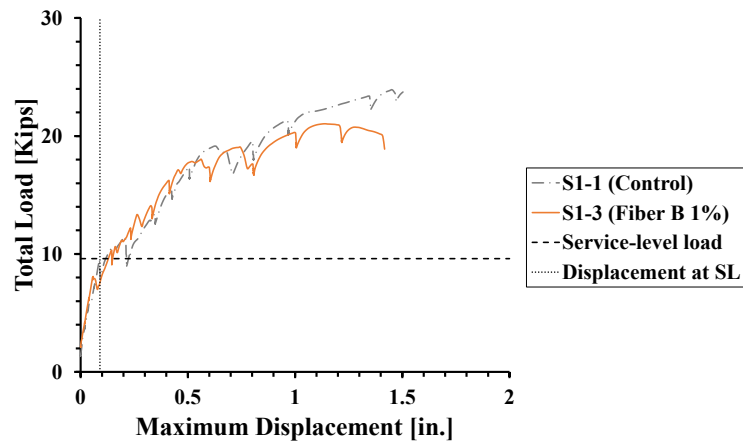
- At a reinforcement stress of 8 ksi, the critical cracks within the S1-3 specimen exceeded the AASHTO crack limits. This means that Fiber B 1% with half reinforcement had lower crack resistance compared to the current TxDOT detail. This might be due to the low slump problem that occurred during casting. However, the specimen stayed crack-free until the service load limit.
- According to the load-displacement curve, the specimen exhibited stiffness and load capacity similar to the control specimen throughout the test.



(a)



(b)



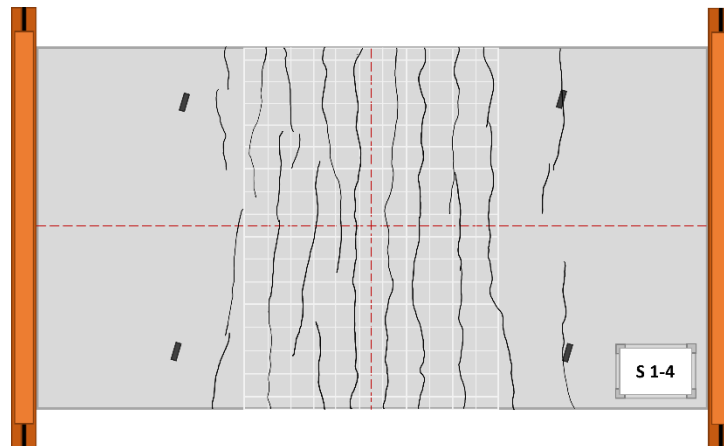
(c)

Figure 4.18 S1-3 specimen test results, (a) stabilized crack pattern, (b) measured critical crack width, and (c) load-displacement curve

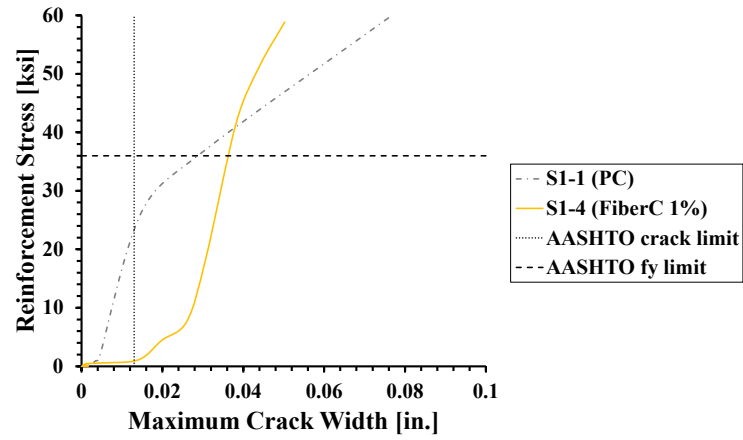
4.6.1.4. S1-4

Specimen S1-4 incorporated a 1% mix of Fiber C as a topping material and featured #4 bars spaced at 18 inches for flexural reinforcement. Figure 4.19 (a), (b), (c), and (d) demonstrate the stabilized crack pattern, crack control ability by rebar stress and total load, and load-displacement curve, respectively. The following section outlines the findings from this experiment.

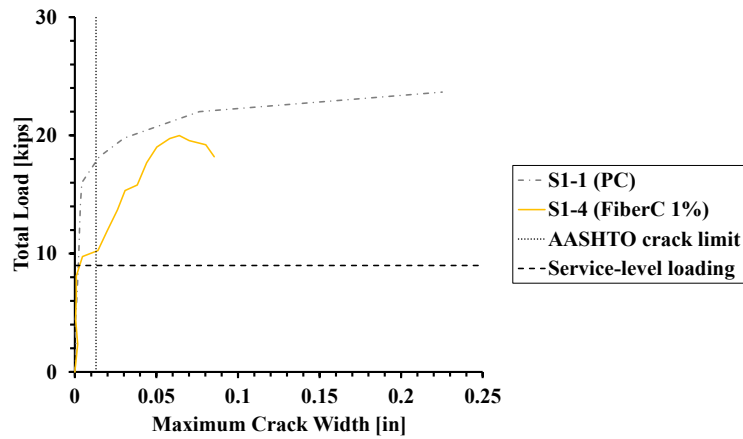
- Critical cracks in the S1-4 specimen surpassed the AASHTO crack limits at a minimal reinforcement stress, indicating a discrepancy between the crack location and the strain gauge position. Consequently, a further comparison of the crack-total load is depicted in Figure 4.19 (c).
- The critical cracks within the S1-4 specimen exceed the AASHTO crack limits at a load of 12 kips, which is lower than the control specimen capacity of 17.5 kips. This means that when compared to the current TxDOT detail, Fiber C 1% with half reinforcement had lower crack resistance. The specimen, however, did not crack until it reached the service-level load limit.
- Throughout the test, the specimen exhibited stiffness and load capacity similar to the control specimen, according to the load-displacement curve.



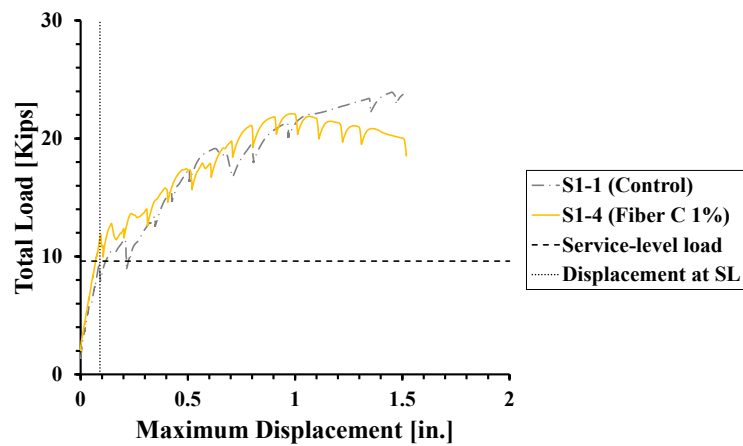
(a)



(b)



(c)



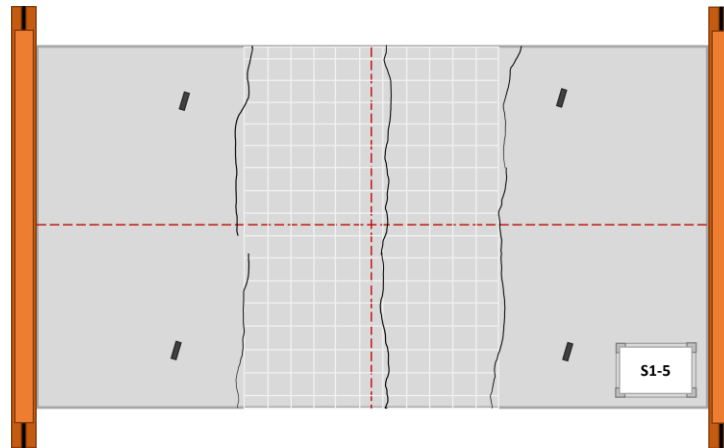
(d)

Figure 4.19 S1-4 specimen test results, (a) stabilized crack pattern, measured critical crack width to rebar stress (b) total load (c) , and (d) load-displacement curve

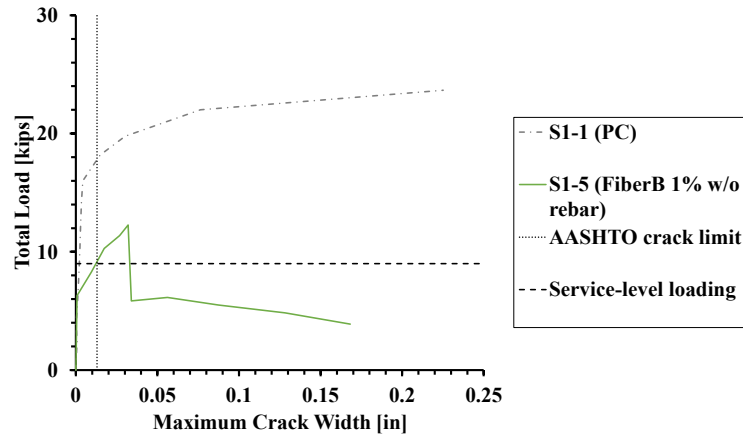
4.6.1.5. S1-5

Specimen S1-5 incorporated Fiber B 1% mix as a topping material. It contained no flexural reinforcement. Its stabilized crack pattern, crack control ability, and load-displacement curve are shown in Figure 4.20 (a), (b), and (c), respectively. The results of this experiment are listed below.

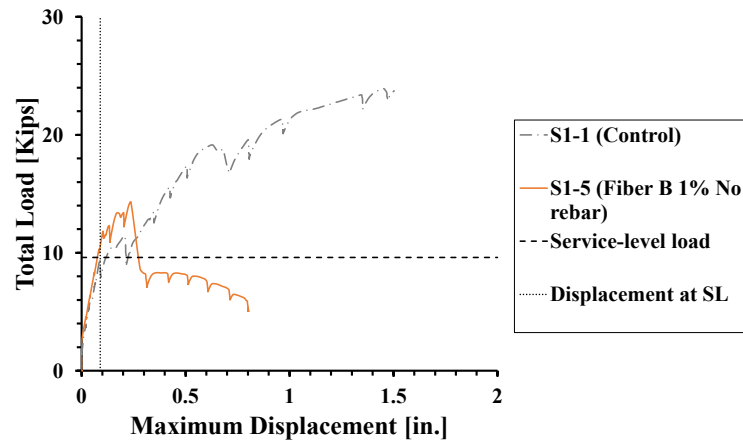
- Due to significant differences between measurements from the dog-bone-shaped concrete strain gauge and #4 rebars, the load-crack width graph was employed to assess the crack resistance of the specimen. At a load of 12 kips, critical cracks in the S1-5 specimen exceeded the AASHTO crack limits, indicating that Fiber B 1% with half reinforcement exhibited lower crack resistance compared to the existing TxDOT detail.
- The specimen formed a single critical crack on the constant moment region, which widened significantly after 14.3 kips loading.
- According to the load-displacement curve, the specimen had higher stiffness and load capacity than the control specimen until the service-level load. Then, however, it lost stiffness at a load of 14.3 kips



(a)



(b)



(c)

Figure 4.20 S1-5 specimen test results, (a) stabilized crack pattern, (b) measured critical crack width, and (c) load-displacement curve

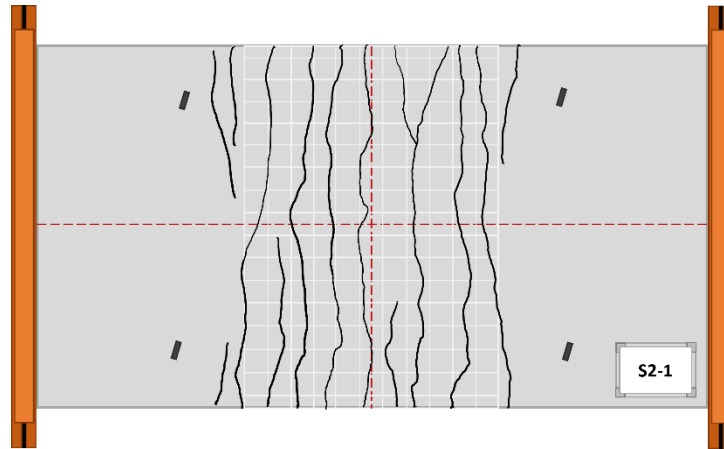
4.6.2. Transverse Direction

The second series of test matrixes replicated the transverse direction of the bridge. Strands were perpendicular to the longitudinal direction reinforcements. There was a 1 in. gap between the panels. Numerous cracks would start to form over the region of the constant moment. After the formation of all stable cracks, the critical crack significantly widened. The critical crack was located at the panel joint for all seven specimens.

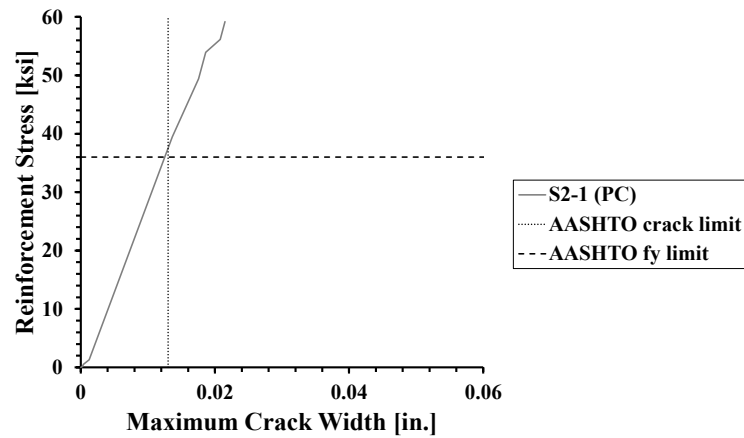
4.6.2.1. S2-1

The transverse direction control specimen, S2-1, featured #4 bars spaced at 9 inches for flexural reinforcement. Figure 4.21 (a), (b), and (c) illustrate the stabilized crack

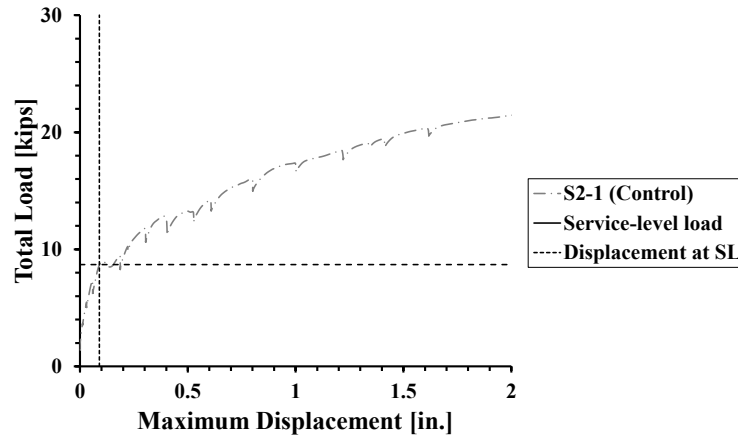
pattern, crack control capability, and load-displacement curve, respectively. The ultimate load capacity reached 22.3 kips, indicating a service-level load of 8.9 kips. The AASHTO crack limit was surpassed at a load of 8.7 kips, where the rebar stress reached 37 ksi.



(a)



(b)



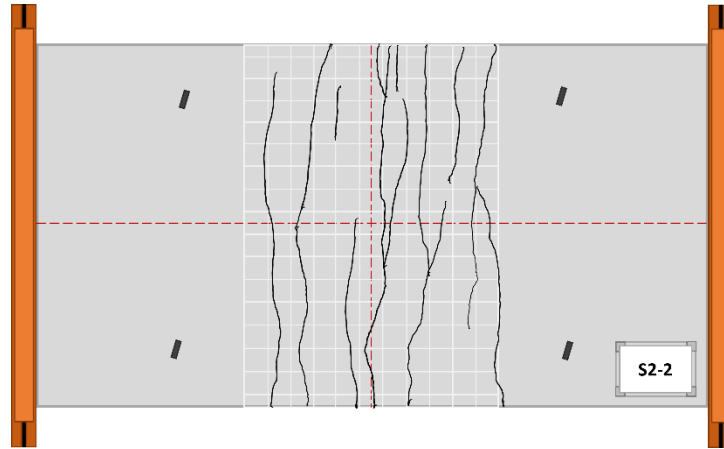
(c)

Figure 4.21 S2-1 specimen test results, (a) stabilized crack pattern, (b) measured critical crack width, and (c) load-displacement curve

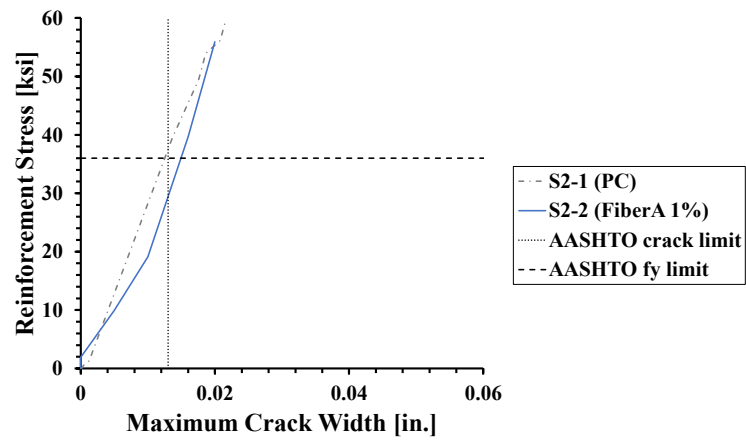
4.6.2.2. S2-2

The Fiber A 1% mix was used as a topping in Specimen S2-2. It had #4 bars every 18 in. for flexural rebars. Figure 4.22 (a), (b), (c), and (d) demonstrate the stabilized crack pattern, crack control ability by rebar stress and total load, and load-displacement curve, respectively. The results of this experiment are presented below.

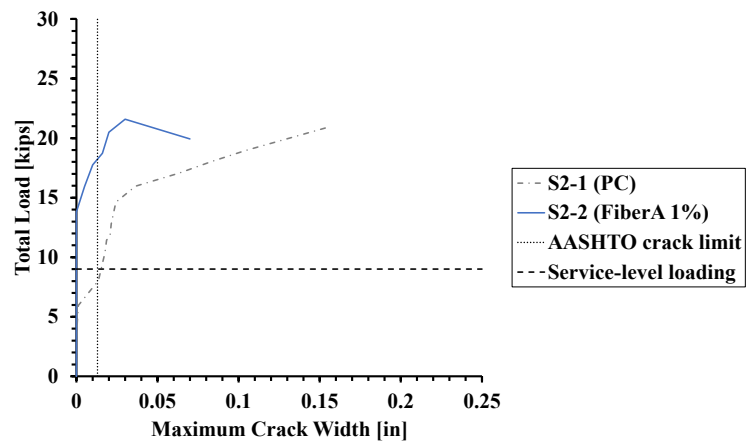
- The crack resistance of the S2-2 specimen exhibited a lower capacity when compared to the TxDOT capacity at the same reinforcement stress. As a result, a more detailed comparison of the crack-total load is provided.
- The critical cracks in the S2-2 sample exceeded the AASHTO crack limits at a load of 17.5 kips. This means that Fiber A 1% with half reinforcement outperformed the current TxDOT detail regarding crack resistance.
- According to the load-displacement curve, the specimen had higher stiffness and load capacity than the control specimen throughout the test.



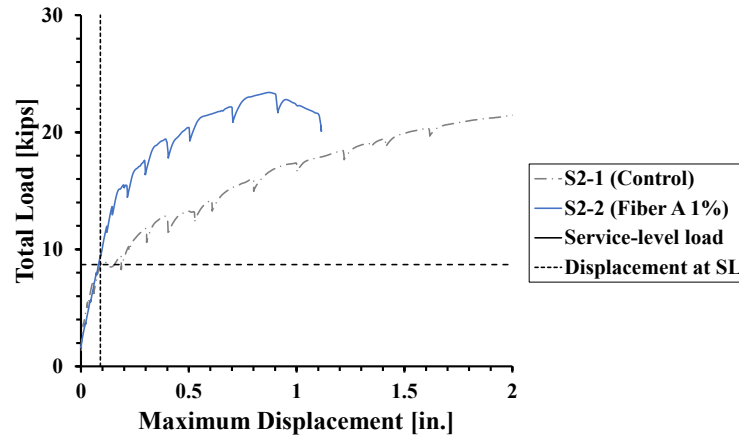
(a)



(b)



(c)



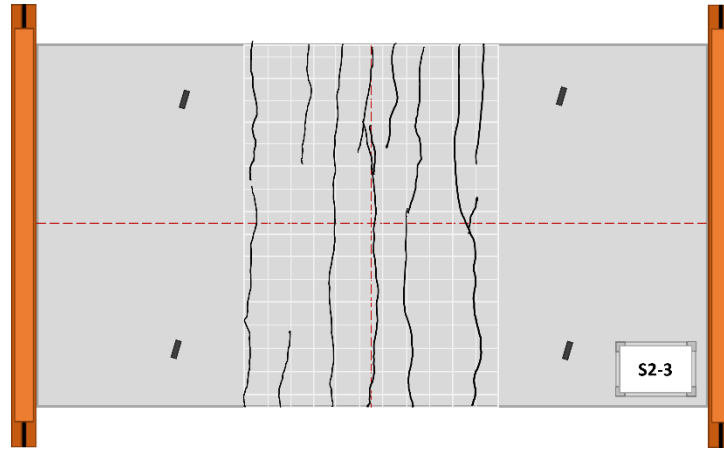
(d)

Figure 4.22 S2-2 specimen test results, (a) stabilized crack pattern, (b) measured critical crack width to rebar stress (c) measured critical crack width to total load, and (d) load-displacement curve

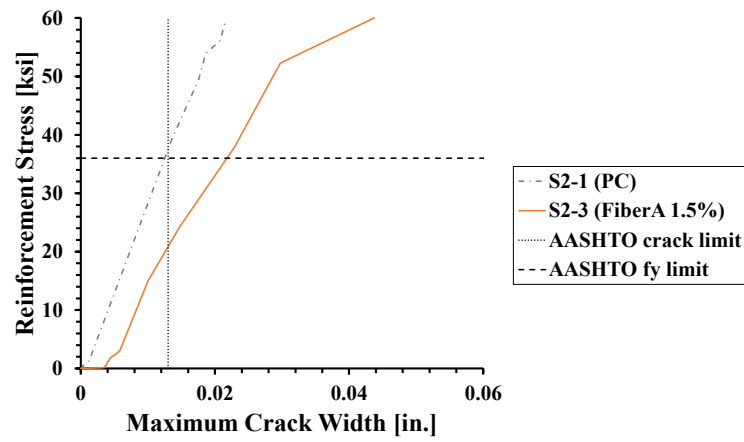
4.6.2.3. S2-3

Specimen S2-3 incorporated a topping with a 1.5% mix of Fiber A and featured #4 bars spaced at 18 inches for flexural reinforcement. Figure 4.23 (a), (b), (c), and (d) illustrate its stabilized crack pattern, crack control ability based on rebar stress and total load, and load-displacement curve, respectively. The findings of this experiment are detailed below.

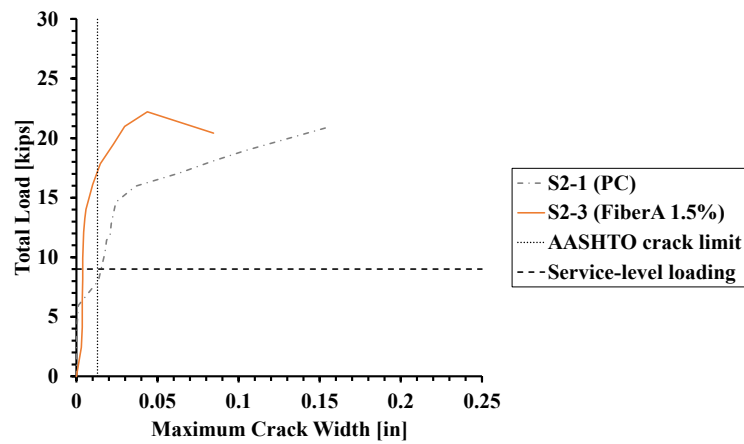
- The S2-3 specimen's crack resistance showed a reduced capacity in comparison to the TxDOT standard at an equivalent reinforcement stress. Therefore, a more in-depth comparison of the total load and crack behavior is presented.
- Critical cracks in the S2-3 specimen surpassed the AASHTO crack limits at a 19 kips load, indicating that Fiber A 1.5% with half reinforcement demonstrated higher crack resistance compared to the existing TxDOT detail.
- During the test, the specimen exhibited greater stiffness and load capacity compared to the control specimen.



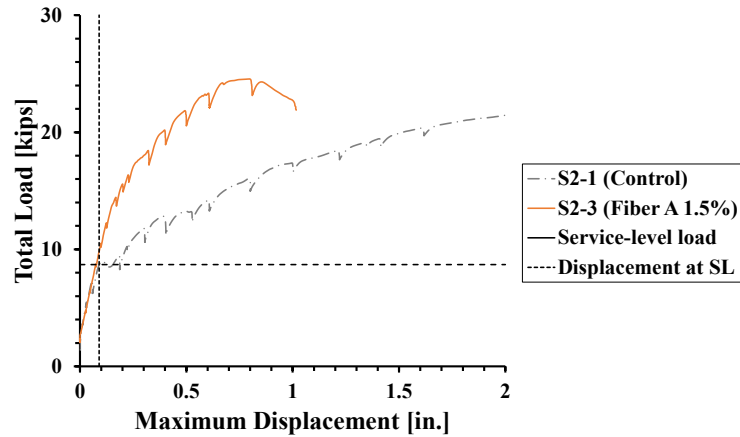
(a)



(b)



(c)



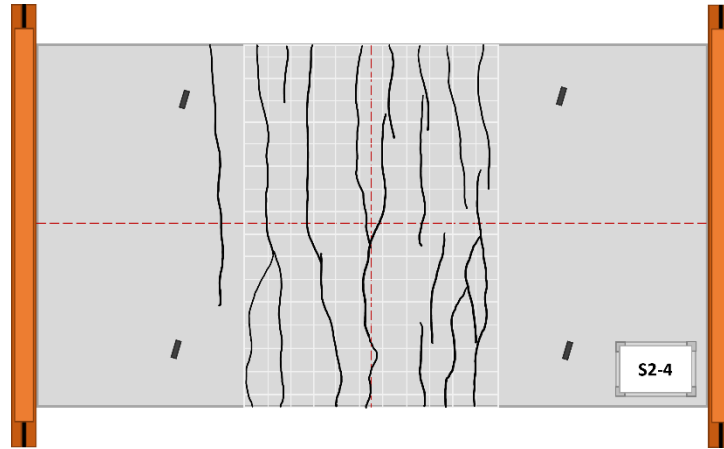
(d)

Figure 4.23 S2-3 specimen test results, (a) stabilized crack pattern, (b) measured critical crack width to rebar stress (c) measured critical crack width to total load, and (d) load-displacement curve

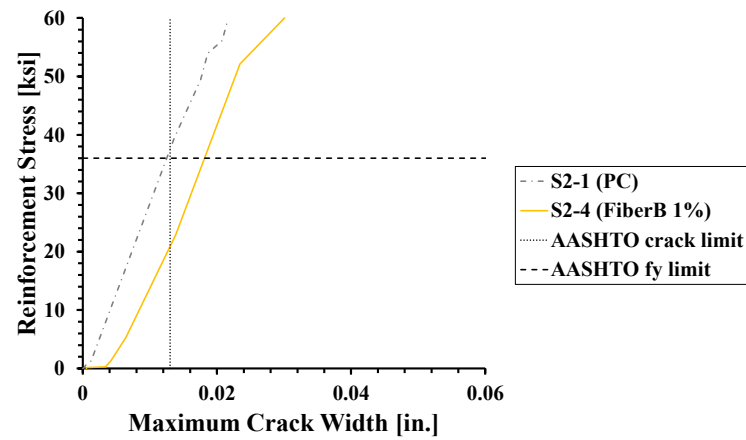
4.6.2.4. S2-4

Specimen S2-4 utilized a topping material with a 1% mix of Fiber B and included #4 bars spaced at 18 inches for flexural reinforcement. Figure 4.24 (a), (b), (c), and (d) depict its stabilized crack pattern, crack control effectiveness based on rebar stress and total load, and load-displacement curve, respectively. The results of this experiment are outlined below.

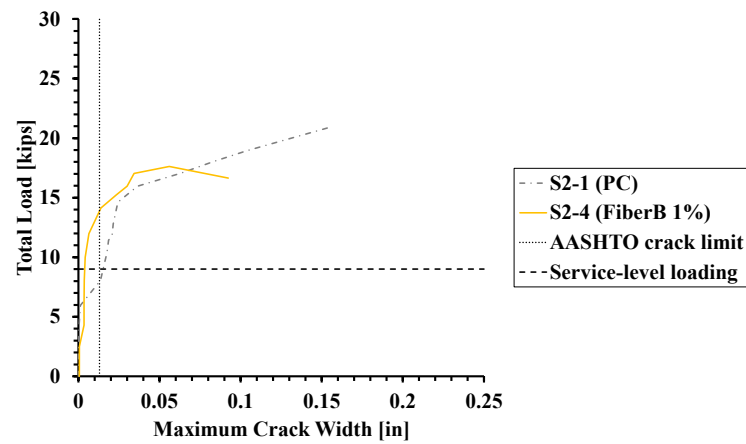
- The crack resistance of the S2-4 specimen exhibited lower capacity when compared to the TxDOT standard under equivalent reinforcement stress. As a result, a more thorough comparison of total load and crack behavior is provided.
- Critical cracks in the S2-4 specimen exceeded AASHTO crack limits at a 14 kips load, indicating that Fiber B 1% with half reinforcement displayed better crack resistance compared to the current TxDOT detail.
- Throughout the test, the specimen demonstrated higher stiffness and load capacity in comparison to the control specimen.



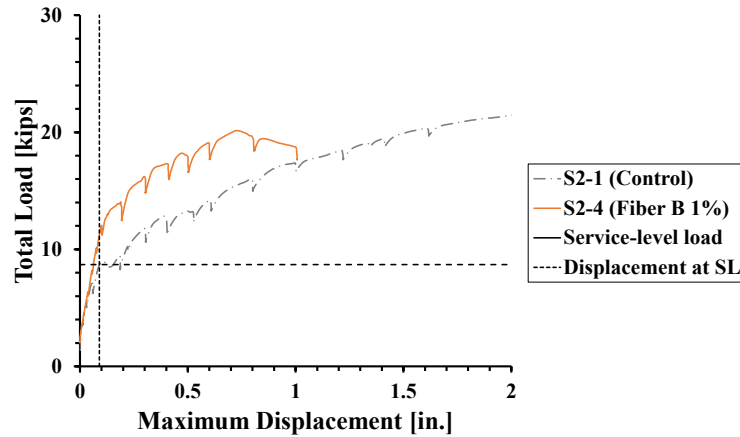
(a)



(b)



(c)



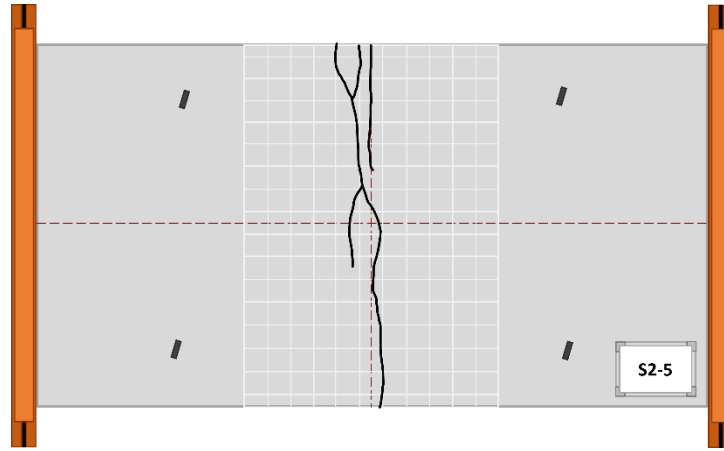
(d)

Figure 4.24 S2-4 specimen test results, (a) stabilized crack pattern, (b) measured critical crack width to rebar stress (c) measured critical crack width to total load, and (d) load-displacement curve

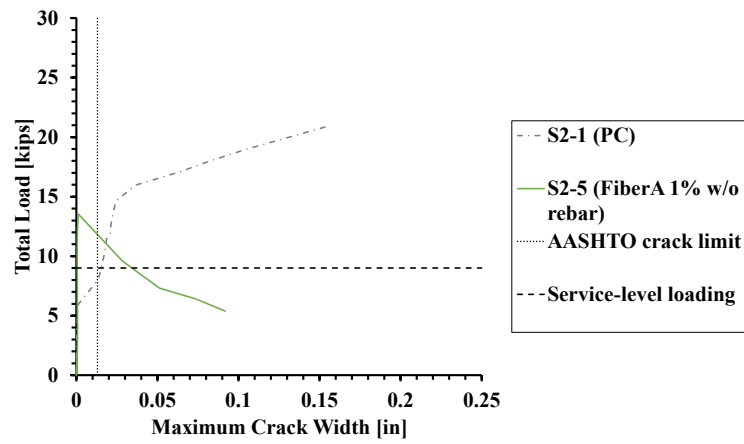
4.6.2.5. S2-5

Specimen S2-5 incorporated Fiber A 1% mix as a topping material. It contained no flexural reinforcement. Its stabilized crack pattern, crack control ability, and load-displacement curve are shown in Figure 4.25 (a), (b), and (c), respectively. The results of this experiment are listed below.

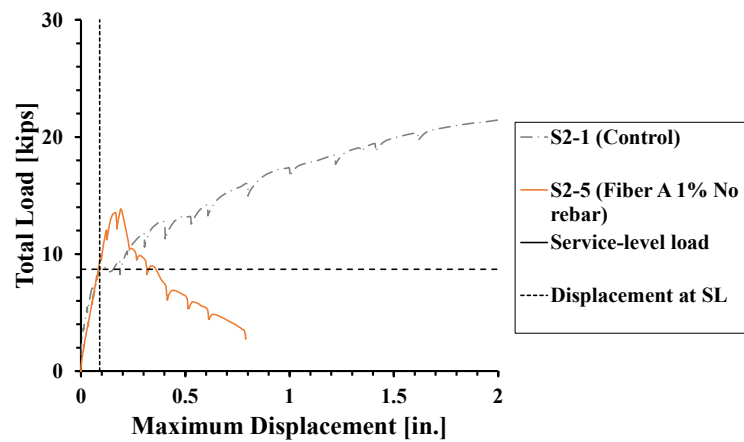
- Due to significant differences between measurements from the dog-bone-shaped concrete strain gauge and #4 rebars, the load-crack width graph was employed to assess the crack resistance of the specimen. At a load of 13.5 kips, the critical cracks in the S2-5 specimen surpass the AASHTO crack limits. This means that Fiber A 1% without reinforcement had higher crack resistance when compared to the current TxDOT detail until service level load.
- However, after 13.9 kips loading, the specimen developed a single critical crack on the constant moment region, which widened significantly.
- The specimen had higher stiffness and load capacity than the control specimen until the service-level load, according to the load-displacement curve. However, it lost stiffness at maximum capacity.



(a)



(b)



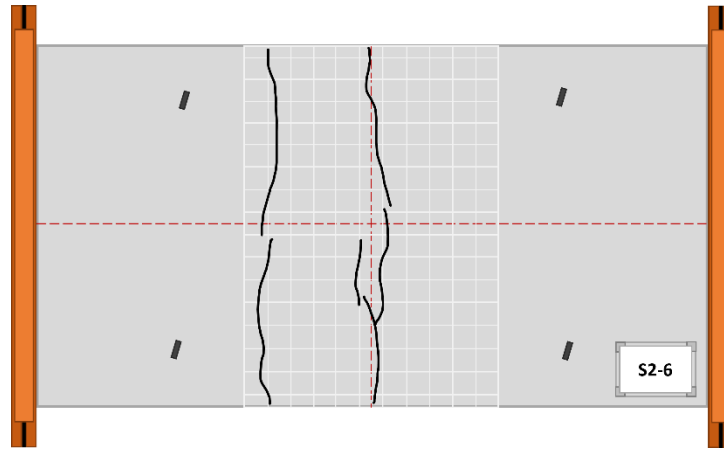
(c)

Figure 4.25 S2-5 specimen test results, (a) stabilized crack pattern, (b) measured critical crack width, and (c) load-displacement curve

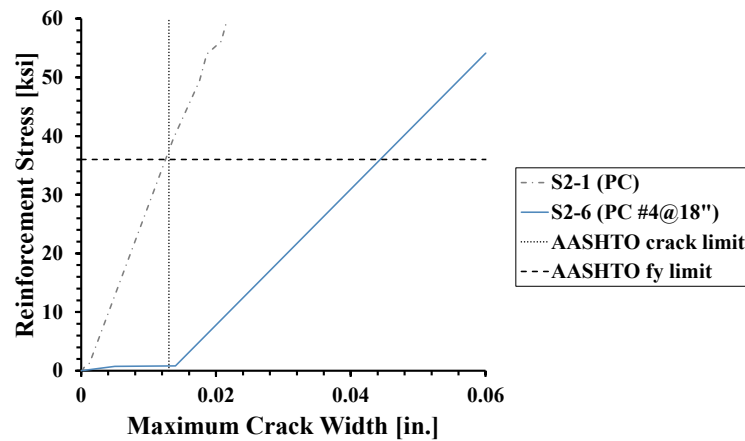
4.6.2.6. S2-6

In order further analyze the effect of SFRC in CIP-PCP bridge deck, specimen S2-6 which have #4 bars spaced at 18 inches casted with plain concrete was fabricated. Figure 4.26 (a), (b), (c), and (d) depict its stabilized crack pattern, crack control effectiveness based on rebar stress and total load, and load-displacement curve, respectively. The results of this experiment are summarized as below.

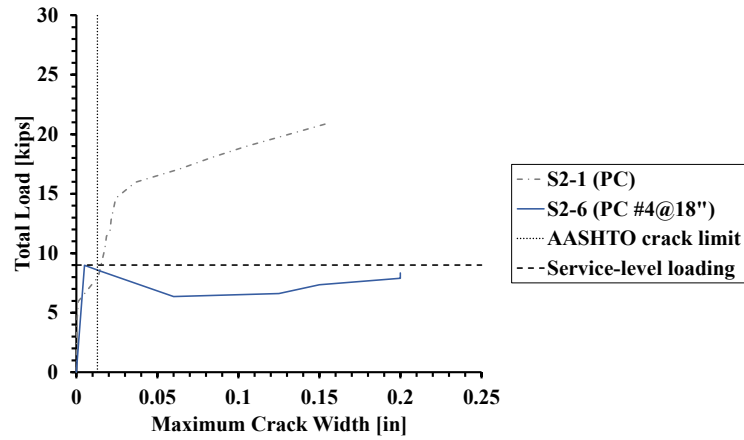
- The crack resistance of the S2-6 specimen demonstrated reduced capacity in comparison to the TxDOT standard at an equivalent reinforcement stress.
- The load-crack width and load-displacement curves show that the specimen has lower crack resistance and load-carrying capacity compared to control specimen.



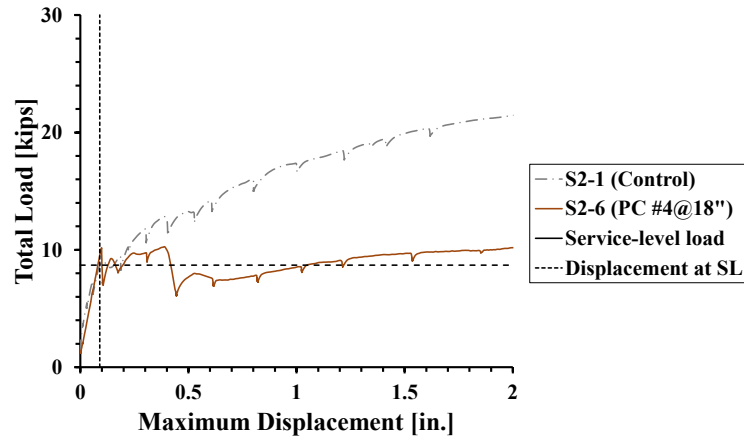
(a)



(b)



(c)



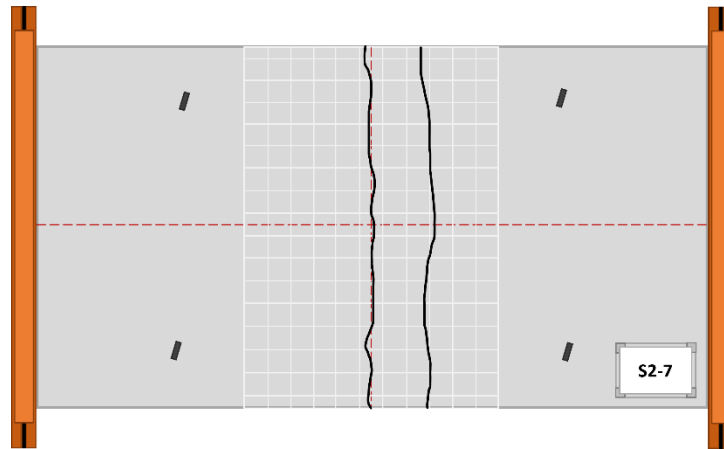
(d)

Figure 4.26 S2-6 specimen test results, (a) stabilized crack pattern, (b) measured critical crack width to rebar stress (c) measured critical crack width to total load, and (d) load-displacement curve

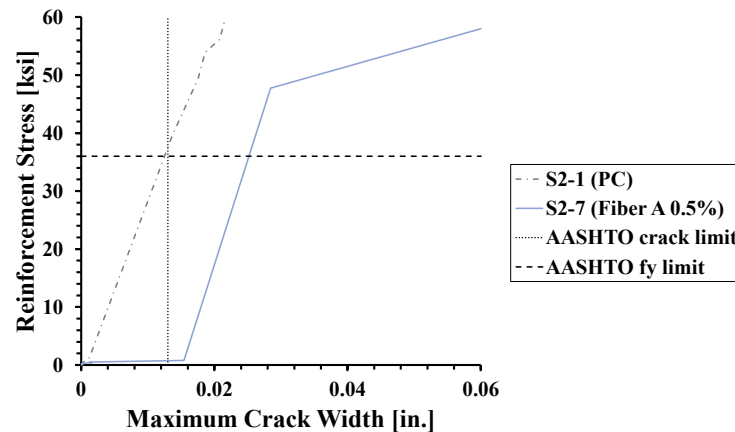
4.6.2.7. S2-7

Specimen S2-7 utilized a topping material with a 0.5% mix of Fiber A and included #4 bars spaced at 18 inches for flexural reinforcement. Figure 4.27 (a), (b), (c), and (d) depict its stabilized crack pattern, crack control effectiveness based on rebar stress and total load, and load-displacement curve, respectively. The results of this experiment are outlined below.

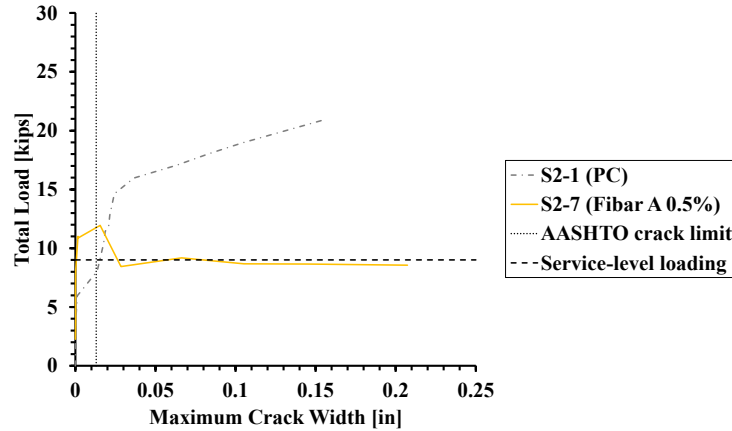
- The crack-stress graph shows that the specimen exhibits lower crack resistance compared to control specimen. On the other hand, the load-crack width graph demonstrates that the crack resistance of the specimen was higher than the control specimen until the service level load.
- The specimen had higher stiffness and load capacity than the control specimen until the service-level load, according to the load-displacement curve. However, it lost stiffness at maximum capacity.



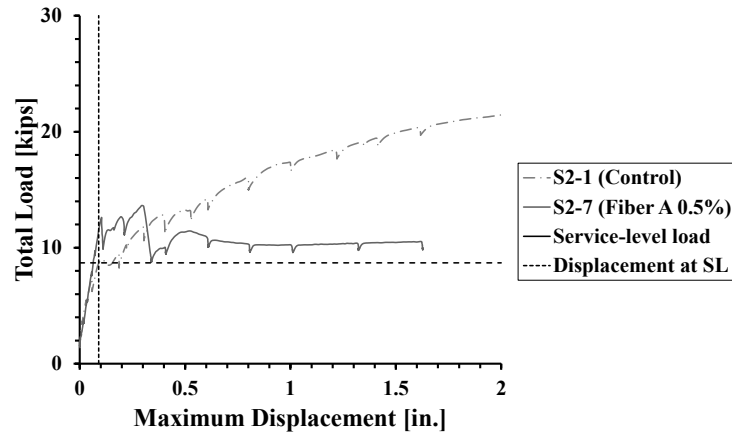
(a)



(b)



(c)



(d)

Figure 4.27 S2-7 specimen test results, (a) stabilized crack pattern, (b) measured critical crack width to rebar stress (c) measured critical crack width to total load, and (d) load-displacement curve

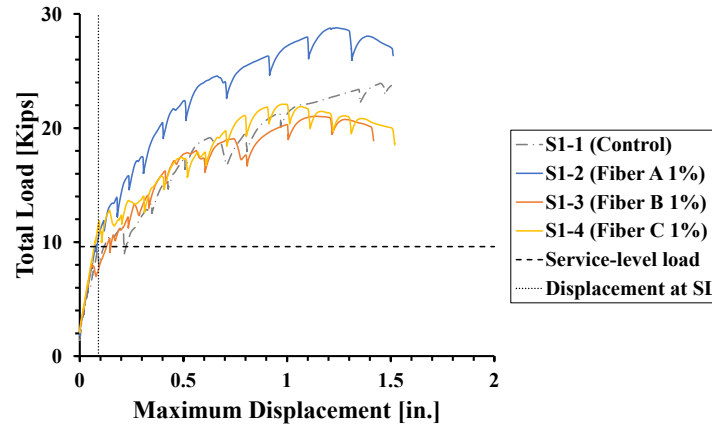
4.7. Test Result Analysis

This section summarizes significant findings from test results. The research team will first identify the best fiber type and dosage for the full-scale specimen. Second, the suitability of specimens without reinforcing steel will be considered.

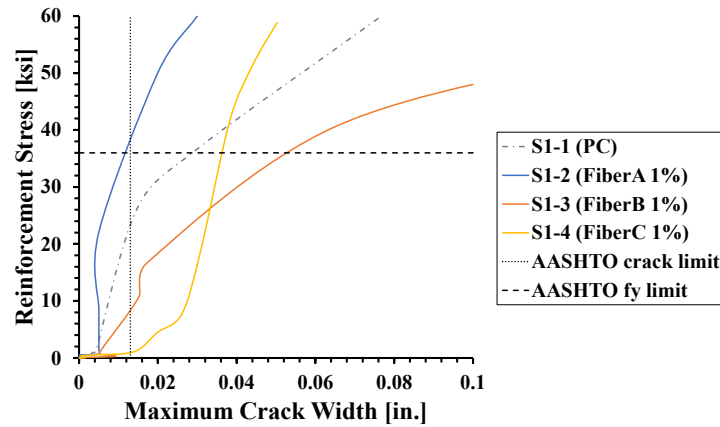
4.7.1. Effect of Fiber Types

Specimen S1-2, S1-3, and S1-4 used 1% SFRC mix having fiber A, B, and C, respectively. Figure 4.28 (a) and (b) show the load-displacement curve and critical crack width. The result shows that all three specimens showed higher or similar performances compared to TxDOT standard. In the material test, 1% Fiber C mix

showed better flexural performance than any other mixes (Figure 4.29). In structural testing, however, the specimen with Fiber A outperformed the Fiber C.



(a)



(b)

Figure 4.28 Fiber type effect: (a) load-displacement curve and (b) critical crack width to rebar stress

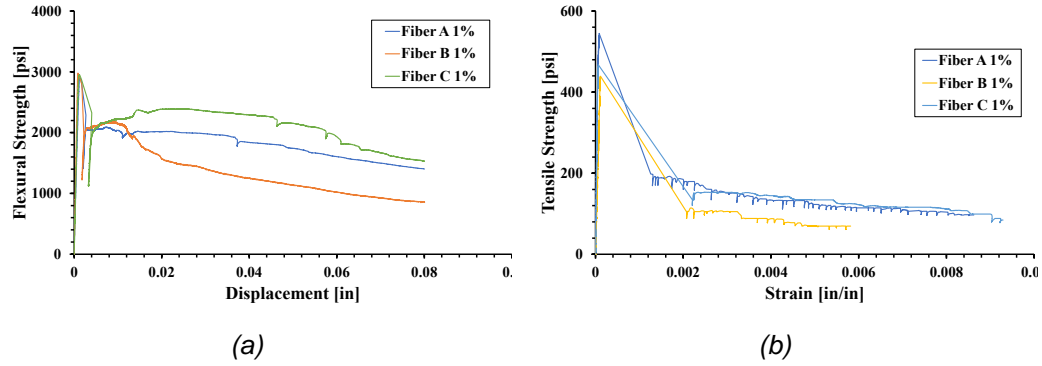
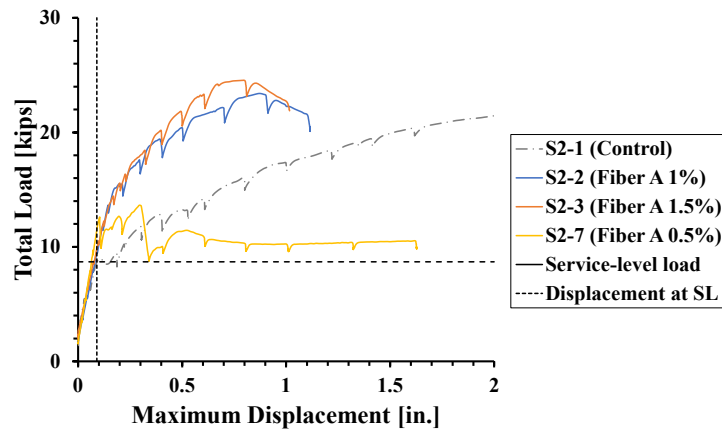


Figure 4.29 Comparison of different fiber types using (a) flexural beam test and (b) direct tension test

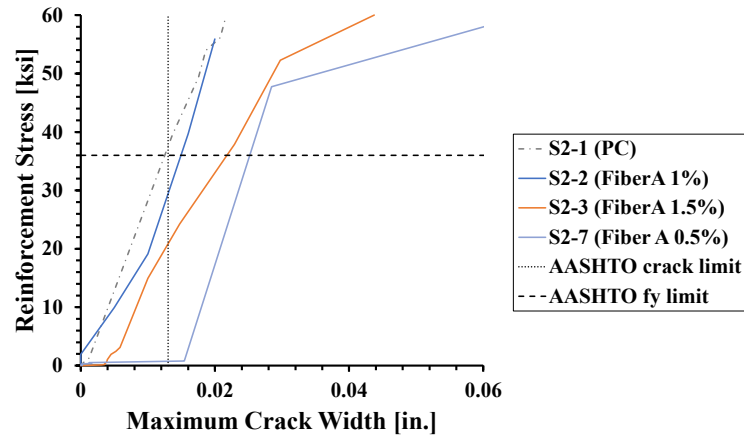
4.7.2. Effect of Fiber Dosage

Specimen S2-2, S2-3, and S2-7 incorporate Fiber A with different dosages, 0.5%, 1.0%, and 1.5%. (c)

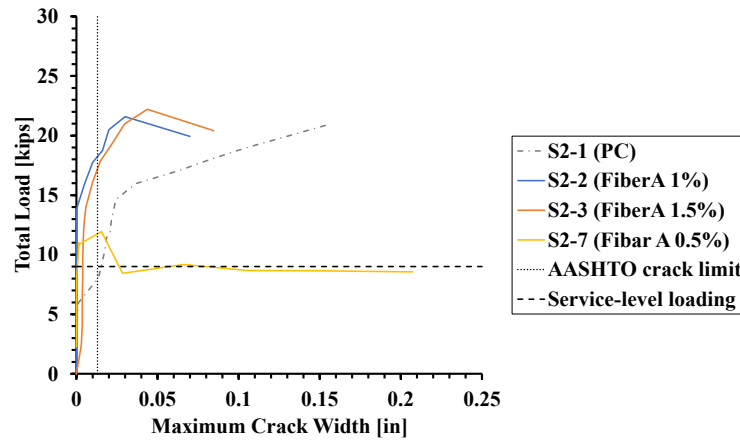
Figure 4.30 (a), (b), and (c) show the load-displacement curve and crack resistance by rebar stress and total load. The specimen containing 0.5% exhibited inferior load-carrying capacity and crack resistance when contrasted with other fiber dosages. When comparing dosages of 1% and 1.5%, it was observed that the specimen with a 1.5% dosage performed similarly to the one with a 1% dosage. Notably, the 1.5% dosage specimen displayed a 5% higher load capacity, although crack resistance remained comparable.



(a)



(b)



(c)

Figure 4.30 Fiber dosage effect: (a) load- displacement curve, (b) measured critical crack width to rebar stress, and (c) measured critical crack width to total load

4.7.3. Specimens without Reinforcement

According to sections 4.6.1.5 and 4.6.2.5, specimens lacking reinforcement exhibited the development of a singular critical crack within the constant moment region. Subsequently, this critical crack exhibited substantial widening once the specimen achieved a relatively low ultimate loading. Nevertheless, these critical cracks retained their size throughout service-level load conditions. Recognizing the divergence in load conditions between the deck strip specimens and the real bridge deck, the team resolved to include regions without reinforcement in order to investigate the feasibility of a zero-reinforced SFRC bridge deck.

4.8. Summary and Conclusions

This section summarizes the findings from the deck strip test. Twelve specimens, five longitudinal and seven transverse, were examined to estimate the crack resistance and load-carrying capacity. Eight conclusions were derived from the structural tests.

1. While steel fibers can be conveniently incorporated at the concrete plant, it is crucial to acknowledge that the workability of SFRC significantly decreases during delivery. To counter this, the addition of chemical mixtures that enhance workability without compromising strength becomes imperative.
2. Compared to the TxDOT standard design, which is plain concrete with 9 in. reinforcement spacing, 1% SFRC mix with reinforcement bars spaced at 18 in. demonstrated higher or comparable load-resisting performance.
3. Fiber C, which has a shorter length than other fibers, exhibits a tendency to clump together, forming problematic fiber balls. This issue can disrupt the concrete casting process when hydraulic pumps are employed. Hence, the prudent decision would be to refrain from using 1 inch twisted shape fiber.
4. A cross-section check revealed that SFRC, with both 1-inch and 1.5-inch fiber lengths, effectively filled a 1-inch gap between the panel and the simulated girder.
5. SFRC specimens without reinforcement could sustain their load-carrying capacity under service-level load conditions. Nevertheless, relying solely on steel fibers proved ineffective in preventing crack enlargement during more extensive loading. To address the disparity between the loading conditions of deck strip specimens and actual bridge decks, the research team incorporated the zero-reinforced SFRC bridge deck into the full-scale test matrix.
6. When comparing the S2-2 and S2-3 specimens, it was observed that a fiber dosage exceeding 1% did not lead to a noticeable increase in load capacity, stiffness, or crack-resistance capacity.
7. The test results for S2-7 indicate that a fiber dosage below 1% is inadequate for replacing the reinforcement of a bridge deck.
8. During the material test, the 1% Fiber C mix exhibited superior flexural performance compared to all other mixes. Surprisingly, in structural testing, Fiber A outperformed Fiber C. This unexpected outcome may be attributed

to the size difference between Fiber C, which is shorter than Fiber A, suggesting a potential size effect.

Chapter 5. Numerical Analysis of Structure

5.1. Overview

This chapter presents summaries of the analyses conducted on the SFRC deck strip tests introduced in Chapter 4. Additionally, we explore various analyses to expand upon the conclusions from the initial experimental program. This supplementary exploration contributes to a deeper and broader understanding of the SFRC deck strip tests, providing a more comprehensive perspective on SFRC as a CIP-PCP topping material.

5.2. Initial Model Assessment

The initial model assessment phase was completed by analyzing a series of SFRC slab specimens tested by Birely et al. (2018). The analyzed specimens were tested in 4-point bending, as shown in Figure 5.1. They had cross-sectional dimensions of 18 x 7.5 in. and had a fiber content of 0.5% by volume. The flexural reinforcement was varied in each specimen, which is indicated by the name (e.g., s7505BTM25 had two No. 5 located near the bottom of the section, and s7505CTR35 had three No. 5 located at the center of the cross-section). Curve-fits of the measured tension and compression stress-strain responses (Figure 5.2) were used in the analyses. The tension stress-strain response was based on direct tension results. Several possibilities were explored, and this method was determined to be the most accurate for this setup of analyses. The concrete damaged plasticity model was used to model concrete regions. The concrete damaged plasticity model is based on a yield surface that assumes failure in concrete is governed by cracking (tension) and crushing (compression). The yield surface is controlled by equivalent plastic strains that are defined by the nonlinear, uniaxial material behaviors (Figure 5.2) and the failure mode. More detailed background information is available elsewhere (Dassault Systems Simulia Corp., 2018). Reinforcement was assumed to behave as an elastic-perfectly-plastic material for all analyses presented in this technical memorandum.

Initially, a three-dimensional, one-quarter slab model was developed, which is shown in Figure 5.3. This model was analyzed in a quasi-static manner using the Abaqus/Explicit solver. In quasi-static analyses, the displacement is applied dynamically at a relatively low velocity. Typically, this is done to reduce convergence problems, but it comes at the expense of additional computation time and complexity. It was also found for these specimens that mass-scaling was required to enable reasonable solution times. Mass-scaling artificially alters the specimen's mass during the analysis to reduce the solution time. The three-

dimensional, quasi-static analyses were compared to two-dimensional, static analyses. Ultimately, the differences in the results were minor (on the order of a few percent), but the analysis time was reduced by one to two orders of magnitude. Therefore, two-dimensional plane stress models were used for the analyses in report. Typical examples of plane stress models are shown in Section 5.3. 8-node biquadratic quadrilateral elements (CPS8) were used for concrete regions, and 2-node linear truss elements (T2D2) were used to model the reinforcement.

In addition to the constitutive relations summarized in Figure 5.2, there were several other concrete material parameters that were calibrated as a part of this Task. They are as follows: the Poisson's ratio, ν (taken as a constant 0.15), the material dilation angle of the plastic potential function, ψ (taken as 40 degrees), the yield surface shape factor, K_c (taken as 0.667, which corresponds to the Rankine criterion (1857)), the ratio of initial equibiaxial compressive yield stress to initial uniaxial compressive yield stress, σ_{b0}/σ_{c0} (taken as 1.16), the flow potential eccentricity, ε (taken as 0.1), and the viscosity parameter, μ (taken as 0.00001). Note that default analysis values were selected for K_c , σ_{b0}/σ_{c0} , and ε . The Poisson's ratio played virtually no role in the analysis results. AASHTO LRFD (2020) recommends a value of 0.2 for uncracked concrete and 0.0 for cracked concrete. The *fib* Model Code (2013) notes that the ratio ranges from 0.14 to 0.26. Ultimately, its selection was somewhat arbitrary over this range, given the limited role it played in the analyses presented in this report. Researchers (Wu et al., 2006; Voyiadjis and Taqieddin, 2009) have recommended a range of 0.2 to 0.3 for the dilatancy parameter in the plastic potential function, which corresponds to a range of 31 to 42 degrees for the dilatation angle. A variety of angles were explored in this study, and 40 degrees was found to provide the best results for the SFRC specimens analyzed in this technical memorandum. The viscosity parameter controls the visco-plastic regularization of the concrete. A value of 0.00001 was found to improve convergence without meaningfully impacting solution accuracy for the specimens discussed in project.

A comparison of the measured and computed load-deflection responses is shown in Figure 5.4. Overall, the load-deflection responses were well predicted by the model. The average tested-to-estimated capacity ratio was 1.02 with a standard deviation equal to 0.09 and a coefficient of variation equal to 0.09. The overall shapes of the load-deflection curves were also well predicted. Therefore, the assumptions and modeling decisions summarized in this initial model phase were used consistently throughout the slab strip and numerical assessment phases.

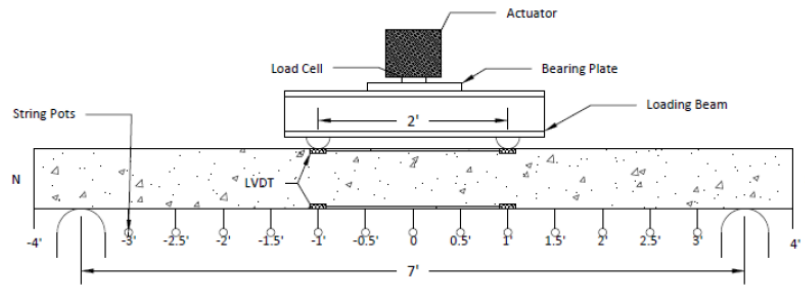
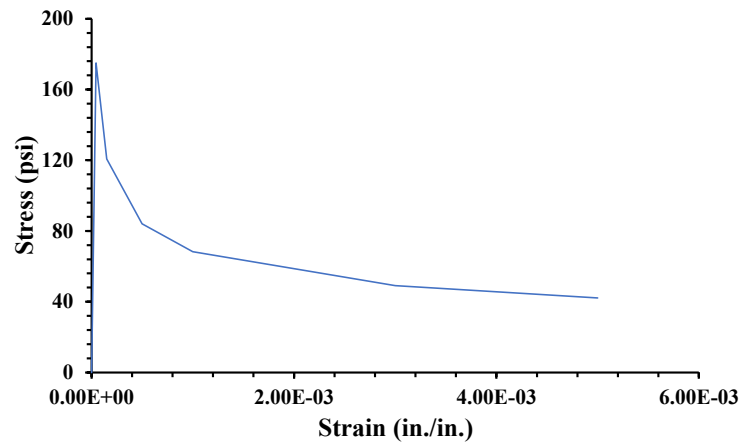
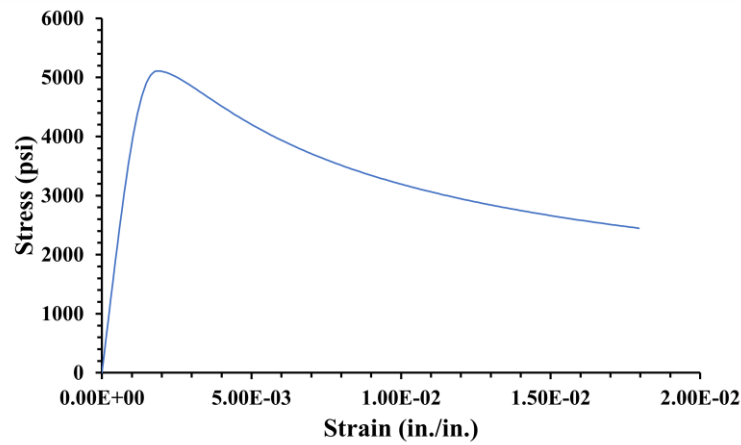


Figure 5.1 Test setup for specimens tested by Birely et al. (2018)



(a) Tension stress-strain curve



(b) Compression stress-strain curve

Figure 5.2 Constitutive models for specimens tested by Birely et al. (2018)

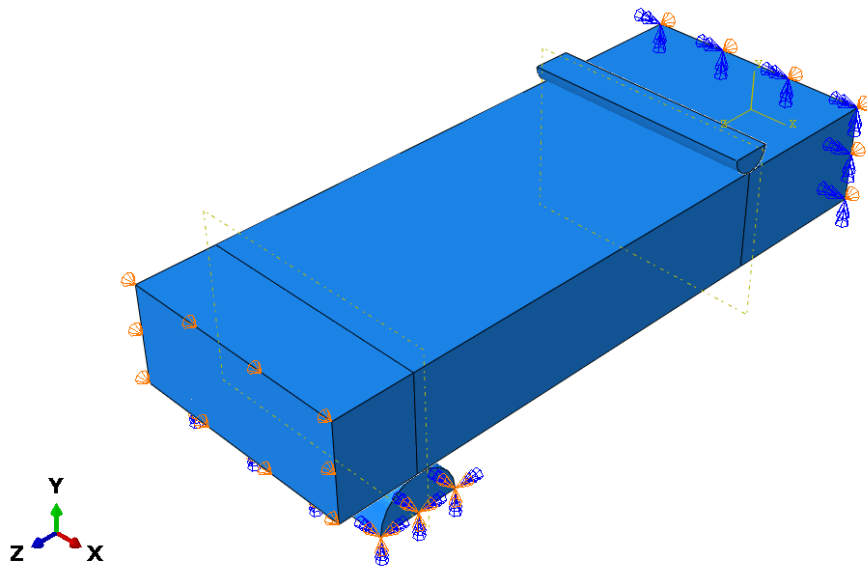
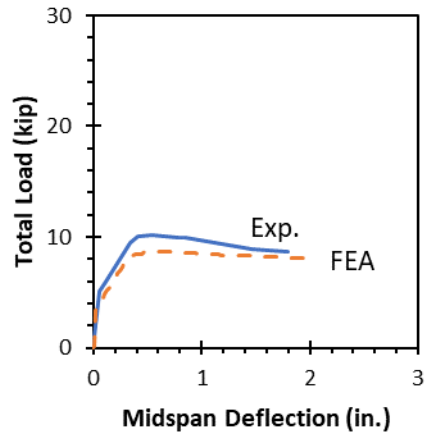
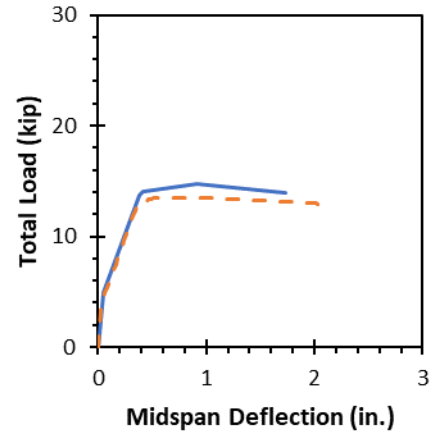


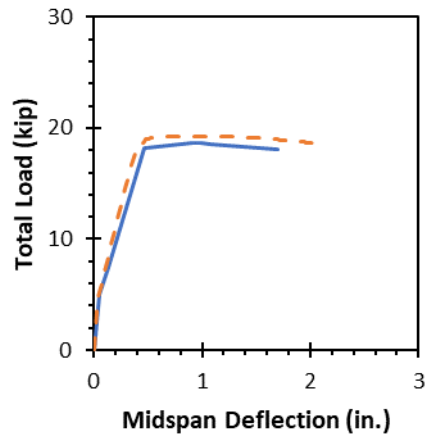
Figure 5.3 Preliminary quarter-symmetry model for specimens tested by Birely et al. (2018)



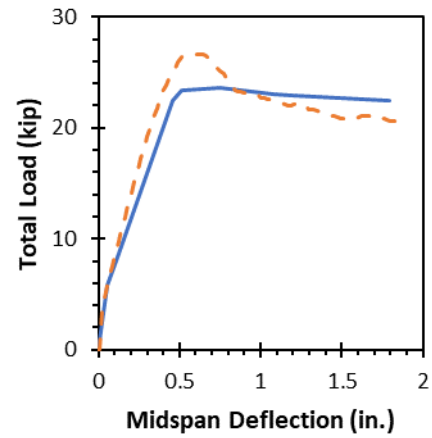
(a) s7505BTM23



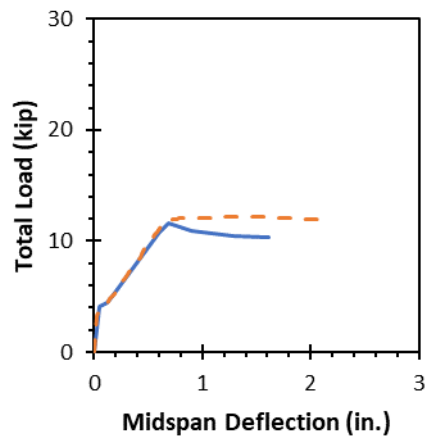
(b) s7505BTM24



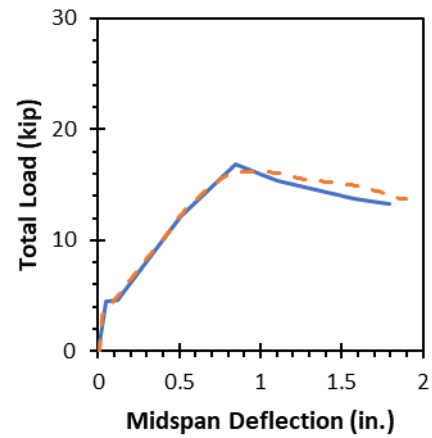
(c) s7505BTM25



(d) s7505BTM35



(e) s7505CTR25



(f) s7505CTR35

Figure 5.4 Nonlinear finite element analysis comparison for specimens tested by Birely et al. (2018)

5.3. Analysis of SFRC Slab Strips

This section summarizes the analysis results for the SFRC slab strips that are being tested.

5.3.1. Series 1

A representative model for the Series 1 specimens is shown in Figure 5.5. A summary of the reinforcement details and fiber content is shown in Table 5.1. Symmetry was considered about the beam midspan. The reinforcement and prestressing strands were perfectly bonded to the surrounding concrete. The interface between the cast-in-place and precast concrete was modeled with a linear-elastic cohesive relationship; however, this was compared with a perfect bond condition, and the results were found to be essentially the same. Thus, it can be stated that the interface between the cast-in-place and precast concrete is not critical to the slab strip flexural behavior if the surface is properly treated prior to casting. Self-weight was modeled as a body force acting on the concrete region, and the concentrated load was applied in displacement control. Popovic's (1973) model was used with the measured compressive strength and modulus of elasticity to estimate the compression response of all concrete regions. Popovic's model was chosen for its accurate representation of low-strength concrete behavior, particularly for concrete with strengths below 8 ksi (Ahmad et al., 2015). The beneficial effects of fibers on post-peak compression response were thus neglected. However, this is of no practical concern in the context of the slab strip analyses because their peak capacity was primarily limited by the yielding of the reinforcement and the residual tension strength of the SFRC. The tension stress-strain response was selected based on the direct tension tests that accompanied each specimen, as shown in Figure 5.6. The cracking load was limited to $4\sqrt{f'_c}$ (input units of psi), and a representative post-cracking residual stress was selected. Ultimately, these simplifications were found to provide drastically improved predictions for the slab strip behavior. Note that only a limited number of direct tension tests were performed for each mix. As a result, it was challenging to determine a simplified tension stress-strain curve that provided adequate predictions of specimen behavior.

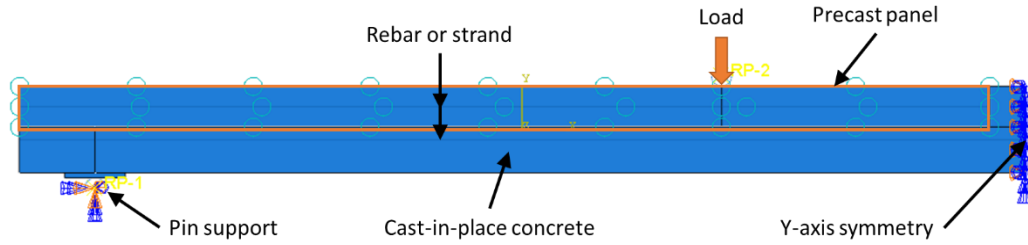


Figure 5.5 Representative Abaqus model for Series 1 specimens

Table 5.1 Summary of Series 1 reinforcement details

| | S 1-1 | S 1-2 | S 1-3 | S 1-4 | S 1-5 |
|---------------|---------|-----------|-----------|-----------|-----------|
| Concrete type | Plain | FiberA 1% | FiberB 1% | FiberC 1% | FiberA 1% |
| Transverse | #4 @ 9" | #4 @ 18" | #4 @ 18" | #4 @ 18" | None |
| Longitudinal | #4 @ 9" | #4 @ 9" | #4 @ 9" | #4 @ 9" | #4 @ 9" |

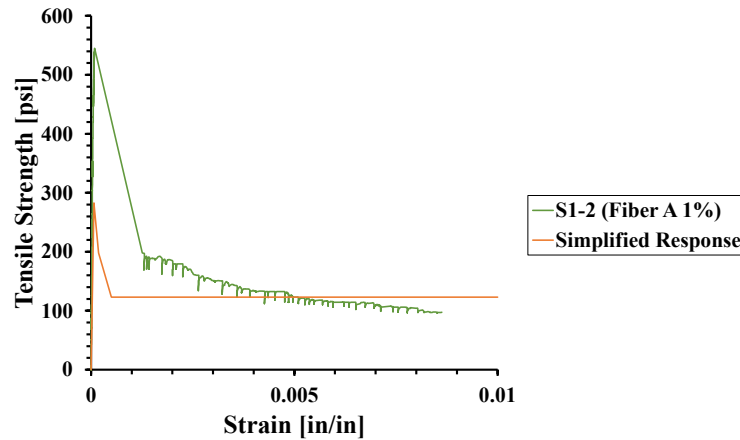


Figure 5.6 Typical tension stress-strain response

An overview of the peak loads from the analyses is summarized in Table 5.2. Typically, the capacities were well predicted. One thing to note is that S1-5 was designed with three No. 3 bars, which is included in actual structure to measure strain using strain gauge. The following sections provide a summary of the analysis results for each Series 1 specimen.

Table 5.2 Overview of Series 1 specimen capacity predictions

| Specimen | Exp. load (kip) | Est. load (kip) | Exp./Est. |
|----------|-----------------|-----------------|-----------|
| S1-1 | 23.7 | 22.4 | 1.06 |
| S1-2 | 27.0 | 28.0 | 0.96 |
| S1-3 | 18.9 | 19.0 | 0.99 |
| S1-4 | 20.0 | 18.8 | 1.06 |
| S1-5 | 14.3 | 13.8 | 1.04 |
| | | Avg. | 1.02 |
| | | Std. Dev. | 0.04 |
| | | CoV | 0.04 |

5.3.1.1. S1-1

Specimen S1-1 was the control specimen for Series 1. It contained No. 4 at 9 in. for flexural reinforcement. For the cast-in-place concrete, the compression strength was 6330 psi, and the modulus of elasticity was 4,300,000 psi. For the precast concrete, the compression strength was 9560 psi, and the modulus of elasticity was 5,100,000 psi. Figure 5.7 shows that the load-deflection response was well predicted. Figure 5.8 shows the crack pattern at approximately 40% of ultimate, which represents service-level loading conditions, and Figure 5.9 shows the stabilized crack pattern that is the final crack pattern when no new cracks form and existing cracks widen until failure occurs. For the simulated response, the crack pattern is represented by the localization of plastic tensile strains, which are shown in lighter colors than the rest of the mesh. In both cases, the simulated response exhibits more cracking than the observed one, but the general crack locations are similar.

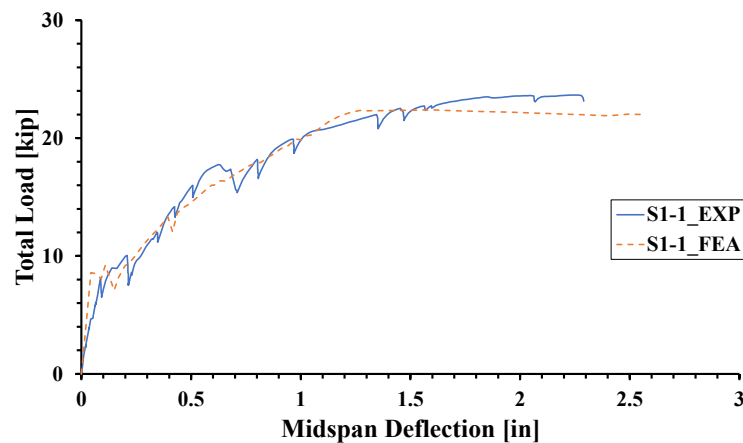
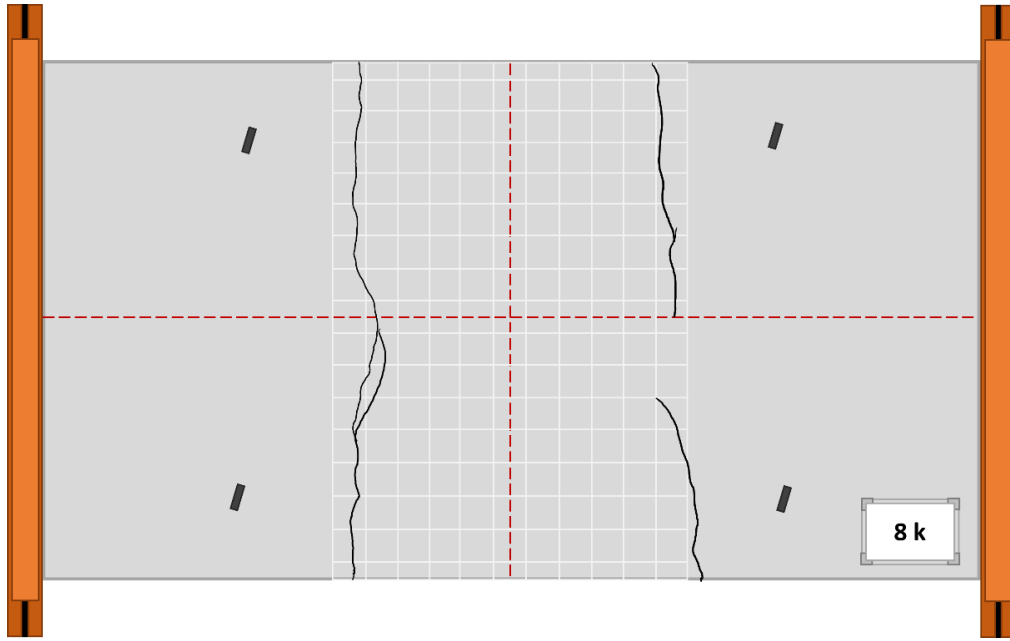
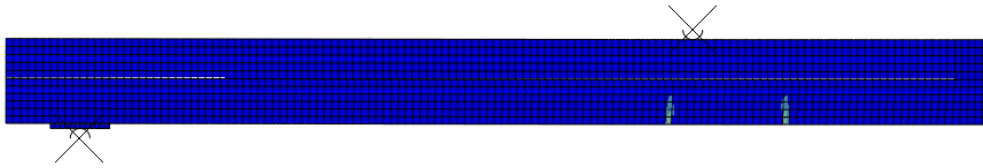


Figure 5.7 Load-deflection comparison for S1-1



(a) Observed crack pattern



(b) Simulated crack pattern

Figure 5.8 Crack pattern for S1-1 at $P = 8$ kip

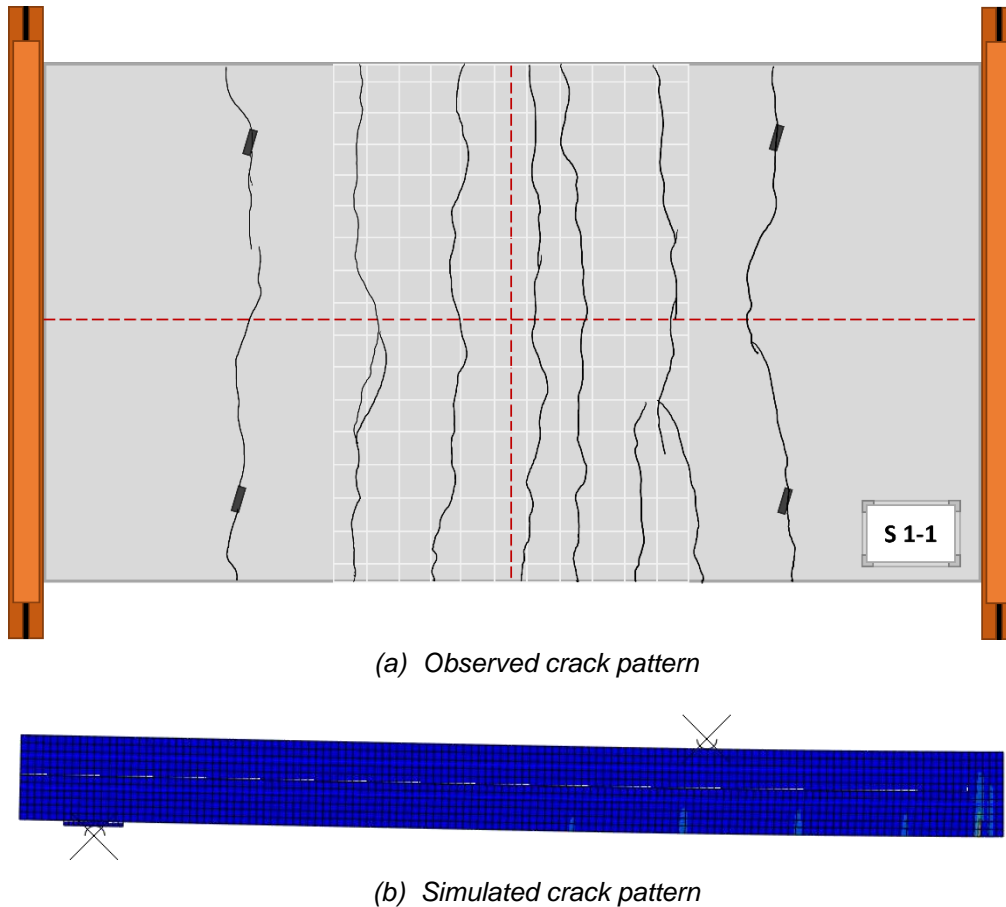


Figure 5.9 Stabilized crack pattern for S1-1

5.3.1.2. S1-2

Specimen S1-2 contained 1% hooked-end fiber by volume. It contained No. 4 at 18 in. for flexural reinforcement. For the cast-in-place concrete, the compression strength was 6200 psi, and the modulus of elasticity was 4,300,000 psi. For the precast concrete, the compression strength was 11,310 psi, and the modulus of elasticity was 5,550,000 psi. Figure 5.10 shows that the load-deflection response was well predicted; however, the initial stiffness was somewhat overpredicted. Figure 5.11 shows the crack pattern at approximately 40% of ultimate, which represents service-level loading conditions, and Figure 5.12 shows the stabilized crack pattern. For the simulated response, the crack pattern is represented by the localization of plastic tensile strains, which are shown in lighter colors than the rest of the mesh. As before, the simulated response exhibits more cracking than the observed one, but the general crack locations are similar. A comparison of Figure 5.9 and Figure 5.12 shows that the analysis model successfully captured the effect of the fibers on concrete cracking behavior. S1-2 has more cracks that are closely

spaced together compared to S1-1. Typically, this results in more uniform, small crack widths.

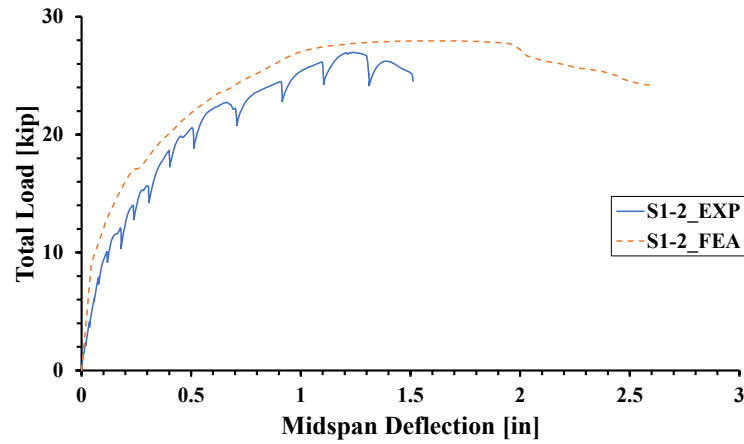
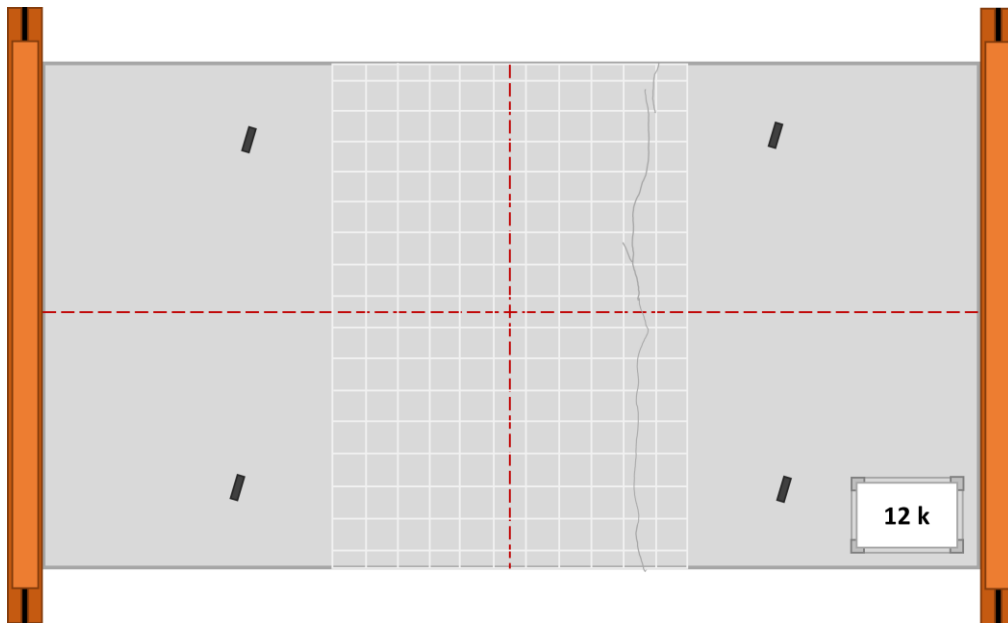
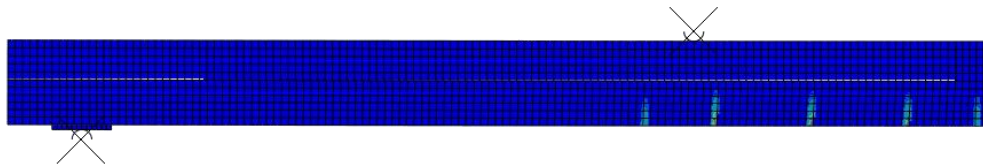


Figure 5.10 Load-deflection comparison for S1-2



(a) Observed crack pattern



(b) Simulated crack pattern

Figure 5.11 Crack pattern for S1-2 at $P = 12$ kip

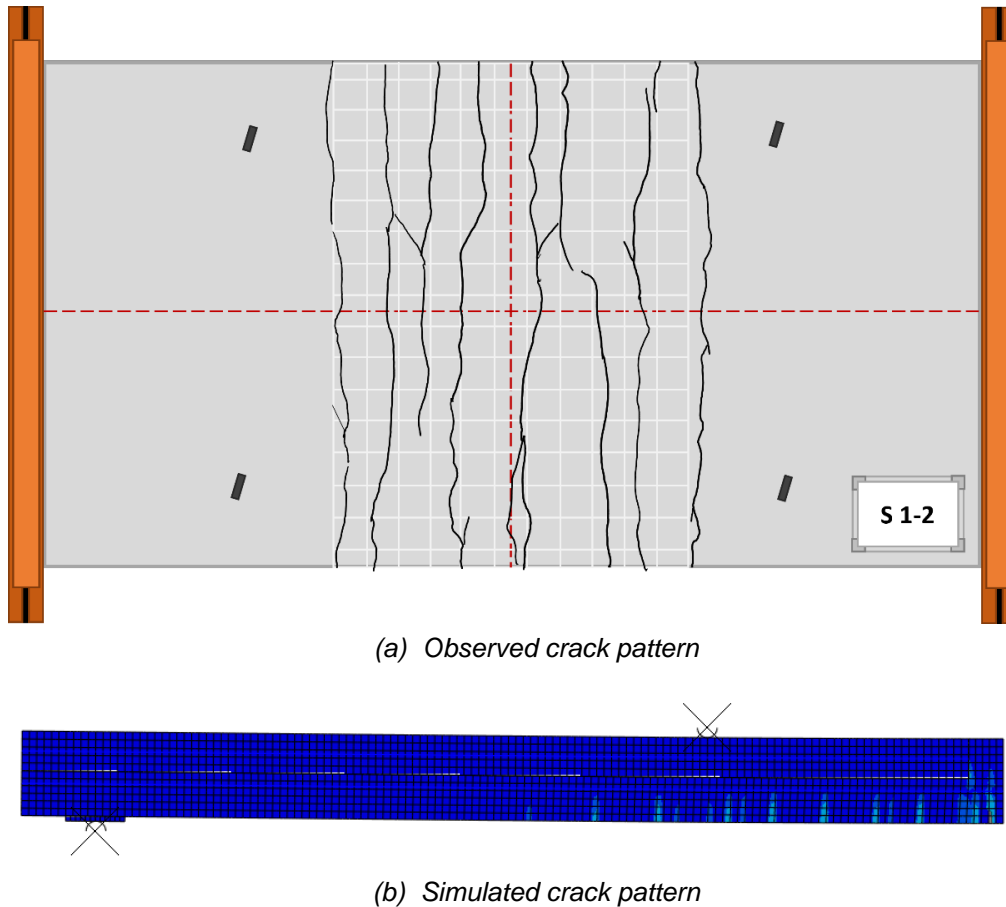


Figure 5.12 Stabilized crack pattern for S1-2

5.3.1.3. S1-3

Specimen S1-3 also contained 1% fiber by volume, but they were crimped instead of hooked-end. It also contained No. 4 at 18 in. for flexural reinforcement. For the cast-in-place concrete, the compression strength was 5340 psi, and the modulus of elasticity was 3,800,000 psi. For the precast concrete, the compression strength was 11,360 psi, and the modulus of elasticity was 5,750,000 psi. Figure 5.13 shows that the load-deflection response was well predicted. Figure 5.14 shows the crack pattern at approximately 40% of ultimate, which represents service-level loading conditions, and Figure 5.15 shows the stabilized crack pattern. For the simulated response, the crack pattern is represented by the localization of plastic tensile strains, which are shown in lighter colors than the rest of the mesh. As before, the simulated response exhibits more cracking than the observed one, but the general crack locations are similar. As was the case for S1-2, the analysis model successfully captured the effect of the fibers on concrete cracking behavior. S1-3 has more cracks that are closely spaced together compared to S1-1. Typically, this results in more uniform, small crack widths.

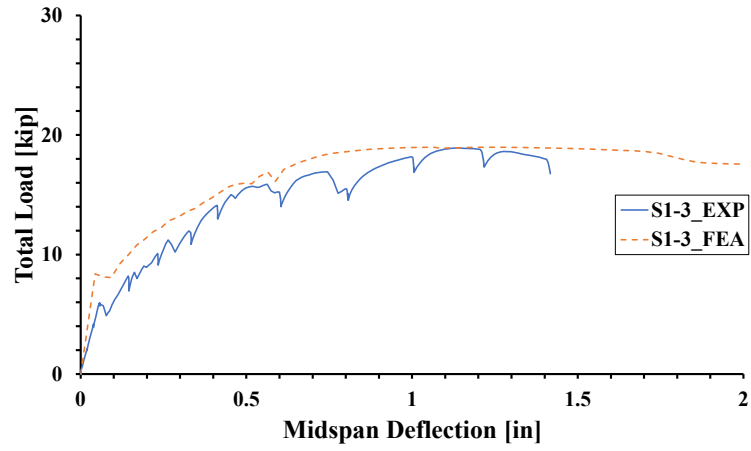
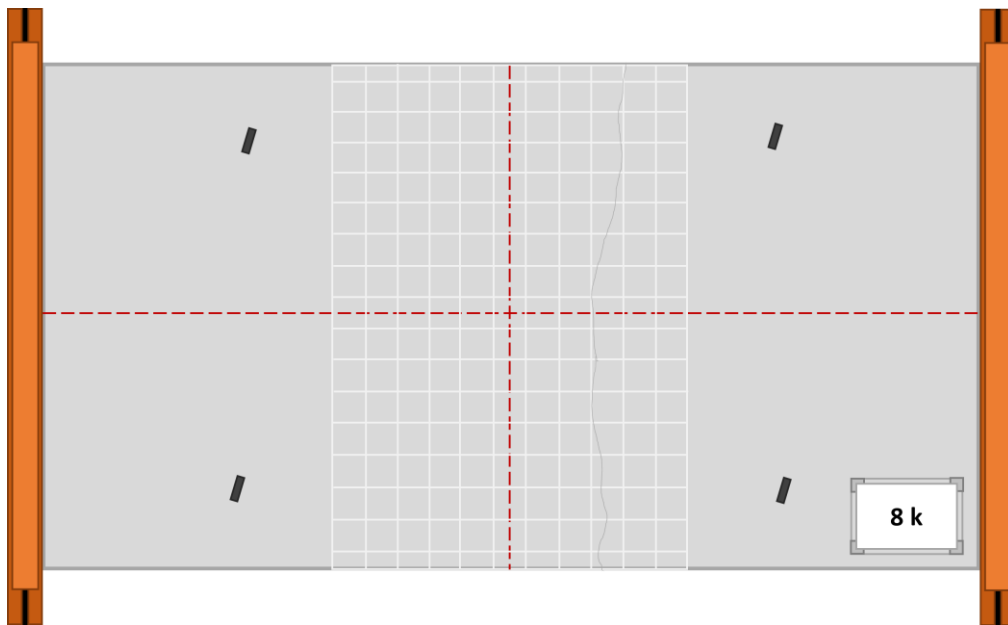
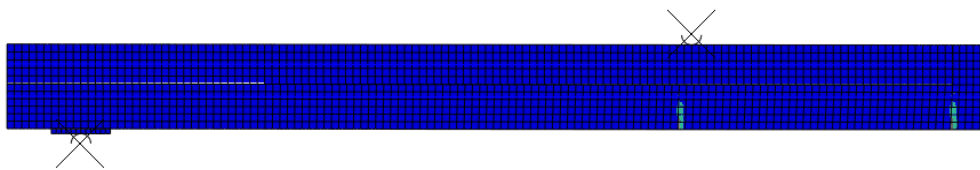


Figure 5.13 Load-deflection comparison for S1-3



(a) Observed crack pattern



(b) Simulated crack pattern

Figure 5.14 Crack pattern for S1-3 at $P = 8$ kip

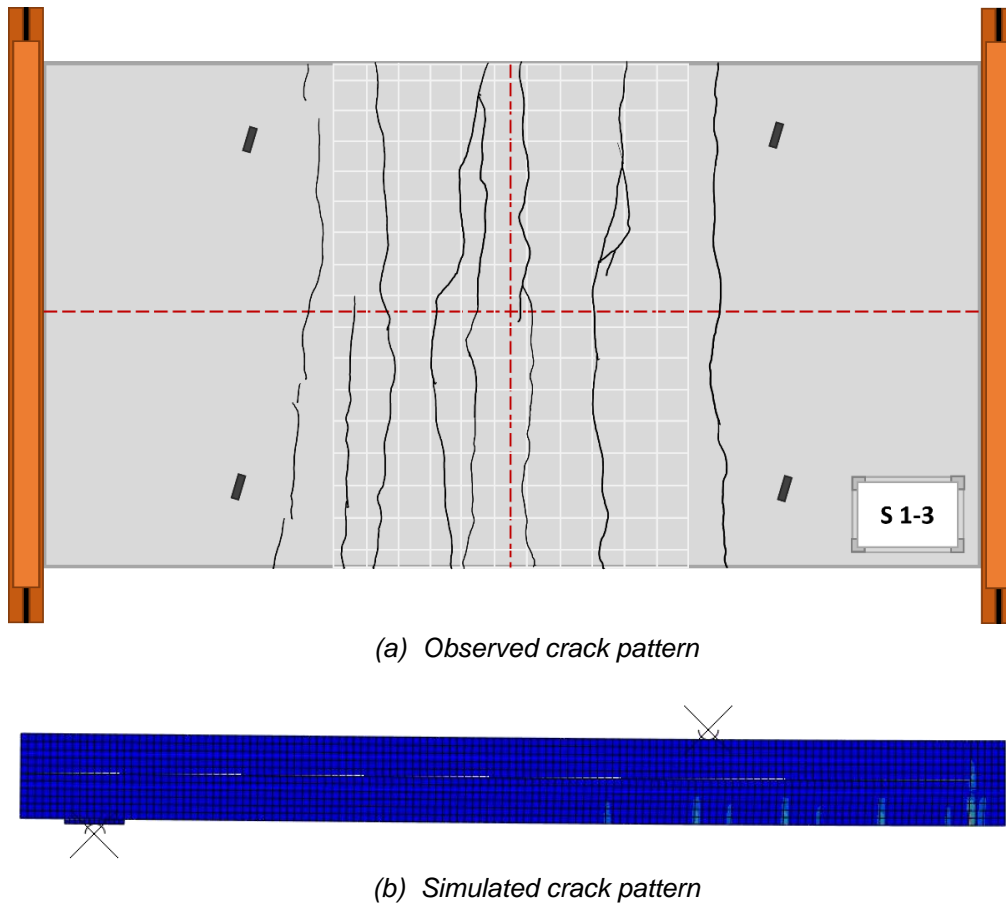


Figure 5.15 Stabilized crack pattern for S1-3

5.3.1.4. S1-4

Specimen S1-4 also contained 1% fiber by volume, but they were twisted type fibers. It also contained No. 4 at 18 in. for flexural reinforcement. For the cast-in-place concrete, the compression strength was 5700 psi, and the modulus of elasticity was 3,900,000 psi. For the precast concrete, the compression strength was 11,250 psi, and the modulus of elasticity was 5,450,000 psi. Figure 5.16 shows that the load-deflection response was well predicted. Figure 5.17 shows the stabilized crack pattern. For the simulated response, the crack pattern is represented by the localization of plastic tensile strains, which are shown in lighter colors than the rest of the mesh. Once again, the simulated response exhibits more cracking than the observed one, but the general crack locations are similar. As was the case for S1-2 and S1-3, the analysis model successfully captured the effect of the fibers on concrete cracking behavior. S1-4 has more cracks that are closely spaced together compared to S1-1. Typically, this results in more uniform, small crack widths.

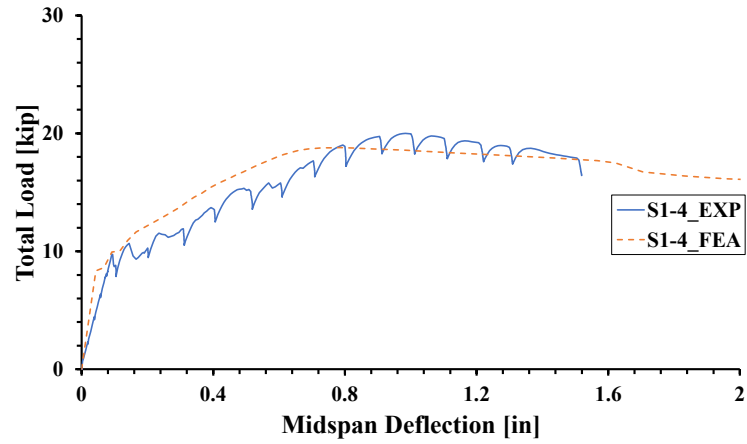
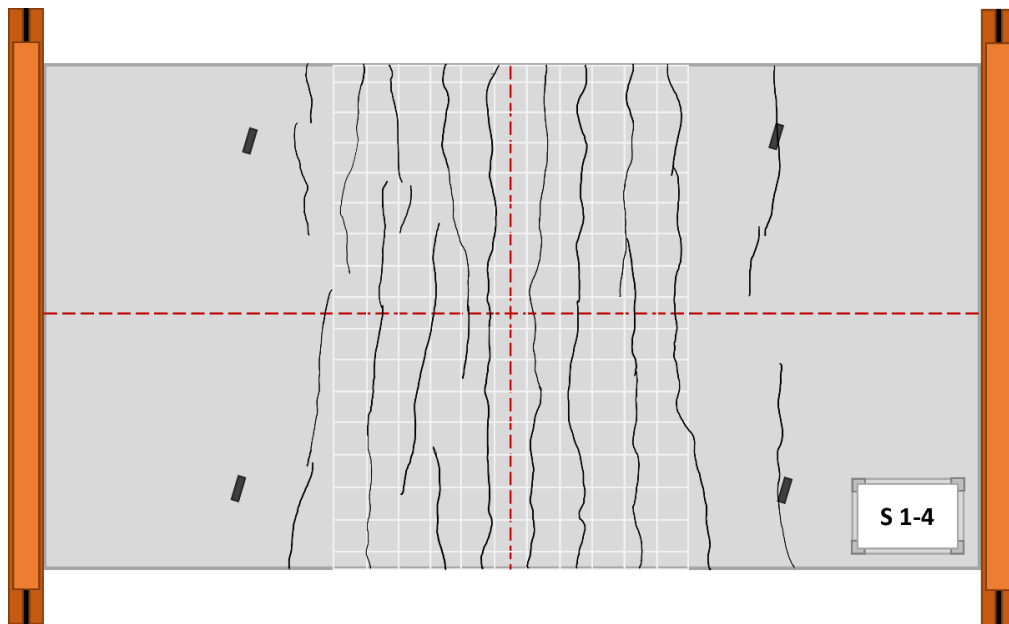
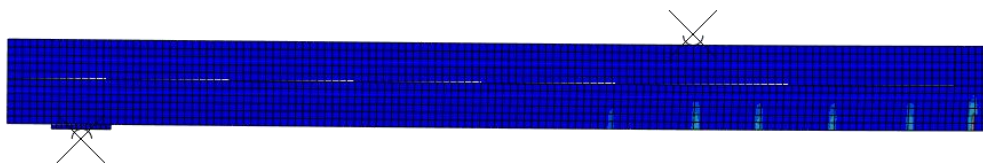


Figure 5.16 Load-deflection comparison for S1-4



(a) Observed crack pattern



(b) Simulated crack pattern

Figure 5.17 Stabilized crack pattern for S1-4

5.3.1.5. S1-5

Specimen S1-5 also contained 1% fiber by volume (crimped), but it only contained three No. 3 distributed across the slab width for flexural reinforcement. For the cast-in-place concrete, the compression strength was 6980 psi, and the modulus of elasticity was 5,150,000 psi. For the precast concrete, the compression strength was 10,740 psi, and the modulus of elasticity was 5,850,000 psi. As shown in Figure 5.18, the capacity was reasonably well predicted. Figure 5.19 shows the stabilized crack pattern. For the simulated response, the crack pattern is represented by the localization of plastic tensile strains, which are shown in lighter colors than the rest of the mesh. Once again, the simulated response exhibits more cracking than the observed one, but the general crack locations are similar. The results from this specimen suggest that the total removal of reinforcement in the deck is not feasible. In addition to less-than-ideal cracking behavior characterized by fewer and wider cracks, the flexural capacity of the deck is effectively limited to the cracking load.

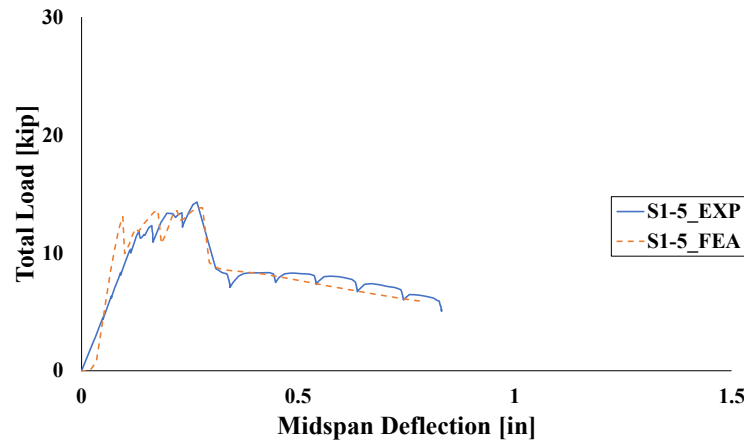
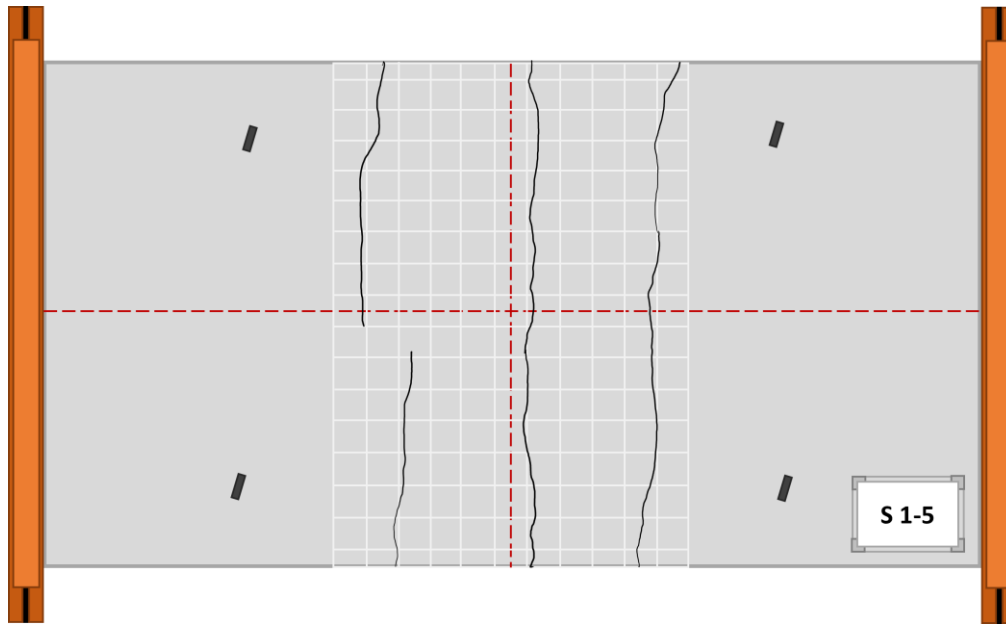
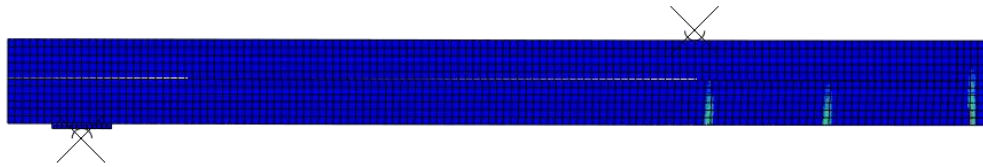


Figure 5.18 Load-deflection comparison for S1-5



(a) Observed crack pattern



(b) Simulated crack pattern

Figure 5.19 Stabilized crack pattern for S1-5

5.3.2. Series 2

A representative model for the Series 2 specimens is shown in Figure 5.20. A summary of the reinforcement details and fiber content is shown in Table 5.3. All modeling decisions were identical to those discussed in the preceding sections.

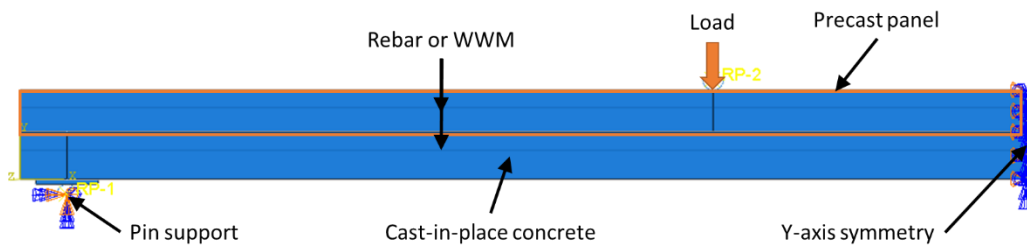


Figure 5.20 Representative Abaqus model for Series 2 specimens

Table 5.3 Summary of Series 2 reinforcement details

| | S 2-1 | S 2-2 | S 2-3 | S 2-4 | S 2-5 |
|---------------|---------|-----------|-------------|-----------|-----------|
| Concrete type | PC | FiberA 1% | FiberA 1.5% | FiberB 1% | FiberA 1% |
| Transverse | #4 @ 9" | #4 @ 9" | #4 @ 9" | #4 @ 9" | #4 @ 9" |
| Longitudinal | #4 @ 9" | #4 @ 18" | #4 @ 18" | #4 @ 18" | None |

An overview of the peak loads from the analyses is summarized in Table 5.4. Typically, the capacities were well predicted. Similar to S1-5, the analysis of S2-5 also incorporated three No. 3 rebars. The following sections provide a summary of the analysis results for each Series 1 specimen.

Table 5.4 Overview of Series 1 specimen capacity predictions

| Specimen | Exp. load (kip) | Est. load (kip) | Exp./Est. |
|----------|-----------------|-----------------|-----------|
| S2-1 | 22.3 | 24.3 | 1.09 |
| S2-2 | 23.4 | 24.3 | 1.04 |
| S2-3 | 24.5 | 25.6 | 1.04 |
| S2-4 | 20.1 | 20 | 1.00 |
| S2-5 | 13.8 | 14.5 | 1.05 |
| | | Avg. | 1.04 |
| | | Std. Dev. | 0.03 |
| | | CoV | 0.03 |

5.3.2.1. S2-1

Specimen S2-1 was the control specimen for Series 2. It contained No. 4 at 9 in. for flexural reinforcement. For the cast-in-place concrete, the compression strength was 5910 psi, and the modulus of elasticity was 3,250,000 psi. For the precast concrete, the compression strength was 11,390 psi, and the modulus of elasticity was 5,100,000 psi. Figure 5.21 shows that the load-deflection response was well predicted. Figure 5.8 shows the crack pattern at approximately 40% of ultimate, which represents service-level loading conditions, and Figure 5.9 shows the stabilized crack pattern that is the final crack pattern when no new cracks form and existing cracks widen until failure occurs. For the simulated response, the crack pattern is represented by the localization of plastic tensile strains, which are shown in lighter colors than the rest of the mesh. In both cases, the simulated response is relatively similar to the observed one.

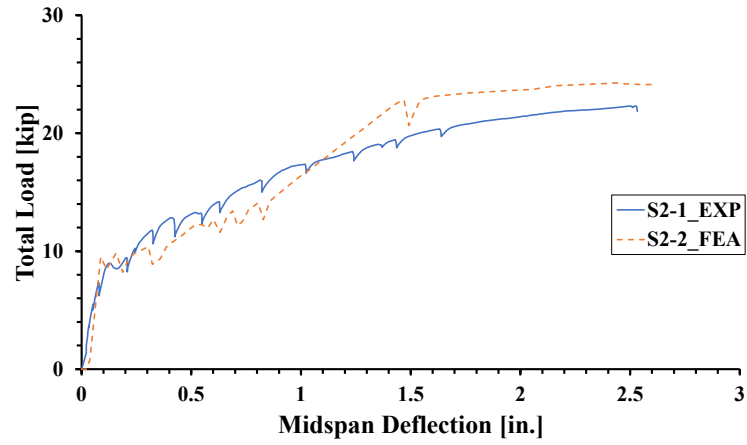
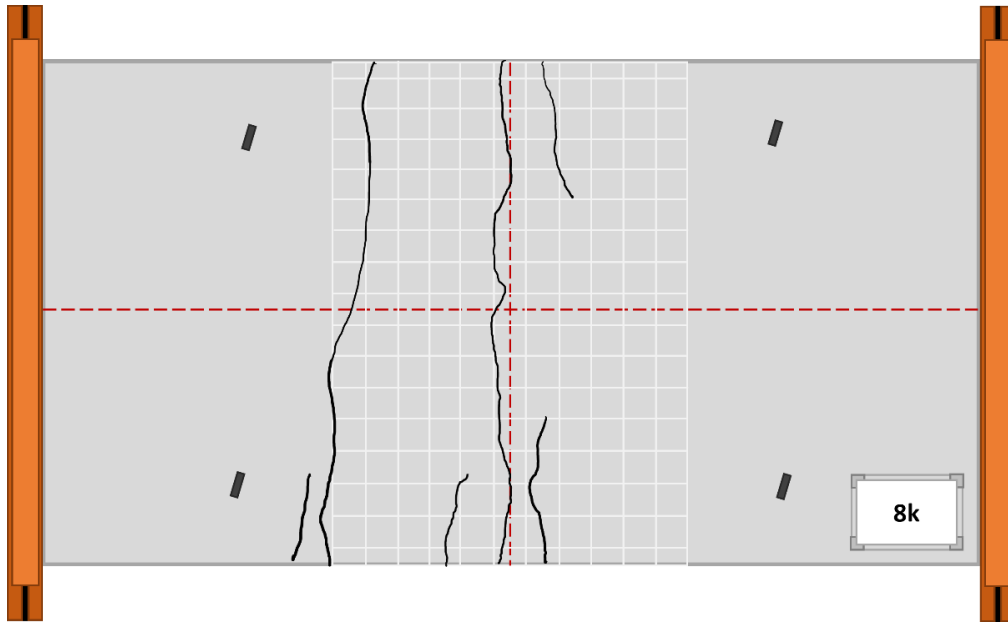
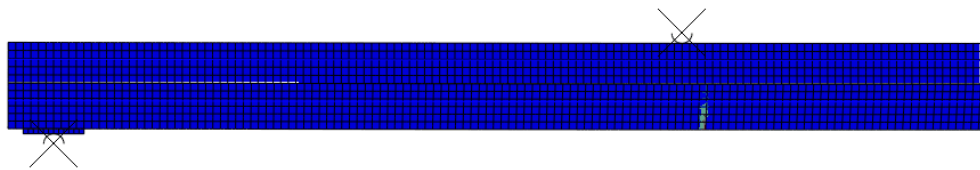


Figure 5.21 Load-deflection comparison for S2-1



(c) Observed crack pattern



(d) Simulated crack pattern

Figure 5.22 Crack pattern for S2-1 at $P = 8$ kip

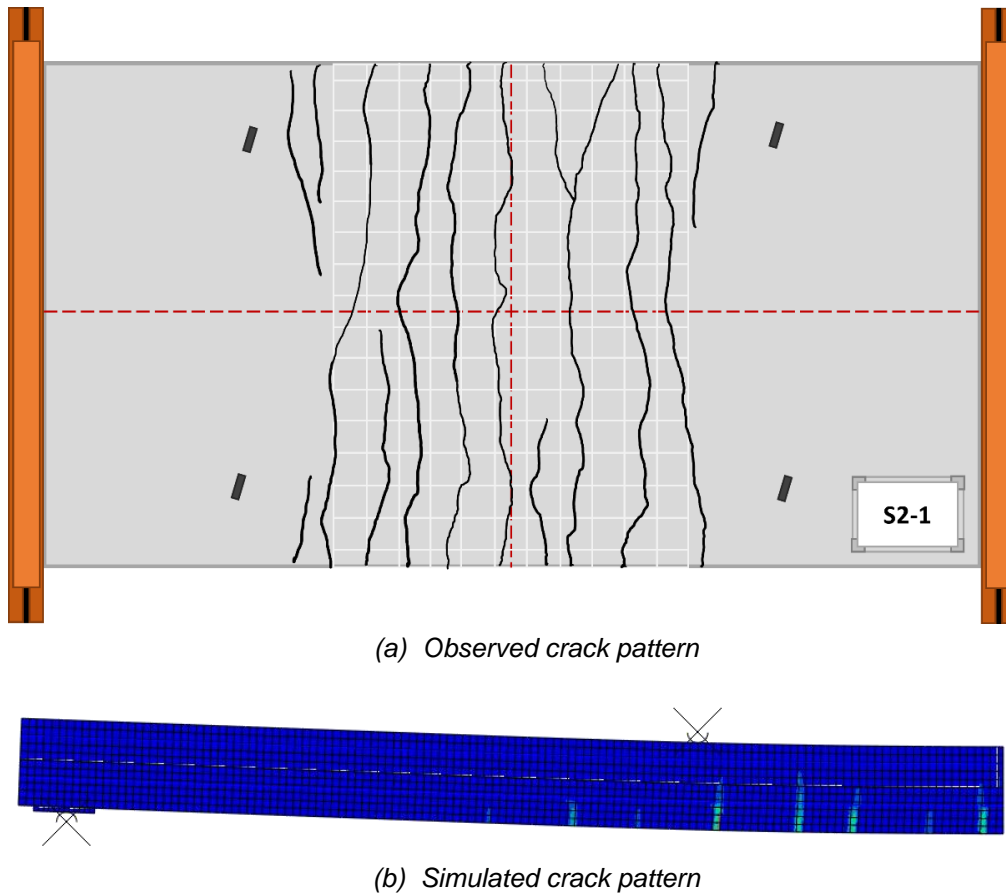


Figure 5.23 Stabilized crack pattern for S2-1

5.3.2.2. S2-2

Specimen S2-2 contained 1% hooked-end fiber by volume. It contained No. 4 at 18 in. for flexural reinforcement. For the cast-in-place concrete, the compression strength was 6290 psi, and the modulus of elasticity was 4,450,000 psi. For the precast concrete, the compression strength was 10,800 psi, and the modulus of elasticity was 5,750,000 psi. Figure 5.24 demonstrates an accurate prediction of the load-deflection response. In Figure 5.25, the stabilized crack pattern is depicted. In the simulated response, the crack pattern is illustrated by the localization of plastic tensile strains, represented in lighter colors compared to the rest of the mesh. Similar to previous observations, the simulated response indicates more cracking than the observed one, yet the general crack locations align. The analysis model effectively captures the influence of fibers on concrete cracking behavior. Notably, S2-2 exhibits a higher density of closely spaced cracks in comparison to S2-1, typically resulting in more uniform and smaller crack widths.

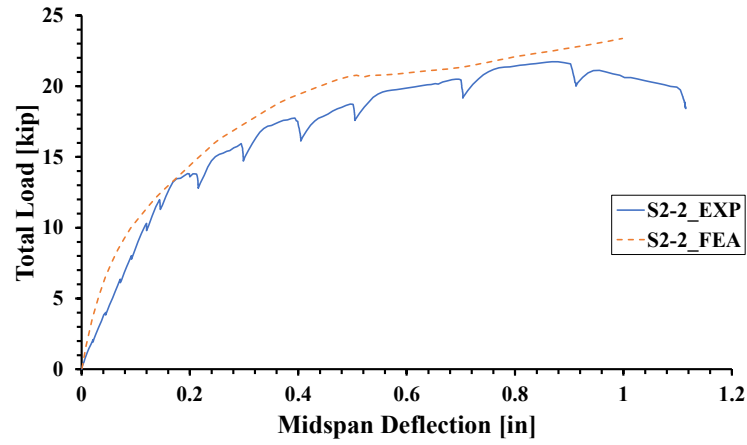
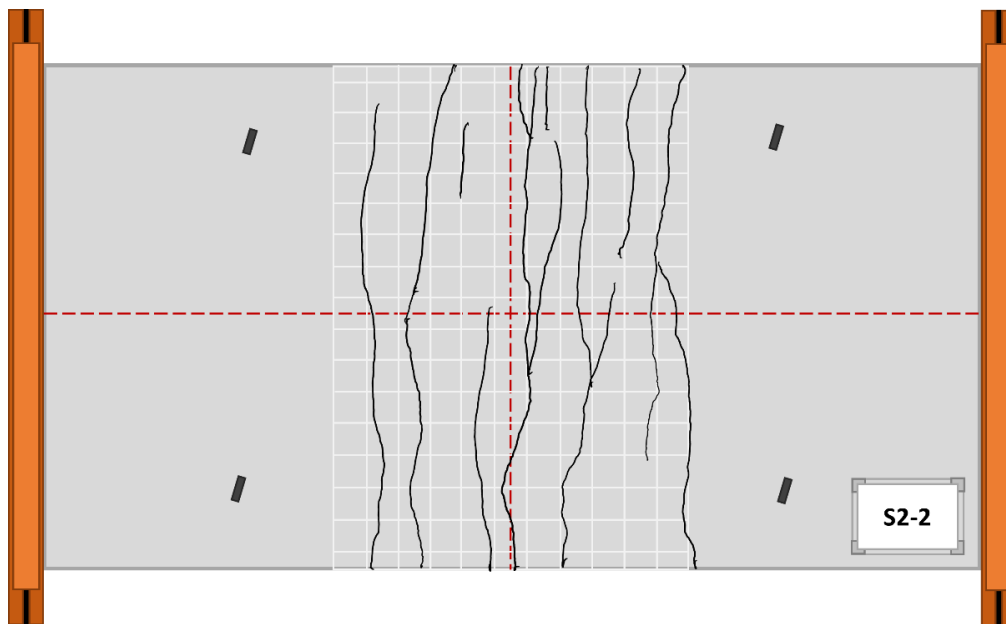
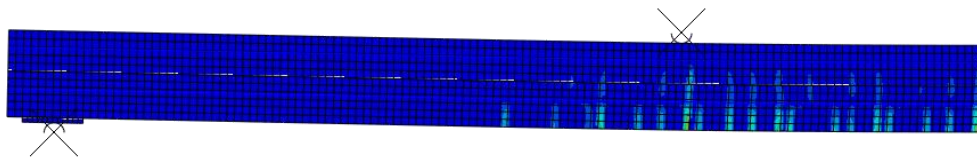


Figure 5.24 Load-deflection comparison for S2-2



(a) Observed crack pattern



(b) Simulated crack pattern

Figure 5.25 Stabilized crack pattern for S2-2

5.3.2.3. S2-3

Specimen S2-3 contained 1.5% hooked-end fiber by volume. It contained No. 4 at 18 in. for flexural reinforcement. For the cast-in-place concrete, the compression strength was 5550 psi, and the modulus of elasticity was 4,200,000 psi. For the precast concrete, the compression strength was 11,190 psi, and the modulus of elasticity was 4,050,000 psi. Once again, Figure 5.26 illustrates a well-predicted load-deflection response. The stabilized crack pattern is presented in Figure 5.27. In the simulated response, the crack pattern is denoted by the localization of plastic tensile strains, showcased in lighter colors relative to the rest of the mesh. The simulated response shows a similar crack pattern compared to the observed test specimen. In addition, the analysis model effectively captures the impact of fibers on concrete cracking behavior.

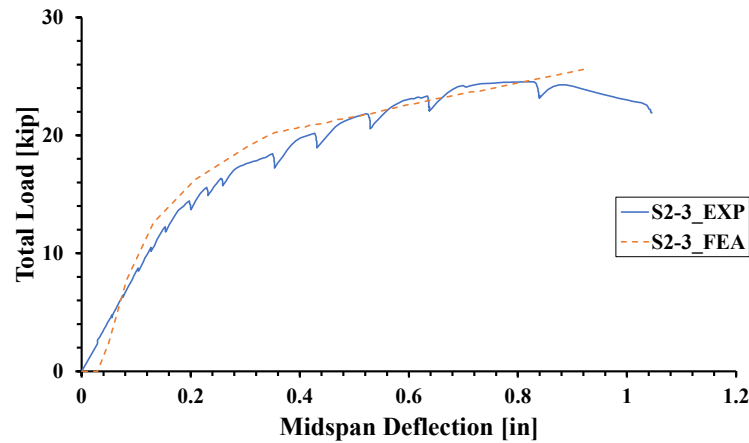
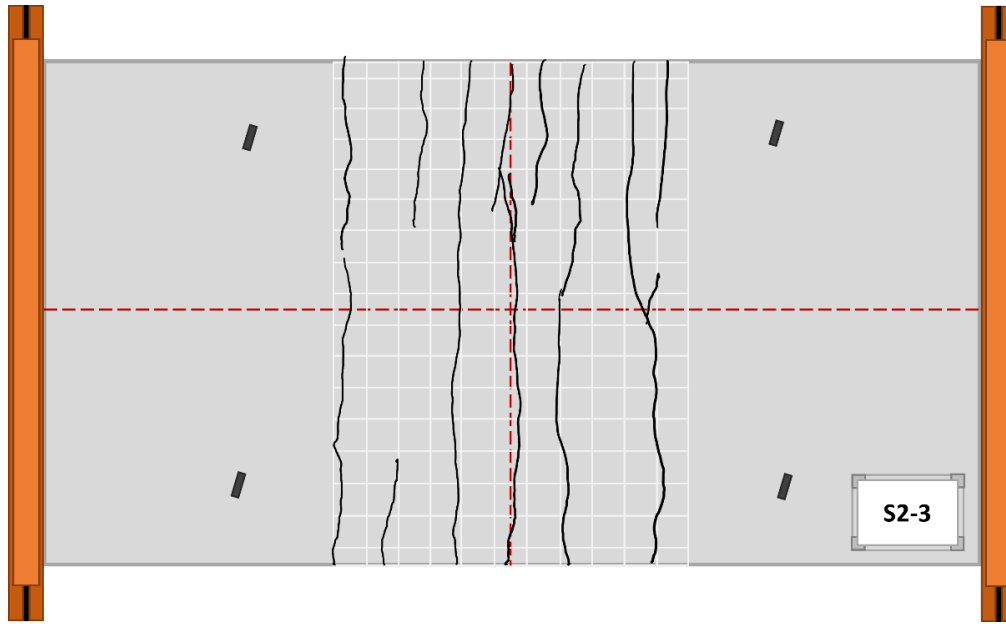
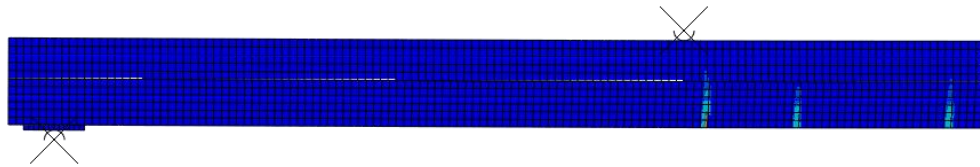


Figure 5.26 Load-deflection comparison for S2-3



(a) Observed crack pattern



(b) Simulated crack pattern

Figure 5.27 Stabilized crack pattern for S2-3

5.3.2.4. S2-4

Specimen S2-4 contained 1% crimped fiber by volume. It contained No. 4 at 18 in. for flexural reinforcement. For the cast-in-place concrete, the compression strength was 6980 psi, and the modulus of elasticity was 5,150,000 psi. For the precast concrete, the compression strength was 10,740 psi, and the modulus of elasticity was 5,850,000 psi. Figure 5.28 indicates a well-predicted load-deflection response, although there is a slight overprediction of the initial stiffness. The stabilized crack pattern is illustrated in Figure 5.29. In the simulated response, the crack pattern is highlighted by the localization of plastic tensile strains, displayed in lighter colors compared to the rest of the mesh. The simulated response closely mirrors the crack pattern observed in the test specimen. Furthermore, the analysis model adeptly captures the influence of fibers on concrete cracking behavior.

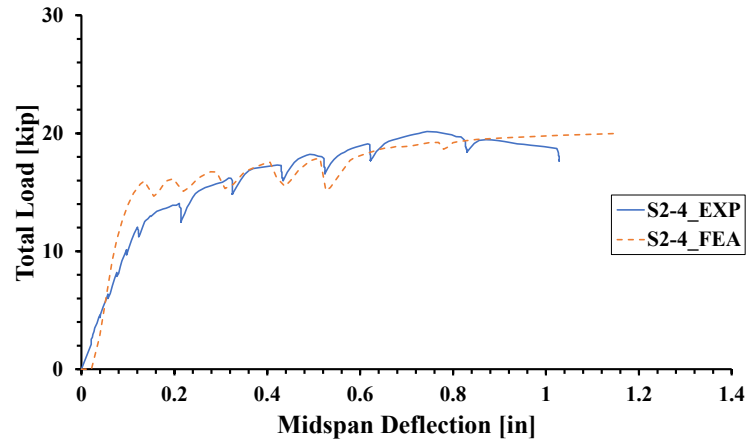
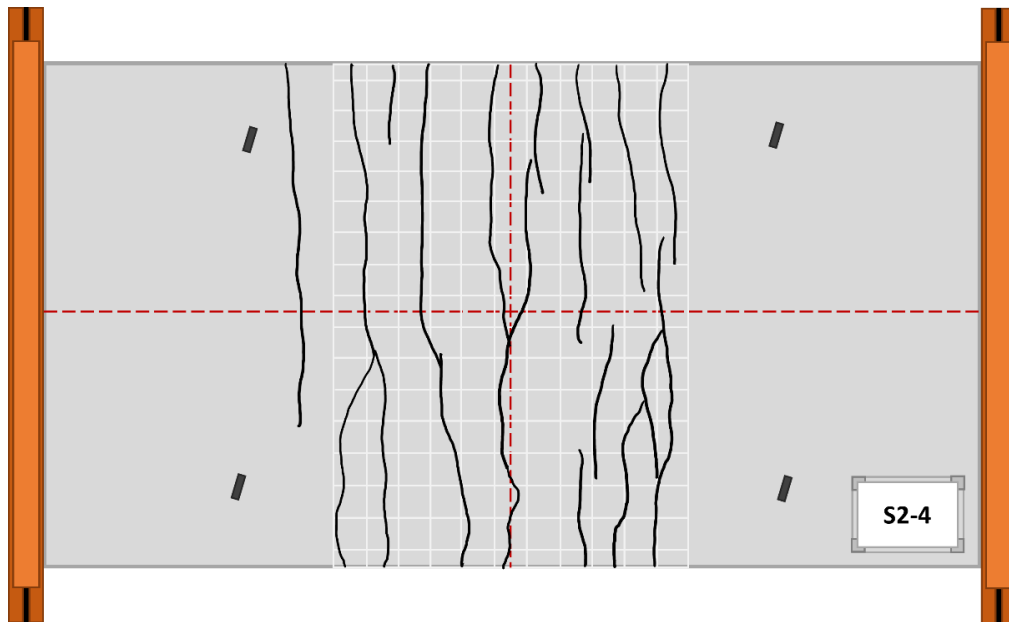
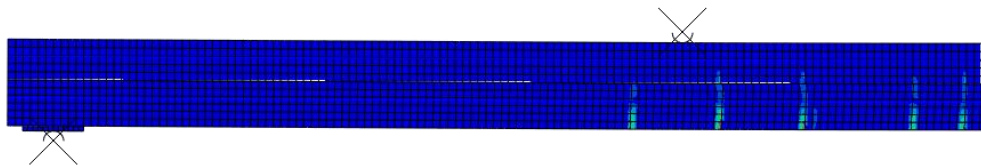


Figure 5.28 Load-deflection comparison for S2-4



(a) Observed crack pattern



(b) Simulated crack pattern

Figure 5.29 Stabilized crack pattern for S2-4

5.3.2.5. S2-5

Specimen S2-5, with 1% fiber by volume (hooked end), featured only three No. 3 bars distributed across the slab width for flexural reinforcement. The cast-in-place concrete had a compression strength of 5200 psi and a modulus of elasticity of 3,895,000 psi. In contrast, the precast concrete had a compression strength of 11,700 psi and a modulus of elasticity of 5,770,000 psi. Figure 5.30 demonstrates a reasonably accurate prediction of the capacity. Figure 5.31 reveals the stabilized crack pattern, with the simulated response representing the crack pattern through the localization of plastic tensile strains, shown in lighter colors than the rest of the mesh. However, unlike the actual experimental results, critical cracks appeared at the loading location in the simulated response. These findings from the specimen suggest that the complete removal of reinforcement in the deck might not be feasible. Additionally, the less-than-ideal cracking behavior, characterized by fewer and wider cracks, imposes an effective limitation on the flexural capacity of the deck, restricting it to the cracking load.

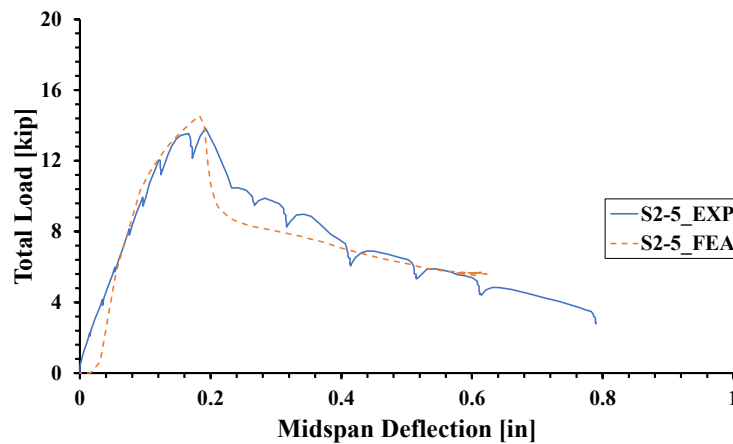


Figure 5.30 Load-deflection prediction for S2-5

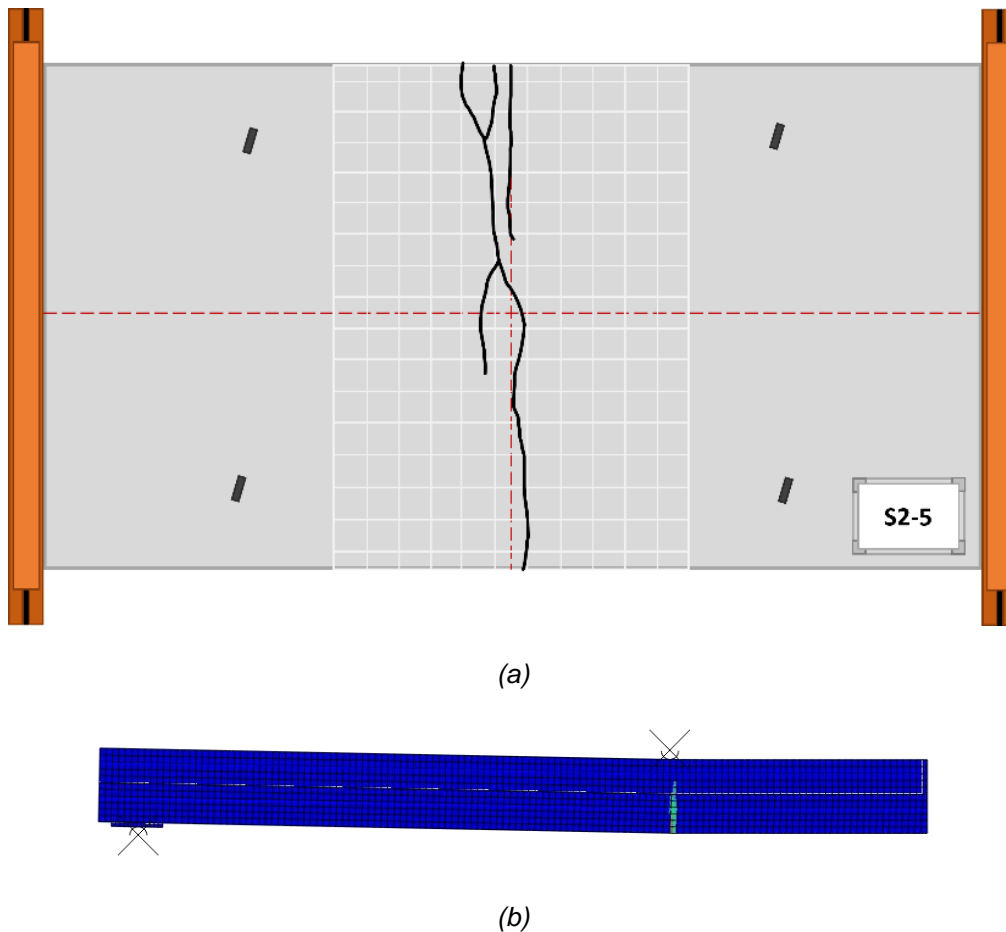


Figure 5.31 Simulated crack pattern for S2-5

5.4. Numerical Assessment of Modified Reinforcement Requirements

To provide a more direct comparison between the specimens, as well as examine alternate variables, a few additional analysis series were carried out. In these series, all concrete properties were identical except for the post-cracking tension response. For the cast-in-place concrete, the compression strength was 5000 psi, and the modulus of elasticity was 4,250,000 psi. For the precast concrete, the compression strength was 10,000 psi, and the modulus of elasticity was 5,400,000 psi. The assumed tension models were based on the average residual strength of hooked-end fiber SFRC, as determined in deck strip tests. The assumed tension models are shown in Figure 5.32.

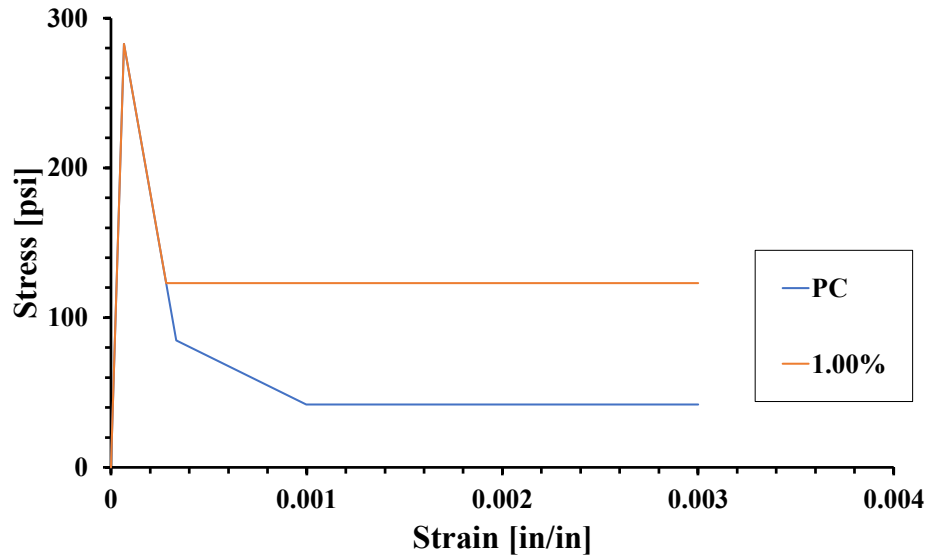


Figure 5.32 Assumed tension behavior for parametric study

The SFRC slab strips tested only took into account half of the conventional amount of deck reinforcement, with the spacing increased from 9 in. to 18 in. Therefore, an additional set of analyses was carried out to determine if alternate spacings could be acceptable. The results of this series are summarized in Figure 5.33 and Figure 5.34. It is obvious from Figure 5.33 that the impact of reducing the amount of conventional reinforcement on the post-cracking, load-carrying capacity. The cracking responses depicted in Figure 5.34 illustrate the cracking behavior, showcased for a service load level approximately equal to 40% of the failure load of the control case. As the amount of conventional reinforcement is reduced, the likelihood of few, very wide cracks forming is increased.

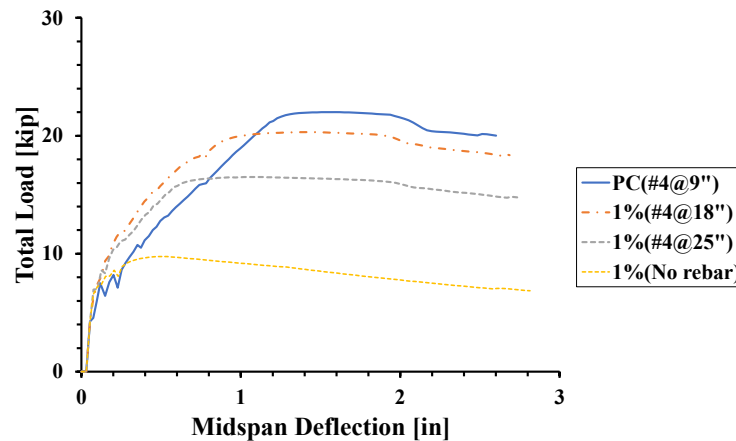


Figure 5.33 Load-deflection comparison for reinforcement spacing study

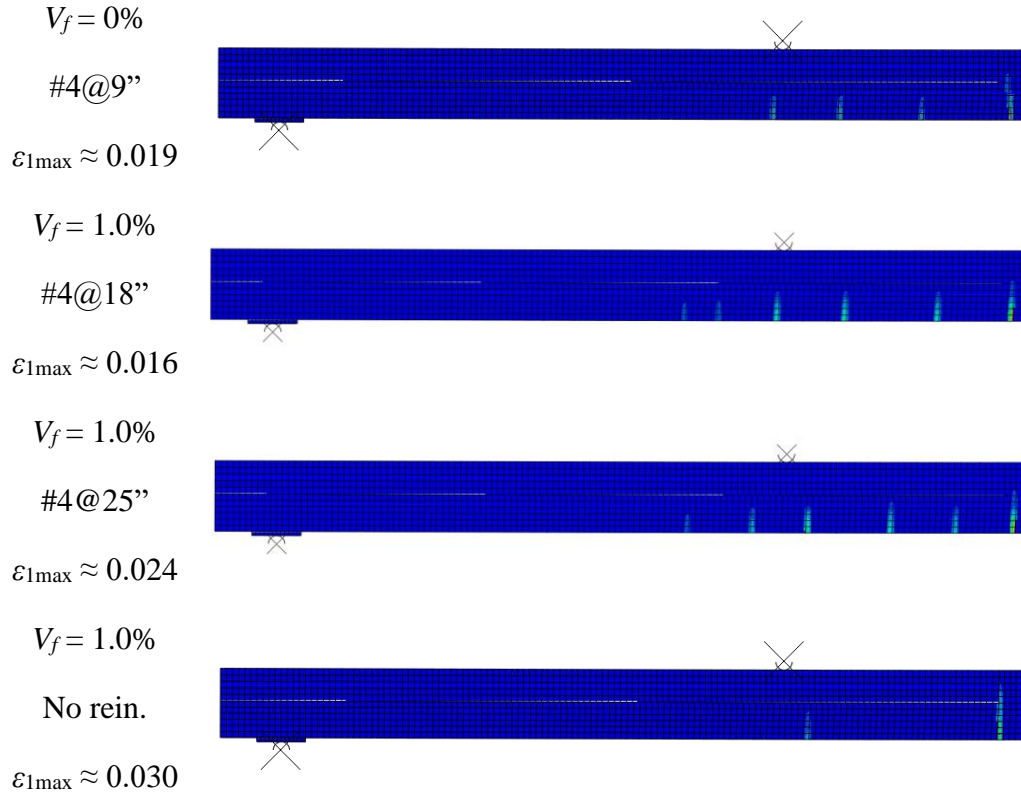


Figure 5.34 Crack pattern comparison for reinforcement spacing study

5.5. Summary and Conclusions

This chapter provides a summary of the results obtained from Nonlinear Finite Element Analysis. Two conclusions can be drawn from these findings.

1. A 1% fiber content appears to be an acceptable minimum content to offset reduced amounts of conventional reinforcement.
2. The spacing for No. 4 deck reinforcement may be increased from 9 in. to 18 in. provided that an adequate fiber content has been added to the concrete. It is questionable to have a reinforcement spacing greater than 18 inches.

Chapter 6. Full-Scale Test

6.1. Overview

In this particular chapter, the research team provides a comprehensive overview of the test results of a full-scale bridge deck specimen using SFRC as a CIP. It covers the test matrix, material properties, test setup, and results. Based on these findings, the research team suggests recommendations for utilizing SFRC as a topping material of CIP-PCP bridge decks.

6.2. Full-Scale Specimen Testing Program

The design of precast concrete panels with an in-situ cast-in-place concrete topping (CIP-PCP) follows the AASHTO-LRFD (2020) empirical design method. The TxDOT design standard aligns with these empirical design procedures, ensuring that the bridge deck conforms to state standards for serviceability, fracture resistance, and structural strength. To better comprehend and predict the behavior of an SFRC CIP-PCP bridge deck as an actual bridge, the research team performed full-scale bridge deck testing. Therefore, in this section, the research team outlines the configuration of the specimen, details the test matrix employed, and the limit states that serve to define failure.

6.2.1. Specimen Configuration and Test Matrix

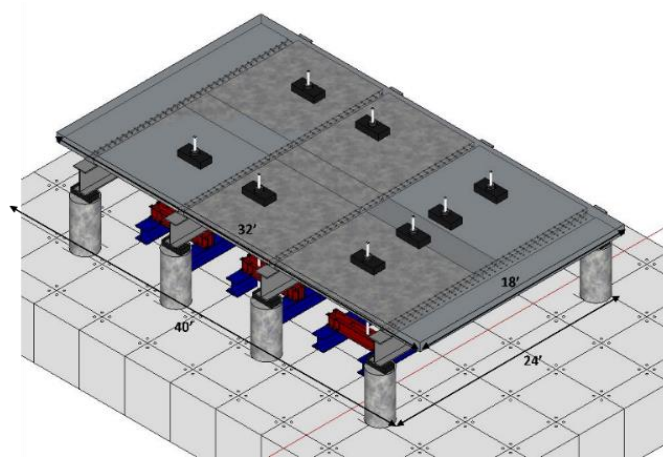
The large-scale SFRC deck test specimen had a typical deck thickness of 8.5 (4-in. thick PCPs with a 4.5-in. CIP topping slab); see Figure 6.1. Within the interior transverse span sections of the deck specimen, six full-size PCPs are deployed. Notably, overhang areas and edges were constructed with CIP SFRC. The transverse spacing of the deck specimen's four girders ranged between 8 and 10 feet, accurately representing both common and demanding deck loading scenarios.

The top mat reinforcement varied both longitudinally and transversely across the slab to assess SFRC bridge deck performance under diverse configurations. The differentiation among the four interior regions stemmed from variations in their reinforcement configuration, the presence of top mat reinforcement, and the applied loading conditions. The loading scenarios encompassed single axle loading, denoted as "S," and tandem axle loading, identified by "T."

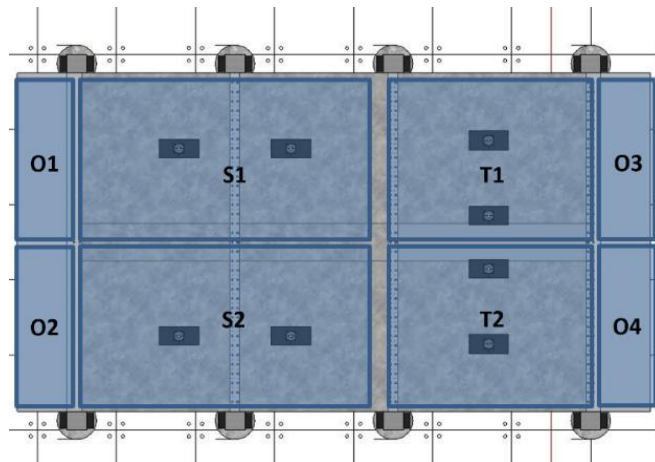
The "O" labeled matrix for overhang regions aimed to reduce the amount of top transverse and bottom longitudinal reinforcement. One series assessed SFRC overhangs without reinforcement. See Figure 6.1 (a), (b), and

| | S1 | S2 | T1 | T2 | O1 | O2 | O3 | O4 |
|------------------------------|-----------------|----------------|-----------------|----------------|-----------------|-----------------|----------------|----------------|
| Top rebar Transverse | #4@18" (50%) | None | #4@18" (50%) | None | #4@9" (42%) | #4@18" (21%) | #4@9" (42%) | None |
| Top rebar Longitudinal | #4@18" (50%) | None | #4@18" (50%) | None | #4@18" | #4@18" | #4@18" | None |
| Bottom rebar Transverse | Panel | Panel | Panel | Panel | #4@18" | #4@18" | #4@18" | None |
| Bottom rebar Longitudinal | Panel | Panel | Panel | Panel | #4@18" (50%) | #4@18" (50%) | #4@9" | None |
| Loading type | Tandem Axel | Tandem Axel | Single Axel | Single Axel | Single Axel | Single Axel | Single Axel | Single Axel |

for details, encompassing two loading scenarios.



(a)



(b)

Figure 6.1 Full-scale (a) dimensions and (b) test regions

Table 6.1 Reinforcement layout for each region

| | S1 | S2 | T1 | T2 | O1 | O2 | O3 | O4 |
|------------------------------|-----------------|----------------|-----------------|----------------|-----------------|-----------------|----------------|----------------|
| Top rebar Transverse | #4@18" (50%) | None | #4@18" (50%) | None | #4@9" (42%) | #4@18" (21%) | #4@9" (42%) | None |
| Top rebar Longitudinal | #4@18" (50%) | None | #4@18" (50%) | None | #4@18" | #4@18" | #4@18" | None |
| Bottom rebar Transverse | Panel | Panel | Panel | Panel | #4@18" | #4@18" | #4@18" | None |
| Bottom rebar Longitudinal | Panel | Panel | Panel | Panel | #4@18" (50%) | #4@18" (50%) | #4@9" | None |
| Loading type | Tandem Axel | Tandem Axel | Single Axel | Single Axel | Single Axel | Single Axel | Single Axel | Single Axel |

6.2.2. Limit States

The AASHTO standard empirical deck design for CIP-PCP addresses various service limit states concerning the bridge deck. These guidelines encompass deflection limits, maximum reinforcement strain, and crack resistance performance. Initially, AASHTO-LRFD section 5.6.7 states that researchers need to regard the bridge decks and submerged substructure within a Class 2 exposure condition. To meet aesthetic standards and mitigate corrosion, an upper bound crack width of 0.013 in. is mandated. Furthermore, the section stipulates that the tensile stress in the reinforcement should not surpass 60 % of rebar yield strength, corresponding to a rebar strain of 0.0013 in./in. In addition, AASHTO-LRFD section 2.5.2.6.2 defines an upper bound of Span/800, translating to 0.12 in. for an 8 ft. span and 0.15 in. for a 10 ft. span. This limit helps ensure that the bridge maintains an acceptable level of comfort and functionality for the users and minimizes potential long-term damage.

In conjunction with these service limit states, an evaluation of the bridge deck's ultimate capacity is carried out to closely examine the factor of safety for the SFRC CIP-PCP bridge deck. The ultimate limit states (ULS), as outlined in the AASHTO standard, are elaborated upon in Table 6.2.

Table 6.2 AASHTO LRFD (2020) load factors and maximum factored load

| Location | Wheel load | Multiple presence factor | Live load factor | Dynamic allowance factor | Maximum factored load |
|--------------|------------|--------------------------|------------------|--------------------------|-----------------------|
| Truck wheel | 16 kips | 1.2 | 1.75 | 1.33 | 45 kips |
| | | | | 1.75 (For joint) | 60 kips |
| Tandem wheel | 12.5 kips | 1.2 | 1.75 | 1.33 | 35 kips |
| | | | | 1.75 (For joint) | 45 kips |

6.3. Specimen Preparation

6.3.1. Precast Panel Fabrication

Valley Precast, Inc. manufactured a total of nine precast panels, comprising four panels measuring 7.5 ft. x 8 ft. x 4 in., two panels measuring 9.5 ft. x 8 ft. x 4 in., two panels measuring 7.5 ft. x 2 ft. x 4 in., and one panel measuring 9.5 ft. x 2 ft. x 4 in. Among the six panels with an 8 ft. width, transverse panel reinforcement was incorporated, featuring 0.5 in. diameter strands prestressed at 14.4 kips per strand, positioned every 6 inches and extending outward by 3 inches. In contrast, the three panels with a 2 ft. width were constructed using #4 reinforcement spaced at 6 inches. All panels, regardless of width, were equipped with additional wire mesh. The fabrication procedure adhered to the same method detailed in section 4.3.1.

6.3.2. Preparation Before Casting

At the outset, four W21x132 steel beams, equipped with stiffeners, were positioned atop concrete columns. To facilitate the flow of concrete onto the steel girder, a 1.5-inch bedding strip was affixed, serving as a foundation for the subsequent placement of precast panels. Following the panel placement, wood formworks were meticulously constructed to shape the cast-in-place (CIP) and overhang sections of the bridge deck. Subsequently, reinforcements were positioned on top of the panels utilizing bolsters. The visual depiction in the figure encapsulates the appearance of the specimen prior to the commencement of the concrete casting process.

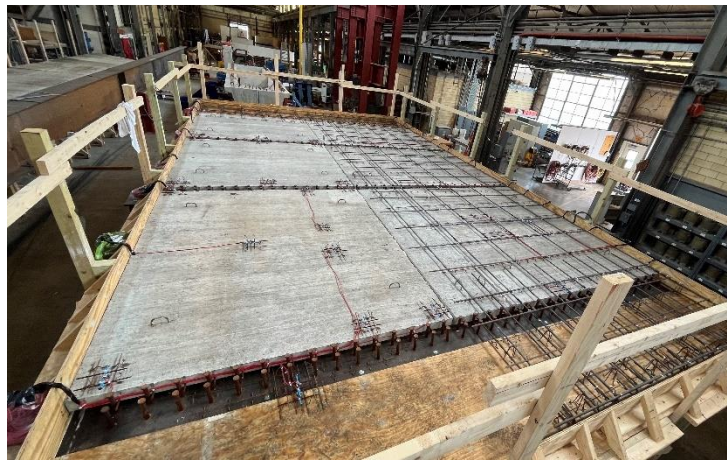


Figure 6.2 Specimen before casting

6.3.3. Concrete Casting

Before the casting phase, the surface of the precast panel was consistently moistened using a pressure sprayer. The SFRC mix was transported to the

laboratory using a concrete truck, with an order of 14 cubic yards of concrete intended for casting both structural and material specimens. Prior to the casting phase, slump tests were conducted to ensure the feasibility of the concrete casting. Following this, the concrete was poured using a concrete bucket (Figure 6.3), and post-casting, precision leveling, and smoothing of the concrete surface were achieved through the use of screed and floats (Figure 6.4). To facilitate curing, the specimen was covered with burlap (Figure 6.5).



Figure 6.3 Concrete casting procedure

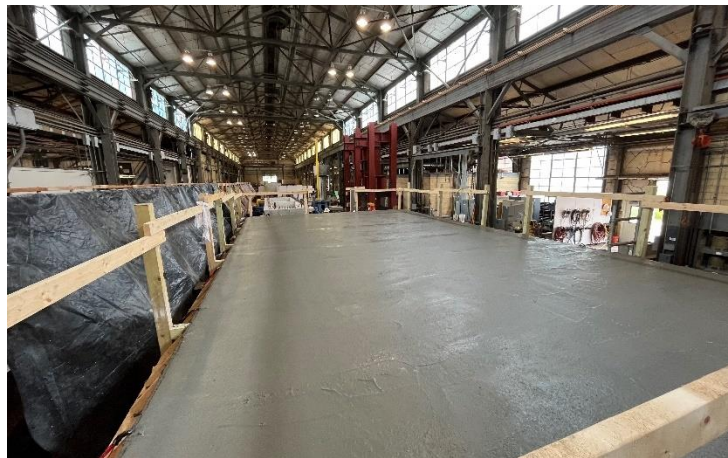


Figure 6.4 Concrete surface after casting



Figure 6.5 Specimen curing using burlap

6.4. Material Testing and Results

The findings from deck strip tests reveal the positive performance of all steel fiber types with a 1.5 in. length. The full-scale specimen employs 1% of Type A fiber SFRC, which features hooked end shapes. To assess the performance of the SFRC structure, evaluating the mechanical properties of the material is essential. This involves conducting three distinct test types—uniaxial compression, uniaxial tension, and flexural tests. Additionally, the workability of the fresh concrete was assessed during the casting process.

6.4.1. Fresh Concrete Properties: Slump Test

From previous experience, incorporating fibers significantly reduces slump and complicates concrete casting. To address this issue, superplasticizers were introduced into the mix to attain a slump exceeding 5 in. The addition of fibers took place at the concrete plant, resulting in a delivered SFRC slump of 8.5 in, (see Figure 6.6).



Figure 6.6 Concrete slump

6.4.2. Uniaxial Compression and MOE Tests

Following the same procedure described in section 4.4.3, the compressive strength and elastic modulus of concrete were measured. The test outcomes are presented in both the Table 6.3 and Figure 6.7. The attained strength of class S concrete, stipulated by TxDOT at a minimum of 4 ksi, surpassed this threshold within one week of the casting process.

Table 6.3 Slab-strip specimen material test results

| Test date | Cast-in-place | | Precast concrete | |
|--------------------|---------------|--------------|------------------|--------------|
| | E_c [ksi] | f'_c [ksi] | E_c [ksi] | f'_c [ksi] |
| 7 days | - | 4.3 | - | - |
| 14 days | - | 5.3 | - | - |
| 21 days | - | 5.8 | - | - |
| 28 days | - | 5.8 | - | - |
| 92 days (S2) | 5015 | 6.4 | 5459 | 9.0 |
| 106 days (S1) | 5501 | 6.7 | 5847 | 9.1 |
| 111 days (T2) | 4487 | 6.2 | 6453 | 8.9 |
| 117 days (T1) | 4580 | 6.9 | 5272 | 8.9 |
| 138 days (O1 & O2) | 5141 | 6.1 | - | - |
| 155 days (O3 & O4) | 5173 | 6.7 | - | - |

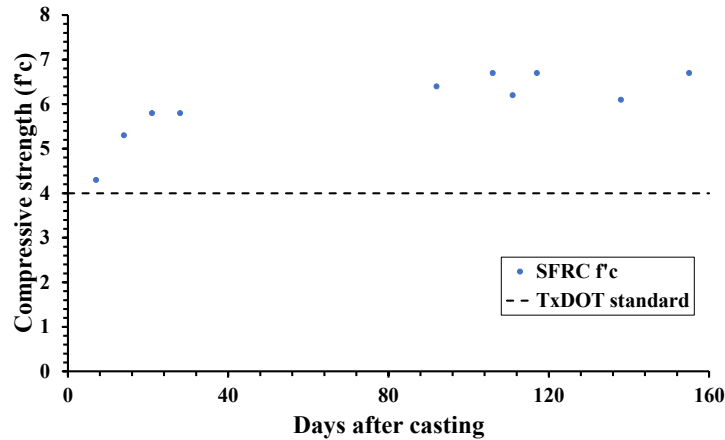


Figure 6.7 Compressive strength of SFRC

6.4.3. Flexural Bending Test (ASTM C1609)

Employing the identical methodology outlined in the preceding section 4.4.4, assessments were conducted for both peak flexural strength and flexural residual strength. The result of flexural tests are shown in both the Table 6.4 and Figure 6.8. After a thorough analysis of the test results during the assessment period, there was no significant correlation found between the age of the concrete and its residual strength. The average residual strength is 0.65 ksi at 0.02 inch displacement (L/600) and 0.45 ksi at 0.08 inch displacement (L/150). The failure of the CIP-PCP bridge deck is closely associated with the serviceability limit, specifically the limit of L/600 (ASTM, 2019). Consequently, to replicate the effects observed in this test result, the flexural beam should exhibit an average residual strength of 0.65 ksi at 0.02 inch displacement.

Table 6.4 ASTM C1609/C1609M Flexural beam test results

| Test date/ Description | C1609 test | | |
|-------------------------------------|--------------|---------------------------------|---------------------------------|
| | f'_r [ksi] | $f'_{res(\frac{L}{600})}$ [ksi] | $f'_{res(\frac{L}{150})}$ [ksi] |
| 28 days | 0.837 | 0.503 | 0.296 |
| 92 days (S2) | 0.906 | 0.684 | 0.475 |
| 111 days (T2) | 0.923 | 0.687 | 0.447 |
| 230 days | 0.982 | 0.575 | 0.423 |
| Avg (from beginning of the test) | 0.937 | 0.649 | 0.448 |

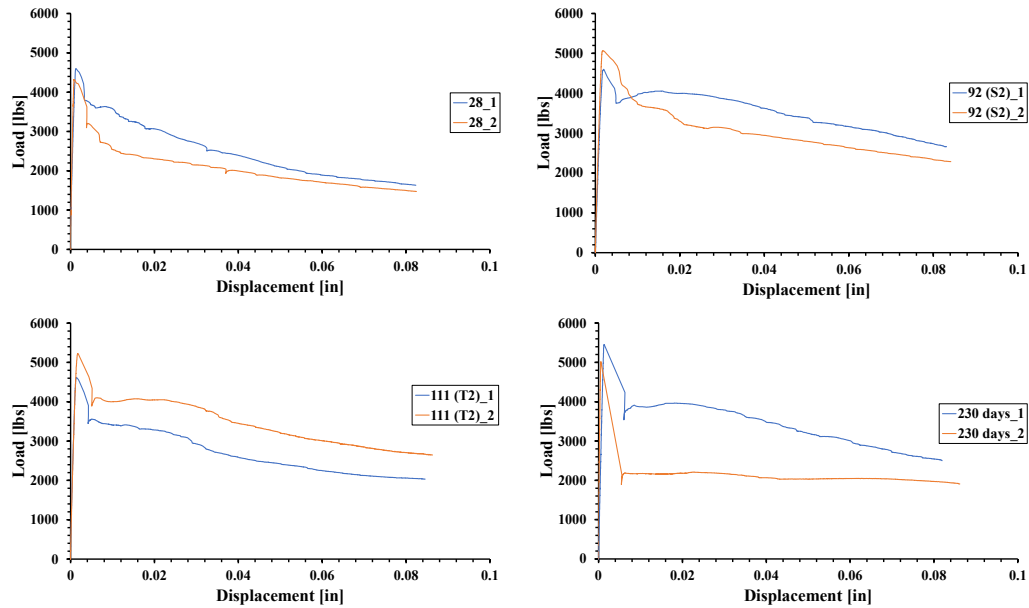


Figure 6.8 Flexural beam test results

6.4.4. Uniaxial Tension Test

Utilizing the methodology delineated in the section 4.4.5, measurements were taken for both uniaxial tensile strength and residual strength. The results of these tests are depicted in both the Table 6.5 and Figure 6.9. Upon thorough examination of the test results throughout the duration of the assessment, no notable correlation was observed between residual strength and the age of the concrete. Nevertheless, in the majority of cases, the residual strength of concrete at a strain of 0.01 in/in exceeded 100 psi.

Table 6.5 Direct tension test results

| Test date/ Description | Direct tension test | | |
|-------------------------------------|---------------------|----------------------|-------------------------|
| | f'_t [ksi] | $f_{res_1}^t$ [ksi] | $f_{res_0.01}^t$ [ksi] |
| 28 days | 0.34 | 0.18 | 0.07 |
| 92 days (S2) | 0.48 | 0.2 | 0.16 |
| 106 days (S1) | 0.52 | 0.2 | 0.10 |
| 168 days | 0.43 | 0.2 | 0.11 |
| Avg (from beginning of the test) | 0.48 | 0.2 | 0.12 |

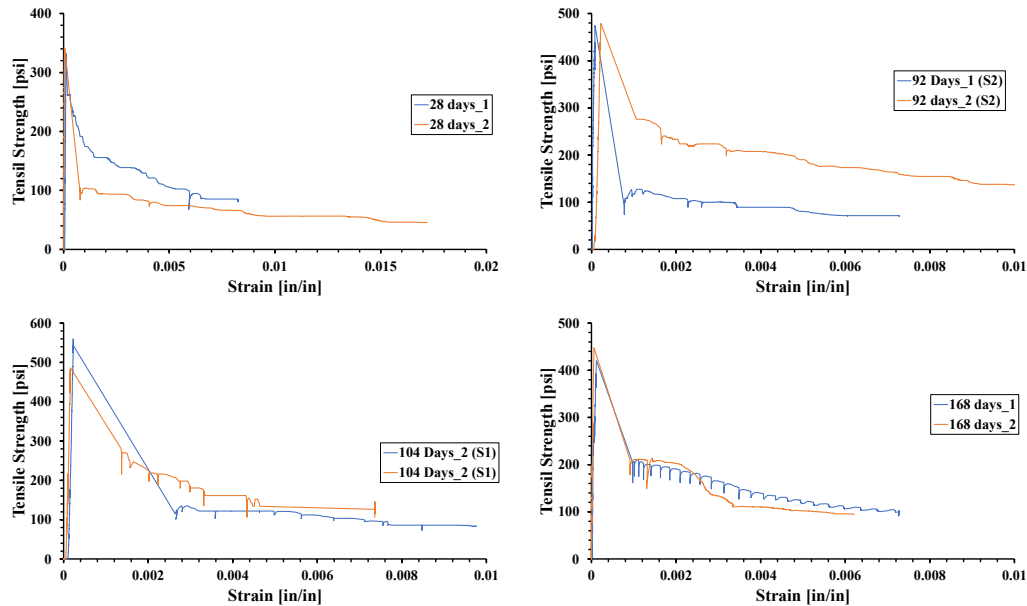


Figure 6.9 Uniaxial tensile test results

6.5. Test Setup and Instrumentation

The research team employed the HL-93 design vehicle and the AASHTO-LRFD Bridge Design Specifications to determine the dimensions and arrangement of applied loads. A contact region measuring 10 in. by 20 in. was needed to replicate wheel loading from an HL-93 truck load on the deck surface. For load application, 200-kip hydraulic rams were utilized, gradually increasing the load for each test. To quantify the applied force, load cells were positioned parallel to the actuator. Loading pauses were scheduled to observe crack development on the deck's upper and panel's bottom surfaces, representing the loading configuration of full-scale testing.

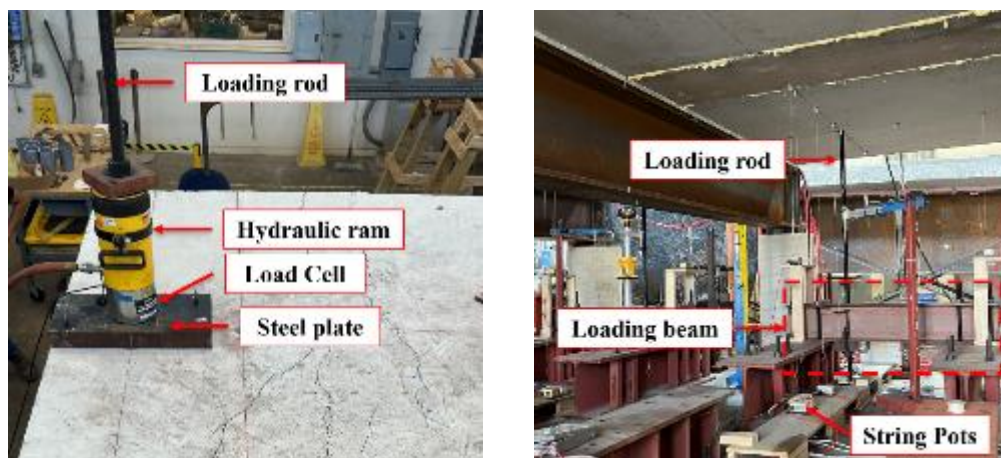
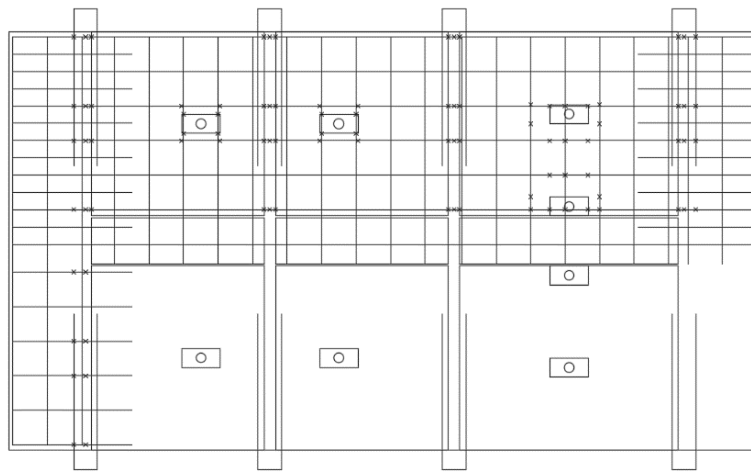
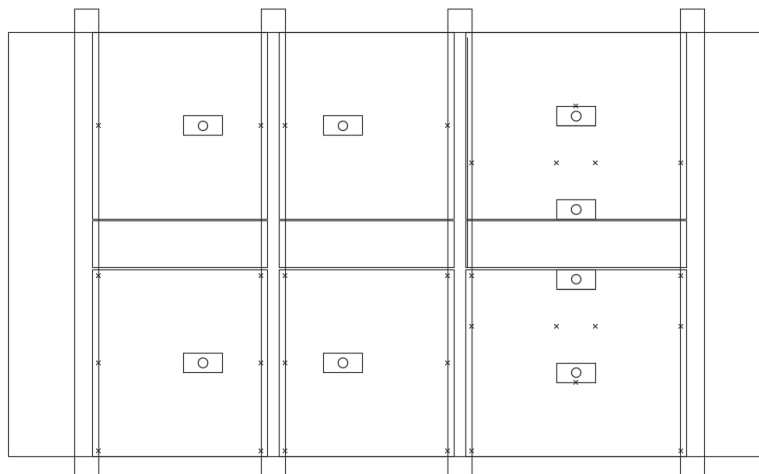


Figure 6.10 Loading method and instrumentation

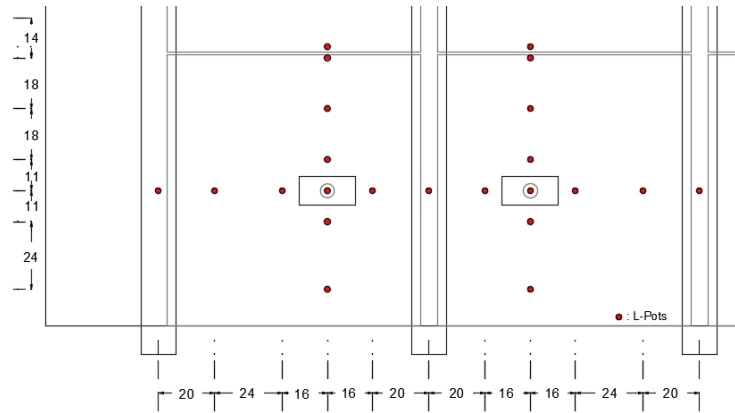
In scenarios involving conventional steel reinforcement, electrical-based strain gauges were attached to monitor steel stress at locations where significant positive and negative moments were expected. Vibrating wire gauges (VWGs) in the shape of a dog bone were incorporated for the testing regions lacking reinforcement. In order to measure the deflection of the SFRC deck, string potentiometers were positioned beneath two load points, spanning the longitudinal and transverse directions. Refer to Figure 6.11 for the locations of string potentiometers and gauges. Furthermore, precise non-contact optical measurement equipment, Optotrak, was employed to accurately detect crack width during testing.



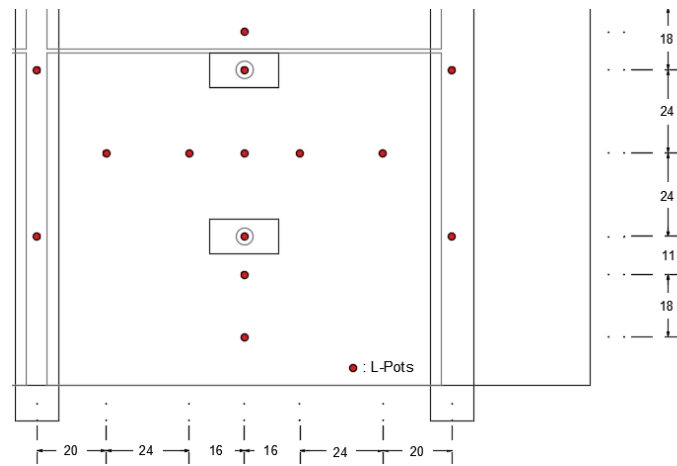
(a)



(b)



(c)



(d)

Figure 6.11 Instrumentations (a) Strain gauge location, (b) VWGs location, (c) Single axle potentiometer locations, and (d) Tandem axle potentiometer locations

6.6. Test Results

This section summarizes the outcomes of the conducted tests for the configurations that are outlined in

| | S1 | S2 | T1 | T2 | O1 | O2 | O3 | O4 |
|----------------------------|-----------------|-------|-----------------|-------|----------------|-----------------|----------------|------|
| Top rebar Transverse | #4@18" (50%) | None | #4@18" (50%) | None | #4@9" (42%) | #4@18" (21%) | #4@9" (42%) | None |
| Top rebar Longitudinal | #4@18" (50%) | None | #4@18" (50%) | None | #4@18" | #4@18" | #4@18" | None |
| Bottom rebar Transverse | Panel | Panel | Panel | Panel | #4@18" | #4@18" | #4@18" | None |

| | | | | | | | | |
|------------------------------|----------------|----------------|----------------|----------------|-----------------|-----------------|----------------|----------------|
| Bottom rebar Longitudinal | Panel | Panel | Panel | Panel | #4@18" (50%) | #4@18" (50%) | #4@9" | None |
| Loading type | Tandem Axel | Tandem Axel | Single Axel | Single Axel | Single Axel | Single Axel | Single Axel | Single Axel |

. The reference points for the service limit state encompassed the AASHTO-defined crack width threshold of 0.013 in. and a reinforcement strain boundary of 0.0013 in./in to meet aesthetic standards and mitigate corrosion. In addition, the allowable deck deflection is restricted to 0.12 inches for the 8-foot interior span, 0.15 inches for the 10-foot interior span, and 0.13 inches for the overhang. Furthermore, the specimen's capacity was assessed up to the strain-hardening phase.

6.6.1. Differential shrinkage measurement

Before initiating the test, shrinkage strains of both PCP and CIP in the crack-prone regions for a duration of 28 days were measured using the installed vibrating gauges. Long-term measurements were not possible due to ongoing preparations and execution of the structural test. The maximum strain results from the measurements indicate that both regions, with and without reinforcement, exhibited minimal differential shrinkage compared to the concrete cracking strain range of 0.0001 to 0.0003 inches per inch (Figure 6.12). Additionally, a thorough examination of the specimen's top surface prior to testing revealed no visible shrinkage cracks.

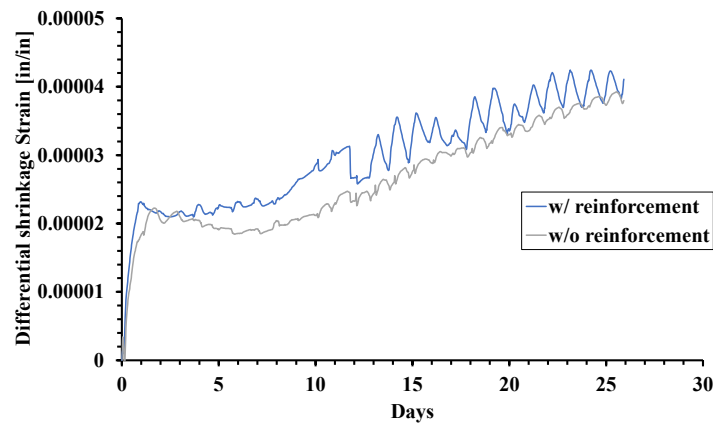


Figure 6.12 Measured differential shrinkage result

6.6.2. Single Axle Load

The longitudinal direction panel joints are subjected to single axle loads, resulting in the generation of maximal negative moments along the girder region. To emulate the effect of a truck moving over the girder line, a configuration is employed involving two steel plates measuring 10 in. x 20 in. These plates were placed 6 ft.

apart (Figure 6.13). This arrangement was devised to produce a scenario representing the most critical case for evaluating the negative moment exerted over the girder while preventing cracking between transverse panel-to-panel joints.

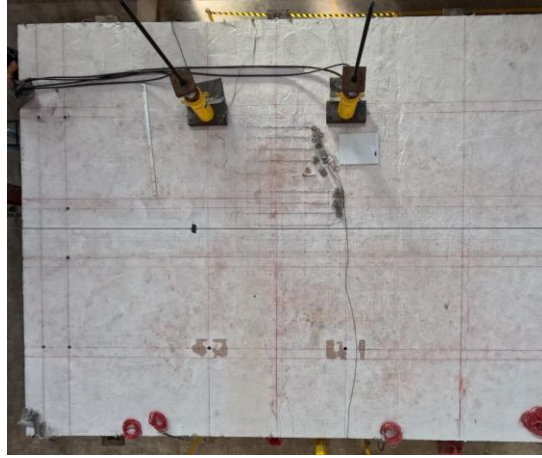
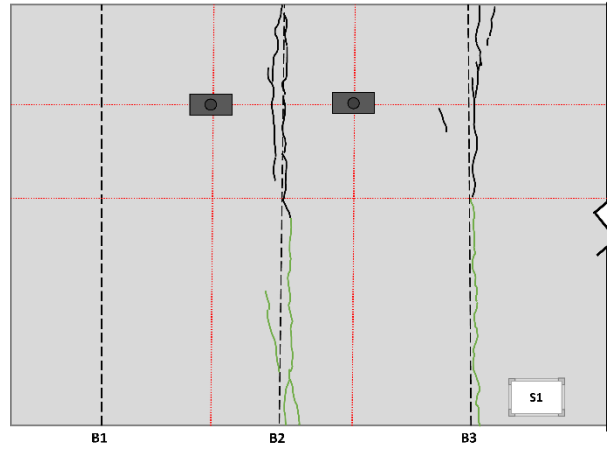


Figure 6.13 Single axle over girder configuration

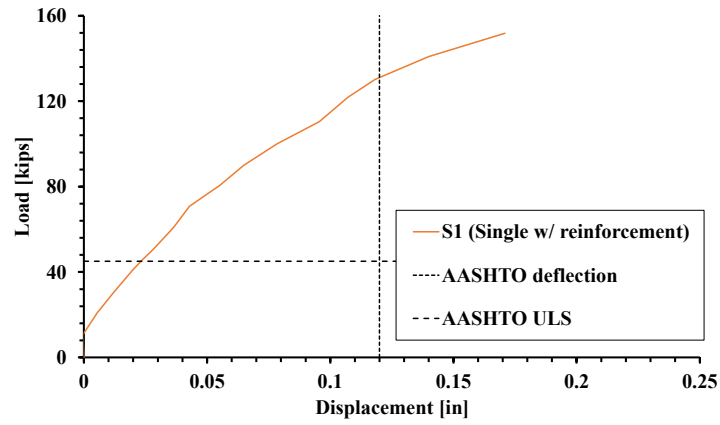
6.6.2.1. S1: Single Axle with #4 at 18 inch Spacing Reinforcement

Series S1 employed #4 reinforcement bars placed at 18 in. spacing for the top mat reinforcement. The results are depicted in Figure 6.14 (a), (b), and (c), presenting the stabilized crack pattern, the load-displacement curve, and the reinforcement strain. The findings from this experimental investigation are delineated as follows:

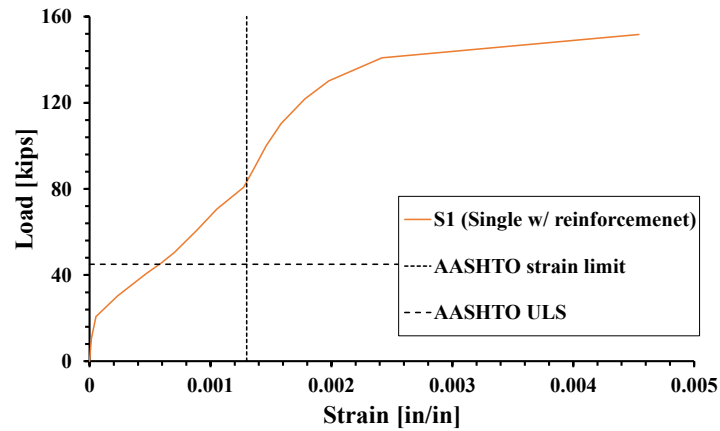
- The load-displacement curve clearly demonstrates that the structural soundness of the section with #4 reinforcement bars every 18 in. endured until it experienced a load of 150 kips. This performance significantly surpasses the required ultimate load capacity of 45 kips. Additionally, it's worth noting that the deck's displacement reached the prescribed service limit of 0.12 in. under a 130 kips load.
- Strain measurements taken across the beam region exceeded the prescribed service strain limit of 0.0013 in./in. at 83.4 kips. This finding validates specimen's strong crack resistance.
- Given the critical nature of the region S2, Single axle without reinforcement, in terms of crack resistance, region without reinforcement was tested earlier. The extent of crack width over the girder region was notably influenced by the outcomes of the preceding test, S2. Therefore, a comprehensive analysis concerning crack width will be expounded upon in the subsequent section 6.6.2.2.



(a)



(b)



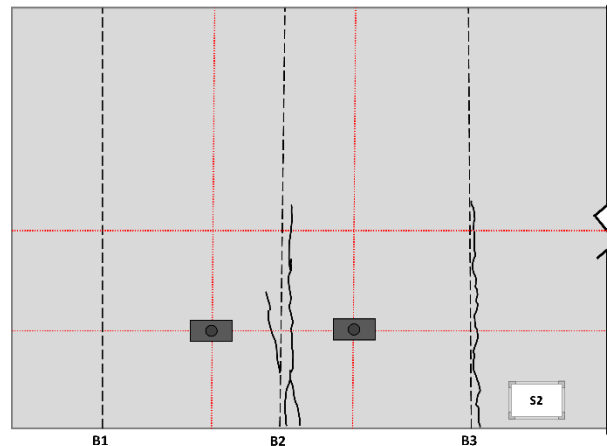
(c)

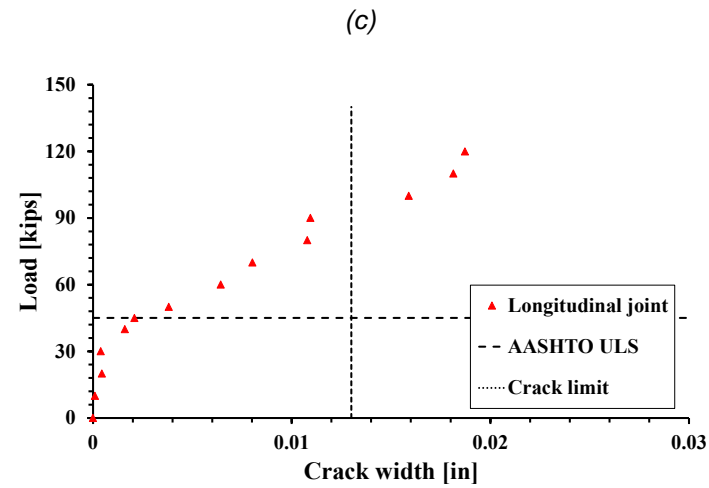
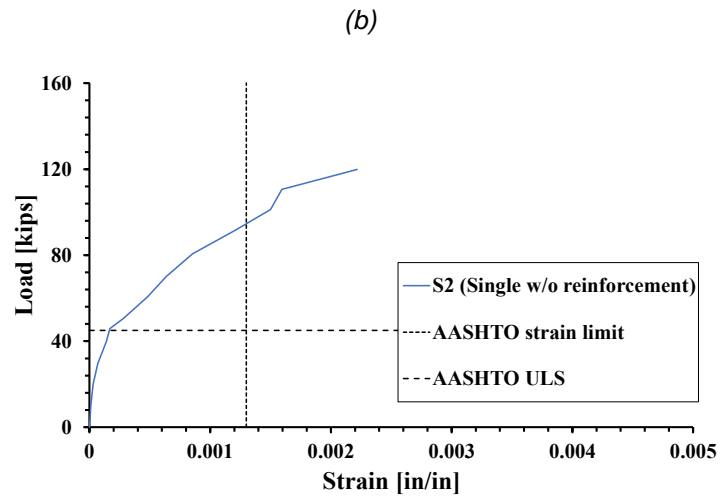
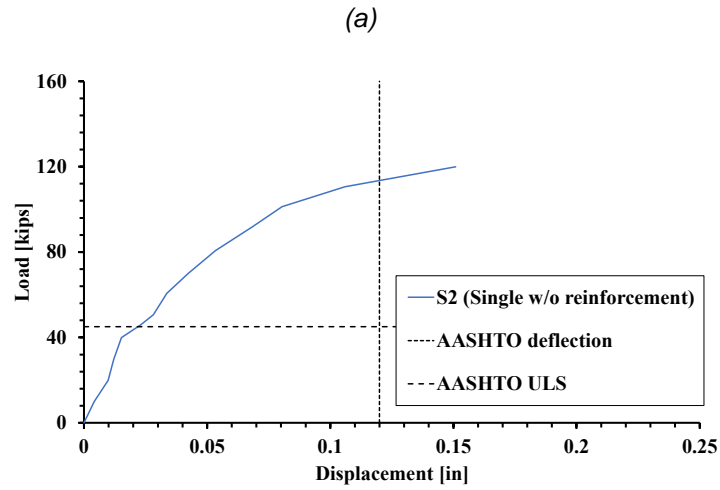
Figure 6.14 S1 region test results, (a) stabilized crack pattern, (b) load-displacement curve, and (c) maximum reinforcement strain

6.6.2.2. S2: Single Axle without Reinforcement

In the context of Series S2, the experimental region was intentionally fabricated without the inclusion of top mat reinforcement. The results of this specific configuration are succinctly presented in Figure 6.15 (a), (b), (c), and (d), which respectively portray the stabilized crack pattern, load-displacement curve, strain measurements using VWGs, and the maximum extent of crack width. The ensuing insights derived from this comprehensive experimentation are expounded upon as follows:

- The load-displacement curve stands as a testament to the structural integrity of the unreinforced section, which exhibited remarkable resilience by sustaining loading until a magnitude of 120 kips. This performance significantly surpasses the required ultimate load capacity of 45 kips. Furthermore, it is noteworthy that the deck's displacement reached the prescribed service limit of 0.12 in. when subjected to a loading of 113.5 kips.
- Strain measurements taken across the beam region exceeded the established service strain limit of 0.0013 in./in. at 94.6 kips. This outcome underscores the specimen's inherent capability to withstand the development of cracks, thus demonstrating an excellent level of crack resistance.
- Initial crack occurred at 70 kips loading. This was followed by the development of more cracks near the panel edges, which widened progressively as the loading continued. Additionally, a specific crack occurrence within the B2 region surpassed the designated width limit of 0.013 in. under a load of 93 kips. This implies that a non-reinforced SFRC topping can adequately bear loads without experiencing excessive cracking.





(d)

Figure 6.15 S2 region test results, (a) stabilized crack pattern, (b) load-displacement curve, (c) maximum reinforcement strain, and (d) maximum crack width

6.6.3. Tandem Axle Load

The transverse direction panel joints were exposed to Tandem axle loads, which produce maximum flexural stresses on the panel and result in cracking occurring in proximity to the transverse panel joint. To replicate the influence of a tandem wheel situated at the transverse joint between precast panels, a configuration was employed involving two steel plates measuring 10 in. x 20 in. (Figure 6.16). These plates are positioned 4 ft. apart within a single panel, with one positioned at the panel joint and the other at the panel's center. This choice of configuration sought to facilitate the observation of the most susceptible bending scenario, with the span length aligned to TxDOT's maximum of 10 ft. Furthermore, this specific setup strategically generated the yield-line in the vicinity of the transverse panel-to-panel joint, thereby capturing a crack-resisting capacity of the panel joint.



Figure 6.16 Tandem axle near panel joints configuration

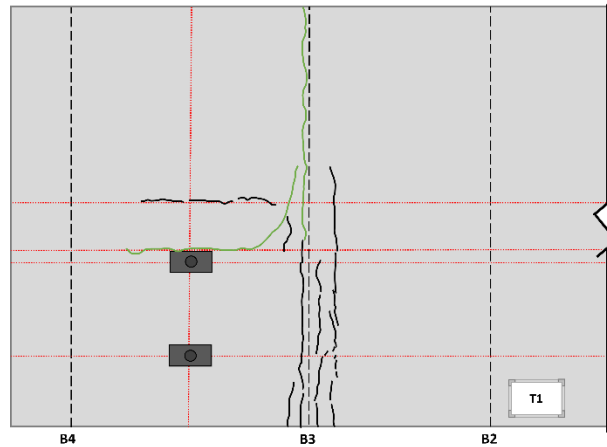
6.6.3.1. T1: Tandem Axle with #4 at 18 inch Spacing Reinforcement

In Series T1, a setup was used where #4 reinforcement bars were placed 18 in. apart, forming the top mat reinforcement. The results of this setup are displayed in Figure 6.17 (a), (b), and (c), which show the stabilized crack pattern, the load-displacement curve, and the reinforcement strain, respectively.

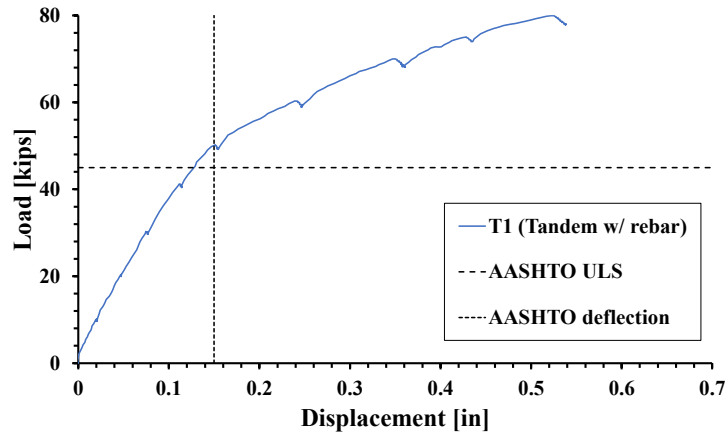
From this experiment, the test results reveal the following:

- The load-displacement curve clearly shows that the part with #4 reinforcement bars every 18 in. stayed strong until it faced a load of 80 kips. This is higher than the required ultimate strength of 45 kips. Also, it is important to mention that when the load was 50.6 kips, the deck's deflection reached the allowed limit of 0.15 in.

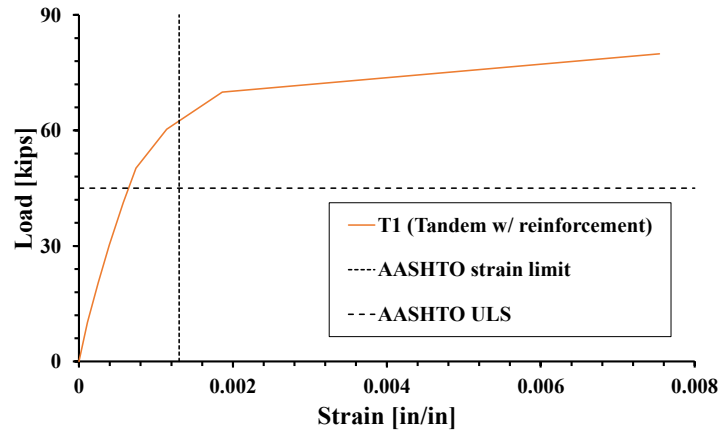
- Strain measurements taken across the beam area went beyond the service limit of 0.0013 in./in. at 62.5 kips. This finding indicates that the specimen can effectively resist cracking.
- The cracks from the earlier test significantly impacted the width of cracks in the girder area. Because the previous test, particularly T2: Tandem axle without reinforcement, is a more critical case in crack resistance, we will provide a detailed explanation of crack width in the following part.



(a)



(b)



(c)

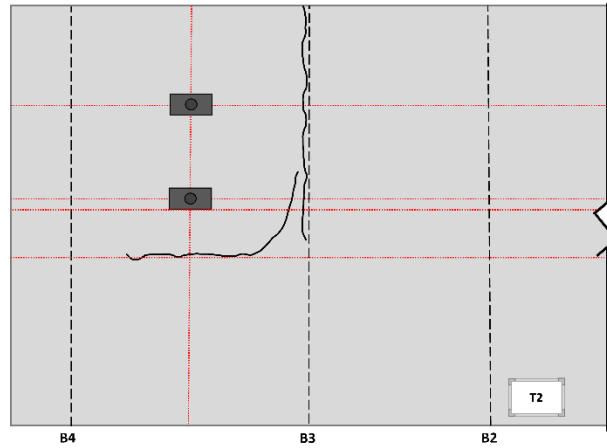
Figure 6.17 T1 region test results, (a) stabilized crack pattern, (b) load-displacement curve, and (c) maximum reinforcement strain

6.6.3.2. T2: Tandem Axle without Reinforcement

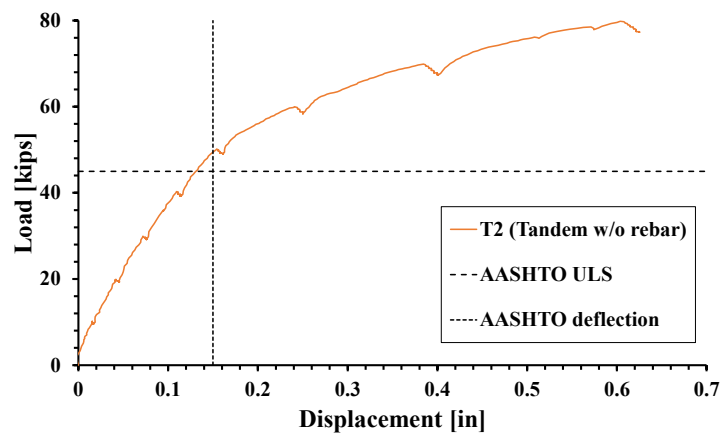
Within Series T2, the designated experimental region was deliberately constructed without the inclusion of top mat reinforcement. The outcomes of this distinct arrangement are concisely depicted in Figure 6.18 (a), (b), (c), (d), and (e), which respectively convey the stabilized crack pattern, load-displacement curve, VWGs strain measurements, and the maximum extent of crack width at both longitudinal and transverse panel joints. The ensuing insights drawn from this thorough experimentation are elaborated upon as follows:

- The load-displacement curve stands as a testament to the structural robustness of the unreinforced section, enduring loading until reaching a magnitude of 80 kips. This significantly surpasses the required ultimate strength of 45 kips. Additionally, it is pertinent to highlight that at a load of 49.3 kips, the deflection of the deck reached the service limit of 0.15 in.
- Strain measurements taken across the beam region exceeded the service limit of 0.0013 in./in. at 80.7 kips. This observation attests to the specimen's ability to effectively resist the formation of cracks.
- The presence of an initial longitudinal crack along the girder-line is attributed to the influence of the preceding test. Subsequently, small hairline cracks progressively widened as loading continued. Notably, a specific crack occurrence within the B3 region exceeded the prescribed width limit of 0.013 in. under a load of 51.7 kips.

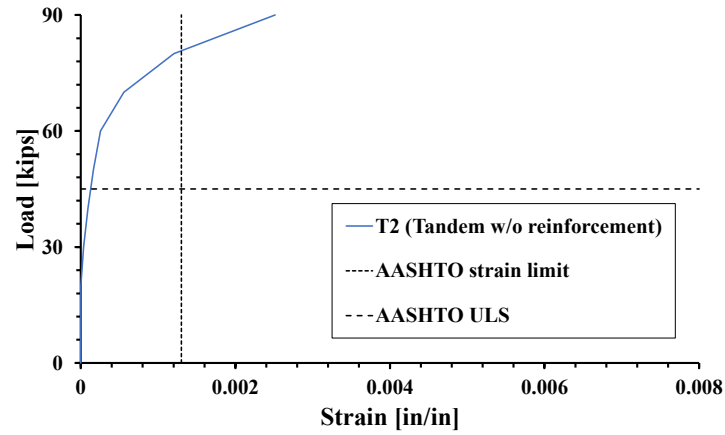
- Conversely, the first crack on the transverse joint emerged at 60 kips, gradually widening with increasing load until reaching the crack limit of 0.013 in. at 71.8 kips.



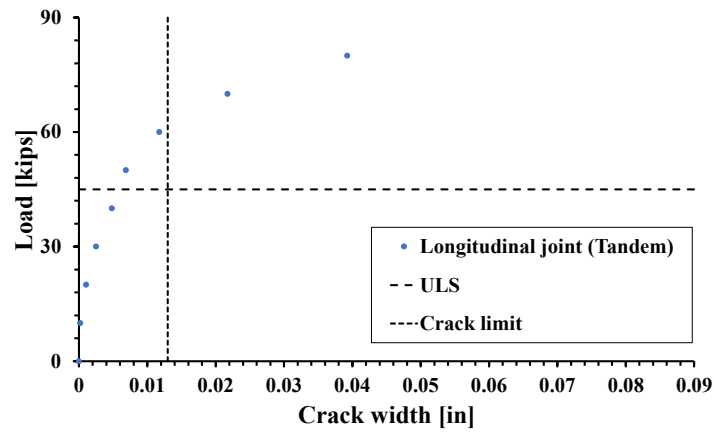
(a)



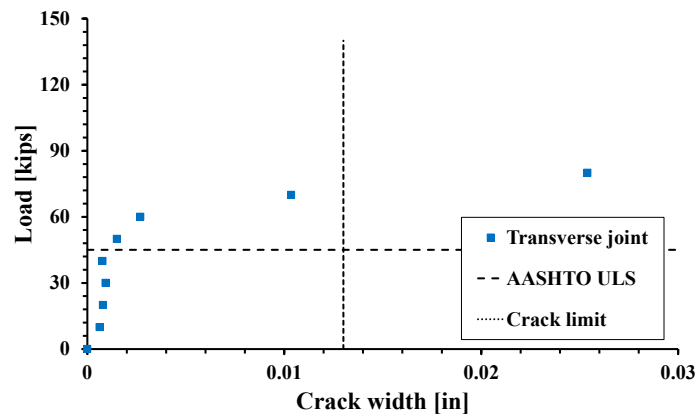
(b)



(c)



(d)



(e)

Figure 6.18 T2 region test results, (a) stabilized crack pattern, (b) load-displacement curve, (c) maximum reinforcement strain, (d) maximum crack width of longitudinal direction, and (e) maximum crack width of transverse direction

6.6.4. Overhang Load

In the evaluation of overhang regions, two distinct loading scenarios were examined: loading at the designated AASHTO-LRFD overhang loading location and loading at the overhang edge. The layout of the edge loading condition is depicted in Figure 6.19. The decision to test the edge loading condition is attributed to the laboratory's constraints on conducting rail impact loading tests. The results from the edge loading scenario informed the utilization of yield-line analysis to estimate appropriate reinforcement layouts for the overhang regions.

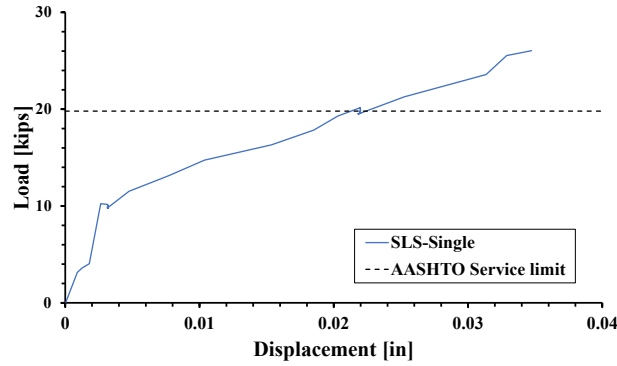
The reinforcement strategies for the overhang region aimed at decreasing the quantity of top transverse and bottom longitudinal reinforcements. The top transverse reinforcements dropped down to 42%, 21%, and 0% (no reinforcement) of the standard TxDOT reinforcement. For bottom longitudinal reinforcement, one section followed the TxDOT standard reinforcement guidelines, while another utilized 50% of the TxDOT standard reinforcement, and the third section had no reinforcement.



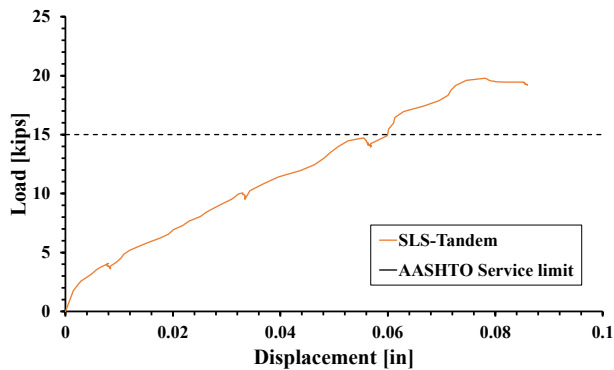
Figure 6.19 Overhang edge loading configuration

6.6.4.1. Overhang Service Limit Test

Initially, single axle and tandem loads were applied at the prescribed AASHTO-LRFD loading position. The outcomes for single and tandem axle tests are shown in Figure 6.20 (a) and (b). The results revealed that the specimen remained within the service displacement limit of 0.13 inches under the service load condition, and there were no visible signs of cracking.



(a)



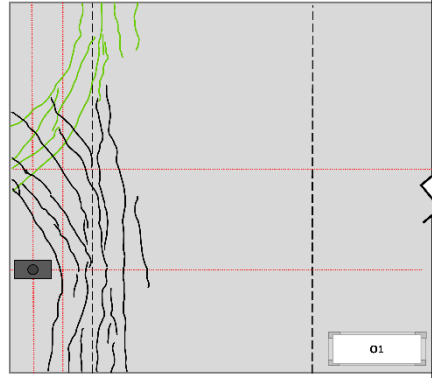
(b)

Figure 6.20 Service level (a) single axle loading and (b) Tandem loading

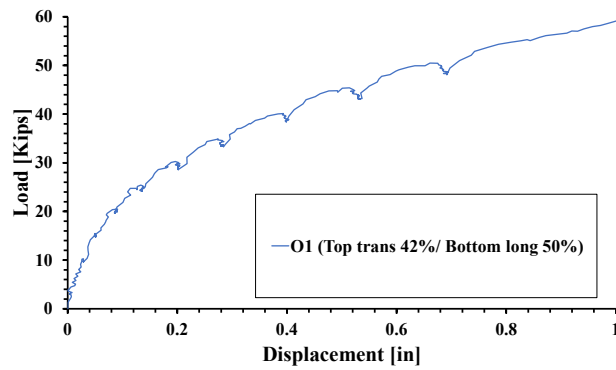
6.6.4.2. O1

Within O1 test, the top transverse reinforcements dropped down to 42% of the standard TxDOT reinforcement. In addition, both longitudinal top and bottom reinforcement were reduced to 50%. Transverse bottom reinforcement followed the TxDOT standard reinforcement guidelines. The outcomes of this distinct arrangement are concisely depicted in Figure 6.21 (a), (b), and (c), which respectively convey the stabilized crack pattern, load-displacement curve, and crack resisting capability, respectively. The ensuing insights drawn from this thorough experimentation are elaborated upon as follows:

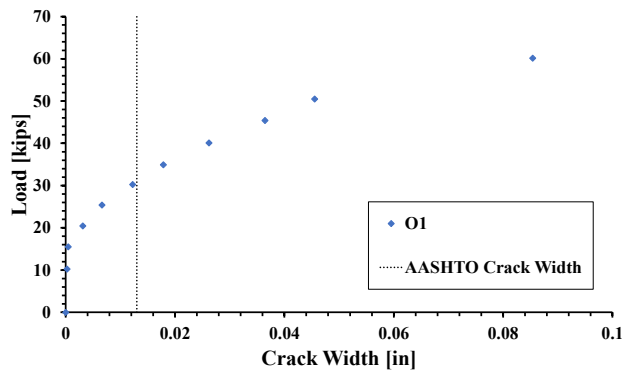
- The load-displacement curve stands as a testament to the structural robustness of the overhang region. The test was performed until 60 kips, and the structure maintained structural integrity up to 60 kips.
- Measurement of cracks utilizing Optotrak and a crack ruler revealed that the maximum crack in the region surpassed the service crack limit at a load of 30.9 kips.



(a)



(b)



(c)

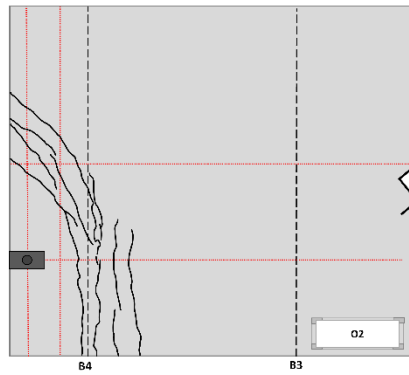
Figure 6.21 O1 region test result: (a) stabilized crack, (b) load-displacement curve, and (c) crack width measurement

6.6.4.3. O2

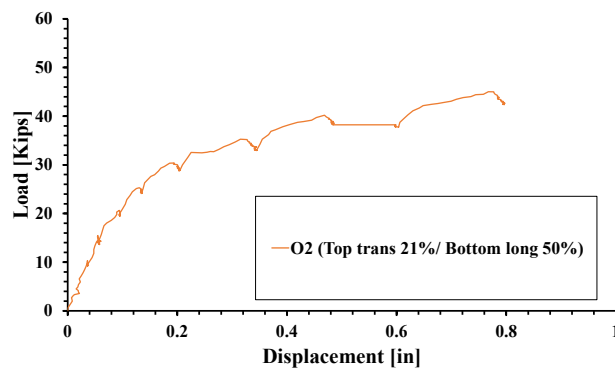
In the O2 test, the upper transverse reinforcements decreased to 21% of the standard TxDOT reinforcement, while both the longitudinal top and bottom reinforcements were reduced to 50%. The transverse bottom reinforcement adhered to the TxDOT

standard guidelines. The results of this specific configuration are succinctly illustrated in Figure 6.22 (a), (b), and (c), which respectively depict the stabilized crack pattern, load-displacement curve, and crack-resisting capability. The subsequent insights derived from this comprehensive experimentation are elucidated as follows:

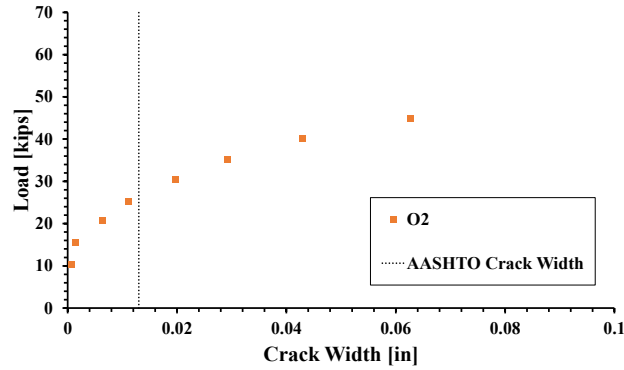
- In the O2 region, a test was conducted up to 45 kips to avoid complete structural collapse. The integrity of the structure was sustained until the end of the test.
- The examination of cracks using Optotrak and a crack ruler unveiled that, at a load of 26.4 kips, the maximum crack in the region exceeded the prescribed service crack limit.



(a)



(b)



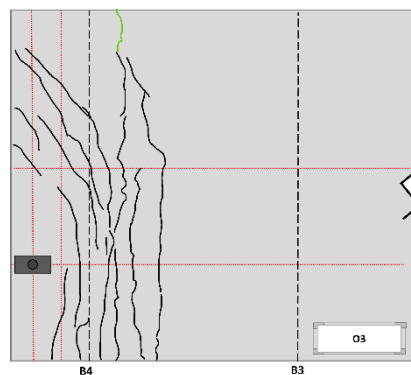
(c)

Figure 6.22 O2 region test result: (a) stabilized crack, (b) load-displacement curve, and (c) crack width measurement

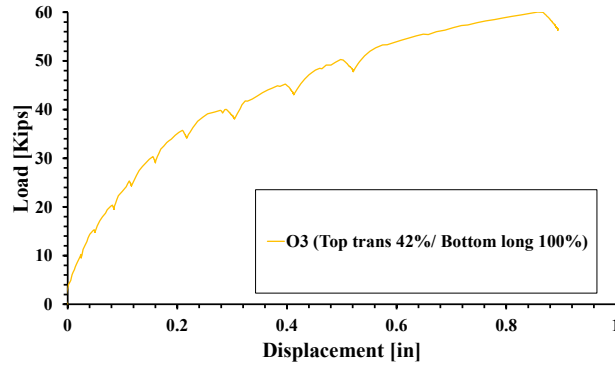
6.6.4.4. O3

During the O3 test, the upper transverse reinforcements were reduced to 42% of the standard TxDOT reinforcement, and the longitudinal top reinforcements were reduced to 50%. The transverse and longitudinal bottom reinforcements adhered to the TxDOT standard guidelines. The outcomes of this arrangement are presented in Figure 6.23 (a), (b), and (c), illustrating the stabilized crack pattern, load-displacement curve, and crack-resisting capability, respectively. The subsequent insights derived from this thorough experimentation are expounded upon as follows:

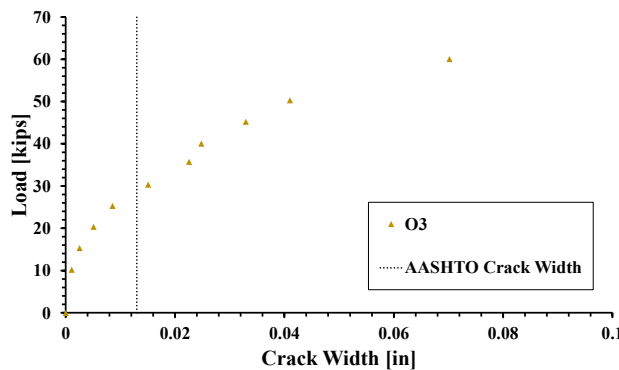
- Within the O3 region, a test was undertaken up to 60 kips to prevent total structural collapse, and the structural integrity remained intact until the conclusion of the test.
- During the test, the maximum crack within the region surpassed the designated service crack limit at a load of 28.7 kips.



(a)



(b)



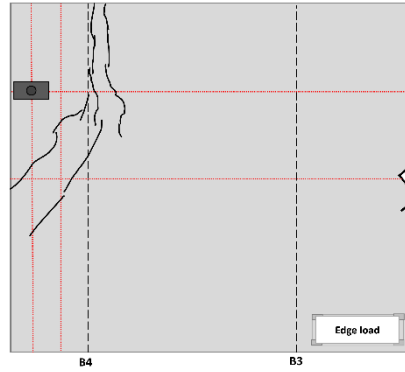
(c)

Figure 6.23 O3 region test result: (a) stabilized crack, (b) load-displacement curve, and (c) crack width measurement

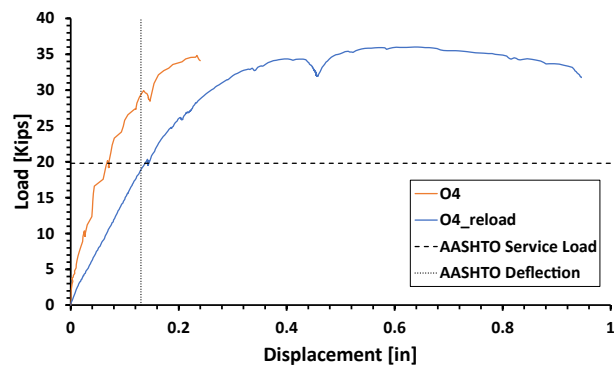
6.6.4.5. O4

Contrary to other regions, O4 did not incorporate any reinforcement. The outcomes of this arrangement are presented in Figure 6.24 (a), (b), and (c), illustrating the stabilized crack pattern, load-displacement curve, and crack-resisting capability, respectively. Observations drawn from this experimentation are elaborated upon as follows:

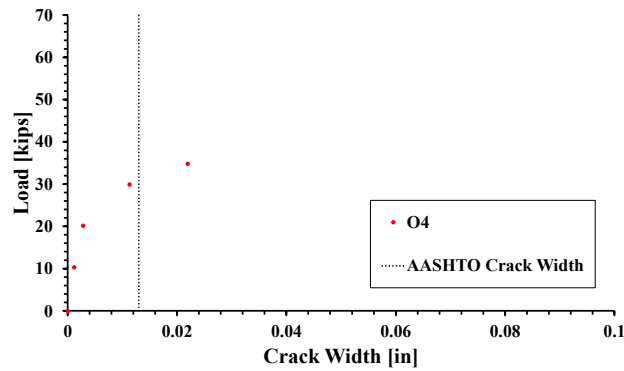
- Initially, the test was conducted up to 35 kips to avert complete structural collapse. Following the experiments of all other overhang regions, an additional test was carried out in the O4 region, revealing structural failure at a 36 kips load.
- the maximum crack within the region exceeded the specified service crack limit at a load of 30.7 kips. Given that region O4 underwent testing before other overhang regions, the result signifies the crack resistance specific to the overhang region.



(a)



(b)



(c)

Figure 6.24 O4 region test result: (a) stabilized crack, (b) load-displacement curve, and (c) crack width measurement

6.7. Analysis of Test Results

This section provides a concise overview of the noteworthy findings extracted from the interior region test results. As the load conditions of the overhang differ from

the actual loading scenario, the analysis of overhang region will be addressed through a yield-line analysis in the subsequent section.

In the section, the research team begins by assessing the structural integrity of the SFRC bridge deck. This evaluation will involve a comparison of load-displacement curves from tandem axle loading cases—considered the most challenging scenario for deck loading—with the AASHTO ultimate load and AASHTO deflection limit. Subsequently, the discussion will delve into the reinforcement strain observed in single axle and tandem axle load cases. Lastly, the section will address the crack resistance performance of specimens lacking reinforcement, covering both longitudinal and transverse panel joints.

6.7.1. Load-Displacement Curves

In this section, the analysis is centered around the most demanding condition for deck loading, characterized by a tandem axle load applied to a panel spanning the longest 10 ft. of a TxDOT bridge deck. As evidenced by the results presented in Figure 6.25, both specimens, one with and the other without reinforcement, exhibited comparable behavior. This observation suggests that the presence of top mat reinforcement is not directly indicative of the capacity of the CIP-PCP bridge deck. Furthermore, the outcomes highlight that the specimens have a factor of safety that is higher than 1.8, confirming their robust structural integrity.

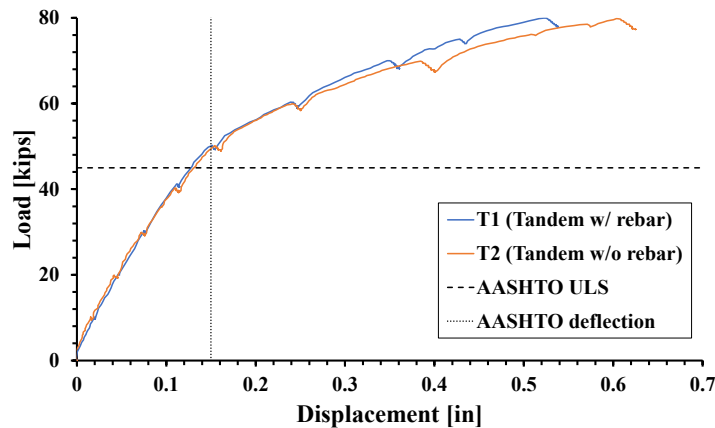


Figure 6.25 Load-displacement curves of Tandem loading cases

6.7.2. Reinforcement Strain Limit

Placed at a longitudinal panel joint with a separation of 6 ft., single axle loads produce maximum negative moment along the girder region. However, the presence of an extant crack in the reinforced region, denoted as S1, imparts a lower

initial stiffness compared to the unreinforced region, labeled as S2 (refer to Figure 1). As the load escalates beyond the 110 kips threshold, S1 showcases a superior load-bearing capacity relative to S2. This underscores that the unreinforced specimen upholds its crack-resistance capabilities up to the substantial load of 110 kips, surpassing the ultimate load by a factor of 2.4. Figure 6.26 provides detailed information.

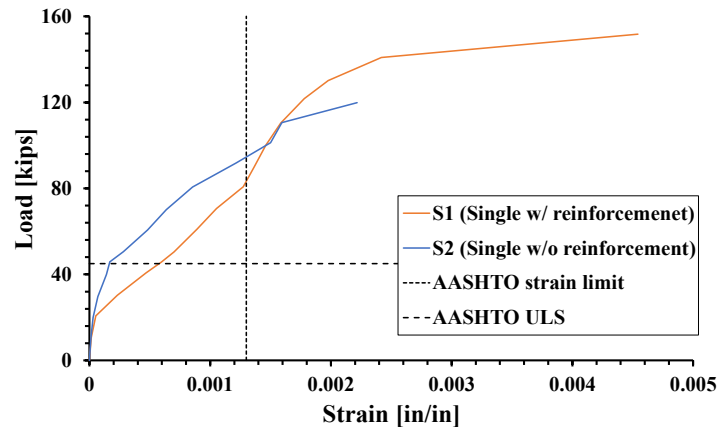


Figure 6.26 Load-strain curves of Tandem loading cases

6.7.3. Crack Resisting Performance

To accurately assess cracks in critical areas, crack width gauges and precise non-contact Optotrak optical measurement equipment were employed. Because the specimen was continuous, the research team marked specific sites to evaluate crack resistance performance. We started by examining areas without reinforcement since the deck strip test results showed improved crack resistance in regions with reinforcement. Test result is described in Figure 6.27. The measurements revealed that the service-level crack width limit of 0.013 in. was surpassed at 93 kips for the longitudinal panel joint, and at 71.8 kips for the transverse panel joint. Remarkably, in both instances, the SFRC deck exhibited functional and aesthetic integrity up to 1.6 times beyond the ultimate load level and 5.5 times beyond the service load level.

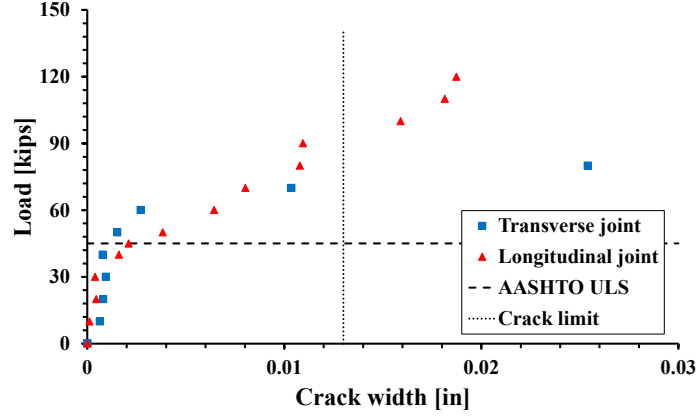


Figure 6.27 Crack measurements at transverse and longitudinal panel joints

6.8. Overhang: Yield-Line Analysis

The aim of yield-line analysis (Wight, 2017) in this research is to assess the experimental outcomes of SFRC overhangs and provide recommendations for reinforcing the overhang region. This method, known as yield-line analysis, is an upper-bound method for determining slab system failure loads, assuming plastic deformation regions create a failure pattern. Slab panels rotate as a unit around yield-lines or axes. As an upper-bound method, all potential failure mechanisms are examined, with the lowest determining the actual collapse load. The theory employs the conservation of work and energy principle, calculating internal and external work to establish specimen failure capacity. Internal and external work are computed as follows:

$$IW = \sum ml\theta \quad (6.1)$$

$$EW = \sum P\delta + w_d A_d \delta_c \quad (6.2)$$

In the context of the analysis, IW represents internal work, while EW represents external work. Here, m stands for the moment capacity per linear foot, θ represents the angle of rotation for the deflected shape, P denotes the externally applied load, δ signifies the deflection measured at the applied load, w_d represents the self-

weight of the concrete slab, A_d is the area encompassed by the failure mechanism, and δ_c indicates the deflection measured at the centroid of the failure mechanism.

The yield-line has been determined from the cracks formed during the test. Figure 6.28 illustrates the observed crack pattern at the O3 region, along with its corresponding yield-line. The negative yield-lines initiated on the deck's top surface near the support beams and extended diagonally to the center of the specimen. Negative yield-lines were represented with dashed lines, while positive yield-lines were depicted with dotted lines.

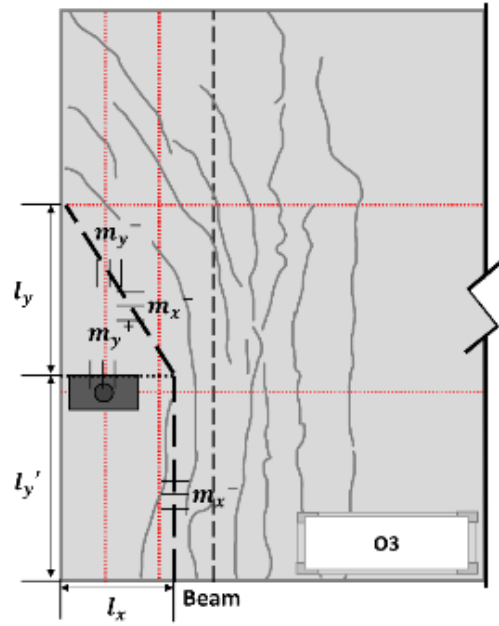


Figure 6.28 Yield-line of O3 region

From the estimated yield-line of the overhang region, the internal and external work equation can be illustrated as follows:

$$EW = P\delta + w_d\left(\frac{l_x l_y}{6} + \frac{l_x l_y'}{2}\right)\delta \quad (6.3)$$

$$IW = \frac{m_x^-}{l_x - 10} (l_y + l_y')\delta + (m_y^+ + m_y^-) \frac{l_x^2}{l_y(l_x - 10)} \delta \quad (6.4)$$

In the equation, x and y represent the transverse and longitudinal directions respectively. Hence, l_x and l_y indicate the lengths of the yield-lines in the transverse and longitudinal directions. l_y' is the length from edge of loading plate to the transverse edge. In addition, m_x^- , m_y^+ , and m_y^- represents unit moment capacities of negative longitudinal, positive transverse, and negative transverse respectively. Additionally, P is the failure load and δ is a vertical displacement at the point where P is applied.

The unit moments employed in the yield-line analysis were determined through moment-curvature calculations used in the deck strip analysis (Appendix A). The post-crack response of SFRC utilized a residual strength of 0.128 ksi, representing the average value obtained from direct tensile tests conducted throughout our experiments. Nominal moment values were extracted from theoretical moment-curvature relationships calculated for different orientations of the SFRC bridge deck. Table 6.6 provides an overview of SFRC unit capacities under various reinforcement conditions.

Table 6.6 Moment capacities calculated for yield-line analysis

| <i>Specimen ID</i> | <i>O1</i> | <i>O2</i> | <i>O3</i> |
|---------------------------|------------------|------------------|------------------|
| m_x^- | 11.2 | 7.9 | 11.2 |
| m_y^+ | 10.8 | 10.8 | 13.9 |
| m_y^- | 8.2 | 8.2 | 8.2 |

The results of the yield-line analysis are presented in Table 6.7. It is important to note that because the tests did not reach failure, there is a larger margin of error in regions O2, which was loaded only up to 45 kips, and O3, a region with higher capacity than O1. Nevertheless, these findings affirm that yield-line analysis establishes upper-bound conditions for the overhang tests. Employing the same methodology, the theoretical capacity of the TxDOT bridge overhang was estimated. The results indicated that the current TxDOT overhang capacity surpasses that of the overhang test conducted during the full-scale test.

By incorporating No. 4 bars at 18-inch spacing (0.135 in²/ft) for transverse bottom and longitudinal top and bottom, the transverse top reinforcement requires 0.45 in²/ft. Alternatively, utilizing No. 4 bars at 4.5-inch spacing (0.53 in²/ft) allows the SFRC overhang to achieve a capacity comparable to the existing TxDOT deck overhang. Furthermore, the findings reveal that under optimal concrete casting conditions, where the residual strength reached a minimum of 100 psi, the overhang's capacity reached 85.7 kips, a value comparable to the TxDOT overhang capacity.

Table 6.7 Summary of yield-line analysis for overhang regions

| | P_{SFRC}^{EXP} [kips] | P_{SFRC}^{Theory} [kips] | Error (%) | P_{PC}^{Theory} [kips] | $P_{Recommend}^{Theory}$ [kips] |
|----|----------------------------|-------------------------------|--------------|-----------------------------|------------------------------------|
| O1 | 60.1 | 64.6 | 7.0 | 85.1 | 89.2 |
| O2 | 45 | 51.4 | 12.5 | | |
| O3 | 60.1 | 68.1 | 11.7 | | |

6.9. Summary and Conclusions

In summary, the test results of the full-scale SFRC CIP-PCP bridge deck yield five key findings. The drawings of the recommended reinforcement layout are presented in Figure 6.29.

1. The flexural tests based on ASTM C1609 were conducted on the SFRC utilized in the CIP section of the full-scale specimen. The measured service residual stresses, represented by $L/600$, ranged from 480 psi to 650 psi. As a result, the suggested design has the potential to accommodate all other SFRC designs with a service residual strength surpassing 480 psi.
2. Fiber A SFRC mix showed comparable load-resisting performance in the interior region, both with and without reinforcement, when compared to the conventional TxDOT standard design that utilizes plain concrete with a 9-inch reinforcement spacing.
3. The analysis of load-displacement behavior across regions with and without reinforcement underscores the similarity in structural capacities of the CIP-PCP bridge deck. This observation suggests that the capacity is not intrinsically tied to the presence of top mat reinforcement.
4. Regions lacking reinforcement demonstrated the ability to uphold serviceability and structural integrity, akin to regions with reinforcement, up to 1.6 times beyond the stipulated AASHTO ultimate load requirement.
5. According to the yield-line analysis, it is recommended to use No. 4 bars at 18-inch spacing ($0.135 \text{ in}^2/\text{ft}$) for transverse bottom and longitudinal top and bottom reinforcement. Additionally, for the top transverse reinforcement, No. 4 bars at 4.5-inch spacing are necessary. The recommended reinforcement layout is described in Figure 6.29. It is important to note that these recommendations are applicable to SFRC with a residual strength exceeding 100 psi.

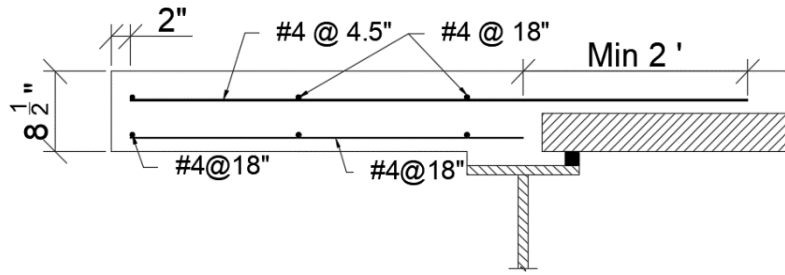


Figure 6.29 Recommended overhang reinforcement layout

Chapter 7. Conclusion and Design Recommendations

7.1. Overview

This section outlines the conclusions drawn from prior tasks and establishes a comprehensive guideline for constructing a bridge deck using steel fiber-reinforced concrete (SFRC). The recommendations include appropriate SFRC mix designs, modified reinforcements layout, and essential considerations for the construction of SFRC CIP-PCP bridge decks.

7.2. Findings from Material Testing Program

The overall findings of this study show that the incorporation of steel fibers into bridge deck concrete mixtures significantly improves the mechanical and durability properties of concrete. Three different shapes of the fibers were tested in combination with various ratios of fibers and binder compositions. When considering the use of steel fibers in bridge decks, it was found that 1 percent steel fibers (by volume) was effective in improving relevant concrete properties and was sufficient to allow for substantial reductions in the amount of reinforcing steel used in bridge decks.

7.3. Findings from Casting Structural Specimen

In the experimental stage of our study, we sourced the concrete from a local ready-mixed concrete plant. The steel fibers were introduced into the concrete mix alongside the aggregate. However, during the delivery process, a disparity emerged between the anticipated and measured slump values. It appears that the inclusion of fibers in the concrete mixture contributed to a reduction in slump during transportation. This inconsistency in slump levels might result in issues such as uneven surfaces and diminished resistance to cracking. Consequently, we recommend that when ordering SFRC from a concrete plant, it is advisable to request concrete with a slump value approximately 3 inches higher than the initially desired level. However, it is essential to acknowledge that increasing the slump may potentially impact the strength of the concrete. Therefore, we suggest achieving the desired slump and enhancing flowability by incorporating chemical admixtures, such as superplasticizers. This approach allows for effective control of slump levels without compromising the overall strength of the concrete.

Another observation noted during the casting process was the occurrence of fiber clumps, commonly referred to as fiber balls, particularly in the case of 1-inch length

twisted fiber SFRC. In addition, during the material phase of the project, instances of fiber balling were observed in some mixtures with a volume fraction of 1.5%. However, SFRC with 1% fiber content generally did not exhibit fiber balling.

It is worth noting that, for the same volume fraction, shorter-length fibers tend to result in a higher number of fibers within the same volume of mix. Therefore, it can be inferred that fiber balling occurs when the quantity of fibers exceeds a certain level. As a result, further research is required to investigate the optimal number of fibers in mass-produced SFRC from plants that do not exhibit fiber balling. This knowledge is crucial for facilitating the broader application of current designs in practical construction scenarios.

Furthermore, inspecting the specimen through cross-section cutting demonstrated that SFRC, equipped with both 1-inch and 1.5-inch fiber lengths, effectively occupied the space between the panel and girders (see Figure 7.1). Consequently, structures with a bedding strip exceeding one inch will enable SFRC to fill the gap in the girder line. Notably, the test did not employ the 0.5-inch bedding strip, the minimum suggested by TxDOT. Therefore, further research assessing SFRC's flowability into a 0.5-inch gap would enhance the applicability of the proposed design.



Figure 7.1 1 inch panel to girder gap check: (a) 1.5 inch hooked end fiber SFRC and (b) 1 inch twisted fiber SFRC

7.4. Findings from Deck Strip Test Result

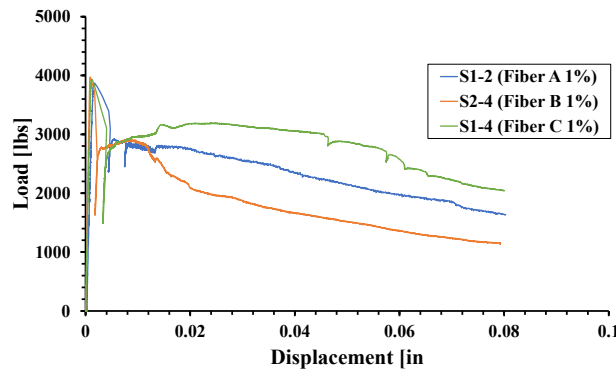
7.4.1. Material Testing

In the deck strip test, material and structural tests were carried out 28 days after casting each specimen. The mechanical properties of SFRC were evaluated through uniaxial compression, uniaxial tension, and flexural tests. In the deck strip test, three fiber types, namely Fiber A, B, and C, were utilized, each possessing distinct

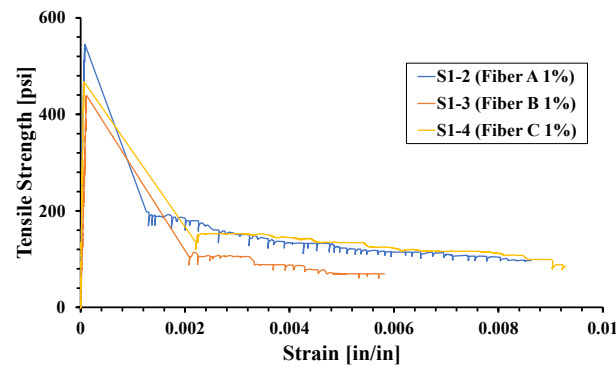
characteristics such as hooked ends with a 1.5-inch length, a crimped shape with a 1.5-inch length, and a twisted shape with a 1-inch length, respectively. Refer to Table 4.2 for detailed specifications.

Initially, results regarding compressive strength and modulus of elasticity indicated no significant differences attributable to fiber types or fiber volume. Consequently, this section predominantly focuses on the findings derived from uniaxial tension and flexural tests.

Results obtained from the uniaxial tension test and flexural beam tests exhibited similar behavior. Figure 7.2 illustrates the comparison across different fiber types, while Figure 7.3 presents the comparison based on fiber dosage. The outcomes revealed that the 1% Fiber C mix exhibited higher residual tensile strength in comparison to the Fiber A 1% and Fiber B 1% mixes. Moreover, as anticipated, higher fiber dosage showed higher capacity.

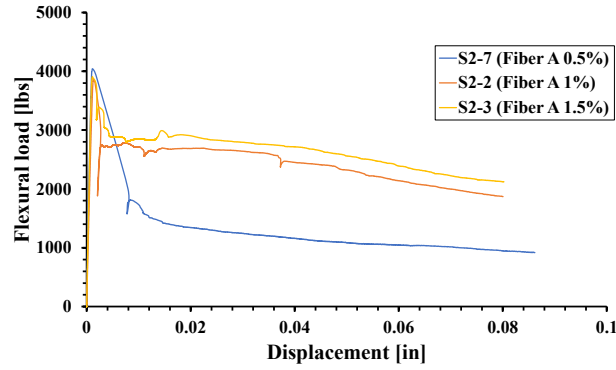


(a)

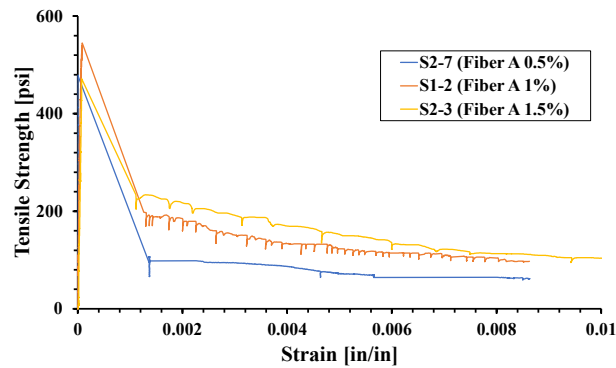


(b)

Figure 7.2 Comparison of different fiber types using (a) flexural beam test and (b) direct tension test



(a)



(b)

Figure 7.3 Comparison by fiber dosages using (a) flexural beam test and (b) direct tension test

7.4.2. Structural Testing

To evaluate the various SFRC mixes in managing fractures and withstanding loads, specialized CIP-PCP deck strip specimens were designed, constructed, and subjected to failure. This section provides a comparative analysis of load resistance and crack resistance, focusing on different fiber types and volumes incorporated into the mixtures. Considering that the specimen loading differs from actual bridge loading, 40% of the ultimate load of the control specimen was assumed as the service level load.

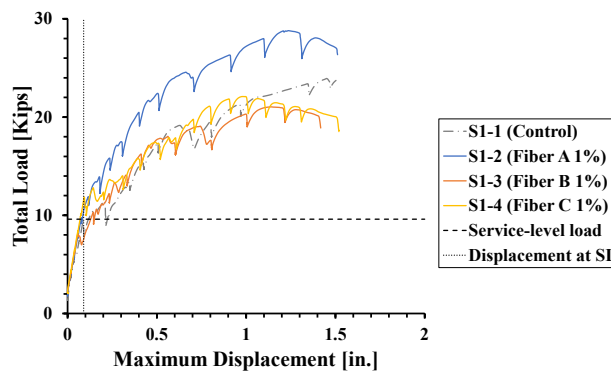
The study examined three distinct fiber types, analyzing their load-displacement curves and crack resistance performances, as shown in Figure 7.4. Remarkably, all three specimens demonstrated higher or comparable load-resisting performance compared to the TxDOT standard specimen. However, cracks on specimens with Fibers B and C had lower crack resistance than the control specimen. Nevertheless, critical cracks in these specimens did not exceed the crack limit until the assumed service level limit. On the other hand, from material testing, the 1% Fiber C mix

exhibited superior flexural performance compared to other mixes. However, in structural testing, SFRC with Fiber A outperformed Fiber C.

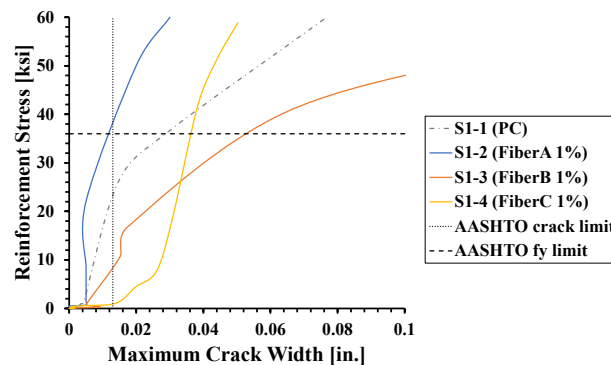
Additionally, the study investigated the influence of fiber volume by comparing SFRC with different fiber volume fractions: 1% and 1.5%. Figure 7.5 illustrates the load-displacement curve and crack resistance performance. The results suggest that these two specimens are comparable, indicating that exceeding a fiber dosage of 1% yields insignificant improvements in strength or crack width control.

In addition, with the exception of the S1-3 specimen, which exhibited a rough finish due to the low slump of concrete, all other specimens did not undergo cracking at the service level loading.

In conclusion, SFRC, with a volume fraction higher than 1% and #4 reinforcement spaced at an 18-inch interval, demonstrated comparable or higher flexural capacity and crack resistance compared to the TxDOT standard reinforcement layout. Additionally, specimens without reinforcement maintained structural integrity up to the assumed service level load of 40% of the control specimen.

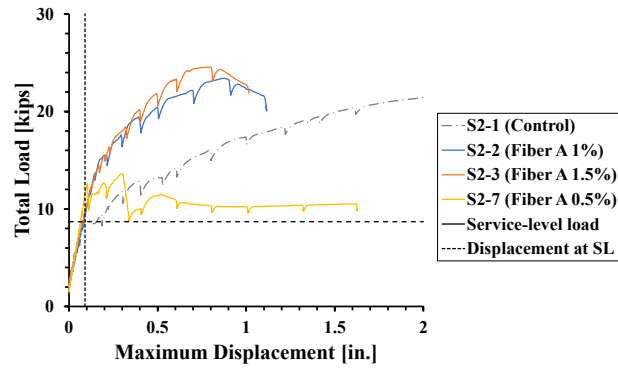


(a)

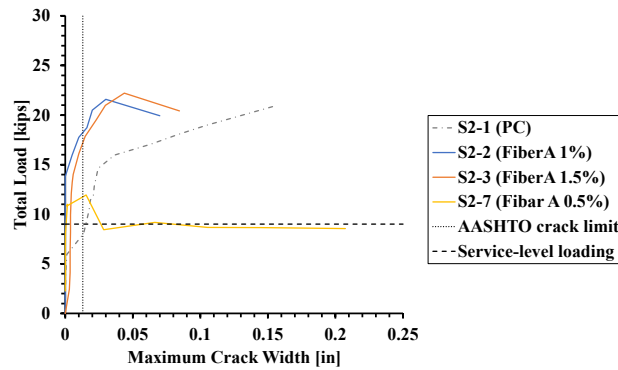


(b)

Figure 7.4 Effect of different fiber types in (a) load-displacement and (b) crack resistance



(a)



(b)

Figure 7.5 Effect of different fiber dosages in (a) load-displacement and (b) crack resistance

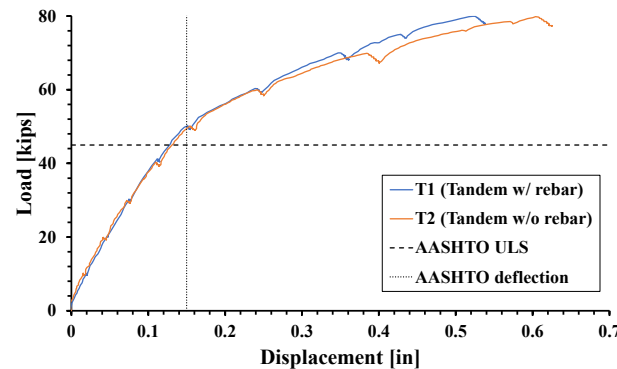
7.5. Findings from Full-Scale Test Result

7.5.1. Structural Testing

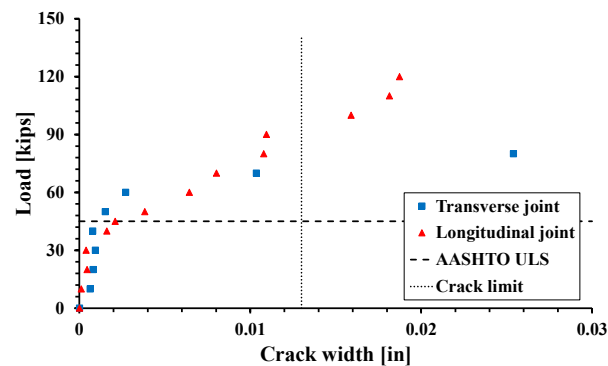
The configuration of the SFRC bridge deck's four interior regions was intentionally crafted to assess its performance under diverse conditions. These configurations involved variations in both reinforcement layouts and applied loading conditions. Specifically, modifications to the reinforcement layouts included a reduction of the existing TxDOT reinforcement by half and, in certain cases, a complete elimination of the reinforcement. Additionally, the study delved into the effects of different loading conditions, conducting simulations for both single-axle and tandem-axle loading scenarios.

In Figure 7.6, a summary of the results from the interior region tests is presented. The findings highlight that both reinforced and unreinforced regions demonstrated the capability to withstand the AASHTO-LRFD factored load, with a factor of safety exceeding 1.6. Notably, at both the girder line and panel joint, the SFRC CIP displayed minimal cracking even at 5.5 times beyond the service load level, underscoring its resilience and structural integrity.

The test period revealed that SFRC's residual flexural strength at $L/600$ is a minimum of 480 psi and an average of 650 psi. Therefore, when constructing the topping parts of the CIP-PCP bridge deck with SFRC having a residual strength higher than 480 psi, reinforcement is deemed unnecessary.



(a)

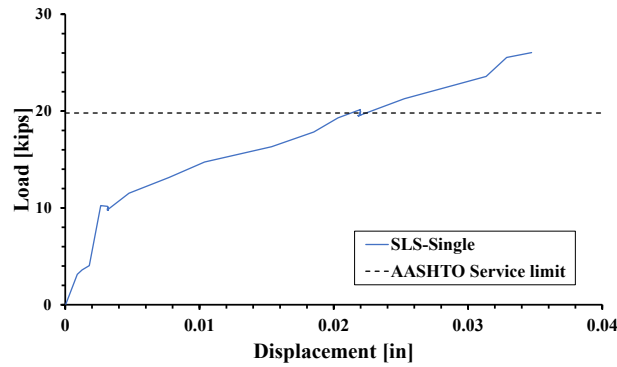


(b)

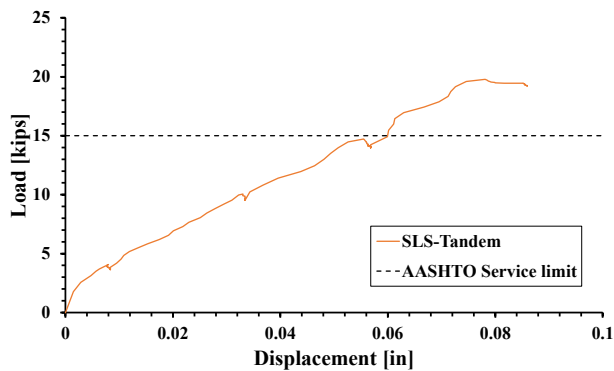
Figure 7.6 Interior test results, (a) load-displacement and (b) crack resistance

In the initial phase of testing for the overhang region, both single axle and tandem loads were applied at the specified AASHTO-LRFD loading position. The results, illustrated in Figure 7.7, demonstrated that the specimen stayed within the service displacement limit of 0.13 inches under the service load condition with no

observable signs of cracking. However, conducting rail impact loading tests in the laboratory was challenging. Therefore, yield-line analysis was employed to estimate suitable layouts for reinforcement in this area to optimize reinforcement for the extreme loading conditions on the overhang region.



(a)



(b)

Figure 7.7 Service level (a) single axle loading and (b) Tandem loading

7.5.2. Yield-line Analysis

The detailed yield-line analysis procedure is described in section 6.8. Utilizing the insights from the yield-line analysis, the reinforcement in the overhang can be further optimized to achieve a comparable capacity to the TxDOT standard. The recommended configuration includes #4 bars at 18-inch spacing ($0.135 \text{ in}^2/\text{ft}$) for the transverse bottom and longitudinal top and bottom, along with No. 4 bars at 4.5-inch spacing ($0.53 \text{ in}^2/\text{ft}$) for the transverse top reinforcement. This optimized reinforcement layout is capable of withstanding an edge loading of 89.2 kips, surpassing the capacity of the TxDOT standard, which stands at 85.1 kips.

7.6. Recommendations

In summary, this project yields five key recommendations. The drawings of the recommended reinforcement layout are presented in Figure 7.8.

1. **Prevent workability loss:** While steel fibers can be conveniently incorporated at the concrete plant, it is crucial to acknowledge that the workability of SFRC significantly decreases during delivery. To counter this, the addition of chemical mixtures that enhance workability without compromising strength becomes imperative. This approach ensures the practical implementation of SFRC in construction projects.
2. **Avoid using fiber shorter than 1 inch:** Fiber C, which has a length of 1 inch, exhibits a tendency to clump together, forming problematic fiber balls. This issue can disrupt the concrete casting process when hydraulic pumps are employed. Hence, the prudent decision would be to refrain from using 1 inch twisted shape fiber.
3. **Optimal fiber choice:** Fiber A emerged as the most effective in reinforcing concrete among the various fiber types examined. Particularly, these fibers significantly enhance the strength of reinforced concrete structures. However, it is noteworthy that exceeding a 1% volume fraction of fiber appears unnecessary.
4. **Interior regions without reinforcement:** The findings from the interior region tests highlight that interior regions without reinforcement can effectively bear traffic loads while simultaneously resisting excessive cracking. Since the minimum flexural residual strength of SFRC was 480 psi, it is advisable to use SFRC with a flexural residual strength at 0.02 inches higher than 480 psi to attain comparable performance.
5. **Overhang reinforcement layout from yield-line analysis:** According to the yield-line analysis, it is recommended to use No. 4 bars at 18-inch spacing (0.135 in²/ft) for transverse bottom and longitudinal top and bottom reinforcement. Additionally, for the top transverse reinforcement, No. 4 bars at 4.5-inch spacing are necessary. The recommended reinforcement layout is described in Figure 7.8.

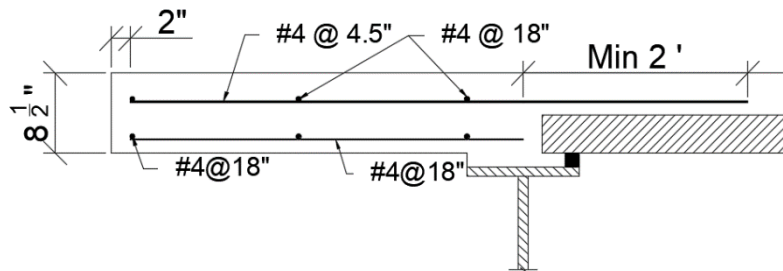


Figure 7.8 Recommended reinforcement layout

Chapter 8. Value of Research

8.1. Introduction

The following chapter introduces the value derived from the research. In assessing the qualitative benefits of the study, four distinct sections were identified and elaborated upon. The Table 8.1 provides a summary of these research benefits.

Table 8.1 Selected Benefit Area of Project 0-7001

| Benefit | Qualitative | Economic | Both | TxDOT | State | Both |
|-----------------------------------|--------------------|-----------------|-------------|--------------|--------------|-------------|
| Contribution to knowledge | X | | | X | | |
| Improvement on Engineering Design | X | | | | | X |
| Cost-effectiveness | X | | | | X | |
| Safety of structure | X | | | | | X |

8.2. Contribution to Knowledge

The construction method widely employed for precast concrete panels with an in-situ cast-in-place concrete topping is prevalent in North America. The design of the cast-in-place precast (CIP-PCP) bridge deck heavily relies on empirical design method, where structural design is determined by practical experience and experimental data. Numerous studies have been conducted to enhance existing design methods for constructing CIP-PCP bridge decks. However, established design codes like AASHTO-LRFD and ACI 318 do not address the knowledge gap concerning the use of steel fiber reinforced concrete (SFRC) as a substitute for reinforcement in the cast-in-place portion of the bridge deck. The primary reason for the limited research on this gap in knowledge is the considerable uncertainty associated with the properties of SFRC. Project 0-7001 proposes design recommendations for CIP-PCP bridge decks incorporating SFRC, including recommended material properties and reinforcement layout. The outcomes of the research are anticipated to provide valuable input for the development of an empirical design approach applicable to CIP-PCP bridge decks, serving as a reference for designers.

8.3. Improvement on Engineering Design

Studying the incorporation of steel fibers in concrete for improved performance, durability, and structural properties began in the mid-20th century. Nevertheless, the substantial uncertainty associated with SFRC hinders its adoption, standardization, and the establishment of comprehensive design codes. Project 0-7001 focused on suggesting the appropriate fiber reinforced concrete that would meet TxDOT Class S concrete for bridge deck and a reinforcement layout when incorporating this SFRC mix as a topping material of CIP-PCP bridge deck. This research proposes the essential properties that SFRC should possess to fulfill durability criteria and effectively implement the recommended reinforcement layout for CIP-PCP structures incorporating SFRC. These criteria, originating from the findings of Project 0-7001, are prepared for application as an empirical design approach. It is expected that structural designers will gain increased confidence in employing steel fibers as an alternative reinforcement in the construction of Cast-in-Place Precast bridge decks.

8.4. Cost-effectiveness

As previously mentioned, project 0-7001 addressed knowledge that can allow using SFRC as a substitute reinforcement for CIP-PCP bridge deck. The project has paved the way for more efficient and cost-effective construction practices by filling in knowledge gaps on using SFRC as topping material for CIP-PCP bridge deck. The proposed design method from this research involves the complete elimination of the interior region of the bridge deck and a 30% reduction in reinforcement for the overhang section. When implementing this method in bridge deck construction, a substantial reduction in labor, construction time, and material expenses is anticipated. Additionally, the incorporation of this approach is expected to enhance durability and crack resistance through the use of Steel Fiber Reinforced Concrete (SFRC), leading to an extended service life and reduced maintenance costs.

8.5. Safety

The conclusions drawn from Project 0-7001 indicate that the recommended design methodology has the potential to enhance the safety of the structure. As an example, the recommended reinforcement layout for the overhang region demonstrates a greater load-carrying capacity with a reduced amount of reinforcement when compared to the currently employed layout used with plain concrete. This indicates that the structure is better equipped to withstand extreme loads, such as those from car crashes on the overhang region.

References

- AASHTO LRFD (2020). *AASHTO LRFD Bridge Design Specifications, 9th Ed.*, American Association of State Highway Transportation Officials, Washington, D.C
- Abas, F. M., Gilbert, R. I., Foster, S. J., & Bradford, M. A. (2013). Strength and serviceability of continuous composite slabs with deep trapezoidal steel decking and steel fibre reinforced concrete. *Engineering Structures*, 49, 866–875. <https://doi.org/10.1016/j.engstruct.2012.12.043>
- ACI Committee 214. (2010). *Guide for Obtaining Cores and Interpreting Compressive Strength Results*. Farmington Hills, MI: ACI.
- ACI Committee 318. (2019). *Building Code Requirements for Structural Concrete (ACI 318-19) and Commentary (ACI 318R-19)*. Farmington Hills, Michigan: ACI.
- ACI Committee 544. (1996). *Report on Fiber Reinforced Concrete* (p. 64). Farmington Hills, Michigan: ACI.
- ACI Committee 544. (2008). *Guide for Specifying, Proportioning, and Production of Fiber-Reinforced Concrete* (p. 16). Farmington Hills, Michigan: ACI.
- ACI Committee 544. (2015). *Report on Design and Construction of Steel Fiber-Reinforced Concrete Elevated Slabs* (p. 44). Farmington Hills, Michigan: ACI.
- ACI Committee 544. (2016a). *Report on Design and Construction of Fiber-Reinforced Precast Concrete Tunnel Segments* (p. 36). Farmington Hills, Michigan: ACI.
- ACI Committee 544. (2016b). *Report on Indirect Method to Obtain Stress-Strain Response of Fiber-Reinforced Concrete (FRC)* (p. 28). Farmington Hills, Michigan: ACI.
- ACI Committee 544. (2017). *Report on the Measurement of Fresh State Properties and Fiber Dispersion of Fiber-Reinforced Concrete* (p. 24). Farmington Hills, Michigan: ACI.
- ACI Committee 544. (2018). *Guide to Design with Fiber-Reinforced Concrete* (p. 44). Farmington Hills, Michigan: ACI.
- Ahmad, S., Pilakoutas, K., Khan, Q. U. Z., & Neocleous, K. (2015). *Stress–strain model for low-strength concrete in uni-axial compression*. *Arabian Journal for Science and Engineering*, 40, 313–328.
- ASTM. (2019). *Standard Test Method for Flexural Performance of Fiber-Reinforced Concrete (Using Beam With Third-Point Loading)* (No. C1609/C1609M; p. 9). West Conshohocken, Pennsylvania: ASTM International.

- Aveston, J., & Kelly, A. (1973). Theory of multiple fracture of fibrous composites. *Journal of Materials Science*, 8(3), 352–362. <https://doi.org/10.1007/BF00550155>
- Barros, J. A. O., & Figueiras, J. A. (1999). Flexural Behavior of SFRC: Testing and Modeling. *Journal of Materials in Civil Engineering*, 11(4), 331–339. [https://doi.org/10.1061/\(ASCE\)0899-1561\(1999\)11:4\(331\)](https://doi.org/10.1061/(ASCE)0899-1561(1999)11:4(331))
- Bayrak, O., Chao, S.-H., Jirsa, J. O., Klingner, R. E., Azimov, U., Foreman, J., ... Woods, A. (2013). *Bridge Deck Reinforcement and PCP Cracking: Final Report* (No. FHWA/TX-12/0-6348-2; p. 356). Austin, Texas: Center for Transportation Research.
- Bencardino, F., Rizzuti, L., Spadea, G., & Swamy, R. N. (2008). Stress-Strain Behavior of Steel Fiber-Reinforced Concrete in Compression. *Journal of Materials in Civil Engineering*, 20(3), 255–263. [https://doi.org/10.1061/\(ASCE\)0899-1561\(2008\)20:3\(255\)](https://doi.org/10.1061/(ASCE)0899-1561(2008)20:3(255))
- Bentz, E. C. (2005). Explaining the riddle of tension stiffening models for shear panel experiments. *Journal of Structural Engineering*, 131(9), 1422–1425. [https://doi.org/10.1061/\(ASCE\)0733-9445\(2005\)131:9\(1422\)](https://doi.org/10.1061/(ASCE)0733-9445(2005)131:9(1422))
- Bieschke, L. A., & Klingner, R. E. (1982). *The Effect of Transverse Strand Extensions on the Behavior of Precast Prestressed Panel Bridges*. Austin, Texas: Center for Transportation Research.
- Birely, A. C., Park, P., McMahon, J. A., Shi, X., & Rew, Y. (2018). *Fiber Reinforced Concrete for Improved Performance of Transportation Infrastructure* (No. FHWA/AZ-18-705; p. 325). College Station, Texas: Texas A&M Transportation Institute.
- BSI. (2005). *Test method for metallic fibre concrete. Measuring the flexural tensile strength (limit of proportionality (LOP), residual)* (p. 20). BSI.
- Carreira, D. J., & Chu, K.-H. (1985). Stress-Strain Relationship for Plain Concrete in Compression. *ACI Journal*, 82(6), 797–804. <https://doi.org/10.14359/10390>
- CEB-FIP. (1978). *Model code for concrete structures* (3rd ed.). Paris, France.
- Chen, G., Hadi, M. N. S., Gao, D., & Zhao, L. (2015). Experimental study on the properties of corroded steel fibres. *Construction and Building Materials*, 79, 165–172. <https://doi.org/10.1016/j.conbuildmat.2014.12.082>
- Cheng, M.-Y., & Parra-Montesinos, G. J. (2010). Evaluation of Steel Fiber Reinforcement for Punching Shear Resistance in Slab-Column Connections - Part I: Monotonically Increased Load. *ACI Structural Journal*, 107(1), 101–109. <https://doi.org/10.14359/51663394>
- Chern, J.-C., & Young, C.-H. (1989). Compressive creep and shrinkage of steel fibre reinforced concrete. *International Journal of Cement Composites and Lightweight Concrete*, 11(4), 205–214. [https://doi.org/10.1016/0262-5075\(89\)90100-0](https://doi.org/10.1016/0262-5075(89)90100-0)

- Chu, S. H., Li, L. G., & Kwan, A. K. H. (2018). Fibre factors governing the fresh and hardened properties of steel FRC. *Construction and Building Materials*, 186, 1228–1238. <https://doi.org/10.1016/j.conbuildmat.2018.08.047>
- Coselli, C. J., Griffith, E. M., Ryan, J. L., Bayrak, O., Jirsa, J. O., Breen, J. E., & Klingner, R. E. (2006). *Bridge Slab Behavior at Expansion Joints* (No. FHWA/TX-05/0-4418-1; p. 101). Austin, Texas: Center for Transportation Research.
- CSA. (2014). Design of concrete structures. In *A23.3-14* (6th ed.). CSA Group.
- Deluce, J. R., Lee, S.-C., & Vecchio, F. J. (2014). Crack Model for Steel Fiber-Reinforced Concrete Members Containing Conventional Reinforcement. *ACI Structural Journal*, 111(1), 93–102. <https://doi.org/10.14359/51686433>
- Destrée, X., & Mandl, J. (2008). Steel Fibre Only Reinforced Concrete in Free Suspended Elevated Slabs: Case Studies, Design Assisted by Testing Route, Comparison to the Latest SFRC Standard Documents. In J. Walraven & D. Stoelhorst (Eds.), *Tailor Made Concrete Structures: New Solutions for our Society*. <https://doi.org/10.1201/9781439828410>
- Dinh, H. H., Parra-Montesinos, G. J., & Wight, J. K. (2011). Shear Strength Model for Steel Fiber Reinforced Concrete Beams without Stirrup Reinforcement. *Journal of Structural Engineering*, 137(10), 1039–1051. [https://doi.org/10.1061/\(ASCE\)ST.1943-541X.0000362](https://doi.org/10.1061/(ASCE)ST.1943-541X.0000362)
- Dunn, M., Brehm, L., Klaiber, F. W., Phares, B. M., & Wood, D. L. (2005). Tama County's Steel Free Bridge Deck. *Proceedings of the 2005 Mid-Continent Transportation Research Symposium*. Presented at the 2005 Mid-Continent Transportation Research Symposium, Ames, Iowa.
- Effect of Steel Fiber Reinforcement on Fresh Mix Properties of Concrete. (1992). *ACI Materials Journal*, 89(4). <https://doi.org/10.14359/9751>
- Elsaigh, W. A., Kearsley, E. P., & Robberts, J. M. (2011). Modeling the Behavior of Steel-Fiber Reinforced Concrete Ground Slabs. II: Development of Slab Model. *Journal of Transportation Engineering*, 137(12), 889–896. [https://doi.org/10.1061/\(ASCE\)TE.1943-5436.0000321](https://doi.org/10.1061/(ASCE)TE.1943-5436.0000321)
- Elsaigh, W. A., Robberts, J. M., & Kearsley, E. P. (2011). Modeling the Behavior of Steel-Fiber Reinforced Concrete Ground Slabs. I: Development of Material Model. *Journal of Transportation Engineering*, 137(12), 882–888. [https://doi.org/10.1061/\(ASCE\)TE.1943-5436.0000276](https://doi.org/10.1061/(ASCE)TE.1943-5436.0000276)
- Elstner, R. C., & Hognestad, E. (1956). Shearing Strength of Reinforced Concrete Slabs. *ACI Journal Proceedings*, 53(7), 29–58. <https://doi.org/10.14359/11501>
- Ezeldin, A. S., & Balaguru, P. N. (1992). Normal- and High-Strength Fiber-Reinforced Concrete under Compression. *Journal of Materials in Civil*

- Engineering*, 4(4), 415–429. [https://doi.org/10.1061/\(ASCE\)0899-1561\(1992\)4:4\(415\)](https://doi.org/10.1061/(ASCE)0899-1561(1992)4:4(415))
- Fall, D., Shu, J., Rempling, R., Lundgren, K., & Zandi, K. (2014). Two-way slabs: Experimental investigation of load redistributions in steel fibre reinforced concrete. *Engineering Structures*, 80, 61–74. <https://doi.org/10.1016/j.engstruct.2014.08.033>
- Fanella, D. A., & Naaman, A. E. (1985). Stress-Strain Properties of Fiber Reinforced Mortar in Compression. *ACI Journal Proceedings*, 82(4), 475–483. <https://doi.org/10.14359/10359>
- Ferrara, L., & Meda, A. (2007). Relationships between fibre distribution, workability and the mechanical properties of SFRC applied to precast roof elements. *Materials and Structures*, 39(4), 411–420. <https://doi.org/10.1617/s11527-005-9017-4>
- Ferrara, L., Park, Y.-D., & Shah, S. P. (2008). Correlation among Fresh State Behavior, Fiber Dispersion, and Toughness Properties of SFRCs. *Journal of Materials in Civil Engineering*, 20(7), 493–501. [https://doi.org/10.1061/\(ASCE\)0899-1561\(2008\)20:7\(493\)](https://doi.org/10.1061/(ASCE)0899-1561(2008)20:7(493))
- fib. (2013). *fib Model Code for Concrete Structures 2010* (1st ed.). Ernst & Sohn: Berlin, Germany. <https://doi.org/10.1002/9783433604090>
- Foster, S. W. (2010). *Reducing Top Mat Reinforcement in Bridge Decks* (Master's thesis). University of Texas at Austin, Austin, Texas.
- Granju, J.-L., & Ullah Balouch, S. (2005). Corrosion of steel fibre reinforced concrete from the cracks. *Cement and Concrete Research*, 35(3), 572–577. <https://doi.org/10.1016/j.cemconres.2004.06.032>
- Gvozdev, A. A. (1960). The Determination of the Value of the Collapse Load for Statically Indeterminate Systems Undergoing Plastic Deformation. *International Journal of Mechanical Sciences*, 1(4), 322–335. [https://doi.org/10.1016/0020-7403\(60\)90051-5](https://doi.org/10.1016/0020-7403(60)90051-5)
- Hrynyk, T. D. (2013). *Behaviour and Modelling of Reinforced Concrete Slabs and Shells Under Static and Dynamic Loads* (Ph.D. thesis). Department of Civil Engineering, University of Toronto, Toronto, Ontario.
- Hrynyk, T. D., & Vecchio, F. J. (2014). Behavior of Steel Fiber-Reinforced Concrete Slabs under Impact Load. *ACI Structural Journal*, 111(5), 1213–1224. <https://doi.org/10.14359/51686923>
- Hrynyk, T. D., & Vecchio, F. J. (2015). Capturing Out-of-Plane Shear Failures in the Analysis of Reinforced Concrete Shells. *Journal of Structural Engineering*, 141(12), 04015058. [https://doi.org/10.1061/\(ASCE\)ST.1943-541X.0001311](https://doi.org/10.1061/(ASCE)ST.1943-541X.0001311)
- Hrynyk, T. D., & Vecchio, F. J. (2017). Modeling of Reinforced and Fiber-Reinforced Concrete Slabs under Impact Loads. *ACI Special Publication*, 321(8), 8.1–8.20.

- Hsu, L. S., & Hsu, C.-T. T. (1994). Stress-Strain Behavior of Steel-fiber High-Strength Concrete Under Compression. *ACI Structural Journal*, 91(4), 448–457. <https://doi.org/10.14359/4152>
- Ingerslev, A. (1923). The Strength of Rectangular Slabs. *Structural Engineering*, 1, 3–14.
- Isla, F., Ruano, G., & Luccioni, B. (2015). Analysis of steel fibers pull-out. Experimental study. *Construction and Building Materials*, 100, 183–193. <https://doi.org/10.1016/j.conbuildmat.2015.09.034>
- Jang, N. S., Kim, Y. H., & Oh, H. S. (2023). Comparison of the Prediction of Effective Moment of Inertia of FRP Rebar-Reinforced Concrete by an Optimization Algorithm. *Materials*, 16(2), 621.
- Johansen, K. W. (1962). *Yield-Line Theory*. London, England: Cement and Concrete Association.
- Kaufmann, W., & Marti, P. (1998). Structural Concrete: Cracked Membrane Model. *Journal of Structural Engineering*, 124(12), 1467–1475. [https://doi.org/10.1061/\(ASCE\)0733-9445\(1998\)124:12\(1467\)](https://doi.org/10.1061/(ASCE)0733-9445(1998)124:12(1467))
- Kaufmann, W., Mata-Falcón, J., & Amin, A. (2019). Compression Field Analysis of Fiber-Reinforced Concrete Based on Cracked Membrane Model. *ACI Structural Journal*, 116(5), 213–224. <https://doi.org/10.14359/51716763>
- Keyvani Someh, A., & Saeki, N. (1996). Prediction for the Stress-Strain Curve of Steel Fiber Reinforced Concrete. *Proceedings of the Japan Concrete Institute*, 18, 1149–1154.
- Khaloo, A. R., & Afshari, M. (2005). Flexural behaviour of small steel fibre reinforced concrete slabs. *Cement and Concrete Composites*, 27(1), 141–149. <https://doi.org/10.1016/j.cemconcomp.2004.03.004>
- Kluge, R. W., & Sawyer, H. A. (1975). Interacting Pretensioned Concrete Form Panels for Bridge Decks. *PCI Journal*, 20(3), 34–61. <https://doi.org/10.15554/pcij.05011975.34.61>
- Kwon, K. Y. (2012). *Design Recommendations for CIP-PCP Bridge Decks* (Ph.D. dissertation). University of Texas at Austin, Austin, Texas.
- Lee, S.-C., Cho, J.-Y., & Vecchio, F. J. (2011a). Diverse Embedment Model for Steel Fiber-Reinforced Concrete in Tension: Model Development. *ACI Materials Journal*, 108(5), 516–525. <https://doi.org/10.14359/51683261>
- Lee, S.-C., Cho, J.-Y., & Vecchio, F. J. (2011b). Diverse Embedment Model for Steel Fiber-Reinforced Concrete in Tension: Model Verification. *ACI Materials Journal*, 108(5), 526–535. <https://doi.org/10.14359/51683262>
- Lee, S.-C., Cho, J.-Y., & Vecchio, F. J. (2013a). Simplified Diverse Embedment Model for Steel Fiber-Reinforced Concrete Elements in Tension. *ACI Materials Journal*, 110(4), 403–412. <https://doi.org/10.14359/51685787>

- Lee, S.-C., Cho, J.-Y., & Vecchio, F. J. (2013b). Tension-Stiffening Model for Steel Fiber-Reinforced Concrete Containing Conventional Reinforcement. *ACI Structural Journal*, 110(4), 639–648. <https://doi.org/10.14359/51685749>
- Lee, S.-C., Cho, J.-Y., & Vecchio, F. J. (2016). Analysis of Steel Fiber-Reinforced Concrete Elements Subjected to Shear. *ACI Structural Journal*, 113(2), 275–285. <https://doi.org/10.14359/51688474>
- Lee, S.-C., Oh, J.-H., & Cho, J.-Y. (2015). Compressive Behavior of Fiber-Reinforced Concrete with End-Hooked Steel Fibers. *Materials*, 8, 1442–1458. <https://doi.org/10.3390/ma8041442>
- Wight, J. K. (2016). Reinforced concrete : mechanics and design / James K. Wight, F. E. Richart, Jr. Collegiate Professor, Department of Civil & Environmental Engineering, University of Michigan. (Seventh edition.). Pearson.
- Mansur, M. A., Chin, M. S., & Wee, T. H. (1999). Stress-Strain Relationship of High-Strength Fiber Concrete in Compression. *Journal of Materials in Civil Engineering*, 11(1), 21–29. [https://doi.org/10.1061/\(ASCE\)0899-1561\(1999\)11:1\(21\)](https://doi.org/10.1061/(ASCE)0899-1561(1999)11:1(21))
- Marcalíková, Z., Procházka, L., Pešata, M., Boháčová, J., & Čajka, R. (2019). Comparison of material properties of steel fiber reinforced concrete with two types of steel fiber. *IOP Conference Series: Materials Science and Engineering*, 549, 012039. <https://doi.org/10.1088/1757-899X/549/1/012039>
- Marcos-Meson, V., Fischer, G., Edvardsen, C., Skovhus, T. L., & Michel, A. (2019). Durability of Steel Fibre Reinforced Concrete (SFRC) exposed to acid attack – A literature review. *Construction and Building Materials*, 200, 490–501. <https://doi.org/10.1016/j.conbuildmat.2018.12.051>
- Marti, P., Pfyl, T., Sigrist, V., & Ulaga, T. (1999). Harmonized Test Procedures for Steel Fiber-Reinforced Concrete. *ACI Materials Journal*, 96(6), 676–685. <https://doi.org/10.14359/794>
- Mashimo, H., Isago, N., Kitani, T., & Endou, T. (2006). Effect of fiber reinforced concrete on shrinkage crack of tunnel lining. *Tunnelling and Underground Space Technology*, 21(3–4), 382–383. <https://doi.org/10.1016/j.tust.2005.12.194>
- Maya, L. F., Fernández Ruiz, M., Muttoni, A., & Foster, S. J. (2012). Punching Shear Strength of Steel Fibre Reinforced Concrete Slabs. *Engineering Structures*, 40, 83–94. <https://doi.org/10.1016/j.engstruct.2012.02.009>
- McMahon, J. A., & Birely, A. C. (2018). Experimental Performance of Steel Fiber Reinforced Concrete Bridge Deck. *Journal of Bridge Engineering*, 23(10), 04018074. [https://doi.org/10.1061/\(ASCE\)BE.1943-5592.0001287](https://doi.org/10.1061/(ASCE)BE.1943-5592.0001287)
- Merrill, B. D. (2002). *Texas' Use of Precast Concrete Stay-in-Place Forms for Bridge Decks*. Presented at the Concrete Bridge Conference.

- Michels, J., Waldmann, D., Maas, S., & Zürbes, A. (2012). Steel fibers as only reinforcement for flat slab construction – Experimental investigation and design. *Construction and Building Materials*, 26(1), 145–155. <https://doi.org/10.1016/j.conbuildmat.2011.06.004>
- Minelli, F., Conforti, A., Cuenca, E., & Plizzari, G. (2014). Are steel fibres able to mitigate or eliminate size effect in shear? *Materials and Structures*, 47(3), 459–473. <https://doi.org/10.1617/s11527-013-0072-y>
- Minelli, F., & Vecchio, F. J. (2006). Compression Field Modeling of Fiber-Reinforced Concrete Members Under Shear Loading. *ACI Structural Journal*, 103(2), 244–252. <https://doi.org/10.14359/15182>
- Mobasher, B., & Destrée, X. (2010). Design and Construction Aspects of Steel Fiber-Reinforced Concrete Elevated Slabs. *ACI Special Publication*, 274(7), 95–107.
- Mohammadi, Y., Singh, S. P., & Kaushik, S. K. (2008). Properties of steel fibrous concrete containing mixed fibres in fresh and hardened state. *Construction and Building Materials*, 22(5), 956–965. <https://doi.org/10.1016/j.conbuildmat.2006.12.004>
- Munsterman, K. (2017). *Designing for Deck Stress Over Precast Panels in Negative Moment Regions* (Master's thesis). University of Texas at Austin, Austin, Texas.
- Naaman, A. E., & Chandrangsu, K. (2004). Innovative Bridge Deck System Using High-Performance Fiber-Reinforced Cement Composites. *ACI Structural Journal*, 101(1). <https://doi.org/10.14359/12998>
- Naaman, A. E., Likhitrungsilp, V., & Parra-Montesinos, G. J. (2007). Punching Shear Response of High-Performance Fiber-Reinforced Cementitious Composite Slabs. *ACI Structural Journal*, 104(2). <https://doi.org/10.14359/18529>
- Nataraja, M. C., Dhang, N., & Gupta, A. P. (1999). Stress–strain curves for steel-fiber reinforced concrete under compression. *Cement and Concrete Composites*, 21(5–6), 383–390. [https://doi.org/10.1016/S0958-9465\(99\)00021-9](https://doi.org/10.1016/S0958-9465(99)00021-9)
- Roesler, J. R., Lange, D. A., Altoubat, S. A., Rieder, K.-A., & Ulreich, G. R. (2004). Fracture of Plain and Fiber-Reinforced Concrete Slabs under Monotonic Loading. *Journal of Materials in Civil Engineering*, 16(5), 452–460. [https://doi.org/10.1061/\(ASCE\)0899-1561\(2004\)16:5\(452\)](https://doi.org/10.1061/(ASCE)0899-1561(2004)16:5(452))
- Shannag, M. J., Brincker, R., & Hansen, W. (1997). Pullout behavior of steel fibers from cement-based composites. *Cement and Concrete Research*, 27(6), 925–936. [https://doi.org/10.1016/S0008-8846\(97\)00061-6](https://doi.org/10.1016/S0008-8846(97)00061-6)
- Shoaib, A., Lubell, A. S., & Bindiganavile, V. S. (2014). Size Effect in Shear for Steel Fiber-Reinforced Concrete Members without Stirrups. *ACI Structural Journal*, 111(5), 1081–1090.

- Simões, T., Octávio, C., Valença, J., Costa, H., Dias-da-Costa, D., & Júlio, E. (2017). Influence of concrete strength and steel fibre geometry on the fibre/matrix interface. *Composites Part B: Engineering*, 122, 156–164. <https://doi.org/10.1016/j.compositesb.2017.04.010>
- Soulioti, D. V., Barkoula, N. M., Paipetis, A., & Matikas, T. E. (2011). Effects of Fibre Geometry and Volume Fraction on the Flexural Behaviour of Steel-Fibre Reinforced Concrete: Effect of Steel Fibres on Concrete Behaviour. *Strain*, 47, e535–e541. <https://doi.org/10.1111/j.1475-1305.2009.00652.x>
- Susetyo, J. (2009). *Fibre Reinforcement for Shrinkage Crack Control in Prestressed, Precast Segmental Bridges* (Ph.D. thesis). Department of Civil Engineering, University of Toronto, Toronto, Ontario.
- Susetyo, J., Gauvreau, P., & Vecchio, F. J. (2013). Steel Fiber-Reinforced Concrete Panels in Shear: Analysis and Modeling. *ACI Structural Journal*, 110(2), 285–296. <https://doi.org/10.14359/51684408>
- Susetyo, J., Vecchio, F. J., & Gauvreau, P. (2011). Effectiveness of Steel Fiber as Minimum Shear Reinforcement. *ACI Structural Journal*, 108(4), 488–496. <https://doi.org/10.14359/51682990>
- Suuronen, J.-P., Kallonen, A., Eik, M., Puttonen, J., Serimaa, R., & Herrmann, H. (2013). Analysis of short fibres orientation in steel fibre-reinforced concrete (SFRC) by X-ray tomography. *Journal of Materials Science*, 48(3), 1358–1367. <https://doi.org/10.1007/s10853-012-6882-4>
- Tan, K. H., & Venkateshwaran, A. (2017). Punching Shear in Steel Fibre Reinforced Concrete Slabs Without Traditional Reinforcement. *IOP Conference Series: Materials Science and Engineering*, 246, 012025. <https://doi.org/10.1088/1757-899X/246/1/012025>
- Texas Department of Transportation (Ed.). (2015). *Bridge Division Standard: Prestressed Concrete Panels Deck Details*. Texas Department of Transportation.
- Vecchio, F. J. (2000). Disturbed Stress Field Model for Reinforced Concrete: Formulation. *Journal of Structural Engineering*, 126(9), 1070–1077. [https://doi.org/10.1061/\(ASCE\)0733-9445\(2000\)126:9\(1070\)](https://doi.org/10.1061/(ASCE)0733-9445(2000)126:9(1070))
- Vecchio, F. J., & Collins, M. P. (1986). The Modified Compression-Field Theory for Reinforced Concrete Elements Subjected to Shear. *ACI Journal*, 83(2), 219–231. <https://doi.org/10.14359/10416>
- Voo, J. Y. L., & Foster, S. J. (2003). Variable Engagement Model for the Design of Fibre Reinforced Concrete Structures. *Advanced Materials for Construction of Bridges, Buildings, and Other Structures III*, 1–10. Davos, Switzerland.
- Wong, P. S., Vecchio, F. J., & Trommels, H. (2013). *VecTor2 & FormWorks user's manual*. Toronto, Ontario: University of Toronto.

- Ye, Z. B., Huang, R. Y., Li, Y. C., Lv, L., Zhao, K., Zhang, Y. L., ... Lin, J. J. (2018). Steel fiber-reinforced concrete under impact loading dynamic constitutive equation. *Construction and Building Materials*, 190, 1049–1055. <https://doi.org/10.1016/j.conbuildmat.2018.09.118>
- Zarrinpour, M. (2015). Investigation of the Size Effect in Shear of Steel Fiber Reinforced Concrete (SFRC) Slender Beams. *High Performance Fiber Reinforced Cement Composites*, 8.
- Zile, E., & Zile, O. (2013). Effect of the fiber geometry on the pullout response of mechanically deformed steel fibers. *Cement and Concrete Research*, 44, 18–24. <https://doi.org/10.1016/j.cemconres.2012.10.014>

Appendix A. Sectional Analysis of Deck Strip

The following findings derived from the deck strip test have been juxtaposed with the nominal moment strength derived from the moment-curvature relationship. The deck strip test model, which disregards the influence of precast panels, is justified by the critical crack region near panel joints being primarily linked to the nominal capacity of the specimen. The compressive strength curve of SFRC adheres to the Hognestad parabola, with the compressive strength determined through ASTM C39 tests conducted concurrently with structural testing. On the other hand, the concrete tensile strength and constant residual strength of SFRC are based on outcomes from the dog-bone direct tensile test. The example of concrete behavior is shown in Figure A.1.

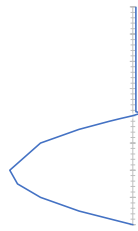


Figure A.1 Assumed concrete behavior for sectional analysis

Comparisons between experimental results and analytical findings are presented in Table A1. The moment curvature model, employed to forecast experimental moment capacity, exhibits an average error of 5.6 percent, with the maximum error reaching 17.5 percent. This significant error in the S1-4 specimen can be attributed to the overestimation of material properties of Fiber C.

Table A1. Analysis Results of Deck Strip Tests

| Specimen ID | SFRC type | Experimental [kips] | Analysis [kips] | Exp/Anlys |
|-------------|--------------|---------------------|-----------------|-----------|
| S1-1 | PC | 12.7 | 13.3 | 1.05 |
| S1-2 | Fiber A 1% | 15.3 | 15.5 | 1.01 |
| S1-3 | Fiber B 1% | 11.6 | 12.1 | 1.05 |
| S1-4 | Fiber C 1% | 12.1 | 14.7 | 1.21 |
| S2-1 | PC | 13.3 | 12.1 | 1.02 |
| S2-2 | Fiber A 1% | 15.5 | 11.9 | 0.95 |
| S2-3 | Fiber a 1.5% | 12.1 | 14.1 | 1.05 |
| S2-4 | Fiber B 1% | 14.7 | 11.5 | 1.04 |
| Maximum | | 1.21 | | |
| Average | | 1.05 | | |
| Std. Dev. | | 0.09 | | |